Advances in Meteorology

# Advances in Remote Sensing to Understand Extreme Hydrological Events

Lead Guest Editor: Dongkyun Kim
Guest Editors: Minha Choi, Jongho Kim, and Ungtae Kim

# Advances in Remote Sensing to Understand Extreme Hydrological Events

Advances in Meteorology

# Advances in Remote Sensing to Understand Extreme Hydrological Events

Lead Guest Editor: Dongkyun Kim
Guest Editors: Minha Choi, Jongho Kim, and Ungtae Kim

# Contents

Hindawi
Advances in Meteorology
Volume 2019, Article ID 8235037, 2 pages
https://doi.org/10.1155/2019/8235037

*Editorial*

# Advances in Remote Sensing to Understand Extreme Hydrological Events

**Dongkyun Kim**,[1] **Minha Choi**,[2] **Jongho Kim**,[3] **and Ungtae Kim**[4]

[1]*Department of Civil Engineering, Hongik University, Seoul, Republic of Korea*
[2]*Department of Water Resources, Graduate School of Water Resources, Sungkyunkwan University, Suwon, Republic of Korea*
[3]*School of Civil and Environmental Engineering, University of Ulsan, Ulsan, Republic of Korea*
[4]*Department of Civil and Environmental Engineering, Cleveland State University, Cleveland, OH, USA*

Correspondence should be addressed to Dongkyun Kim; kim.dongkyun@hongik.ac.kr

Received 17 October 2019; Accepted 17 October 2019; Published 12 November 2019



Hydrological extreme events [1, 2] often lead to catastrophes for humans [3] and the environment [4]. The identification, understanding, modeling, validation, and prediction of hydrological extreme events are crucial in preventing such catastrophes and eventually developing a system that is resilient to them, but such tasks are challenging. This is because it is difficult to obtain a comprehensive understanding of extreme events in which spatiotemporal characteristics vary significantly, and the corresponding damage that typically occurs over a spatial extent of several thousand kilometers.

The weather radar and the satellite-based remote sensing techniques are two major research branches to resolve these issues. Weather radar provides the near-real-time precise and accurate observation of precipitation over the spatial coverage encompassing several hundred kilometers. While traditional studies regarding weather radar have focused on the calibration [5, 6], bias correction [7], validation, and uncertainty estimation [8, 9] of radar measurements, recent studies investigated the topics of merging ground and radar precipitation data [10–12], storm movement tracking and forecast [13–15], application to urban flash flood and warning [16, 17], and design parameter estimation [18, 19]. The satellite remote sensing techniques allow us to observe a variety of components of hydrological cycle at a global scale. They have been developed for the estimation of water and energy fluxes between the land surface and atmosphere in terms of space and time. The major water and energy fluxes are land surface temperature, soil moisture, evapotranspiration, snow water equivalent, and vegetation/land cover [20].

In addition, technologies regarding radar and satellite sensors and satellite launchers have been advancing remarkably. The X-band radar instruments have been developed to figure out the Z-R relationships based on the shape of the rain drops and to capture rainfall intensity at the spatial resolutions of a few meters within a few kilometers of radius [21, 22]; the acquisition period for optical and SAR satellite images is already getting as shorter as less than one day [23].

This dramatic advance in the remote sensing techniques will eventually revolutionize the design and management framework to make current anthropogenic systems more agile and efficient against natural disasters. For example, the radar-gauge merging techniques and the accumulating length of the radar precipitation records enable a more thorough understanding of the characteristics of extreme precipitation including their whole spatial pattern, temporal progress, and interactions with other environmental variables, which subsequently yields more realistic and cost-effective design parameters [24] and agile real-time flood warning systems customized to the urban areas as small as several square kilometers [25].

In this era of abundant remote sensing data, the mission of hydrologists is evident: actively utilizing the data; extending the dimension of our understanding of nature; and returning the benefits to the human and environment.

## Conflicts of Interest

The editors declare that there are no conflicts of interest regarding the publication of this issue.

## Acknowledgments

We would like to give our special thanks to all reviewers for their constructive comments to improve the quality of the submitted papers. The efforts of Dr. Dongkyun Kim to handle the submitted manuscripts and writing this editorial were financially supported by a grant (MOIS-DP-2015-05) through the Disaster and Safety Management Institute funded by Ministry of the Interior and Safety of Korean Government.

*Dongkyun Kim*
*Minha Choi*
*Jongho Kim*
*Ungate Kim*

## References

[1] M. L. Bernhardt, J.-L. Briaud, A. V. Govindsamy et al., "Mississippi river levee failures: June 2008 flood," *International Journal of Geoengineering Case Histories*, vol. 2, no. 3, pp. 127–162, 2011.

[2] J. Yang, D. Gong, W. Wang, M. Hu, and R. Mao, "Extreme drought event of 2009/2010 over southwestern China," *Meteorology and Atmospheric Physics*, vol. 115, no. 3-4, pp. 173–184, 2012.

[3] J. O. Ogutu and N. Owen-Smith, "ENSO, rainfall and temperature influences on extreme population declines among African savanna ungulates," *Ecology Letters*, vol. 6, no. 5, pp. 412–419, 2003.

[4] A. R. Gitlin, C. M. Sthultz, M. A. Bowker et al., "Mortality gradients within and among dominant plant populations as barometers of ecosystem change during extreme drought," *Conservation Biology*, vol. 20, no. 5, pp. 1477–1486, 2006.

[5] E. N. Anagnostou, M. N. Anagnostou, W. F. Krajewski, A. Kruger, and B. J. Miriovsky, "High-resolution rainfall estimation from X-band polarimetric radar measurements," *Journal of Hydrometeorology*, vol. 5, no. 1, pp. 110–128, 2004.

[6] M. N. Anagnostou and E. N. Anagnostou, *Precipitation: Advances in Measurement, Estimation and Prediction*, S. Michaelides, Ed., Springer, Berlin, Germany, 2008.

[7] D.-J. Seo, J. Breidenbach, and E. R. Johnson, "Real-time estimation of mean field bias in radar rainfall data," *Journal of Hydrology*, vol. 223, no. 3-4, pp. 131–147, 1999.

[8] R. V. Calheiros and I. Zawadzki, "Reflectivity-rain rate relationships for radar hydrology in Brazil," *Journal of Climate and Applied Meteorology*, vol. 26, no. 1, pp. 118–132, 1987.

[9] W. F. Krajewski and J. A. Smith, "Radar hydrology: rainfall estimation," *Advances in Water Resources*, vol. 25, no. 8–12, pp. 1387–1394, 2002.

[10] S. Sinclair and G. Pegram, "Combining radar and rain gauge rainfall estimates using conditional merging," *Atmospheric Science Letters*, vol. 6, no. 1, pp. 19–22, 2005.

[11] E. Goudenhoofdt and L. Delobbe, "Evaluation of radar-gauge merging methods for quantitative precipitation estimates," *Hydrology and Earth System Sciences*, vol. 13, no. 2, pp. 195–203, 2009.

[12] S. Ochoa-Rodriguez, L.-P. Wang, P. Willems, and C. Onof, "A review of radar-rain gauge data merging methods and their potential for urban hydrological applications," *Water Resources Research*, vol. 55, no. 8, pp. 6356–6391, 2019.

[13] L. Han, S. Fu, L. Zhao, Y. Zheng, H. Wang, and Y. Lin, "3D convective storm identification, tracking, and forecasting—an enhanced TITAN algorithm," *Journal of Atmospheric and Oceanic Technology*, vol. 26, no. 4, pp. 719–732, 2009.

[14] N. Peleg and E. Morin, "Convective rain cells: radar-derived spatiotemporal characteristics and synoptic patterns over the eastern Mediterranean," *Journal of Geophysical Research: Atmospheres*, vol. 117, no. D15, 2012.

[15] D. Tiranti, R. Cremonini, F. Marco, A. R. Gaeta, and S. Barbero, "The defense (debris Flows triggEred by storms—nowcasting system): an early warning system for torrential processes by radar storm tracking using a Geographic Information System (GIS)," *Computers & Geosciences*, vol. 70, pp. 96–109, 2014.

[16] P. B. Bedient, A. Holder, J. A. Benavides, and B. E. Vieux, "Radar-based flood warning system applied to Tropical Storm Allison," *Journal of Hydrologic Engineering*, vol. 8, no. 6, pp. 308–318, 2003.

[17] J. A. Smith, M. L. Baeck, K. L. Meierdiercks, A. J. Miller, and W. F. Krajewski, "Radar rainfall estimation for flash flood forecasting in small urban watersheds," *Advances in Water Resources*, vol. 30, no. 10, pp. 2087–2097, 2007.

[18] F. Olivera, J. Choi, D. Kim, and M.-H. Li, "Estimation of average rainfall areal reduction factors in Texas using NEXRAD data," *Journal of Hydrologic Engineering*, vol. 13, no. 6, pp. 438–448, 2008.

[19] F. Lombardo, F. Napolitano, and F. Russo, "On the use of radar reflectivity for estimation of the areal reduction factor," *Natural Hazards and Earth System Science*, vol. 6, no. 3, pp. 377–386, 2006.

[20] T. J. Schmugge, W. P. Kustas, J. C. Ritchie, T. J. Jackson, and A. Rango, "Remote sensing in hydrology," *Advances in Water Resources*, vol. 25, no. 8–12, pp. 1367–1385, 2002.

[21] S. Y. Matrosov, K. A. Clark, B. E. Martner, and A. Tokay, "X-band polarimetric radar measurements of rainfall," *Journal of Applied Meteorology*, vol. 41, no. 9, pp. 941–952, 2002.

[22] M. Thurai, K. V. Mishra, W. Krajewski, and V. Bringi, "Evaluating the use of X-band specific attenuation for rainfall estimates using Iowa XPol-5 radar scans over a network of 25 rain gauges," in *Proceedings of the 2019 13th European Conference on Antennas and Propagation (EuCAP)*, pp. 1–5, IEEE, Krakow, Poland, March 2019.

[23] Planet Team, "Planet application program interface," in *Space for Life on Earth*, Planet Team, San Francisco, CA, USA, 2017.

[24] J. Kim, J. Lee, D. Kim, and B. Kang, "The role of rainfall spatial variability in estimating areal reduction factors," *Journal of Hydrology*, vol. 568, pp. 416–426, 2019.

[25] S. Thorndahl, J. E. Nielsen, and D. G. Jensen, "Urban pluvial flood prediction: a case study evaluating radar rainfall nowcasts and numerical weather prediction models as model inputs," *Water Science and Technology*, vol. 74, no. 11, pp. 2599–2610, 2016.

Hindawi
Advances in Meteorology
Volume 2019, Article ID 6542410, 17 pages
https://doi.org/10.1155/2019/6542410

*Research Article*

# Assessing the Applicability of Random Forest, Stochastic Gradient Boosted Model, and Extreme Learning Machine Methods to the Quantitative Precipitation Estimation of the Radar Data: A Case Study to Gwangdeoksan Radar, South Korea, in 2018

**Ju-Young Shin, Yonghun Ro, Joo-Wan Cha, Kyu-Rang Kim, and Jong-Chul Ha**

*Applied Meteorology Research Division, National Institute of Meteorological Sciences, 33, Seohobuk-ro, Seogwipo-si, Jeju-do 63568, Republic of Korea*

Correspondence should be addressed to Yonghun Ro; royh1@korea.kr

Received 12 March 2019; Revised 23 July 2019; Accepted 23 August 2019; Published 7 October 2019

Guest Editor: Jongho Kim



Machine learning algorithms should be tested for use in quantitative precipitation estimation models of rain radar data in South Korea because such an application can provide a more accurate estimate of rainfall than the conventional ZR relationship-based model. The applicability of random forest, stochastic gradient boosted model, and extreme learning machine methods to quantitative precipitation estimation models was investigated using case studies with polarization radar data from Gwangdeoksan radar station. Various combinations of input variable sets were tested, and results showed that machine learning algorithms can be applied to build the quantitative precipitation estimation model of the polarization radar data in South Korea. The machine learning-based quantitative precipitation estimation models led to better performances than ZR relationship-based models, particularly for heavy rainfall events. The extreme learning machine is considered the best of the algorithms used based on evaluation criteria.

## 1. Introduction

Quantitative precipitation estimation (QPE) using remote sensing data has been widely used to investigate the spatial characteristics of precipitation events [1, 2]. This method can be used to obtain rainfall estimation at ungauged locations, cloud characteristics, and areal rainfall depth [3–6]. The spatial resolution of rain radar data is the finest of all these. While the spatial resolution of satellite images is greater than approximately 10 km, the spatial resolution of rain radar data is approximately 1 km [7–9]. Because of the spatial resolution of rain radar data, it is often applied into rainfall-runoff modeling, particularly in terms of flash flood and urban flood modeling [10, 11]. The accurate forecast of these extreme hydrological events can mitigate damages on the hydraulic infrastructure and prevent the crisis of water-related disaster on human life. The accurate QPE of radar data is the key for the accurate forecast of extreme hydrological events.

Reflectivity and rainfall rate (ZR) relationship-based models have been used broadly for QPE models of rain radar data [12–14]. Because ZR relationship can be changed based on the characteristics of the rainfall event and the radar instrument used, various methodologies are applied to build ZR relationship-based QPE models and correct their estimations [15–18]. However, the ZR relationship-based model still has high uncertainty in a rainfall estimation [19–21].

Machine learning (ML) algorithms have been widely employed to create functional relationships for natural phenomena and data processing. Many ML algorithms were developed and employed to model a function in fields such as meteorology, hydrology, and agriculture. Applications of ML algorithms can provide accurate models of natural phenomena [22–25] and thus can be good candidates for

QPE of rain radar data. Recently, random forest (RF), stochastic gradient boosted model (GBM), and extreme learning machine (ELM) have been actively employed as ML algorithms [26–28]. These advanced ML algorithms, which have been tested recently, would increase our capacity to build QPE model. Chiang et al. [29], proposed a QPE model using a recurrent neural network and three-dimensional radar data. They reported that the ML-based model produced more accurate estimations than the ZR relation-based model. Yu et al. [30] attempted to develop quantitative precipitation forecast (QPF) models of rain radar data using RF and support vector regression. Their proposed methodology focused on QPF models for typhoons in Taiwan and performed well.

To the best of our knowledge, advanced ML algorithms, e.g., RF, GBM, and ELM, have not been employed for QPE of rain radar data in South Korea. This should be resolved because applying ML algorithms may provide more accurate rainfall estimation of rain radar data than the conventional ZR relation-based model. Therefore, this study investigated the applicability of the ML algorithms for QPE using Gwangdeoksan radar station, South Korea, as a case study in order to enhance performance of QPE in radar data. RF, GBM, and ELM are the ML algorithms used; their applicability is investigated using four rainfall events, and their performances for the QPE model are compared. This study can provide fundamental information on the development of QPE model using ML algorithms in South Korea. Particularly, the characteristics of ML algorithm for QPE model of radar data can be briefly investigated in the study. This result can enhance our capacity to understanding ML algorithms in the QPE of radar data. In addition, the most plausible candidate among the employed QPE models will be selected for ML-based QPE model of radar data in South Korea. The selected QPE model can lead to improvements in accuracy of QPE, particularly in extreme rainfall events that cause extreme hydrological events. The improvement in accuracy of QPE may help to mitigate impacts from extreme hydrological events on the destruction of property and human life.

This paper is organized as follows. In Section 2, the characteristics of the radar and ground gauge rainfall data are presented. Section 3 presents a description of the methods employed, e.g., ZR relationship and ML algorithms. The application methodology for the case studies is presented in Section 4. In Section 5, the results of tested QPE models for all events and each event are presented. Finally, the conclusions are presented in Section 6.

## 2. Data

*2.1. Radar and Ground Rainfall Gauge.* Gwangdeoksan weather radar station, which has a dual-polarization weather radar with an S-band, is located on the border of Gyeonggi-do and Gangwon-do provinces close to Seoul (latitude $38^{\circ}7'2.5''$, longitude $127^{\circ}26'1''$, and elevation 1064 m), the capital of the Republic of Korea. The observation range of the Gwangdeoksan radar is 240 km, which is enough to cover the northern part of South Korea. Radar data within the effective observation range, 100 km, are applied to QPE. Considering the high elevation of this radar station, the relationship between the radar and ground rainfall gauge data is increased with the application of PPI0. PPI (plan-position indicator) is an intensity-modulated display on which echo signals are shown in plan view with range and azimuth angle displayed in polar coordinates. PPI0 is volume scanned data when the azimuth angle is 0 which represents a condition that can be observed by minimizing blocking in a flat state. Data with a spatial resolution of 1 km × 1 km and stored at 10-minute interval are applied to estimate radar rainfall.

The three main polarization parameters of the radar, i.e., reflectivity, differential reflectivity, and specific differential phases, are applied to QPE in this study. Radar reflectivity refers to the ratio between the transmitted and received energies. The differential reflectivity is the ratio between horizontal and vertical radar reflectivity; it can provide information on the sizes and shapes of raindrops. Specific differential phases are the rate of change of the range in pulse phases, because these are not affected by attenuation, partial beam blockage, or radar miscalibration; they are an attractive parameter to use in QPE [31].

Rainfall rate data from ground gauge stations in Seoul and Gyeonggi-do province within the radar umbrella are analyzed in this study. All stations obtain rainfall data every minute, but the QPE in this study uses rainfall rate data at 10-min intervals. This is to compare the radar data and to minimize the fluctuation of ground gauge data. Figure 1 shows the ground gauges densely distributed across the Korean peninsula; of these, 20 gauges within the radar effective range are selected. The number of 20 stations is located in near Seoul and had severe storm damage in the past. The location of Gwangdeoksan radar and the selected rainfall gauges are described in the zoomed area in Figure 1, and information on each station is given in Table 1. The used data can be downloaded from the data base of Korea Ministration Administration (KMA) at data.kma.go.kr.

*2.2. Rainfall Events.* Rainfall events for which the depth of the observed daily rainfall exceeded 30 mm from August to November 2018 are used. Four events are selected as case studies. Two events (the first and second) occurred from August 28–29 (event #1) and on September 3 (event #2). The third event occurred from October 5–6 (event #3), and the fourth event happened on November 8 (event #4). Heavy precipitation was observed in Korea, brought on by a rainy front (the Changma front) for event #1 and by low pressure in the northern area for event #2. Event #3 occurred as part of Typhoon KONG-REY, and event #4 was accompanied by the collision of a cold and a warm front.

Table 2 summarizes information on the total rainfall, mean rainfall rate, and standard deviation for each event at the station in Seoul (#108). The amount of rain that fell during event #1 was the largest (larger than 100 mm) in two days. Both events #1 and #4 show that the weather front greatly affected the increase in rainfall or cloud formation. The average rainfall is very large in the rainy season and

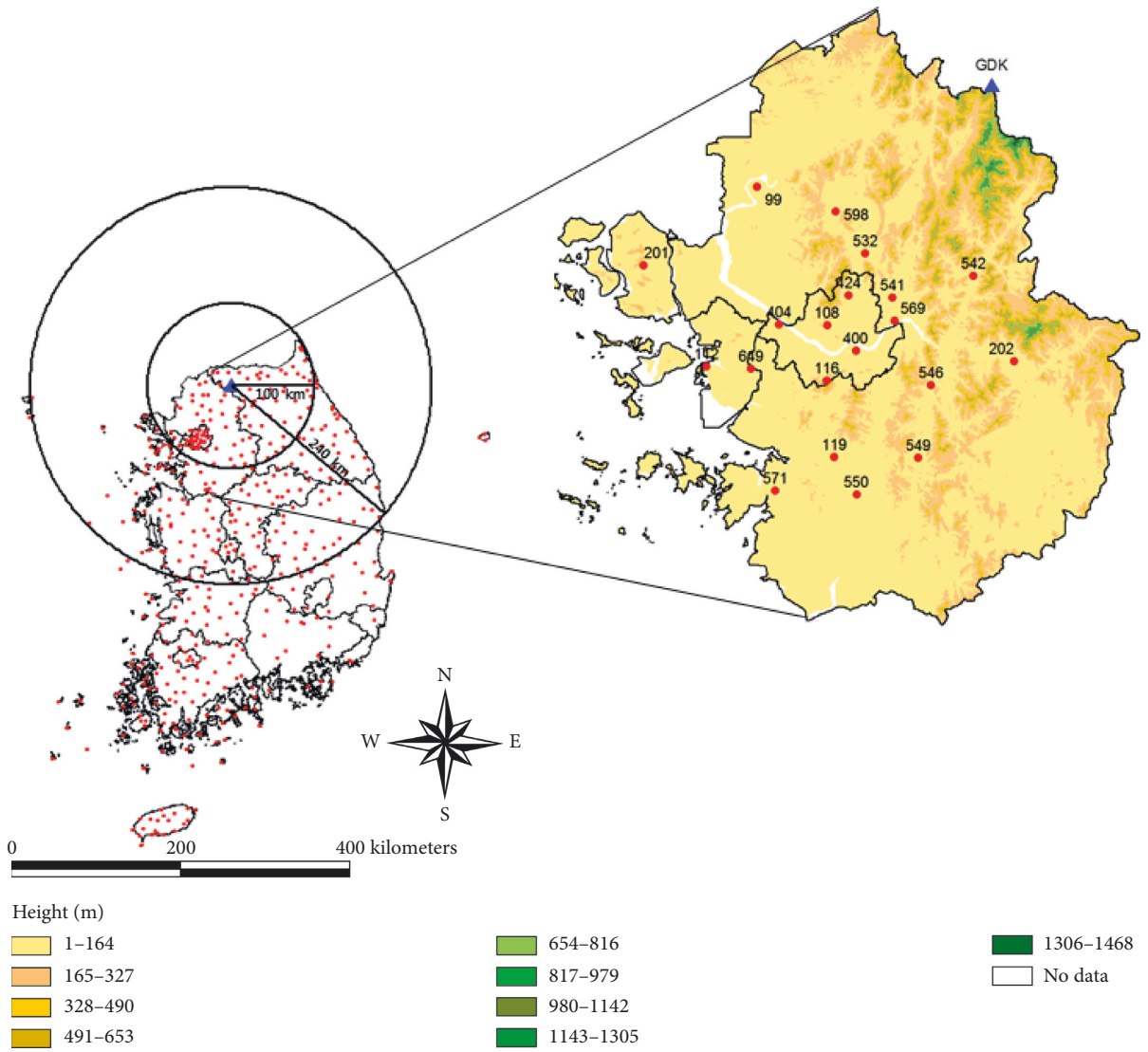


FIGURE 1: Locations of the Korea Meteorological Administration ground gauge stations (red dots) and Gwangdeoksan (GDK) radar (blue triangle) with its radar umbrella (effective radius: 100 km; maximum observation radius: 240 km). The figure in the right-hand panel presents the locations of the ground gauge stations (red dots) used in the current study.

typhoons, such as in events #1 and #3. The largest variance was observed in event #1. This heavy rainfall during the rainy season is representative of the summer monsoon climate in South Korea.

## 3. Methods

*3.1. ZR Relationship.* Radar rainfall can be defined by the relationship between radar parameters and rainfall gauge data. A variety of synthetic algorithms have been proposed to estimate quantitative radar rainfall based on the polarization parameters applied [32, 33]. The basic form of the equation, which is well-known as ZR relationship, is given as follows:

$$R = \theta_0 x_1^{\theta_1}, \ \ldots, x_d^{\theta_d}, \quad (d = 1, 2, \ \ldots, n), \tag{1}$$

where $R$ is the ground gauge rainfall rate (mm/h), $x_1, \ \ldots, x_d$ are radar polarization parameters such as reflectivity, differential reflectivity, and specific differential phase, and $\theta_0, \ \ldots, \theta_d$ are the parameters of the ZR relationship. The main radar polarization parameters are defined as the following equations:

$$\begin{aligned} Z &= 10 \log (Z_{\mathrm{H}}), \\ \mathrm{DR} &= 10 \log \left( \frac{Z_{\mathrm{H}}}{Z_{\mathrm{V}}} \right), \\ \mathrm{KD} &= \left| \frac{\varnothing_{\mathrm{DP}} (r_2) - \varnothing_{\mathrm{DP}} (r_1)}{r_2 - r_1} \right|, \end{aligned} \tag{2}$$

where $Z$ is the radar reflectivity, (changed from $\mathrm{mm}^6\mathrm{m}^{-3}$ to dBZ); $Z_{\mathrm{H}}$ and $Z_{\mathrm{V}}$ are horizontal and vertical reflectivity; DR is differential reflectivity (dB); KD is specific differential phase (deg $\mathrm{km}^{-1}$); and $\varnothing_{\mathrm{DP}}$ and $r$ are phases of the radar beam pulse and given range, respectively. Because the ZR relationship stands on the physical phenomena, the results

Table 1: Ground precipitation gauge stations selected for this study.

| Name | Code | Latitude | Longitude |
|---|---|---|---|
| Paju | 99 | 37.885 | 126.766 |
| Seoul | 108 | 37.571 | 126.965 |
| Incheon | 112 | 37.477 | 126.624 |
| Suwon | 119 | 37.272 | 126.985 |
| Ganghwa | 201 | 37.707 | 126.446 |
| Yangpyeong | 202 | 37.488 | 127.494 |
| Gwanak | 116 | 37.445 | 126.964 |
| Gangnam | 400 | 37.513 | 127.046 |
| Gangseo | 404 | 37.573 | 126.829 |
| Gangbuk | 424 | 37.639 | 127.025 |
| Uijeongbu | 532 | 37.734 | 127.073 |
| Namyangju | 541 | 37.634 | 127.150 |
| Daeseongri | 542 | 37.684 | 127.380 |
| Gwangju | 546 | 37.435 | 127.259 |
| Yongin | 549 | 37.270 | 127.221 |
| Osan | 550 | 37.187 | 127.048 |
| Guri | 569 | 37.582 | 127.156 |
| Hwaseong | 571 | 37.195 | 126.820 |
| Yangju | 598 | 37.831 | 126.990 |
| Bupyeong | 649 | 37.472 | 126.750 |

Table 2: Precipitation events selected based on observed rainfall data from Seoul station.

| No. | Periods of precipitation events | Total (mm) | Mean (mm/h) | Standard deviation (mm/h) |
|---|---|---|---|---|
| 1 | 2018.08.28. 11 : 50–2018.08.29. 22 : 20 | 138.5 | 4.0 | 11.9 |
| 2 | 2018.09.03. 08 : 50–2018.09.03. 21 : 30 | 34.5 | 2.7 | 5.8 |
| 3 | 2018.10.05. 08 : 20–2018.10.06. 12 : 20 | 92.0 | 3.3 | 3.3 |
| 4 | 2018.11.08. 01 : 30–2018.11.08. 23 : 40 | 64.0 | 2.8 | 3.5 |

of ZR relationship can be used to interpret characteristics of precipitation events, unlike the ML algorithms. The ML algorithms used in this study are the predictive models. Though they can be used to predict rain rate, extracting physical meaning from the results is difficult. For example, the parameters of ZR relationship can be used to identify type of cloud, type of precipitation, and type of storm events. In the case of the ML algorithms, prediction models for each variable of interest such as type of cloud, type of precipitation, and type of storm events have to be individually built.

### 3.2. Machine Learning (ML) Algorithms

*3.2.1. Random Forest.* RF has been widely applied in regression and forecasting problems [34–37]. It was proposed by Breiman [38] and uses bagging (called bootstrapping in statistics) to build a number of decision trees with a controlled variance. Each decision tree in the RF is grown using randomly selected samples. Subsequently, the nodes in each tree use randomly selected features (called input variables). The RF has two major steps: (1) randomness and (2) ensemble learning. The randomness in the RF comes from random sampling of the entire data set, and the selection of features with which every classification and regression tree (CART) is built. The data set is randomly sampled with replacement to create a subset with which to train one CART. At each node, optimal split rule is determined by using the one of the randomly selected features from the employed features.

The ensemble learning method in the RF means that all individual decision trees in a collection of decision trees (called an ensemble) contribute to a final prediction. A training subset is created after the random selection step. The CART without pruning is used to construct a single decision tree. To grow K trees in the ensemble, this process (resampling a subset and training an individual tree) is repeated K times. The final predicted value comes from averaging the results of all the individual trees. The *ranger* library in *r package* is used to construct the RF model in the current study [39].

*3.2.2. Stochastic Gradient Boosted Model.* GBM is a method widely used in classification and regression problems; it was proposed by Friedman [40]. Decision stumps or regression trees are used widely as weak classifiers in the GBM [40–42]. In the GBM, weak learners are trained to decrease loss functions, e.g., mean square errors. Residuals in the former weak learners are used to train the current weak learners. Therefore, the value of the loss function in the current weak learners decreases. The bagging method is employed to reduce correlation between weak learners, and each weak learner is trained with subsets sampled without replacement from the entire data set. The final prediction is obtained by combining predictions by a set of weak learners.

The GBM and RF adapted ensemble learning with a decision tree model (the weak learner). Both models produce

one prediction based on a combination of predictions from a set of weak learners. Though the methods seem to be similar, they are based on different concepts. The major difference between the GBM and RF is that the tree in the GBM is fit on the residual of a subset of the former trees while the RF trains a set of weak learners using a number of subsets. Therefore, the GBM can reduce bias of prediction while the RF method can reduce variance of prediction. Therefore, the RF can be trained in parallel computing, whereas the GBM cannot. The *gbm* library in *r package* (https://github.com/gbm-developers/gbm) is used to construct a GBM in the current study.

*3.2.3. Regularized Extreme Learning Machine.* ELM was originally developed and then extended to generalized single-hidden layer feed-forward networks in which the hidden layer need not to be neuron alike. ELM is a single-layer network in which the weights and biases between input and hidden layers are randomly generated [43]. Unlike traditional iterative learning algorithms, the randomly initiated input weights and biases of ELM remain fixed without need to iteratively tuned, and the output weights are determined analytically. Hence, the model can be trained in a single iteration which significantly reduces the training time of ELM and makes ELM efficient for online and real-time applications. The ELM can be formulized using the following equations:

$$\mathbf{Y} = \mathbf{H}\boldsymbol{\beta}, \tag{3}$$

where $\mathbf{Y}$, $\boldsymbol{\beta}$, and $\mathbf{H}$ are the outputs, weight matrix between hidden and output layers, and the output vector of the hidden layer (called nonlinear feature mapping), respectively, and

$$\mathbf{H} = f_{\mathrm{a}}(\mathbf{X}\mathbf{W} + \mathbf{B}), \tag{4}$$

where $f_{\mathrm{a}}(\cdot)$, $\mathbf{W}$, $\mathbf{B}$, and $\mathbf{x}$ are the activation function, weight matrix between the input to hidden layer, bias, and inputs, respectively. In the current study, the sigmoid function ($f_{\mathrm{a}}(x) = 1/(1 + \exp(-x))$) is used as the activation function in the ELM. Since the weights ($\mathbf{W}$) and bias ($\mathbf{B}$) are randomly generated and the activation function ($f_{\mathrm{a}}(\cdot)$) is known in the ELM, $\mathbf{H}$ represents the deterministic variables from a data set. Thus, only $\boldsymbol{\beta}$ needs to be estimated in the ELM.

In the ELM, finding an appropriate weight set is to avoid overfitting. Tuning weights in the ELM can be considered a fitting linear regression model using the ordinary least square method. Ridge regression was employed to attenuate multicollinearity in the data set by adding the norm of the parameters to the parameter estimations in the regression model [44]. The ELM model also adapted this strategy for weight tuning. The ELM attempts to perform better generalization by achieving the smallest training error and the smallest output weight norm. This minimization problem can take the form of ridge regression or regularized least squares as follows [45]:

$$\min \frac{1}{2}\|\boldsymbol{\beta}\|^2 + \frac{C}{2}\|\mathbf{H}\boldsymbol{\beta} - \mathbf{Y}\|^2, \tag{5}$$

where the first term of the objective function is $l_2$, the norm regularization term that controls the complexity of the model; the second term is the training error associated with the learned model; and $C > 0$ is a tuning parameter. The ELM gradient equation can be solved analytically, and the closed-form solution can be written as follows:

$$\hat{\boldsymbol{\beta}} = \left(\mathbf{H}^T\mathbf{H} + \frac{1}{C}\mathbf{I}\right)^{-1}\mathbf{H}^T\mathbf{Y}, \tag{6}$$

where $\mathbf{I}$ is an identity matrix. The ELM models used in this study are the regularized ELM model.

## 4. Application Methodology

To examine the applicability of the three ML algorithms, their input variables and hyperparameters should be defined. $Z$, DR, and KD in the polarization radar data have been widely employed as input variables for the QPE model. Therefore, these variables are used as input variable candidates in the ML algorithms. The tested models with input variable combinations are presented in Table 3.

Three ML algorithms use variables from both lag-zero (L0) and lag-one (L1) radar data for input variable while lag-zero and lag-one radar data, respectively, are used to construct ZR relationships. Since radar data measure the amount of cloud in the air, there is a short time difference between radar data and ground gauge observation. The time difference depends on the precipitation event conditions such as wind speed, cloud movements, and types of cloud. As the ZR relationship cannot account for time lag in its formula, QPE models based on the ZR relationship are constructed using different time-lag data and their appropriateness are investigated.

The ML algorithms can use both lag-zero and lag-one radar data simultaneously. In addition, the number of variables from the radar data (three) is much smaller than the number of data points (greater than thousands). A larger number of input variables might improve the predictability of the ML algorithms employed. Additionally, since this input variable setting can take the time lag in modeling into account automatically, additional processes such as the ZR relationship are unnecessary in ML-based models.

To evaluate the performances of the models constructed, the data set should be grouped into training and test data sets. The data from stations #112, #201, #400, #546, and #571 are used as randomly selected test data. The data at the other stations are used for the training data set. For the case of all events, the numbers of training and test data are 3652 and 1209, respectively. The numbers of training data for event 1 to 4 are 1079, 319, 1173, and 1081, respectively. The numbers of test data for event 1 to 4 are 318, 107, 441 and 343, respectively. To build a regression model using ML algorithms, their hyperparameters should be tuned. The number of the trees is the most sensitive hyperparameter for the RF and GBM [30]; hence, the number of trees for the RF and GBM are optimized. The tuning parameter and the number of

Table 3: Tested models for quantitative precipitation estimation from radar data.

| Model | Input variables | | | | |
|---|---|---|---|---|---|
| | Z | Z, DR | Z, KD | DR, KD | Z, DR, KD |
| ZR-L1 | ZR1-L1 | ZR2-L1 | ZR3-L1 | ZR4-L1 | ZR5-L1 |
| ZR-L0 | ZR1-L0 | ZR2-L0 | ZR3-L0 | ZR4-L0 | ZR5-L0 |
| RF | RF1 | RF2 | RF3 | RF4 | RF5 |
| GBM | GBM1 | GBM2 | GBM3 | GBM4 | GBM5 |
| ELM | ELM1 | ELM2 | ELM3 | ELM4 | ELM5 |

hidden nodes are the hyperparameters of the ELM. The relationship between the tuning parameter and the number of hidden nodes presents a trade-off relationship such as the Pareto frontier. Thus, after one parameter is fixed, another will be optimized. In this study, the tuning parameter is fixed ($C = 0.5$), and the number of hidden nodes is optimized.

In the current study, leave-one-out cross-validation (LOOCV) is employed to optimize the hyperparameters of the three ML algorithms. The root-mean-square error (RMSE) between the estimates and observations is calculated for the ML algorithms trained by the data set that does not include any station among all those in the training set. The expected numbers of train and test data are 3227 (approximate 94%) and 233 (approximate 6%), respectively. The fifteen models were trained, and their performances were evaluated using the test data set. The RMSEs without each station are calculated, and average value of these RMSEs is the criterion for measuring appropriateness of the hyperparameters. The results of the LOOCV are presented in Figure 2. The optimal numbers of the tree for the RF and GBM are 380 and 4200, respectively; any numbers greater than these do not lead to significant improvements in increasing the performance of the RF and GBM. The optimal number of hidden nodes for the ELM is 950. These numbers are used for the hyperparameters of ML algorithms.

QPE models are built for five case studies. The first case study uses all data including the four precipitation events. The other case studies built QPE models for each of the precipitation events. The first case study was carried out to evaluate the overall performances of the QPE models constructed. The results of the other case studies may provide detailed examinations of the performance of the different rainfall events. The RMSE, Pearson correlation, mean absolute error (MAE), mean bias (Mbias), and relative root-mean-square error (RRMSE) are employed as evaluation criteria. Equation (7) gives the equation of the RMSE:

$$\mathrm{RMSE} = \sqrt{\frac{1}{n}\sum_{i=1}^{n}(E_i - O_i)^2}, \tag{7}$$

where $E_i$, $O_i$, and $n$ are $i$th radar estimation, $i$th observed precipitation data point, and the number of data points, respectively. The correlation can be calculated using the following equation:

$$\mathrm{correlation} = \sqrt{\frac{\sum_{i=1}^{n}(E_i - \overline{E})(O_i - \overline{O})}{\sum_{i=1}^{n}(E_i - \overline{E})\sum_{i=1}^{n}(O_i - \overline{O})}}, \tag{8}$$

where $\overline{E}$ and $\overline{O}$ are the means of the radar estimates and observed precipitation data, respectively. MAE, Mbias, and RRMSE equations are given in equations (9)–(11), respectively.

$$\mathrm{MAE} = \frac{1}{n}\sum_{i=1}^{n}\left|E_i - O_i\right|, \tag{9}$$

$$\mathrm{MBias} = \frac{1}{n}\sum_{i=1}^{n}(E_i - O_i), \tag{10}$$

$$\mathrm{RRMSE} = \frac{\mathrm{RMSE}}{\overline{o}} \times 100. \tag{11}$$

## 5. Results

*5.1. Overall Performance of the QPE Models.* The overall performances of the constructed QPE models are evaluated using rainfall and radar data for all the events. The training and test data sets are constructed from the data set that included all the rainfall events. Evaluation criteria for the constructed QPE models are applied to the test data set. Results of evaluation criteria are presented in Figure 3. The ML-based models lead to lower RMSEs than ZR relationship-based models.

When the number of input variables increases, the RMSE becomes smaller. For the ZR relationship-based models, RMSEs of ZR-L1-based models are smaller than those of ZR-L0-based models. The result means that usage of lag-data may provide more information onto QPE of the employed radar data. Models that include all the available input variables lead to lowest RMSE values. The second lowest RMSE is observed for models that use $Z$ and DR as input variables. Models using DR and KD lead to the largest RMSE. Based on RMSE, the ELM5 (using $Z$, DR, and KD) is the best model for QPE of the radar data. Correlation results are similar to the results of the RMSE. The ML-based models give larger correlations than ZR relationship-based models. For correlation, the cases using all input variables provide the largest correlation values. Based on MAE, models using $Z$ and DR as input variables lead to the smallest MAE. The best model based on MAE is the ELM2 (using $Z$ and DR). Based on MBias, ZR-L0-based models are the best models, with an MBias close to zero. Estimations by ZR-L1-based models have positive biases except for the ZR4-L1, while those of ML-based models have negative biases. RRMSEs of all employed QPE models are larger than 100%. Based on the RRMSEs, the ELM is the best model for QPE of radar data. The second best model is the RF.

Estimation-verse observation plots are presented in Figure 4. Rainfall rate estimations are underestimated for large amounts of rainfall rates (larger than 40 mm/h). These underestimations for large amount of rainfall rate are clearly observed in the results of ZR-L0-based models.

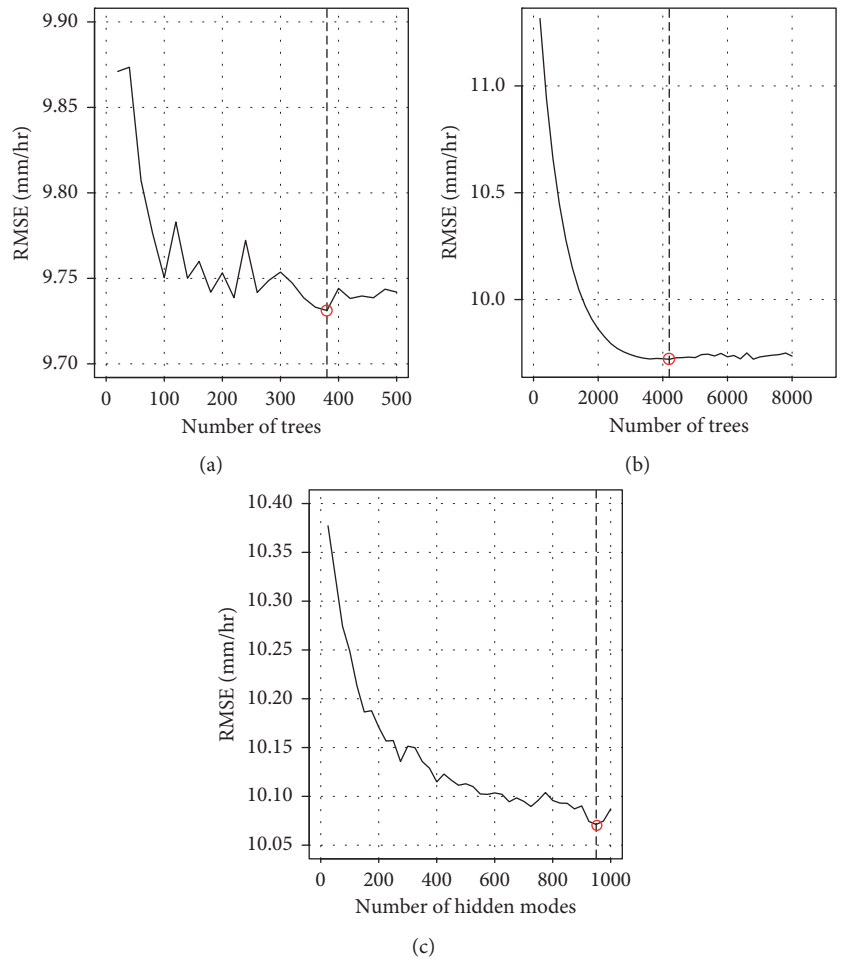


Figure 2: Leave-one-out cross-validation results of hyperparameters for the random forest (the number of trees), stochastic gradient boosted model (the number of trees), and extreme learning machine (the number of hidden nodes) models. The red circles indicate the selected optimal points of the employed hyperparameters based on the root-mean-square error. LOOCV results of (a) RF, (b) GBM, and (c) ELM.

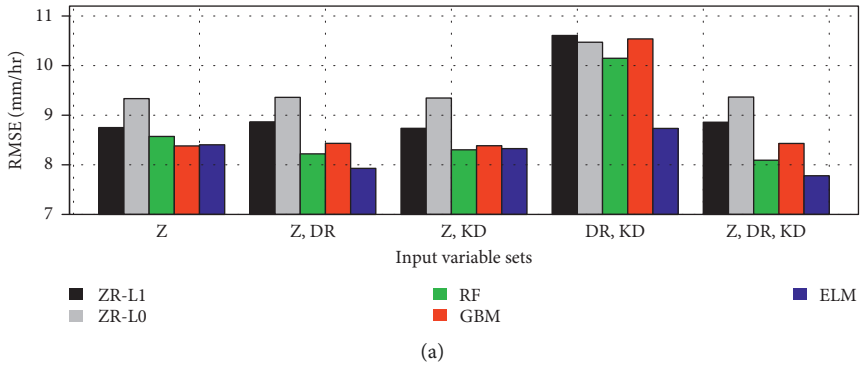


Figure 3: Continued.

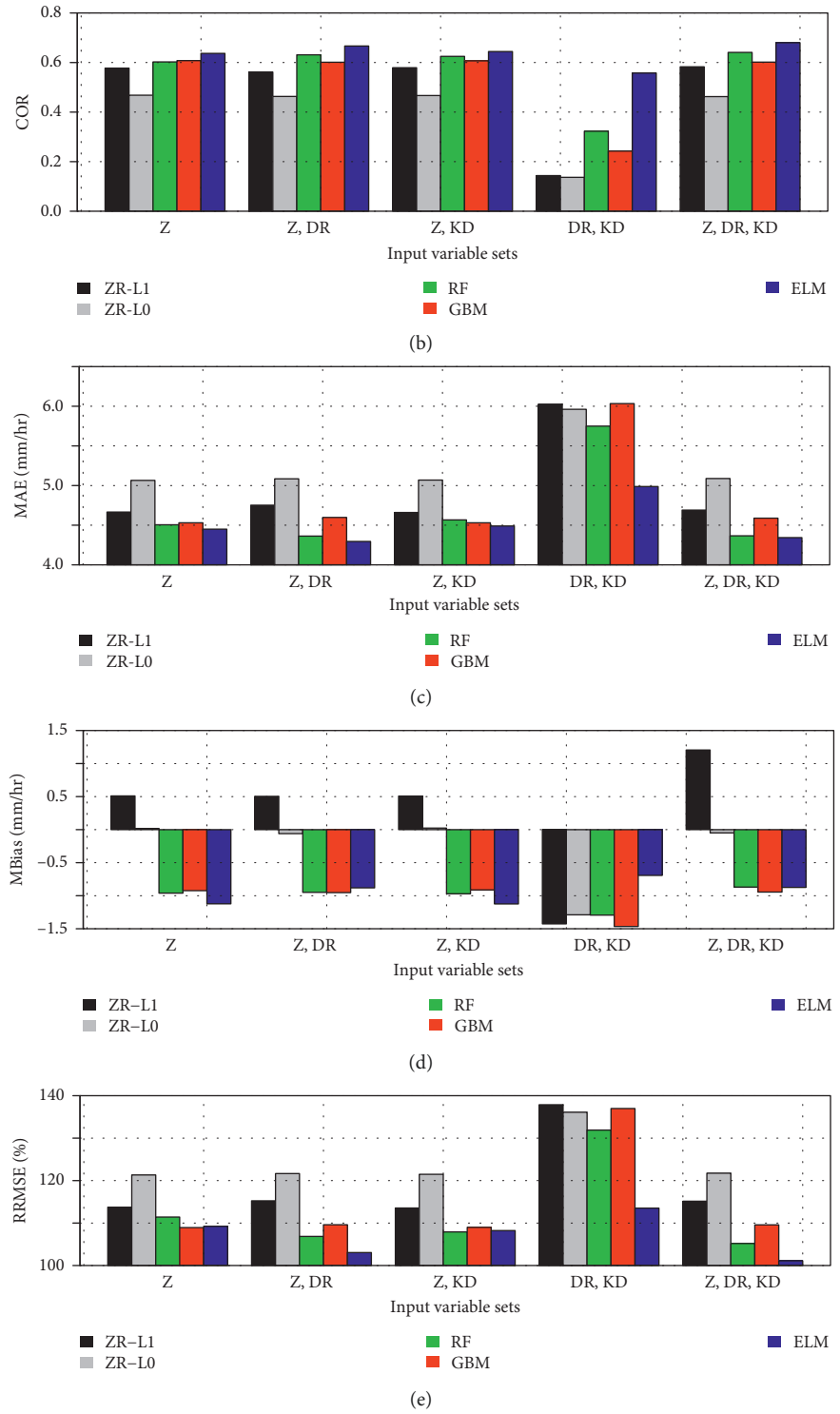


Figure 3: (a) Root-mean-square error (RMSE), (b) correlation (COR), (c) mean absolute error (MAE), (d) mean bias (Mbias), and (e) relative RMSE (RRMSE) of rainfall rate estimations by the tested quantitative precipitation estimation models for all rainfall events studied.

Mbias of ZR-L0-based models is close to zero. To meet the value of Mbias estimate, rainfall rate estimations for small and medium amounts of rainfall rates are overestimated. Mbias of ZR-L1-based models have positive values, and estimations are underestimated for large amount of precipitation, which indicates that a large overestimation occurs for a small amount of precipitation. These overestimations also are observed in Figure 4. The ELM5 leads to the best estimation performance in Figure 4. Circles by the ELM5 are located closer to the diagonal line than other models, while ZR5-L1

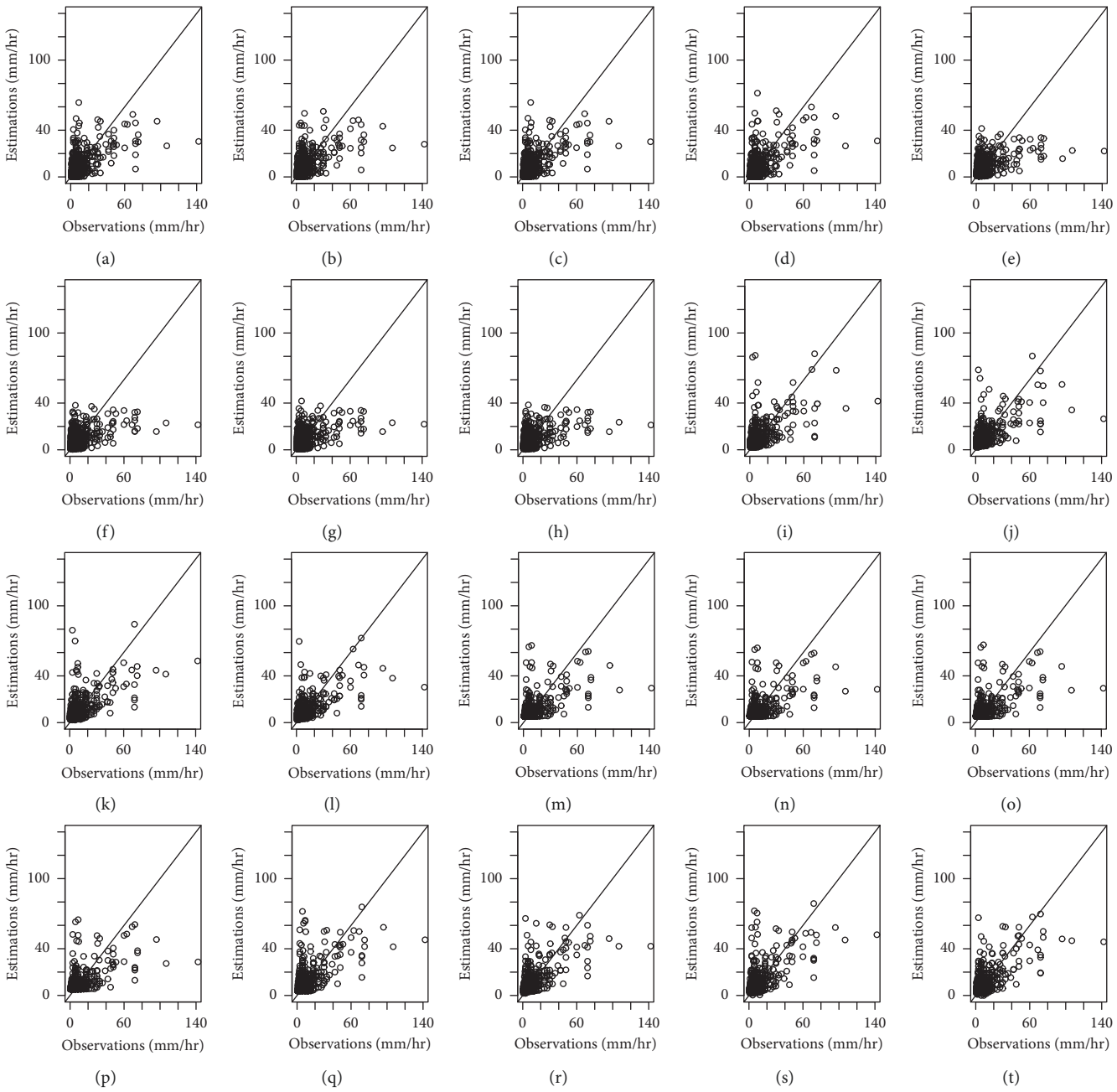


Figure 4: Plots of rainfall rate estimation versus observations for the models tested for all precipitation events studied. (a) ZR1-L1 (RMSE: 8.75, *R*: 0.58). (b) ZR2-L1 (RMSE: 8.87, *R*: 0.56). (c) ZR3-L1 (RMSE: 8.74, *R*: 0.58). (d) ZR5-L1 (RMSE: 8.86, *R*: 0.58). (e) ZR1-L0 (RMSE: 9.33, *R*: 0.47). (f) ZR2-L0 (RMSE: 9.36, *R*: 0.46). (g) ZR3-L0 (RMSE: 9.35, *R*: 0.47). (h) ZR5-L0 (RMSE: 9.37, *R*: 0.46). (i) RF1 (RMSE: 8.56, *R*: 0.6). (j) RF2 (RMSE: 8.26, *R*: 0.63). (k) RF3 (RMSE: 8.36, *R*: 0.62). (l) RF5 (RMSE: 8.18, *R*: 0.63). (m) GBM1 (RMSE: 8.38, *R*: 0.61). (n) GBM2 (RMSE: 8.43, *R*: 0.61). (o) GBM3 (RMSE: 8.38, *R*: 0.24). (p) GBM5 (RMSE: 8.43, *R*: 0.6). (q) ELM1 (RMSE: 8.37, *R*: 0.64). (r) ELM2 (RMSE: 7.99, *R*: 0.66). (s) ELM3 (RMSE: 8.33, *R*: 0.64). (t) ELM5 (RMSE: 7.91, *R*: 0.67).

and GBM5 models seem to provide poor performances. The circle distribution for these models is L-shaped (orthogonal shape) in Figure 4.

*5.2. Performances of the Constructed QPE Models for Single-Rainfall Events.* Parameters of ZR relationship differ depending on rainfall events characteristics. The performances of the QPE model differ from the rainfall events. Hence, to obtain an accurate QPE, the QPE model should be built for every rainfall event. To investigate the applicability and performance of QPE models, all the tested QPE models are built using data from each precipitation event. RMSEs of the tested QPE models for single-rainfall events are presented in Table 4. ML-based models are selected for the best models based on RMSEs. For events #1 and #2, the ELM5 and ELM3 lead to the lowest RMSEs, respectively. Based on RMSEs, RF2 and RF5 lead to the best performance for events

Table 4: Root-mean-square errors (RMSEs) of rainfall rates estimated by quantitative precipitation estimation models for selected rainfall events.

| Event no. | Model | Input variables | | | | |
|---|---|---|---|---|---|---|
| | | Z | Z, DR | Z, KD | DR, KD | Z, DR, KD |
| 1 | ZR-L1 | 11.97 | 11.91 | 11.98 | 18.12 | 11.92 |
| | ZR-L0 | 14.59 | 14.62 | 14.62 | 17.86 | 14.66 |
| | RF | 11.29 | 11.30 | 11.01 | 15.52 | 11.20 |
| | GBM | 11.05 | 11.05 | 11.03 | 16.33 | 11.06 |
| | ELM | 10.30 | 10.11 | 10.21 | 13.12 | *10.06* |
| 2 | ZR-L1 | 5.39 | 5.26 | 5.40 | 7.00 | 5.30 |
| | ZR-L0 | 6.13 | 5.99 | 6.15 | 7.51 | 6.00 |
| | RF | 5.25 | 5.16 | 5.14 | 6.34 | 5.10 |
| | GBM | 5.08 | 5.16 | 5.07 | 6.53 | 5.15 |
| | ELM | 4.93 | 5.17 | *4.71* | 5.99 | 5.05 |
| 3 | ZR-L1 | 3.33 | 3.33 | 3.33 | 3.57 | 3.33 |
| | ZR-L0 | 3.34 | 3.33 | 3.34 | 3.57 | 3.33 |
| | RF | 3.47 | *3.17* | 3.43 | 3.54 | 3.20 |
| | GBM | 3.35 | 3.31 | 3.35 | 3.48 | 3.32 |
| | ELM | 3.64 | 3.91 | 3.75 | 3.85 | 3.99 |
| 4 | ZR-L1 | 2.88 | 2.86 | 2.88 | 3.24 | 2.86 |
| | ZR-L0 | 3.05 | 3.02 | 3.05 | 3.26 | 3.02 |
| | RF | 2.93 | 2.97 | 2.89 | 3.39 | *2.85* |
| | GBM | 2.89 | 2.86 | 2.88 | 3.22 | 2.86 |
| | ELM | 2.91 | 2.90 | 2.90 | 3.08 | 2.89 |

Italicized numbers indicate the smallest RMSEs among those calculated during the same rainfall events.

#3 and #4, respectively. Overall, RMSEs of the models using $Z$ and KD data are lower than those in the models using other input variable sets for event #2. For event #3, RMSEs of the models using $Z$ and DR data are lower than the models using other input variable sets. Differences between RMSEs of ML and ZR relationship-based models are very small in event #4. Although RF5 is selected as the best model in the event #4 based on RMSEs, the difference between RMSEs of RF5 and ZR5-L1 is 0.01. Practically, the performances of ZR-L1-based models are the best for event #4 based on RMSEs.

Table 5 presents the correlations of the tested QPE models for single-rainfall events. The correlations of the QPE models for events #1 and #2 are much larger than those for events #3 and #4. While the RMSEs of events #1 and #2 are larger than events #3 and #4, their correlations are higher than those of events #3 and #4. Results indicate that the QPE models lead to good estimation performance for heavy rainfall events. The largest correlation values are observed in ML-based models. ELM2 and ELM3 lead to the largest correlations for events #1 and #2, respectively. RF2 and RF5 provide the largest correlations for events #3 and #4, respectively. Results of MAE are similar to the results of RMSE. Based on Mbias, ZR-L1-, ZR-L0-, GBM-, and ELM-based models lead to the best performance for events #1 to #4, respectively. Detailed MAE and MBias results are not contained in the current manuscript.

Table 6 presents the RRMSEs of the tested QPE models for single-rainfall events. The correlations of the QPE models for events #3 and #4 are smaller than those for events #1 and #2, unlike the results of RMSE and correlation. The smallest

Table 5: Correlations of rain rate estimations by quantitative precipitation estimation models for each selected rainfall event.

| Event no. | Model | Input variables | | | | |
|---|---|---|---|---|---|---|
| | | Z | Z, DR | Z, KD | DR, KD | Z, DR, KD |
| 1 | ZR-L1 | 0.750 | 0.753 | 0.749 | 0.154 | 0.752 |
| | ZR-L0 | 0.603 | 0.600 | 0.600 | 0.201 | 0.597 |
| | RF | 0.785 | 0.785 | 0.800 | 0.513 | 0.796 |
| | GBM | 0.799 | 0.799 | 0.800 | 0.425 | 0.799 |
| | ELM | 0.829 | *0.837* | 0.830 | 0.687 | 0.836 |
| 2 | ZR-L1 | 0.721 | 0.736 | 0.721 | 0.455 | 0.732 |
| | ZR-L0 | 0.615 | 0.639 | 0.611 | 0.332 | 0.637 |
| | RF | 0.745 | 0.750 | 0.749 | 0.593 | 0.756 |
| | GBM | 0.758 | 0.749 | 0.759 | 0.559 | 0.750 |
| | ELM | 0.793 | 0.785 | *0.805* | 0.649 | 0.788 |
| 3 | ZR-L1 | 0.308 | 0.309 | 0.308 | 0.007 | 0.308 |
| | ZR-L0 | 0.287 | 0.292 | 0.286 | −0.056 | 0.292 |
| | RF | 0.228 | *0.423* | 0.230 | 0.208 | 0.404 |
| | GBM | 0.298 | 0.362 | 0.298 | 0.207 | 0.358 |
| | ELM | 0.364 | 0.417 | 0.355 | 0.371 | 0.389 |
| 4 | ZR-L1 | 0.418 | 0.431 | 0.419 | 0.047 | 0.429 |
| | ZR-L0 | 0.275 | 0.299 | 0.279 | −0.065 | 0.298 |
| | RF | 0.433 | 0.418 | 0.449 | 0.018 | *0.459* |
| | GBM | 0.422 | 0.435 | 0.423 | −0.004 | 0.433 |
| | ELM | 0.395 | 0.409 | 0.400 | 0.258 | 0.415 |

Italicized numbers indicate the largest correlations among those calculated during the same rainfall events.

Table 6: Relative root-mean-square errors (RRMSEs) of rain rate estimations by quantitative precipitation estimation models for each selected rainfall event.

| Event no. | Model | Input variables | | | | |
|---|---|---|---|---|---|---|
| | | Z | Z, DR | Z, KD | DR, KD | Z, DR, KD |
| 1 | ZR-L1 | 85.5 | 85.1 | 85.6 | 129.5 | 85.2 |
| | ZR-L0 | 104.3 | 104.5 | 104.5 | 127.6 | 104.7 |
| | RF | 81.1 | 80.2 | 78.5 | 112.2 | 79.8 |
| | GBM | 78.8 | 79.0 | 79.1 | 116.8 | 79.2 |
| | ELM | 73.5 | 72.1 | 72.9 | 93.5 | *71.8* |
| 2 | ZR-L1 | 77.8 | 75.9 | 77.9 | 101.0 | 76.4 |
| | ZR-L0 | 88.5 | 86.4 | 88.8 | 108.4 | 86.6 |
| | RF | 76.4 | 74.0 | 74.5 | 91.6 | 73.6 |
| | GBM | 73.1 | 74.6 | 73.2 | 94.1 | 74.5 |
| | ELM | 71.2 | 75.0 | *68.1* | 86.5 | 72.6 |
| 3 | ZR-L1 | 63.6 | 63.7 | 63.6 | 68.3 | 63.7 |
| | ZR-L0 | 63.8 | 63.8 | 63.8 | 68.3 | 63.8 |
| | RF | 66.3 | *60.6* | 65.6 | 67.4 | 60.8 |
| | GBM | 64.1 | 63.4 | 64.1 | 66.6 | 63.4 |
| | ELM | 69.6 | 75.8 | 71.9 | 73.3 | 76.9 |
| 4 | ZR-L1 | 63.5 | 63.0 | 63.5 | 71.4 | 63.0 |
| | ZR-L0 | 67.4 | 66.7 | 67.3 | 72.0 | 66.7 |
| | RF | 64.7 | 65.3 | 64.1 | 75.0 | *63.0* |
| | GBM | 63.6 | 63.0 | 63.5 | 71.4 | 63.0 |
| | ELM | 64.2 | 63.8 | 63.8 | 68.0 | 63.4 |

Italicized numbers indicate the smallest RRMSEs among those calculated during the same rainfall events.

RRMSEs for events #1 and #2 (heavy rainfall events) are 71.8% and 68.1%, respectively. For events #3 and #4 (light rainfall events), the smallest RRMSEs are 60.6% and 63.0%,

respectively. Overall difference between the smallest RRMSEs of heavy and light rainfall events are approximately 10%. The difference between the smallest RMSE of heavy and light rainfall events is approximately 4.3 mm/hr. Because 4.3 mm/hr is larger than the smallest RMSE of event #3, the RRMSE difference is relatively smaller than RMSE difference. The result indicates that the QPE models provide similar performances for heavy and light rainfall events based on RRMSE measures.

To evaluate the tested QPE models for single-rainfall events, rainfall rate estimation versus observation plots for event #1 and #4 is presented in Figures 5 and 6, respectively. The tested models excluding ZR-L0-based models lead to good estimation performances for event #1. Of the tested models, ELM5 gives the best estimation performance. Some circles are aligned to approximately 80 mm/h based on observations in Figure 5. This is a recurrent issue in QPE of rain radar data. When the observed rainfall rates are the same but the observed parameters of radar data are different, this phenomenon occurs. This result indicates that all tested QPE models cannot solve this issue. For event #4 in Figure 6, all the tested QPE models lead to poor performances of rainfall rate estimation. In the observed small magnitude of rainfall rates, the QPE models tend to overestimate rainfall rates. On the other hand, the QPE models provide an underestimation for the observed large magnitude of rainfall rates. Five lines are observed at approximately 3 mm/h, 6 mm/h, 9 mm/h, 12 mm/h, and 15 mm/h based on observations in all the subfigures presented in Figure 6. The observed rainfall depths for these small rainfall rates are 0.5 mm, 1 mm, 1.5 mm, 2 mm, and 2.5 mm, and their duration is 10 minutes. Because event #4 is light, a large number of small rainfall rates are observed. The phenomena wherein parameters of radar are different for the same amount of observed rainfall rate occur frequently. Due to this phenomenon, the tested QPE models show poor performances in event #4.

Radar rainfall rate fields for events #1 and #4 are illustrated to investigate the difference between ZR relation- and ML-based models in Figures 7 and 8. Figure 7 presents radar rainfall rate fields of event #1 at 20 : 10, 28$^{th}$ August 2018. The range of rainfall rates is from 0 to 100 mm/h for event #1. The ML-based QPE models provide larger magnitudes of rainfall rates for very small magnitudes of rainfall rates based on estimates by ZR2-L1. For heavy magnitudes of rainfall rates, estimates of all QPE models are similar. The GBM leads to the largest magnitude of rainfall rate estimation in Figure 7. Rainfall rate estimates on ground gauge stations for the ZR2-L1 are larger than those of ML-based models. Due to the high magnitude of rainfall rate at these points, the ZR2-L1 overestimates rainfall rate in Figure 3. In areas where there are no ground gauge stations, the ZR2-L1 estimates smaller rainfall rates than other models. Figure 8 presents radar rainfall rate fields of event #4 at 12 : 40, 8$^{th}$ November 2018. Rainfall rates range from 0 to 15 mm/h for event #4. Overall results of rainfall rate estimates by the tested models are similar to the results shown in Figure 7. The ELM leads to the largest magnitude of rainfall rate estimation.

## 6. Discussion

The comparison results of the ZR relationship- and ML-based models show that the application of ML algorithms can lead to an improvement in the QPE of radar data in the tested rainfall events. This result supports the notion that the ML algorithm could be used in the development of QPE models of radar data in South Korea. Increasing the number of variables for the input variables of the ZR relationship-based models results in very small improvements. In some events, this increment does not improve performances of QPE models. It can be inferred that $Z$ is the most critical variable for the ZR relationship-based model. Additionally, the application of other variables is often an inefficient way to build the ZR relationship-based model.

The performances of the ML-based models improve when $Z$ and additional variables such as DR and KD are applied as input variables. In particular, a combination of $Z$ and DR for input variables of the ML-based models leads to a good QPE performance. Studies have reported that this combination leads to the best performance among combinations of $Z$, DR, and KD for the ZR relationship-based model [46, 47]. In many cases, application of DR, except for combinations of DR and KD, lead to a large improvement in the QPE using the ML-based model, unlike the ZR relationship-based model. The results imply that the ML-based models could consider other variables in QPE. Because the ML-based model can extract a large amount of information from the input variables and use this information in QPE of rain radar data, performances of the ML-based models may be better than those of ZR relationship-based models. Based on results of RMSE for individual events, the RF model with three variables provided the smallest RMSEs in events #2 and #4. Otherwise, RMSEs of other RF models were smaller than those of the RF model with three variables. In addition, there is a very small difference (0.06 mm/hr) between RSMEs of RF models with three variables and with $Z$ and KD. The RF model with $Z$ and KD is the best model when taking into consideration of parsimony for event #2. Hence, the RF model with three variables can be considered for suboptimal in events #1, #2, and #3.

Computation times to build QPE models differ depending on the ML algorithms employed. RF has the shortest computation time, and its computation time with the data sets of all events is approximately 1 minute. The computation times of the GBM and ELM are approximately 7 minutes and 3 minutes, respectively. As the measuring interval of rainfall data is 10 minutes, the computation time should be shorter than 5 minutes. The RF- and ELM-based models proposed in the current study can be applied for QPE, but the GBM has to be modified before application.

Based on the results of this study, a comparison of the performances of the employed algorithms can be carried out. The ELM leads to the best performance for the case that includes all the events. For single events, the best algorithms are different. The ELM provides a good performance for heavy rainfall events, while the RF is considered a good algorithm for light rainfall events. The difference in performance between the RF and ELM is small in the light

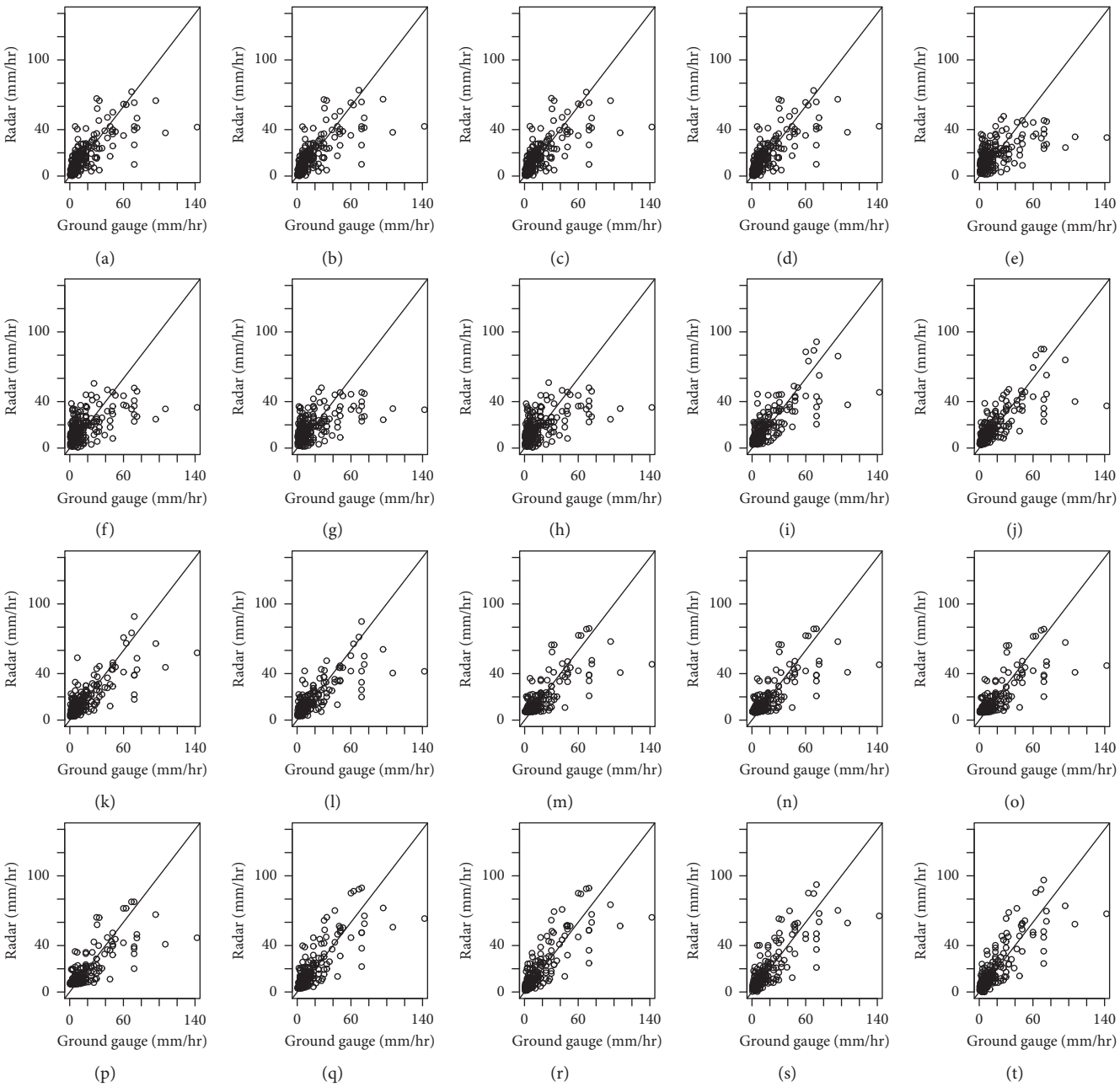


Figure 5: Plots of rainfall rate estimations versus observations of tested models for precipitation event #1. (a) ZR1-L1 (RMSE: 11.97, *R*: 0.75). (b) ZR2-L1 (RMSE: 11.91, *R*: 0.75). (c) ZR3-L1 (RMSE: 11.98, *R*: 0.75). (d) ZR5-L1 (RMSE: 11.92, *R*: 0.75). (e) ZR1-L0 (RMSE: 14.59, *R*: 0.6). (f) ZR2-L0 (RMSE: 14.62, *R*: 0.6). (g) ZR3-L0 (RMSE: 14.62, *R*: 0.6). (h) ZR5-L0 (RMSE: 14.66, *R*: 0.6). (i) RF1 (RMSE: 11.29, *R*: 0.79). (j) RF2 (RMSE: 11.3, *R*: 0.79). (k) RF3 (RMSE: 11.01, *R*: 0.8). (l) RF5 (RMSE: 11.2, *R*: 0.8). (m) GBM1 (RMSE: 11.05, *R*: 0.8). (n) GBM2 (RMSE: 11.05, *R*: 0.8). (o) GBM3 (RMSE: 11.03, *R*: 0.42). (p) GBM5 (RMSE: 11.06, *R*: 0.8). (q) ELM1 (RMSE: 10.3, *R*: 0.83). (r) ELM2 (RMSE: 10.11, *R*: 0.84). (s) ELM3 (RMSE: 10.21, *R*: 0.83). (t) ELM5 (RMSE: 10.06, *R*: 0.84).

rainfall events. Hence, the best ML algorithm for case studies performed in the current study is the ELM. Each ML algorithm tested in this study uses popular setting. The comparison results of the ML algorithm for QPE models can be altered by adopted setting and used data. For example, in this study, the CART is used for the decision tree in the RF. Other decision tree models can be used in the RF such as inference dichotomiser 3 and chi-squared automatic iteration detection. RF with other decision tree models can outperform to the ELM model for QPE in South Korea. Thus, the results in the current study should be restricted to these data sets and the ML algorithms with adopted setting.

Variation of neural network models like artificial neural, recurrent neural, and deep neural networks may have a high applicability building QPE models of radar data in South Korea, because the ELM is developed based on a neural network. Additionally, enhancing the precision of rainfall gauges may lead to improvements in the performance of

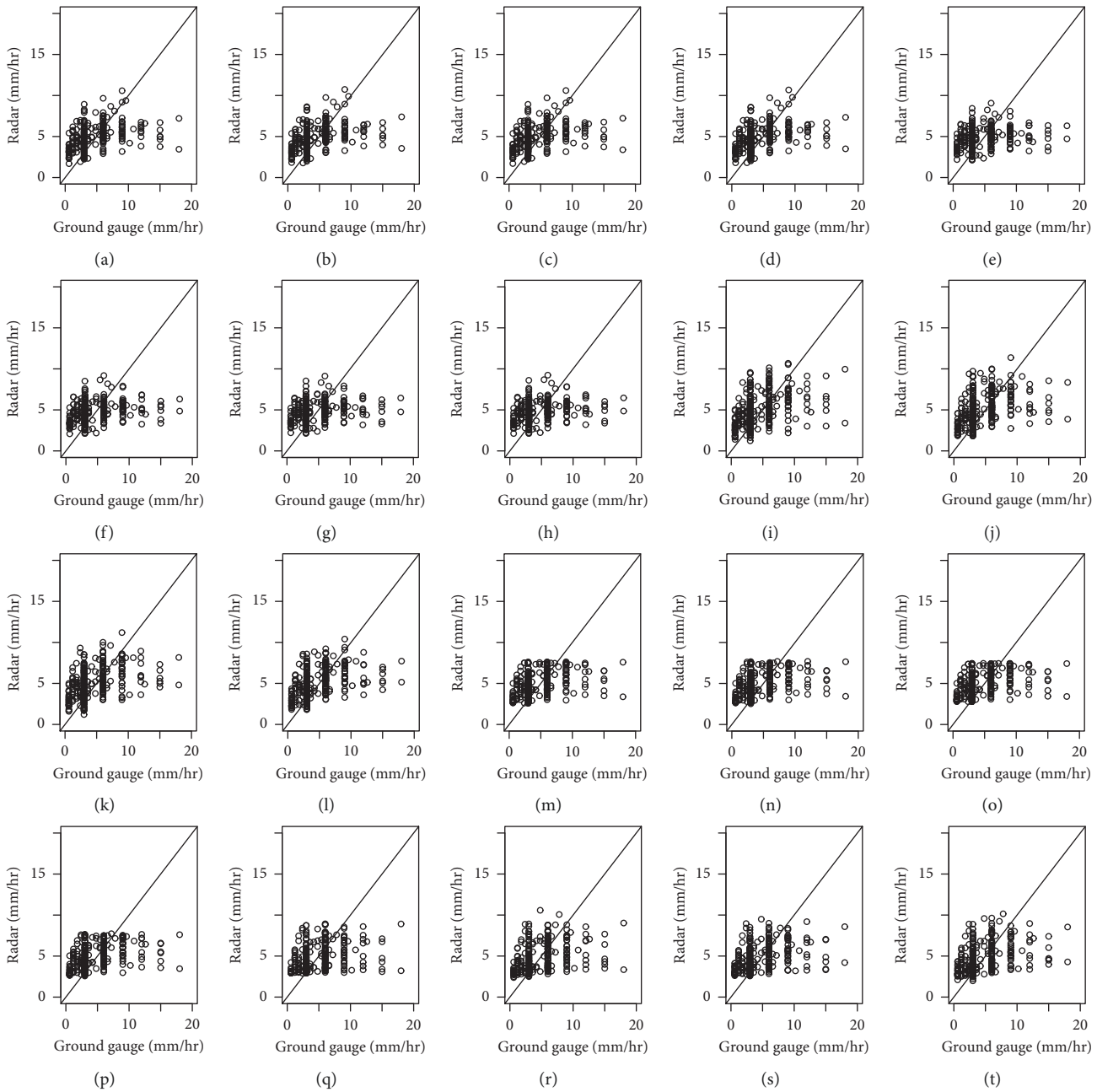


Figure 6: Plots of rainfall rate estimations versus observations of tested models for precipitation event #4. (a) ZR1-L1 (RMSE: 2.88, *R*: 0.42). (b) ZR2-L1 (RMSE: 2.86, *R*: 0.43). (c) ZR3-L1 (RMSE: 2.88, *R*: 0.42). (d) ZR5-L1 (RMSE: 2.86, *R*: 0.43). (e) ZR1-L0 (RMSE: 3.05, *R*: 0.27). (f) ZR2-L0 (RMSE: 3.02, *R*: 0.3). (g) ZR3-L0 (RMSE: 3.05, *R*: 0.28). (h) ZR5-L0 (RMSE: 3.02, *R*: 0.3). (i) RF1 (RMSE: 2.93, *R*: 0.43). (j) RF2 (RMSE: 2.97, *R*: 0.42). (k) RF3 (RMSE: 2.89, *R*: 0.45). (l) RF5 (RMSE: 2.85, *R*: 0.46). (m) GBM1 (RMSE: 2.89, *R*: 0.42). (n) GBM2 (RMSE: 2.86, *R*: 0.42). (o) GBM3 (RMSE: 2.88, *R*: 0.42). (p) GBM5 (RMSE: 2.86, *R*: 0.43). (q) ELM1 (RMSE: 2.91, *R*: 0.39). (r) ELM2 (RMSE: 2.9, *R*: 0.41). (s) ELM3 (RMSE: 2.9, *R*: 0.4). (t) ELM5 (RMSE: 2.89, *R*: 0.41).

QPE models for light rainfall events. Precision for some of the employed rainfall gauges is 3 mm/hr. Although this precision is good enough to measure rainfall rates for long duration or heavy rainfall events, it should be higher for estimating rainfall rates of light rainfall events. For example, when parameters of radar data for two points are different but their observed rainfall rates are the same, the QPE model has to fail estimations of rainfall rates at two points. If the precision of the rainfall gauge increases, the observed rainfall rates may be different and could result in a more accurate constructed QPE model. As shown in Figure 6, three lines can be observed in all the subfigures. Values of ground gauge for first, second, and third lines are 3, 6, and 9 mm/hr. These three lines indicate that the observed rainfall rates at ground gauge station are the same when the parameters of radar data are different. If precisions of these gauge stations become

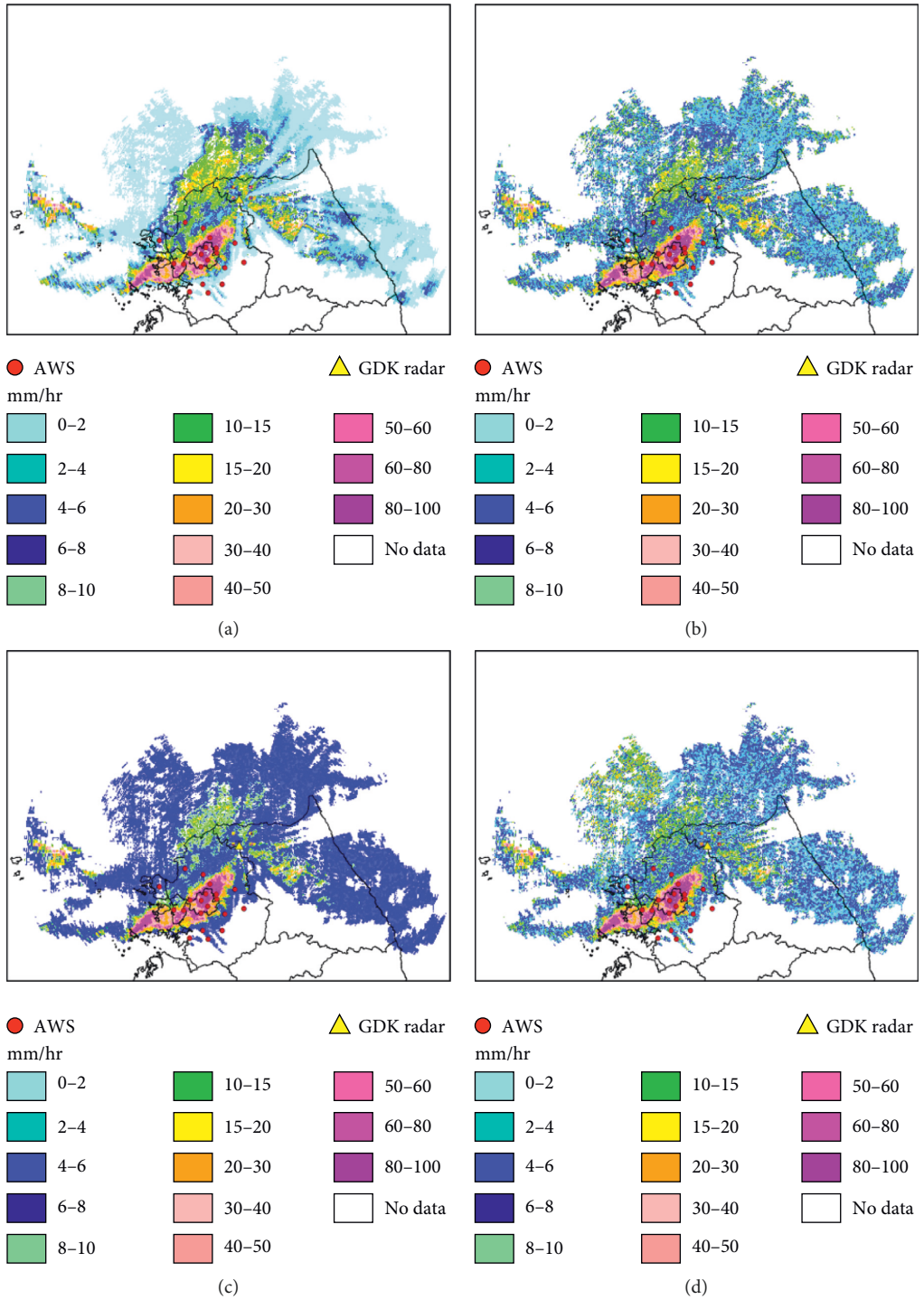


Figure 7: Radar rainfall rate fields for four selected quantitative precipitation estimation models (ZR2–L1, RF3, GBM3, and ELM5) for event #1 (August 28, 2018; 20 : 10). (a) ZR. (b) RF. (c) GB. (d) EL.

better, these lines may be disappeared and the data points in the lines are dissipated. This dispersion of data points, caused by the high precision of measuring instrument, may lead to improvement of the performance of QPE models for light rainfall event.

The tested QPE models lead to good performances for heavy rainfall events but not for light rainfall events. This characteristic of QPE with rain radar data is also observed in this study. ML-based QPE models outperform ZR relationship-based models for events #3 and #4, albeit insignificantly. As mentioned above, the ML-based QPE models show good performances by efficiently extracting information from given radar data. If additional variables can be applied in QPE models, the performance of the QPE

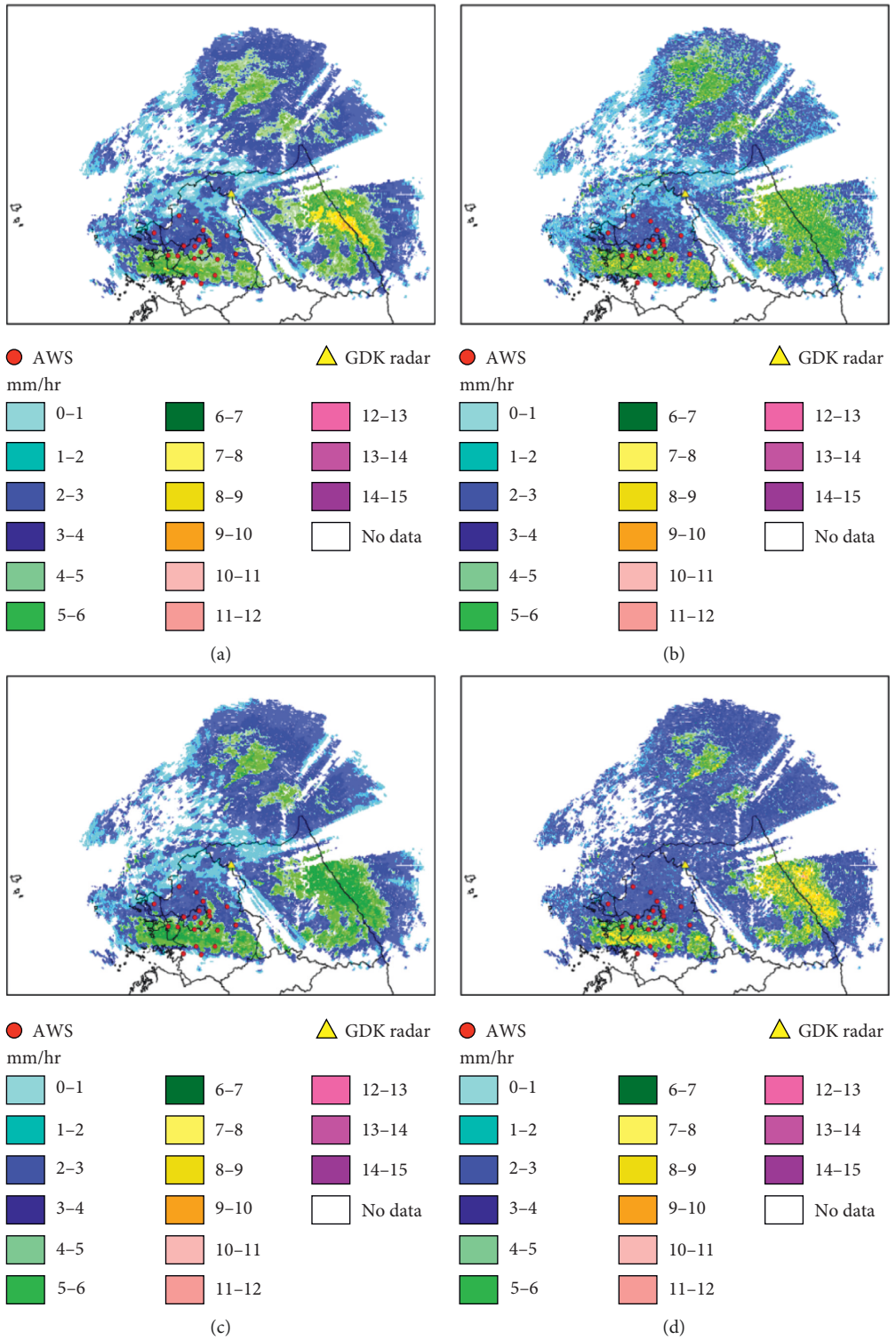


Figure 8: Radar rainfall rate fields of four selected quantitative precipitation estimation models (ZR2–L1, RF5, GBM2, and ELM5) for event #4 (November 8, 2018; 12 : 40). (a) ZR2-L1. (b) RF5. (c) GBM2. (d) ELM5.

model may improve, particularly for light rainfall events. Thus, various sets of input variables that are frequently used in conventional QPE algorithms should be tested for ML-based QPE models to improve the performance of QPE models for light rainfall events.

## 7. Conclusions

The applicability of three ML algorithms in QPE models is investigated using case studies of polarization radar data of four rainfall events from Gwangdeoksan radar station, Gyeonggi-do,

South Korea. Various combinations of input variable sets are also tested for QPE models. Conventional ZR relation-based models are also constructed and compared to ML-based models. In the current study, we reach the following conclusions:

(1) ML algorithms can be applied to build a QPE model of polarization radar data. Overall, the ML-based QPE models outperform or are equal to ZR relationship-based models. ML algorithms can extract information from radar data more efficiently than the ZR relationship, which leads to an improvement in QPE of the radar data.

(2) Application of the ML algorithms for QPE models improves rainfall rate estimations for heavy events in South Korea by far. The performances of the ML-based QPE model are significantly improved based on performances of ZR relationship-based models for heavy rainfall events. This improvement will be helpful in modeling floods and forecasting flash floods.

(3) ELM algorithm may be the best ML algorithm among the tested ML algorithm with the adopted setting for QPE models of radar data in South Korea. Overall, the ELM outperforms other tested QPE models in QPE of radar data employed in the current study. Based on evaluation results of single-rainfall events, the ELM also leads to the best performance in two heavy rainfall events. Although the ELM is not the best QPE model for the two light rainfall events, the performances of QPE models using ELM are comparable to other QPE models.

In the current study, four rainfall events in 2018 were employed to evaluate the applicability of ML algorithms for the QPE model of polarization radar data as the radar instrument in Gwangdeoksan radar was updated. Future rainfall events should be included in data sets to further investigate the applicability and characteristics of ML algorithms in the QPE of polarization radar data in South Korea. In addition, the applicability of ML algorithms for QPF should be examined. Because ML algorithms show high applicability in QPE, they make good candidates for modeling functions between radar data and QPF.

## Data Availability

The data used to support the findings of this study are available from the corresponding author upon request.

## Conflicts of Interest

The authors declare that they have no conflicts of interest.

## Acknowledgments

This work was funded by the Korea Meteorological Administration Research and Development Program "Development of Application Technology on Atmospheric Research Aircraft" under Grant (1365003069).

## References

[1] B. Martens, P. Cabus, I. De Jongh, and N. E. C. Verhoest, "Merging weather radar observations with ground-based measurements of rainfall using an adaptive multiquadric surface fitting algorithm," *Journal of Hydrology*, vol. 500, pp. 84–96, 2013.

[2] S. Yang and S. W. Nesbitt, "Statistical properties of precipitation as observed by the TRMM precipitation radar," *Geophysical Research Letters*, vol. 41, no. 15, pp. 5636–5643, 2014.

[3] W. F. Krajewski and J. A. Smith, "Radar hydrology: rainfall estimation," *Advances in Water Resources*, vol. 25, no. 8–12, pp. 1387–1394, 2002.

[4] J. Kim, J. Lee, D. Kim, and B. Kang, "The role of rainfall spatial variability in estimating areal reduction factors," *Journal of Hydrology*, vol. 568, pp. 416–426, 2019.

[5] W. Cho, J. Lee, J. Park, and D. Kim, "Radar polygon method: an areal rainfall estimation based on radar rainfall imageries," *Stochastic Environmental Research and Risk Assessment*, vol. 31, no. 1, pp. 275–289, 2017.

[6] T. Park, T. Lee, D. Ko, J. Shin, and D. Lee, "Assessing spatially dependent errors in radar rainfall estimates for rainfall-runoff simulation," *Stochastic Environmental Research and Risk Assessment*, vol. 31, no. 7, pp. 1823–1838, 2016.

[7] J. Simpson, R. F. Adler, and G. R. North, "A proposed tropical rainfall measuring mission (TRMM) satellite," *Bulletin of the American Meteorological Society*, vol. 69, no. 3, pp. 278–295, 1988.

[8] R. J. Joyce, J. E. Janowiak, P. A. Arkin, and P. Xie, "CMORPH: a method that produces global precipitation estimates from passive microwave and infrared data at high spatial and temporal resolution," *Journal of Hydrometeorology*, vol. 5, no. 3, pp. 487–503, 2004.

[9] Y. Wang and V. Chandrasekar, "Quantitative precipitation estimation in the CASA X-band dual-polarization radar network," *Journal of Atmospheric and Oceanic Technology*, vol. 27, no. 10, pp. 1665–1676, 2010.

[10] G. Delrieu, I. Braud, A. Berne et al., "Weather radar and hydrology," *Advances in Water Resources*, vol. 32, no. 7, pp. 969–974, 2009.

[11] T. Lee, J. Shin, T. Park, and D. Lee, "Basin rotation method for analyzing the directional influence of moving storms on basin response," *Stochastic Environmental Research and Risk Assessment*, vol. 29, no. 1, pp. 251–263, 2015.

[12] N. Balakrishnan, D. S. Zrnić, J. Goldhirsh, and J. Rowland, "Comparison of simulated rain rates from disdrometer data employing polarimetric radar algorithms," *Journal of Atmospheric and Oceanic Technology*, vol. 6, no. 3, pp. 476–486, 1989.

[13] A. V. Ryzhkov and D. S. Zrnić, "Comparison of dual-polarization radar estimators of rain," *Journal of Atmospheric and Oceanic Technology*, vol. 12, no. 2, pp. 249–256, 1995.

[14] S. Verrier, L. Barthès, and C. Mallet, "Theoretical and empirical scale dependency of Z-R relationships: evidence, impacts, and correction," *Journal of Geophysical Research: Atmospheres*, vol. 118, no. 14, pp. 7435–7449, 2013.

[15] J. A. Smith and W. F. Krajewski, "Estimation of the mean field bias of radar rainfall estimates," *Journal of Applied Meteorology*, vol. 30, no. 4, pp. 397–412, 1991.

[16] M.-K. Suk, K.-H. Chang, J.-W. Cha, and K.-E. Kim, "Operational real-time adjustment of radar rainfall estimation over the South Korea region," *Journal of the Meteorological Society of Japan. Ser. II*, vol. 91, no. 4, pp. 545–554, 2013.

[17] C. Yoo, C. Park, J. Yoon, and J. Kim, "Interpretation of mean-field bias correction of radar rain rate using the concept of linear regression," *Hydrological Processes*, vol. 28, no. 19, pp. 5081–5092, 2014.

[18] L. Yang, Y. Yang, P. Liu, and L. Wang, "Radar-Derived quantitative precipitation estimation based on precipitation classification," *Advances in Meteorology*, vol. 2016, Article ID 2457489, 16 pages, 2016.

[19] D.-J. Seo and J. A. Smith, "Rainfall estimation using raingages and radar—A Bayesian approach: 1. Derivation of estimators," *Stochastic Hydrology and Hydraulics*, vol. 5, no. 1, pp. 17–29, 1991.

[20] D.-J. Seo and J. A. Smith, "Rainfall estimation using raingages and radar—A Bayesian approach: 2. An application," *Stochastic Hydrology and Hydraulics*, vol. 5, no. 1, pp. 31–44, 1991.

[21] Q. Dai, M. A. Rico-Ramirez, D. Han, T. Islam, and S. Liguori, "Probabilistic radar rainfall nowcasts using empirical and theoretical uncertainty models," *Hydrological Processes*, vol. 29, no. 1, pp. 66–79, 2013.

[22] A. Mosavi, P. Ozturk, and K.-w. Chau, "Flood prediction using machine learning models: literature review," *Water*, vol. 10, no. 11, p. 1536, 2018.

[23] P. Ganguli and M. J. Reddy, "Ensemble prediction of regional droughts using climate inputs and SVM-copula approach," *Hydrological Processes*, vol. 28, no. 19, pp. 4989–5009, 2013.

[24] D. J. Gagne II, A. McGovern, and M. Xue, "Machine learning enhancement of storm-scale ensemble probabilistic quantitative precipitation forecasts," *Weather and Forecasting*, vol. 29, no. 4, pp. 1024–1043, 2014.

[25] Y. Tao, X. Gao, A. Ihler, S. Sorooshian, and K. Hsu, "Precipitation identification with bispectral satellite information using deep learning approaches," *Journal of Hydrometeorology*, vol. 18, no. 5, pp. 1271–1283, 2017.

[26] X. Lu, Y. Ju, L. Wu, J. Fan, F. Zhang, and Z. Li, "Daily pan evaporation modeling from local and cross-station data using three tree-based machine learning models," *Journal of Hydrology*, vol. 566, pp. 668–684, 2018.

[27] B. T. Nolan, C. T. Green, P. F. Juckem, L. Liao, and J. E. Reddy, "Metamodeling and mapping of nitrate flux in the unsaturated zone and groundwater, Wisconsin, USA," *Journal of Hydrology*, vol. 559, pp. 428–441, 2018.

[28] H. I. Erdal and O. Karakurt, "Advancing monthly streamflow prediction accuracy of CART models using ensemble learning paradigms," *Journal of Hydrology*, vol. 477, pp. 119–128, 2013.

[29] Y.-M. Chiang, F.-J. Chang, B. J.-D. Jou, and P.-F. Lin, "Dynamic ANN for precipitation estimation and forecasting from radar observations," *Journal of Hydrology*, vol. 334, no. 1-2, pp. 250–261, 2007.

[30] P.-S. Yu, T.-C. Yang, S.-Y. Chen, C.-M. Kuo, and H.-W. Tseng, "Comparison of random forests and support vector machine for real-time radar-derived rainfall forecasting," *Journal of Hydrology*, vol. 552, pp. 92–104, 2017.

[31] M. R. Kumjian, "Principles and applications of dual-polarization weather radar. Part I: description of the polarimetric radar variables," *Journal of Operational Meteorology*, vol. 1, no. 19, pp. 226–242, 2013.

[32] A. V. Ryzhkov, S. E. Giangrande, and T. J. Schuur, "Rainfall estimation with a polarimetric prototype of WSR-88d," *Journal of Applied Meteorology*, vol. 44, no. 4, pp. 502–515, 2005.

[33] R. Cifelli, V. Chandrasekar, S. Lim, P. C. Kennedy, Y. Wang, and S. A. Rutledge, "A new dual-polarization radar rainfall algorithm: application in Colorado precipitation events," *Journal of Atmospheric and Oceanic Technology*, vol. 28, no. 3, pp. 352–364, 2011.

[34] T. Yang, A. A. Asanjan, E. Welles, X. Gao, S. Sorooshian, and X. Liu, "Developing reservoir monthly inflow forecasts using artificial intelligence and climate phenomenon information," *Water Resources Research*, vol. 53, no. 4, pp. 2786–2812, 2017.

[35] J. Fan, W. Yue, L. Wu et al., "Evaluation of SVM, ELM and four tree-based ensemble models for predicting daily reference evapotranspiration using limited meteorological data in different climates of China," *Agricultural and Forest Meteorology*, vol. 263, pp. 225–241, 2018.

[36] B. Pang, J. Yue, G. Zhao, and Z. Xu, "Statistical downscaling of temperature with the random forest model," *Advances in Meteorology*, vol. 2017, Article ID 7265178, 11 pages, 2017.

[37] C. Choi, J. Kim, J. Kim, D. Kim, Y. Bae, and H. S. Kim, "Development of heavy rain damage prediction model using machine learning based on big data," *Advances in Meteorology*, vol. 2018, Article ID 5024930, 11 pages, 2018.

[38] L. Breiman, "Random forests," *Machine Learning*, vol. 45, no. 1, pp. 5–32, 2001.

[39] M. N. Wright and A. Ziegler, "Ranger: a fast implementation of random forests for high dimensional data in C++ and R," *Survival Analysis*, vol. 77, no. 1, p. 17, 2017.

[40] J. H. Friedman, "Stochastic gradient boosting," *Computational Statistics & Data Analysis*, vol. 38, no. 4, pp. 367–378, 2002.

[41] A. Torres-Barrán, Á. Alonso, and J. R. Dorronsoro, "Regression tree ensembles for wind energy and solar radiation prediction," *Neurocomputing*, vol. 326-327, pp. 151–160, 2019.

[42] S. A. Naghibi, H. R. Pourghasemi, and B. Dixon, "GIS-based groundwater potential mapping using boosted regression tree, classification and regression tree, and random forest machine learning models in Iran," *Environmental Monitoring and Assessment*, vol. 188, no. 1, p. 44, 2016.

[43] G.-B. Huang, Q.-Y. Zhu, and C.-K. Siew, "Extreme learning machine: theory and applications," *Neurocomputing*, vol. 70, no. 1–3, pp. 489–501, 2006.

[44] M. Peña and H. van den Dool, "Consolidation of multimodel forecasts by ridge regression: application to pacific sea surface temperature," *Journal of Climate*, vol. 21, no. 24, pp. 6521–6538, 2008.

[45] G. B. Huang, H. Zhou, X. Ding, and R. Zhang, "Extreme learning machine for regression and multiclass classification," *IEEE Transactions on Systems, Man, and Cybernetics, Part B (Cybernetics)*, vol. 42, no. 2, pp. 513–529, 2012.

[46] M. J. Simpson and N. I. Fox, "Dual-polarized quantitative precipitation estimation as a function of range," *Hydrology and Earth System Sciences*, vol. 22, no. 6, pp. 3375–3389, 2018.

[47] B.-C. Seo, B. Dolan, W. F. Krajewski, S. A. Rutledge, and W. Petersen, "Comparison of single- and dual-polarization-based rainfall estimates using NEXRAD data for the NASA Iowa flood studies project," *Journal of Hydrometeorology*, vol. 16, no. 4, pp. 1658–1675, 2015.

Hindawi
Advances in Meteorology
Volume 2019, Article ID 5789358, 10 pages
https://doi.org/10.1155/2019/5789358

*Research Article*

# Coverage of China New Generation Weather Radar Network

**Chao Min,[1,2] Sheng Chen,[1,2] Jonathan J. Gourley,[3] Haonan Chen,[4,5] Asi Zhang,[1,2] Yong Huang,[6] and Chaoying Huang[7]**

[1]*School of Atmospheric Sciences, Guangdong Province Key Laboratory for Climate Change and Natural Disaster Studies, Sun Yat-sen University, Guangzhou 510275, China*
[2]*Southern Marine Science and Engineering Guangdong Laboratory (Zhuhai), Zhuhai 519082, China*
[3]*NOAA/National Severe Storms Laboratory, Norman 73072, USA*
[4]*Colorado State University, Fort Collins 80523, USA*
[5]*NOAA/Earth System Research Laboratory, Boulder 80305, USA*
[6]*Anhui Meteorological Bureau, Hefei 230061, China*
[7]*Key Laboratory of Environment Change and Resources Use in Beibu Gulf, Guangxi Teachers Education University, Nanning 530011, China*

Correspondence should be addressed to Sheng Chen; chensheng@mail.sysu.edu.cn

Received 10 March 2019; Revised 11 May 2019; Accepted 20 May 2019; Published 16 June 2019

Guest Editor: Dongkyun Kim



The China Meteorological Administration has deployed the China New Generation Weather Radar (CINRAD) network for severe weather detection and to improve initial conditions for numerical weather prediction models. The CINRAD network consists of 217 radars comprising 123 S-band and 94 C-band radars over mainland China. In this paper, a high-resolution digital elevation model (DEM) and beam propagation simulations are used to compute radar beam blockage and evaluate the effective radar coverage over China. Results show that the radar coverage at a height of 1 km above ground level (AGL) is restricted in complex terrain regions. The effective coverage maps at heights of 2 km and 3 km AGL indicate that the Yangtze River Delta, the Pearl River Delta, and North China Plain have more overlapping radar coverage than other regions in China. Over eastern China, almost all areas can be sampled by more than 2 radars within 5 km above mean sea level (MSL), but the radars operating in Qinghai-Tibet Plateau still suffer from serious beam blockage caused by intervening terrain. Overall, the radars installed in western China suffer from much more severe beam blockage than those deployed in eastern China. Maps generated in this study will inform users of the CINRAD data of their limitations for use in precipitation estimation, as inputs to other weather and hydrological models, and for satellite validation studies.

## 1. Introduction

As the climate changes, the temporal and spatial distributions of precipitation characteristics are experiencing changes. Torrential precipitation events have become more frequent [1–3], which often lead to floods and debris flows causing large property damages and casualties. With the high spatiotemporal continuity of radar data, forecasters can identify the location of heavy precipitation and issue early warnings and watches. Understanding realistic spatial coverage maps associated with an operational radar network is vital for using the data in applications [4, 5]. Klazura and Imy simulated a coverage map at 10,000 ft (about 3.0 km) above the radar site level for radar sites in the contiguous United States (CONUS), showing vast areal coverage extents even in the western United States [6]. Nevertheless, the altitude of western WSR-88D sites varies greatly (the elevation of radar sites ranges from near sea level to more than 10,000 ft). Some researchers have pointed out that precipitation is orographically enhanced within 1-2 km above the topography [7–9]. Thus, Klazura and Imy optimistically overestimated the radar coverage over western mountains, and it is difficult to interpret meaningful information from their work of a radar coverage map [10, 11]. Westrick et al. evaluated the limitation of the WSR-88D radar network over the mountainous West of the US and defined that the radar

scanning range is effective if more than 50% of the beam is unblocked [11]. Subsequently, Maddox et al. developed radar coverage maps over the CONUS in more detail [10]. More reports about the terrain blockage of regional radars can be found in [12, 13].

When constructing a weather radar network, terrain blockage is a significant factor to affect siting radars. Considering this, Minciardi et al. developed an approach to optimally deploy the weather radar network in Italy [14]. Inggs et al. provided a quantitative method for evaluating radar coverage to improve future construction and siting of radars [15]. Weather radar data are the most reliable remote sensing data in detecting precipitation. However, the radar beam usually encounters partial or total beam blockage caused by high buildings and mountains. Additionally, some previous studies use beam propagation models to provide beam blockage correction factors to enhance precipitation estimates. The bias between radar quantitative precipitation estimation (QPE) and ground gauge data will be reduced by using these factors [16–19]. Geng and Katsumata analysed beam blockage of radars on board the Mirai and showed that details about beam blockage improves quality control of radar data of Mirai [4].

Similar to the NEXRAD network in the US, the China Meteorological Administration (CMA) has deployed the China Next Generation Weather Radar (CINRAD) network. Currently, the CINRAD network is composed of 217 Doppler weather radars (94 C-band radars and 123 S-band radars) over mainland China. These radars are distributed densely across China except in complex terrain where beam blockages are more likely to have negative consequences on derived quantitative precipitation estimation (QPE) [11, 12, 20]. Additionally, there are four WSR-88D radars installed in Taiwan and one WSR-98D radar installed in Hong Kong. Previous studies evaluated the radar coverage over selected regions of southern China where the topography is relatively flat compared to western China, indicating decent coverage [21]. Wang et al. expanded the study of radar coverage to mainland China using a single tilt at 0.5-degree elevation angle [22]. However, the national CINRAD coverage map still needs to be investigated and improved due to the absence of effective coverage by higher elevation angles. Furthermore, the CMA has supplemented 58 more radars over China since the initial study of CINRAD coverage had approximately 160 radars in 2011 [22]; thus, the effective coverage maps need to be updated accordingly. Therefore, it is necessary to investigate the radar network's coverage over China which can serve as an important reference for radar data users, especially for weather forecasters in operational offices. In order to make better use of weather radar network for monitoring and early warning of extreme weather events, this study quantifies the coverage of the renewed radar network over China, including four radars in Taiwan and the one in Hong Kong.

## 2. Methodology

*2.1. Study Area.* The complex topography in China shows a staircase-like distribution from low altitude in the east to high altitude in the west. Spatiotemporal precipitation spectra show a significant diurnal and seasonal variation over China [23, 24]. Heavy precipitation is common in summer, and these storms can trigger severe floods and mudslides. Figure 1 depicts the digital elevation map of China and the distribution of the CINRAD network. The altitude ranges from near sea level to more than 8000 m over the Qinghai-Tibet Plateau. In total, there are 222 radars (composed of 128 S-band and 94 C-band radars) in operation to detect weather phenomena over China when the radars in Hong Kong and Taiwan are taken into account. S-band radars have the advantage of detecting precipitation from longer distances (~460 km) with little attenuation in rain. Geographically, eastern China is much flatter than western China (such as the Tibet plateau). Economically, most of large cities (e.g., Beijing, Shanghai, Shenzhen, and Guangzhou) are in eastern China where more than 90% of population lives. The total gross domestic product (GDP) of these cities accounts for more than 90% of the total GDP of China. Meteorologically, eastern China is impacted significantly by the East Asia monsoon which brings a lot of disastrous heavy precipitation events including tornadoes and typhoons. Therefore, S-band radars are deployed in eastern China to help monitor heavy precipitation events and provide early warnings for the government and the public when the radar observations are assimilated in the numerical forecast models like the Weather Research and Forecasting (WRF) model. In contrast, western China has lots of high-altitude mountains like Kunlunshan Mountain in Tibet plateau and Hengduan Mountains in southeastern Qinghai plateau. These mountains cause serious radar beam blockage. Additionally, few people live in the western China where the GDP is a small percentage of the total GDP of China. Furthermore, few disastrous weather events occur and the precipitation intensity is weaker than that in the middle and eastern China. For these reasons, it makes sense to use the lower-cost C-band radars in western China despite the disadvantages with shorter ranges for precipitation detection and reflectivity losses in rain due to attenuation of the radar signal.

The radar distributions are sparse in the west especially on the Qinghai-Tibet Plateau, while the radars are more closely spaced in the east. A national map of slope derived from 30 arc sec (90 m) Shuttle Radar Topography Mission (SRTM) high-resolution digital elevation model (DEM) data by using ArcGIS, which is one of the contributing factors for landslides, is shown in Figure 2. The steep slope areas are Tianshan Mountains, northern Qinghai-Tibet Plateau, south-eastern Qinghai-Tibet Plateau, Yunnan-Guizhou Plateau, and northern Sichuan province where radars are distributed more sparsely. Figure 3 shows the ideal coverage map of CINRAD without beam blockage and national meteorological stations. The shaded area represents coverage (without beam blockage) of 230 km for S-band and 150 km for C-band radar. There are large areas in south-eastern XinJiang, Qinghai-Tibet Plateau, and northern Inner Mongolia with no radar coverage while almost the rest of China is well detected by the CINRAD network in this optimal coverage map. The complex topography in China

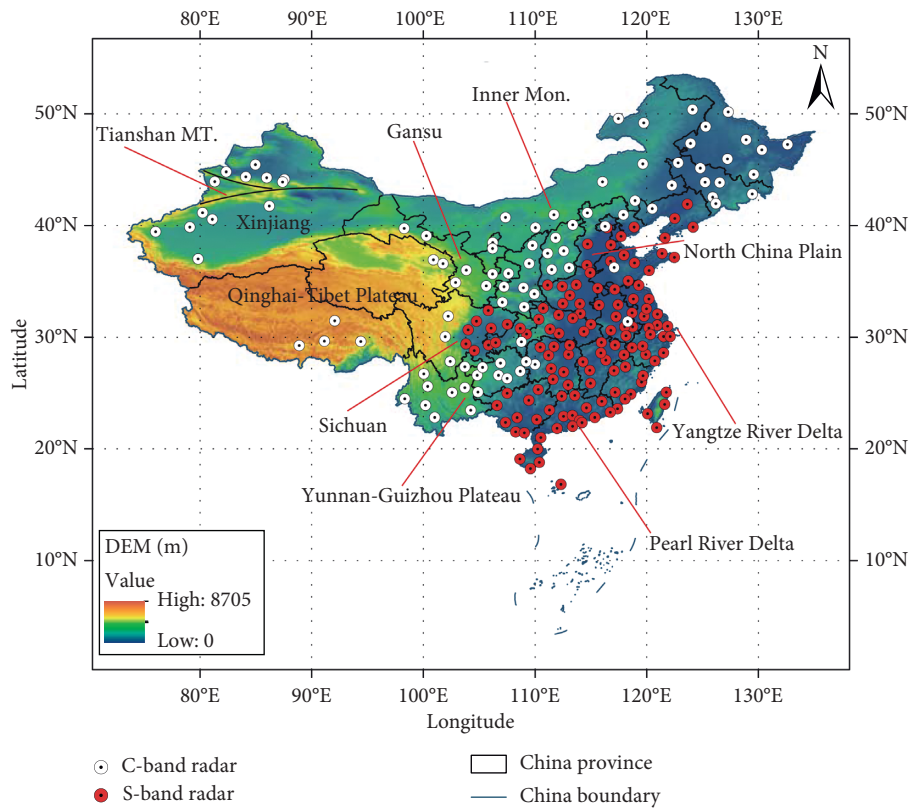


Figure 1: Topography (m) map of China with distributions of the CINRAD. White dots represent C-band radars, and red dots denote the S-band radars.

will induce serious beam blockages causing bias in radar quantitative precipitation estimation (QPE) especially in mountainous western China. Meanwhile, the ground-based gauges are rare in these areas without radar coverage, especially on the Qinghai-Tibet Plateau called water tower of Asia. It is difficult to make accurate precipitation forecast there due to the lack of radar coverage and the sparseness of ground-based gauges.

*2.2. Data and Computing Method.* The 30 arc sec (90 m) Shuttle Radar Topography Mission (SRTM) high-resolution digital elevation model (DEM) data (available at http://srtm.csi.cgiar.org/SELECTION/inputCoord.asp) are used in this study to depict the terrain over China and then compared with the height of the center of the radar beam. Similar analysis methods [10, 11] have been employed to compute radar coverage over the US. It is known that the antenna elevation angle depends on the scan strategies employed for the network. The new generation weather radar supplies two volume coverage patterns (VCP), namely, precipitation scan mode and clear sky scan mode. The precipitation scan mode contains two VCPs (i.e., VCP-11 and VCP-21). In operational practice, VCP-21 is generally used while VCP-11 is rarely used. The VCP-21 scan mode is to complete 9 elevation tilts' scans (e.g., 0.5°, 1.5°, 2.4°, 3.4°, 4.3°, 6.0°, 9.9°, 14.6°, and 19.5°) within 6 minutes. In order to alleviate beam blockage caused by complex topography, the hybrid scan is constructed from a composite of elevation angles to optimize low-level coverage needed for precipitation estimation [25]. Now, radar data users usually use whichever elevation angle is closest (and above) to the ground. So, the lowest 0.5° elevation angle is now used when the area of concern is closer to radar [26]. According to this, this paper applies the new method, which is illustrated in Figure 4, to evaluate realistic radar coverage. For instance, when the radar beam encounters a mountain in the propagation path and the mountain is high enough to obstruct the radar beam up to 50%, the second tilt will be adopted. If the mountain is still too high to overcome and the radar beam is still blocked by 50% or more, the third tilt will be adopted. The remaining tilts can be adopted in the same manner.

The following principles are used in this study. Firstly, the location information (longitude, latitude, and altitude) of each radar site is determined and mapped with the DEM data around the radar site. The height of the center of the beam at each sampling point (every 50 m for a sampling point) is calculated with range at each azimuthal angle (at intervals of 0.1°). Next, the height of the beam center is compared with the corresponding point on the DEM and if the center of the radar beam is lower than the terrain, it is considered to be blocked and no longer propagates at farther ranges. The height of the radar beam is computed by the following equation with the assumption that the radar beam propagates in standard atmosphere [27]:

$$h = \sqrt{r^2 + R^2 + 2rR\sin(\theta)} - R + h_0, \quad (1)$$

where $h$ is the height of radar beam, $r$ is the range from radar site, $R$ (approximately 8500 km) is the effective earth radius

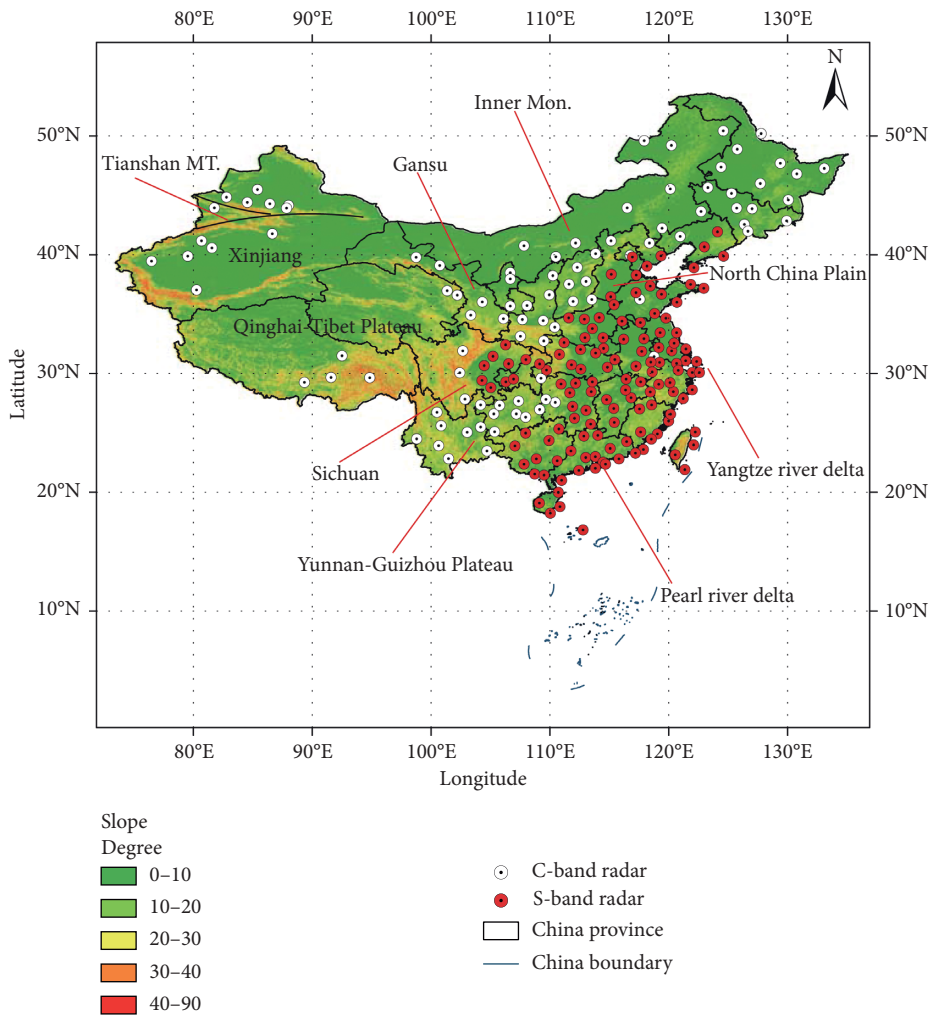


FIGURE 2: Slope (degree) map of China showing distributions of the CINRAD. White dots represent C-band radars, and red dots refer to the S-band radars.

obeying standard atmospheric refraction, $\theta$ is the elevation angle, and $h_0$ is the height of radar antenna. The range of a radar scan is limited by earth curvature, intervening blockages and attenuation of the radar signal. Attenuation is more prevalent with C-band radars, so this study computes the radar coverage out to 230 km for S-band radars and 150 km for C-band radars. Key specifications of the CINRAD systems are shown in Table 1.

To verify the beam propagation simulation effectiveness, the reflectivity of example radars (Shenzhen radar and Zhuhai radar) and simulation results are presented in Figure 5. Figures 5(a) and 5(c) show the radar coverage of the first tilt (0.5°) of Shenzhen radar and Zhuhai radar revealing a similarity with the corresponding reflectivity maps (Figures 5(b) and 5(d)) though there are some notable differences too. These inconsistencies may be caused by ground clutter, biological scatterers, sea clutter, etc. This indicates that beam propagation simulations used in this study can effectively depict the terrain blockage. Further validation would be possible using reflectivity observations in widespread rain.

## 3. Results

In this study, both radar coverage maps at heights above ground level (AGL) and constant altitudes in MSL are calculated to estimate the coverage condition of the CINRAD network. Heights of 1 km, 2 km, and 3 km AGL and 3 km and 5 km MSL are set as constraints.

During the cool season, the height of the bright band is relatively low and orographic precipitation processes enhance growth in the lowest 1-2 km above topography [7–9]. When radar data users are applying the measurements for studying or monitoring storms where microphysical and dynamical processes occur at low levels (e.g., cool season precipitation and quasi-linear convective system tornadoes), radar data should be gathered near the ground [10]. Correspondingly, radar coverage at 1 km and 2 km AGL are shown in Figures 6(a) and 6(b), respectively. Figure 6(a) shows that there are large areas with no radar coverage in western China especially on the Qinghai-Tibet Plateau. In addition, there are severe beam blockages on the Yunnan-Guizhou Plateau owing to the complex terrain. However, an

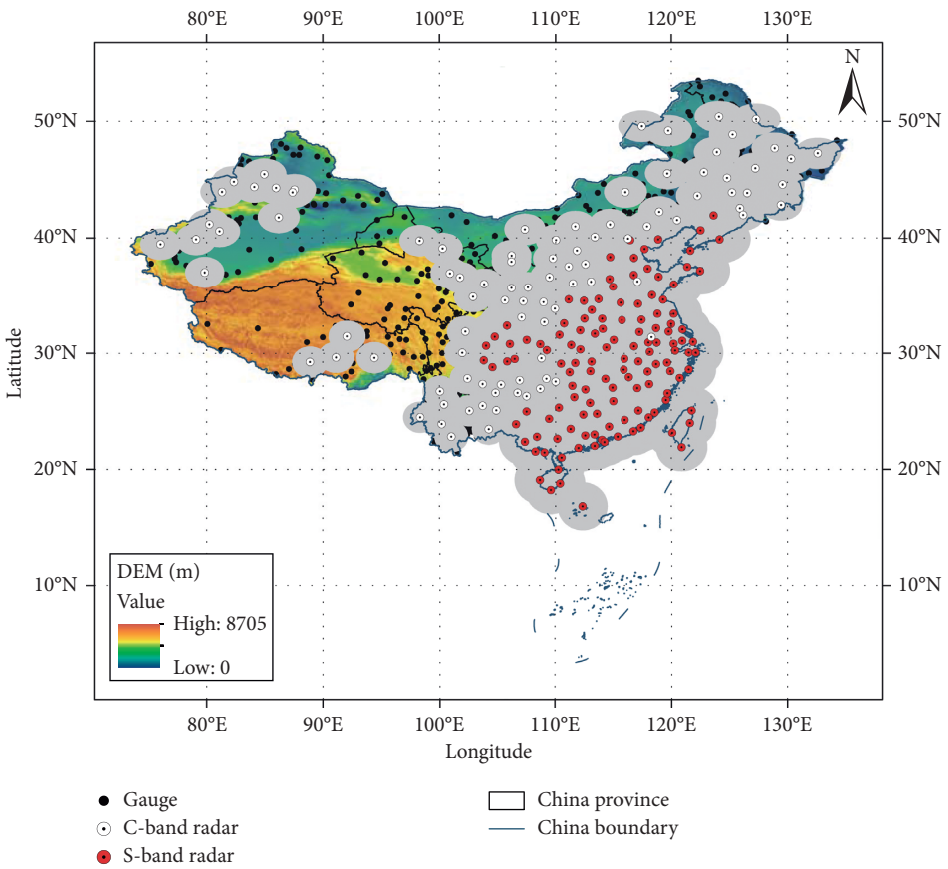


Figure 3: CINRAD coverage map (without beam blockage) of 230 km for S-band and 150 km for C-band radar. White dots represent C-band radars, red dots denote the S-band radars, and black dots refer to national meteorological stations.

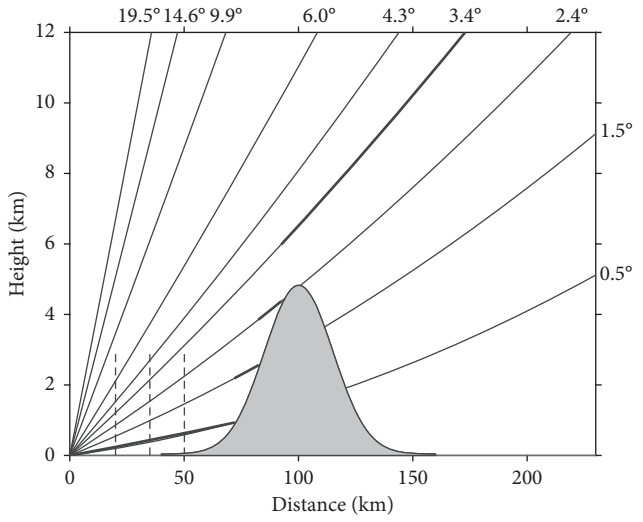


Figure 4: The computing method of radar effective coverage using all elevation tilts with considering terrain blockage. The radar is supposed to locate at original point (0, 0). The shadowed area denotes a mountain which blocks radar beams. The black bold lines are the adopted beams from the radar, and the dash lines represent different distances (e.g., 20 km, 35 km, and 50 km) from radar site.

exception is that the radar coverage in the northern regions of Tianshan Mountains in Xinjiang province is relatively good. In contrast to the coverage status in the western area,

Table 1: System specifications of China Next Generation Weather Radars.

| Radar type | S-band radar | C-band radar |
|---|---|---|
| Wavelength (cm) | ~10 | ~5.6 |
| Antenna gain (dB) | ≥44 | ≥43 |
| Diameter of the antenna dish (m) | 8~9 | 4.5 |
| Range resolution (m) | ≤150 | ≤150 |
| Beam width (°) | ≤1.0 | ≤1.0 |
| Pulse power (kW) | ≥650 | ≥250 |
| Noise figure (dB) | ≤4 | ≤4 |
| Dynamic range (dB) | ≥95 | ≥95 |

overlapping radar coverage in eastern China is better at 1 km AGL. Radar coverage at 2 km AGL (Figure 6(b)) depicts limited coverage in western China while the CINRAD network covers the east quite well. For example, there are more than 3 radars overlapping in the Yangtze River Delta and the Pearl River Delta, which are the important economic and prosperous areas in China. Generally speaking, when areas are covered by more than one radar, the radar QPE will be more accurate. Because biases of radar QPE increase with longer ranges from the radar site, low-level coverage is maximized using radar data that have been mosaicked [17, 28]. However, the steep slope areas (e.g., Tianshan Mountains, northern Qinghai-Tibet Plateau, south-eastern Qinghai-Tibet Plateau, Yunnan-Guizhou Plateau, and

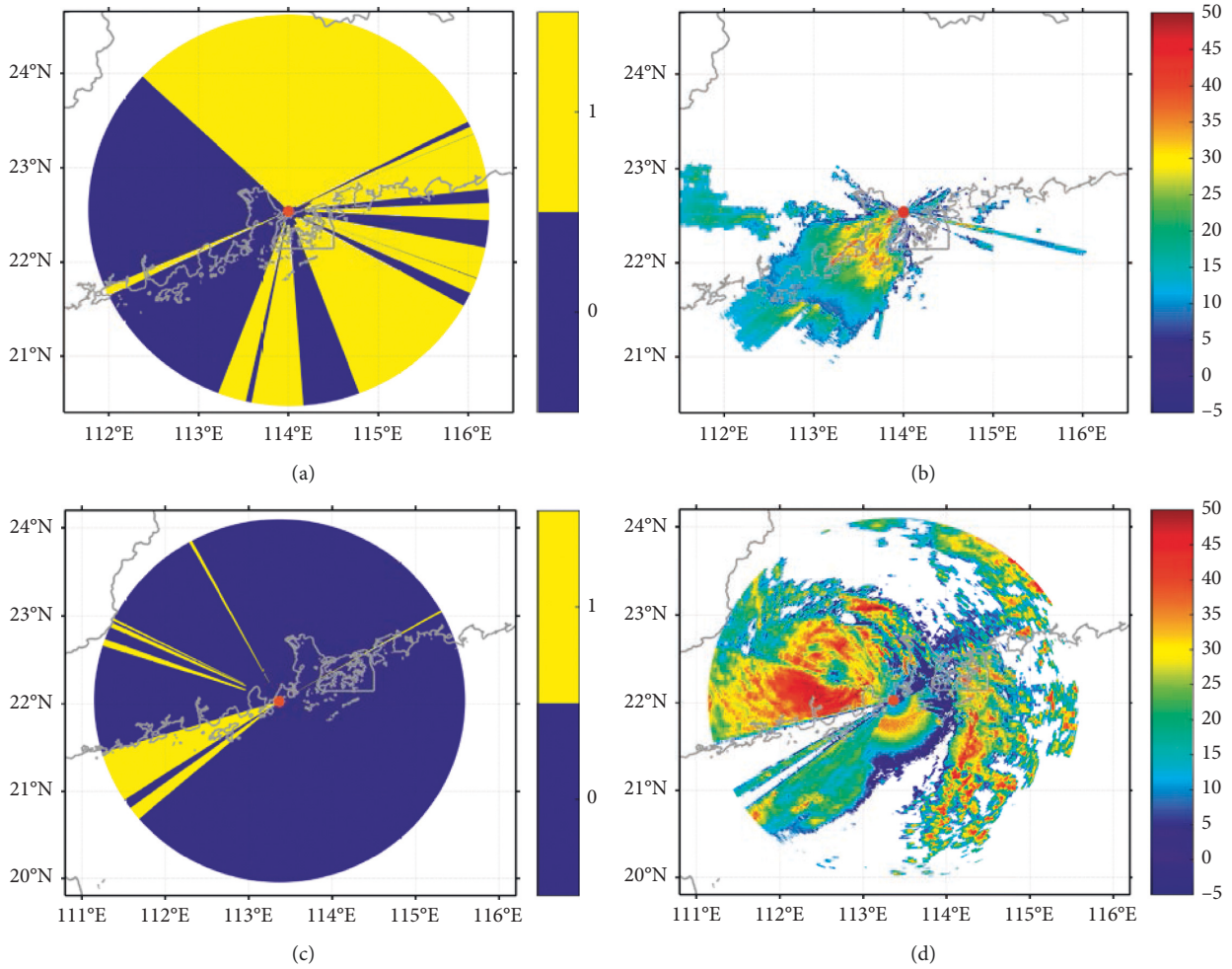


Figure 5: (a) The effective coverage map of Shenzhen radar using the first tilt (0.5°) simulation, and the blue area denotes coverage area while the yellow area represents no radar coverage area. (b) The reflectivity at UTC 0000 4 September 2017 is used to validate the simulation result. (c) The effective coverage map of Zhuhai radar using the first tilt (0.5°) simulation, and the blue area refers to coverage area while the yellow area indicates no radar coverage area. (d) The reflectivity at UTC 1512 23 August 2017 is used to validate the simulation result. The red dot corresponds to the radar site.

northern Sichuan province) shown in Figure 2 are almost with little radar coverage according to Figures 6(a) and 6(b). Topographic slope is a contributing factor for landslides when heavy precipitation occurs. So, it will be challenging to issue early warnings and watches of heavy precipitation, mudslides, and landslides in these regions.

The CINRAD network coverage map at a height within 3 km AGL is exhibited in Figure 6(c). It is noted that the coverage and overlapping maps are to some extent different from those in Wang et al. [22]. The main reasons why these two coverage maps are different are as follows: Firstly, 58 radars have been added to the CINRAD network since the initial study. Secondly, the merged data of multiple elevation angles to construct the hybrid scan represent the coverage map in this paper. In the new coverage map shown in Figure 6(c), it can be seen that western China suffers from restricted coverage at 3 km AGL except the northern Xinjiang province and some regions of the southern Tianshan Mountains. Eastern China and central China are well sampled by the CINRAD network except for some parts of the northeast where radars are sparse. For instance, there are large areas covered by as many as 3–6 radars in the North China Plain and 4–7 radars in the Pearl River Delta area. The Yangtze River Delta is sampled by 4–9 radars. Therefore, it is best covered by the CINRAD network in China and facilitates water resources management, severe thunderstorm monitoring and warning, and forecasting through assimilation in numerical weather prediction models. In summer, precipitation amounts, occurrence frequencies, and intensities reach their peak values in most of China, especially in the eastern Qinghai-Tibet Plateau and Yunnan-Guizhou Plateau where there is sparse radar coverage [23, 24]. Plus, the freezing levels are higher compared to the cool season. Thus, the radar coverage map at 3 km AGL in Figure 6(c) is a preferable reference for interpreting the capability of the CINRAD network to detect warm season storms. For the Qinghai-Tibet Plateau, the large data voids present great challenges

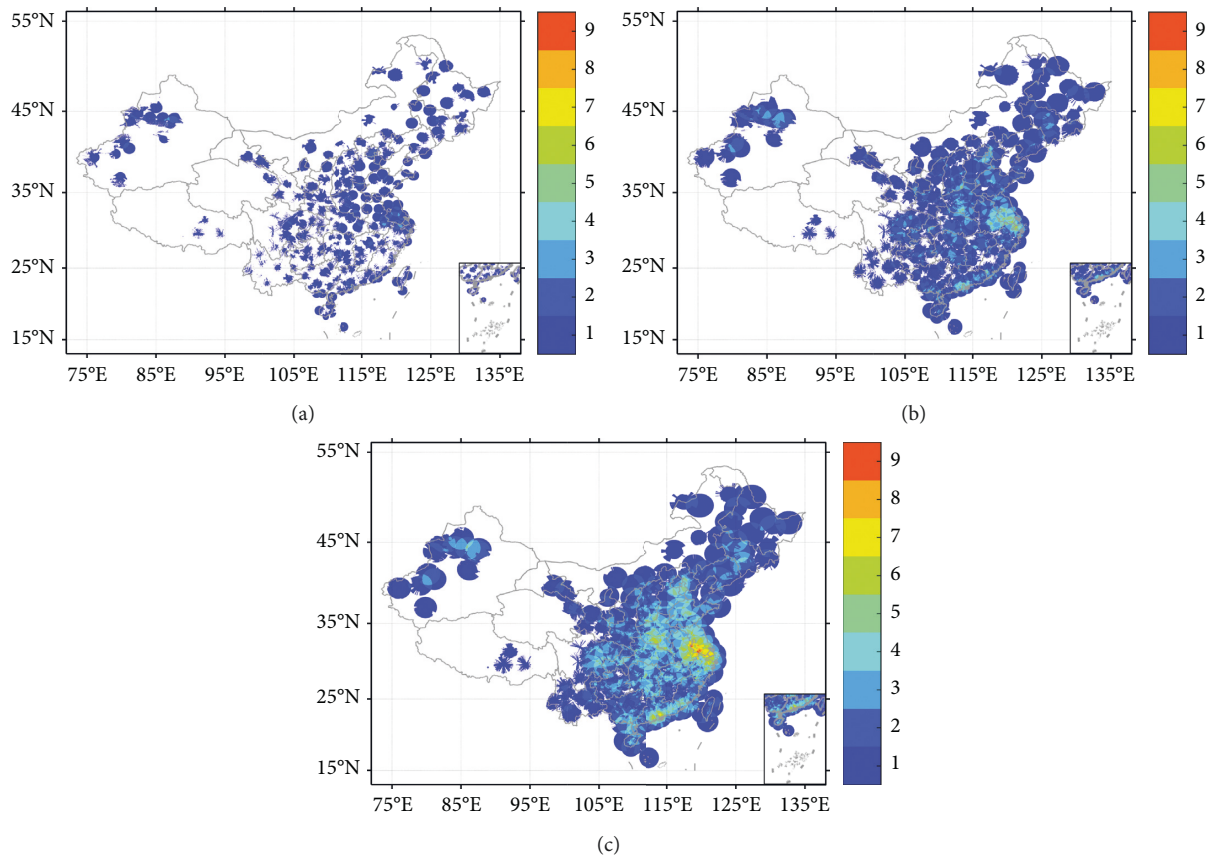


Figure 6: Effective coverage map of CINRAD network at heights of (a) 1 km, (b) 2 km, and (c) 3 km AGL over China. The legend refers to the number of overlapping radars covering a given point in space, and the subgraph at the bottom right corner of each panel represents the South China Sea.

for radar data users to estimate precipitation occurring in this region.

The atmospheric conditions like temperature, wind, troughs, and ridges are usually analysed at mandatory levels of 700 hPa pressure level and 500 hPa pressure level in weather forecast. Gou et al. calculated the maximum ranges of radar coverage and the altitudes of multiradar hybrid mosaic reflectivity over eastern Sichuan province (e.g., well-covered area in this study) and further studied radar reflectivity for storms at different altitudes and propagation directions [29]. So, CINRAD coverage maps at heights above MSL are also estimated in this study with the aim of offering reference when designing mosaicking schemes for locations that are covered by more than one radar. Figures 7(a) and 7(b) show the CINRAD network coverage at a height of 3 km above MSL (i.e., near the 700 hPa isobaric surface) and 5 km above MSL (i.e., near the 500 hPa isobaric surface), respectively. Figures 6(c) and 7(a) show a significantly different situation in terms of coverage in western China. As shown in Figure 7(a), there are larger areas with data voids at a height of 3 km above MSL because the elevation of many radar sites in western China is at or higher than 3 km above MSL. There is nearly no radar coverage on the Qinghai-Tibet Plateau and very poor radar coverage on the Yunnan-Guizhou Plateau, Inner Mongolia Autonomous Region (Inner Mon.), Gansu province, and the southeastern Xinjiang province. In contrast, the radar coverage map (Figure 7(a)) reveals overlapping coverage in the east, sampled by more than 2 radars in the North China Plain, the Pearl River Delta area, and the Yangtze River Delta. The coverage map of the CINRAD network at a height of 5 km above MSL still shows limitations in the west, while eastern China and central China are almost completely covered with more than 2 radars overlapping in almost all regions (Figure 7(b)). There are more than 4 radars overlapping in the North China Plain, southern China, eastern Sichuan province, and the Yangtze River Delta.

For further analysis, radar coverage indexes such as coverage area (including the border areas and coastal areas) and coverage ratio are also used in this study. As seen in Table 2, the statistical result shows that the CINRAD coverage area of 1 km AGL (AGL1) is about $2.5 \times 10^6$ km$^2$ and the coverage ratio is about 26%. With the increasing of height of AGL and height above MSL, the coverage area and ratio are increasing. The coverage area of 2 km AGL (AGL2) is about $5.3 \times 10^6$ km$^2$, and the coverage ratio is about 55%, respectively. Within 3 km AGL, the coverage area and ratio are about $6.6 \times 10^6$ km$^2$ and 69%, respectively. Within 3 km above MSL, the coverage area and ratio are similar to these indexes within 2 km AGL. The coverage area ($7.0 \times 10^6$ km$^2$)

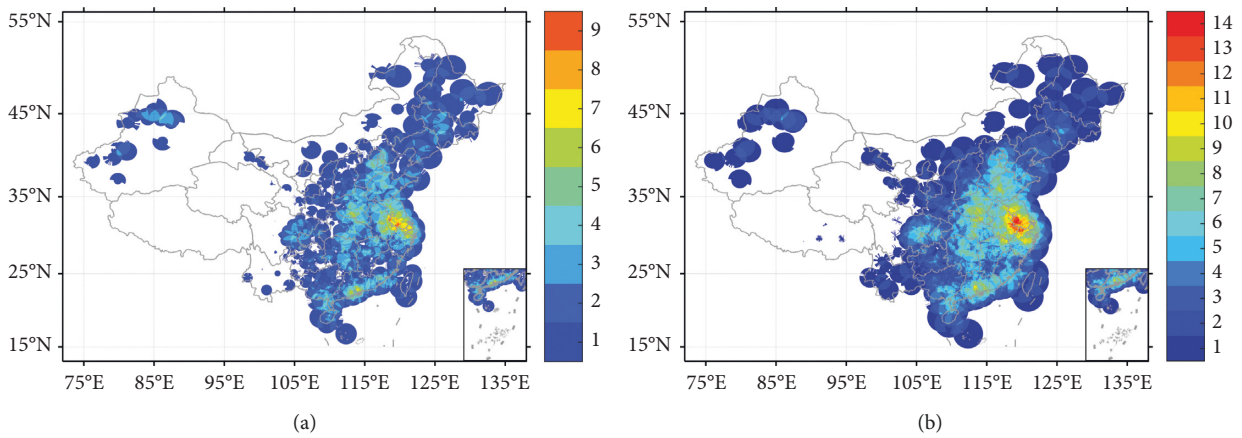


Figure 7: Effective coverage map of CINRAD network at heights of (a) 3 km and (b) 5 km above MSL over China. The legend refers to the number of overlapping radars covering a given point in space and the subgraph at the bottom right corner of each panel represents the South China Sea.

Table 2: Coverage index of China Next Generation Weather Radars.

| Height | Coverage area ($km^2$) | Coverage ratio (%) |
|---|---|---|
| AGL1 | $2.5 \times 10^6$ | 26 |
| AGL2 | $5.3 \times 10^6$ | 55 |
| AGL3 | $6.6 \times 10^6$ | 69 |
| MSL3 | $5.3 \times 10^6$ | 55 |
| MSL5 | $7.0 \times 10^6$ | 73 |

and ratio (73%) reach maximum when the height is within 5 km above MSL.

## 4. Conclusions and Recommendations

The 30 arc sec (90 m) high-resolution DEM data are used with a model for beam propagation estimated in a standard atmosphere to calculate beam occultation and the effective coverage maps of the Chinese national weather radar network. The main findings of this study are as follows:

(1) The coverage map at 1 km AGL shows extremely limited coverage especially in the mountainous west such as the Qinghai-Tibet Plateau and the Yunnan-Guizhou Plateau.

(2) At 2 km AGL, the coverage extent improves for radars deployed in eastern and central China, covering most of those areas. In particular, the Yangtze River Delta and the Pearl River Delta are generally sampled by more than 3 radars. However, the radars are still insufficient to estimate precipitation that occurs on the Qinghai-Tibet Plateau.

(3) At a height of 3 km AGL, CINRAD network provides good coverage east of 105°E although there is no radar coverage in many regions of the Inner Mongolia Autonomous Region. There are still large parts in western China with no radar coverage, which poses challenges in estimating precipitation.

(4) At 3 km above MSL, the radar coverage map (Figure 7(a)) is significantly different from the one at 3 km AGL (Figure 6(c)) over the mountainous west due to radar sittings at high altitudes, while the coverage remains good in eastern and central China.

(5) At 5 km above MSL, the CINRAD network shows much better coverage than at 3 km above MSL and thus can monitor most areas in China except the Qinghai-Tibet Plateau, the Inner Mongolia province, and the southeast of Xinjiang province. There are more than 4 radars overlapping in the North China Plain, southern China, eastern Sichuan province, and the Yangtze River Delta.

With the rapid economic development of China in recent years, many high buildings have been constructed throughout the country, which can cause additional blockages to the radar beams. These anthropogenic changes are not represented in the DEM used in this study and thus not represented in the coverage maps presented herein. Although there are some limitations, this study can provide a reference for the future construction of the CINRAD network in China (e.g., identifying areas where radar coverage is insufficient to add a new radar or using our model to select candidate sites for radar construction) and radar coverage maps could be used to guide radar data mosaicking schemes in the future. If we can attain the latest DEM data with higher accuracy (e.g., 10 m or higher resolution DEM data) or add the heights of newly built high buildings into the DEM, the beam propagation simulations will be improved. It is recommended that users identify and document additional blockages by examining long-term precipitation accumulations or reflectivity frequency maps. However, these radar datasets are not presently available.

## Data Availability

The 30 arc sec (90 m) Shuttle Radar Topography Mission (SRTM) high-resolution digital elevation model (DEM) data used to depict the terrain over China are available at http://srtm.csi.cgiar.org/SELECTION/inputCoord.asp. The latitude, longitude, and elevation information of radar stations as well as radar reflectivity data is confidential.

## Conflicts of Interest

The authors declare that there are no conflicts of interest regarding the publication of this paper.

## Acknowledgments

This research was partially sponsored by the "100 Top Talents Program" (74110–52601108) at Sun Yat-Sen University, Guangzhou, Guangdong, China; "100 Top Talents Program" of Guangxi Zhuang Autonomous Region, Guangxi Scientific Technology Development Program (2014DD29090); High-Level Talents Training and Teacher Qualities and Skills Promotion Plan for Guangxi Colleges and Universities (8844); the National Natural Science Foundation of China (41875182, 51579162, 41661021, and 41866001); and Guangxi Natural Fund of Innovative Team Project (2016JJF15001). Thanks are given to assistant engineer Mingfeng Li at Ruili Meteorological Bureau and Dr. Zhiheng Liao at School of Atmospheric Sciences, Sun Yat-Sen University, for their help in processing partial codes and valuable advice.

## References

[1] V. V. Kharin, F. W. Zwiers, X. Zhang, and G. C. Hegerl, "Changes in temperature and precipitation extremes in the IPCC ensemble of global coupled model simulations," *Journal of Climate*, vol. 20, no. 8, pp. 1419–1444, 2007.

[2] P. A. O'Gorman and T. Schneider, "The physical basis for increases in precipitation extremes in simulations of 21st-century climate change," *Proceedings of the National Academy of Sciences*, vol. 106, no. 35, pp. 14773–14777, 2009.

[3] Y. Sun, S. Solomon, A. Dai, and R. W. Portmann, "How often will it rain?," *Journal of Climate*, vol. 20, no. 19, pp. 4801–4818, 2007.

[4] B. Geng and M. Katsumata, "Beam blockage identification for weather radars on board the R/V Mirai using archived data," *JAMSTEC Report of Research and Development*, vol. 22, pp. 1–12, 2016.

[5] T. Pellarin, G. Delrieu, G.-M. Saulnier, H. Andrieu, B. Vignal, and J.-D. Creutin, "Hydrologic visibility of weather radar systems operating in mountainous regions: case study for the ardèche catchment (France)," *Journal of Hydrometeorology*, vol. 3, no. 5, pp. 539–555, 2002.

[6] G. E. Klazura and D. A. Imy, "A description of the initial set of analysis products available from the NEXRAD WSR-88d system," *Bulletin of the American Meteorological Society*, vol. 74, no. 7, pp. 1293–1311, 1993.

[7] R. T. Bruintjes, T. L. Clark, and W. D. Hall, "Interactions between topographic airflow and cloud/precipitation development during the passage of a winter storm in Arizona," *Journal of the Atmospheric Sciences*, vol. 51, no. 1, pp. 48–67, 1994.

[8] J. D. Marwitz, "The kinematics of orographic airflow during sierra storms," *Journal of the Atmospheric Sciences*, vol. 40, no. 5, pp. 1218–1227, 1983.

[9] R. M. Rauber, "Microphysical structure and evolution of a central sierra Nevada orographic cloud system," *Journal of Applied Meteorology*, vol. 31, no. 1, pp. 3–24, 1992.

[10] R. A. Maddox, J. Zhang, J. J. Gourley, and K. W. Howard, "Weather radar coverage over the contiguous United States," *Weather and Forecasting*, vol. 17, no. 4, pp. 927–934, 2002.

[11] K. J. Westrick, C. F. Mass, and B. A. Colle, "The limitations of the WSR-88D radar network for quantitative precipitation measurement over the coastal western United States," *Bulletin of the American Meteorological Society*, vol. 80, no. 11, pp. 2289–2298, 1999.

[12] W. F. Krajewski, A. A. Ntelekos, and R. Goska, "A GIS-based methodology for the assessment of weather radar beam blockage in mountainous regions: two examples from the US NEXRAD network," *Computers & Geosciences*, vol. 32, no. 3, pp. 283–302, 2006.

[13] P. A. Kucera, W. F. Krajewski, and C. B. Young, "Radar beam occultation studies using GIS and DEM technology: an example study of Guam," *Journal of Atmospheric and Oceanic Technology*, vol. 21, no. 7, pp. 995–1006, 2004.

[14] R. Minciardi, R. Sacile, and F. Siccardi, "Optimal planning of a weather radar network," *Journal of Atmospheric and Oceanic Technology*, vol. 20, no. 9, pp. 1251–1263, 2003.

[15] M. Inggs, G. Lange, and Y. Paichard, "A quantitative method for mono- and multi-static radar coverage area prediction," in *Proceedings of the IEEE National Radar Conference*, pp. 707–711, Washington, DC, USA, May 2010.

[16] J. Bech, B. Codina, J. Lorente, and D. Bebbington, "The sensitivity of single polarization weather radar beam blockage correction to variability in the vertical refractivity gradient," *Journal of Atmospheric and Oceanic Technology*, vol. 20, no. 6, pp. 845–855, 2003.

[17] J. Bech, U. Gjertsen, and G. Haase, "Modelling weather radar beam propagation and topographical blockage at northern high latitudes," *Quarterly Journal of the Royal Meteorological Society*, vol. 133, no. 626, pp. 1191–1204, 2007.

[18] A. Fornasiero, J. Bech, and P. P. Alberoni, "Enhanced radar precipitation estimates using a combined clutter and beam blockage correction technique," *Natural Hazards and Earth System Sciences*, vol. 6, no. 5, pp. 697–710, 2006.

[19] P. C. Shakti, M. Maki, S. Shimizu et al., "Correction of reflectivity in the presence of partial beam blockage over a mountainous region using X-band dual polarization radar," *Journal of Hydrometeorology*, vol. 14, no. 3, pp. 744–764, 2013.

[20] C. B. Young, B. R. Nelson, A. A. Bradley et al., "An evaluation of NEXRAD precipitation estimates in complex terrain," *Journal of Geophysical Research: Atmospheres*, vol. 104, no. D16, pp. 19691–19703, 1999.

[21] H. Yang, P. Zhang, M. Cheng et al., "The valid mosaic data region of the CINRAD network," *Journal of Applied Meteorological Science*, vol. 20, no. 1, pp. 47–55, 2009, in Chinese.

[22] S. Wang, C. Pei, Z. Guo, and N. Shao, "Evaluations on Chinese next generation radar coverage and terrain blockage based on STRM data," *Climatic and Environment Research*, vol. 16, no. 4, pp. 459–468, 2011, in Chinese.

[23] S. Chen, Y. Tian, A. Behrangi et al., "Precipitation spectra analysis over China with high-resolution measurements from optimally merged satellite/gauge observations—part I: spatial and seasonal analysis," *IEEE Journal of Selected Topics in Applied Earth Observations and Remote Sensing*, vol. 9, no. 7, pp. 2966–2978, 2016.

[24] S. Chen, A. Behrangi, Y. Tian et al., "Precipitation spectra analysis over China with high-resolution measurements from optimally-merged satellite/gauge observations-Part II: diurnal variability analysis," *IEEE Journal of Selected Topics in Applied Earth Observations and Remote Sensing*, vol. 9, no. 7, pp. 2979–2988, 2016.

[25] J. Zhang, Y. Qi, D. Kingsmill, and K. Howard, "Radar-based quantitative precipitation estimation for the cool season in complex terrain: case studies from the NOAA

hydrometeorology testbed," *Journal of Hydrometeorology*, vol. 13, no. 6, pp. 1836–1854, 2012.

[26] J. Zhang and Y. Qi, "A real-time algorithm for the correction of brightband effects in radar-derived QPE," *Journal of Hydrometeorology*, vol. 11, no. 5, pp. 1157–1171, 2010.

[27] R. E. Rinehart, *Radar for Meteorologists*, University of North Dakota, Grand Forks, North Dakota, USA, 2rd edition, 1991.

[28] V. Chandrasekar, Y. Wang, and H. Chen, "The CASA quantitative precipitation estimation system: a five year validation study," *Natural Hazards and Earth System Sciences*, vol. 12, no. 9, pp. 2811–2820, 2012.

[29] Y. Gou, Y. Ma, H. Chen, and Y. Wen, "Radar-derived quantitative precipitation estimation in complex terrain over the eastern Tibetan Plateau," *Atmospheric Research*, vol. 203, pp. 286–297, 2018.

Hindawi
Advances in Meteorology
Volume 2019, Article ID 3572431, 13 pages
https://doi.org/10.1155/2019/3572431

*Research Article*

# Combination of Radar and Rain Gauge Information to Map the Snowy Region in Jeju Island, Korea: A Case Study

**Jung Mo Ku**[1] **and Chulsang Yoo**[2]

[1]*Research Assistant Professor, School of Civil, Environmental and Architectural Engineering, College of Engineering, Korea University, Seoul 136-705, Republic of Korea*
[2]*Professor, School of Civil, Environmental and Architectural Engineering, College of Engineering, Korea University, Seoul 136-705, Republic of Korea*

Correspondence should be addressed to Chulsang Yoo; envchul@korea.ac.kr

Received 1 February 2019; Revised 1 May 2019; Accepted 7 May 2019; Published 2 June 2019

Guest Editor: Dongkyun Kim



Hallasan Mountain is located at the center of Jeju Island, Korea. Even though Hallasan Mountain has a height of just 1,950 m, the temperature during the winter decreases below −20 degrees Celsius. On the contrary, the temperature on the coastal areas remains just above freezing. Therefore, large snowfalls in the mountain and rainfall in the coastal areas are very common in Jeju Island. Most of the rain gauges are available around highly populated coastal areas, and snow measurements are available at just four locations on the coastal areas. Therefore, it is practically impossible to distinguish the rainfall and snowfall in Jeju Island. Fortunately, two radars (Seongsan and Gosan radars) operate on Jeju Island, which fully covers Hallasan Mountain. This study proposes a method of using both the radar and rain gauge information to map the snowy region in Jeju Island, including Hallasan Mountain. As a first step, this study analyzed the $Z$-$R$ and $Z$-$S$ relationships to derive a fixed threshold of radar reflectivity to separate snowfall from rainfall, and, in the second step, this study additionally considered the observed rain rate information to implement the problem of using the fixed threshold. This proposed method was applied to radar reflectivity data collected during November 1, 2014, to April 30, 2015, and the results indicate that the method considering both the radar and rain gauge information was satisfactory. This method also showed good performance, especially when the rain rate was very low.

## 1. Introduction

Mapping the snowy region is very important in our daily lives. In some places it rains, but in other places, maybe in high-elevation areas, it can snow. If it snows, it may be necessary to limit vehicle traffic, remove snow from the road and roadsides, and sometimes warn climbers against trespassing. Accurately predicting the snowline is thus important, especially where the rainfall and snowfall simultaneously occur.

Jeju Island, which is located in the southernmost part of the Korean Peninsula, is likely the only place where both rainfalls in the plain coastal area and the snowfall in mountainous areas can be observed at the same time. This is mainly because Hallasan Mountain is located at the center of Jeju Island. With a height of 1,950 m, Hallasan Mountain is known to have a strong orographic precipitation. During winter, from December to February, the mean temperature in the coastal area is around 6.5~7.3°C, but that in the mountain area decreases to around −2.3~1.0°C. At the mountain top, the temperature easily drops below −10°C [1].

There are two main roads in Jeju Island: one is the beltway along the sea shore and the other an expressway that connects two big cities, Jeju City and Seogwipo City, in Jeju Island. In particular, the expressway passes the side of Hallasan Mountain at an elevation of 700 m. Unfortunately, this expressway is frequently closed due to heavy snowfall during the winter. Four access roads to Hallasan Mountain run up to an elevation of 1,000 m.

However, in Jeju Island, it is practically impossible to divide areas of the rainfall and snowfall. The Jeju Regional Meteorological Administration (JRMA) operates a total of 24 rain gauges, but 13 rain gauges are located near the sea

shore (elevation 0 to 250 m from the sea level) where the population is high. Rain gauges in the high-elevation mountain area are very limited. Snowfall observations are carried out at four locations over Jeju Island (Jeju, Seogwipo, Seongsan, and Gosan), but these are all in the coastal areas where snowfall is very rare. Rain gauges in the mountainous area can measure snowfall according to water depth, but it is not easy to distinguish snowfall from rainfall.

Radar data may be used as an alternative to divide areas between the rainfall and snowfall. Basically, radar reflectivity on rain drops is different from that on snow flakes. For example, the $Z$-$R$ relationships between the radar reflectivity ($Z$) and rain rate ($R$, mm/hr) are $Z = 200R^{1.6}$ [2], $Z = 31R^{1.71}$ [3], $Z = 486R^{1.37}$ [4], etc. On the contrary, the $Z$-$S$ relationships between radar reflectivity ($Z$) and snow rate (unit of mm/hr, the same as $R$) are $Z = 2{,}000S^{2.0}$ [5], $Z = 2{,}100S^{2.0}$ [6], $Z = 427S^{1.09}$ [7], etc. The two relationships are markedly different in their proportional constants, i.e., the proportional constant of the $Z$-$S$ relationship is generally much larger than that of the $Z$-$R$ relationship.

However, the problem is that, for a given radar reflectivity, it is impossible to distinguish the snowfall and rainfall. This is the main issue in this study. Currently, classification of rainfall and snowfall fully relies on the information of air temperature. It is generally assumed that snow cannot exist if the temperature is higher than 5°C [8]. Also, the guideline from the Korean Meteorological Administration (KMA) shows that the precipitation is assumed to be snowfall if the temperature is lower than 1.2°C [9]. So the problem is that the range between the obvious rainfall and obvious snowfall is too wide. This range of temperature corresponds to the elevation difference around 500 m. In case the prediction of snowline much matters such as in Jeju Island, the temperature information may not be a sufficient indicator.

The objectives of this study are as follows. First, this study will analyze the $Z$-$R$ and $Z$-$S$ relationships reported so far worldwide to characterize their difference. The difference between the two may give us an idea of separating the snowfall from rainfall. Second, as the known range of radar reflectivity of rainfall is much wide and includes that of the snowfall, simply a fixed radar reflectivity value may not be useful to map the snowy region [10]. In this case, additional information must be used to successfully achieve the study objective. In this study, rain gauge data will be considered as secondary information to separate snowfall from rainfall, as it is generally accepted that radar reflectivity is proportional to the rain rate.

This manuscript is composed of a total of five sections, including Introduction and Conclusions. In the second section, the $Z$-$R$ and $Z$-$S$ relationships are reviewed to derive their difference. In the third section, the study area and the data are explained. Finally, the fourth section explains the methodology and application examples using the data collected by both radar and rain gauges in Jeju Island, Korea.

## 2. $Z$-$R$ and $Z$-$S$ Relationships

The equation for the so-called $Z$-$R$ relationship has the following form [11]:

$$Z = AR^b, \tag{1}$$

where $Z$ is the radar reflectivity ($mm^6/m^3$), $R$ is the rain gauge rain rate (mm/hr), and $A$ and $b$ are parameters. These two parameters are known to vary so widely regionally and depending on storm types. Table 1 introduces some $Z$-$R$ relationships collected from past studies and reports worldwide.

Similar to the $Z$-$R$ relationship to estimate the radar rain rate from the radar reflectivity, the so-called $Z$-$S$ relationship is used to estimate the radar snow rate [15]. The basic form of the equation for the $Z$-$S$ relationship is the same as that for the $Z$-$R$ relationship:

$$Z = AS^b, \tag{2}$$

where the snow rate $S$ has the same unit of mm/hr as the rain rate. Table 2 shows some $Z$-$S$ relationships collected from past studies and reports. In this table, $Z_e$ has the relation with $Z$ such as $Z_e = 0.244 \times Z$. This relation was proposed in [22] for melted snowflakes.

The variability of the parameters for the $Z$-$R$ and $Z$-$S$ relationships is quite different from each other. Figure 1 compares the box plots of parameters $A$ and $b$ of the two relationships collected in this study. As can be seen in this figure, the range of parameter $A$ of the $Z$-$R$ relationship is 16.6~730 and that for parameter $b$ is 1.0~2.87. On the contrary, the range of parameter $A$ of the $Z$-$S$ relationship is 160~3,300 and that for the parameter $b$ is 1.09~2.21; that is, the ranges of parameter $A$ are very different, but those of parameter $b$ are similar to each other.

Simply plotting the $Z$-$R$ relationships and $Z$-$S$ relationships collected in this study produces Figure 2. The log-log scale was used in this figure, so all relationships are shown linearly over the $Z$-$R$ and $Z$-$S$ planes. Comparing these two panels, one can easily find that the slopes of the lines are similar to each other. In fact, this is a natural result because parameter $b$ is similar in both relationships. However, the intercept, which is related to parameter $A$, is found to be very different from each other.

This study used the concept of a confidence interval to summarize the $Z$-$R$ relationships and $Z$-$S$ relationships. In general, the confidence interval is derived as a fixed one about the given mean. However, in this study, the confidence interval was derived for the entire range of the radar reflectivity as a function of $R$ or $S$. The radar reflectivity $Z$ for a given $R$ or $S$ was assumed to follow the Gaussian distribution. The 95% confidence intervals (i.e., 2.5~97.5% range) derived for the $Z$-$R$ relationship and $Z$-$S$ relationship also overlapped in Figures 2(a) and 2(b), respectively. As can be seen in a comparison of these two confidence intervals, $Z$ for $S$ is distinctly higher than that for $R$. However, it is also true that these two confidence intervals overlap a bit to make a separation of snowfall from rainfall become very complicated.

## 3. Study Area and Data

*3.1. Study Area.* Jeju Island is located in the southernmost region of the Korean Peninsula. In fact, Jeju Island is composed of the main island, eight inhabited islands, and 55

Table 1: $Z$-$R$ relationships collected from past studies and reports.

| Precipitation type | $Z$-$R$ relationship | Reference |
|---|---|---|
| Stratiform | $Z = 200R^{1.60}$ | [2] |
| Convective | $Z = 16R^{1.55}$ | [3] |
| All storms | $Z = 372R^{1.47}$ | [4] |
| Thundershowers | $Z = 435R^{1.48}$ | |
| Rainshowers | $Z = 370R^{1.31}$ | |
| Continuous | $Z = 311R^{1.43}$ | |
| Cold front | $Z = 208R^{1.39}$ | [12] |
| Continuous | $Z = 322R^{1.33}$ | [13] |
| Warm air advection | $Z = 207R^{1.50}$ | [14] |
| Cold air advection | $Z = 205R^{1.50}$ | |
| Weak gradient type | $Z = 201R^{1.50}$ | |
| Thunderstorms | $Z = 291R^{1.50}$ | |
| Warm air advection | $Z = 183R^{1.50}$ | |
| Cold air advection | $Z = 200R^{1.50}$ | |
| Weak gradient type | $Z = 191R^{1.50}$ | |
| Thunderstorms | $Z = 254R^{1.50}$ | |
| Warm air advection | $Z = 200R^{1.50}$ | |
| Cold air advection | $Z = 255R^{1.50}$ | |
| Weak gradient type | $Z = 206R^{1.50}$ | |
| Thunderstorms | $Z = 318R^{1.50}$ | |

Table 2: $Z$-$S$ relationships collected from past studies and reports.

| Precipitation type | $Z$-$S$ relationship | $Z_e$-$S$ relationship | Reference |
|---|---|---|---|
| Snowflakes | $Z = 500S^{1.60}$ | $Z_e = 112S^{1.60}$ | [16] |
| | $Z = 1{,}800S^{1.60}$ | $Z_e = 403S^{1.60}$ | |
| | $Z = 1{,}200S^{1.60}$ | $Z_e = 269S^{1.60}$ | |
| Snowflakes | $Z = 2{,}000S^{2.0}$ | $Z_e = 448S^{2.0}$ | [5] |
| Snowflakes | | | [6] |
| Dry ($\overline{T} < 0^\circ$) | $Z = 540S^{2.0}$ | $Z_e = 120S^{2.0}$ | |
| Wet ($\overline{T} > 0^\circ$) | $Z = 2{,}100S^{2.0}$ | $Z_e = 470S^{2.0}$ | |
| Snowflakes | $Z = 1{,}780S^{2.21}$ | $Z_e = 399S^{2.21}$ | [17] |
| Snowflakes consisting of the following crystal types: | | | |
| Plates and columns | $Z = 400S^{1.60}$ | $Z_e = 60S^{1.60}$ | [18] |
| Needle crystals | $Z = 930S^{1.90}$ | $Z_e = 208S^{1.90}$ | |
| Stellar crystals | $Z = 1{,}800S^{1.50}$ | $Z_e = 403S^{1.50}$ | |
| Spatial dendrites | $Z = 3{,}300S^{1.70}$ | $Z_e = 739S^{1.70}$ | |
| Single crystals | $Z = 160S^{2.0}$ | $Z_e = 36S^{2.0}$ | [19] |
| Snowflakes | | | [20] |
| Dry ($\overline{T} < 0^\circ$) | $Z = 1{,}050S^{2.0}$ | $Z_e = 235S^{1.60}$ | |
| Wet ($\overline{T} > 0^\circ$) | $Z = 1{,}600S^{2.0}$ | $Z_e = 358S^{1.60}$ | |
| Snowfall (1 g = 0.03 mm/h) | $Z = 427S^{1.09}$ | $Z_e = 96S^{1.09}$ | [7] |
| Hail | $Z = 320S^{1.60}$ | $Z_e = 72S^{1.60}$ | [21] |
| Graupel | $Z = 900S^{1.60}$ | $Z_e = 202S^{1.60}$ | |

$\overline{T}$ = mean air temperature.

uninhabited islands. Figure 3 shows Jeju Island and its administrative districts.

Jeju Island is a volcanic island composed of about 360 small-scale volcanoes and volcanic cones [1]. Hallasan Mountain is located at the center of Jeju Island, and it sits at a height of 1,950 m. Hallasan Mountain has a gentle slope of about 3° along the east–west direction, but a steeper slope of about 5° along the north–south direction (Jeju Special Self-Governing Province, http://www.jeju.go.kr). The shape of the island is elliptical, with a major axis length of 73 km along the east–west direction and a minor axis length of 31 km along the north–south direction. The total area for Jeju Island is 1,848 km$^2$, and the coastal area whose elevation above the sea level is less than 200 m covering 55.3% of the island's total area.

*3.2. Rain Gauge and Radar Data.* In 1990, the Korea Meteorological Administration (KMA) started to introduce automated weather stations (AWSs) in Jeju Island [23]. Now, a total of 24 AWSs are in operation [24]. Among them, 16 rain gauges are located in the coastal area with an elevation of less than 250 m, four in between 250 and 500 m,

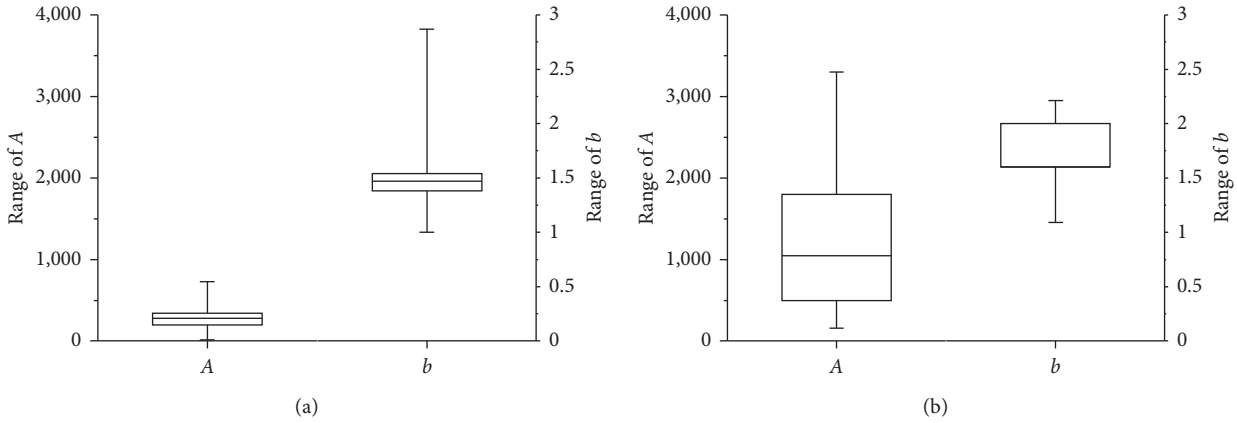


Figure 1: Comparison of the (a) *Z*-*R* and (b) *Z*-*S* relationships with their box plots of parameters *A* and *b*.

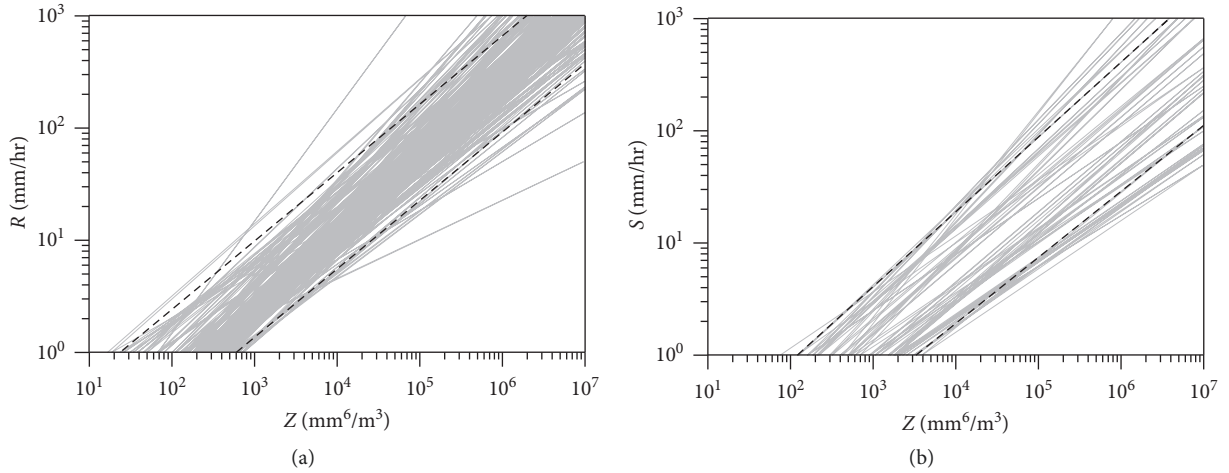


Figure 2: 95% confidence intervals derived for the (a) *Z*-*R* and (b) *Z*-*S* relationships.

two in between 750 and 1,000 m, one in between 1,250 and 1,500 m, and one at 1,500 m or higher. The locations of the rain gauges are shown in Figure 4.

KMA operates the Gosan radar and Seongsan radar in Jeju Island. The Gosan radar, which was originally a C-band radar, started tracking typhoons in 1991 but was replaced by an S-band radar in 2006. The Seongsan radar was introduced in 2006 to supplement the Gosan radar, specifically to remove the blind spot caused by Hallasan Mountain. Seongsan radar is also an S-band radar, and both radars possess an observation radius of 240 × 240 km and a resolution of 1 × 1 km. The major specifications of the Gosan and Seongsan radars are summarized in Table 3.

From both the Gosan and Seongsan radars, a total of eight radar reflectivity fields were prepared from an elevation of 250 m to 2,000 m in intervals of 250 m. That is, from each radar, 0.25 km CAPPI, 0.50 km CAPPI, 0.75 km CAPPI, 1.00 km CAPPI, 1.50 km CAPPI, 1.75 km CAPPI, and 2.00 km CAPPI data were prepared. These data were used to produce a composite field at each elevation. When data were available from both radar systems, their arithmetic mean was calculated to make the representative reflectivity. The radar reflectivity data that were used were captured from November to April from 2007 to 2016. A total of 21 AWSs data were used in Jeju Island during the same period.

## 4. Mapping the Snowy Region

*4.1. Using Only the Radar Information.* In this study, the mapping of the snowy region was first attempted based on the difference between the *Z*-*R* and *Z*-*S* relationships. The radar reflectivity data were collected for the winter period from the year 2007 to 2016. In most cases, the data collected in the coastal area are for the rainfall and those in the mountain area the snowfall. However, as the snowline varies so widely in both space and time, it is not easy to separate the snowfall from rainfall simply by analyzing the radar reflectivity value. In this study, among the data collected, those within the 95% significance range of *Z*-*R* relationship were selected, as shown in Figure 5(a), for the elevation zone of 250–500 m, as an example. Those within the 95% significance range of the *Z*-*S* relationship were also selected, as shown in Figure 5(b). Even though it was impossible to check if these two datasets were really rainfall or snowfall,

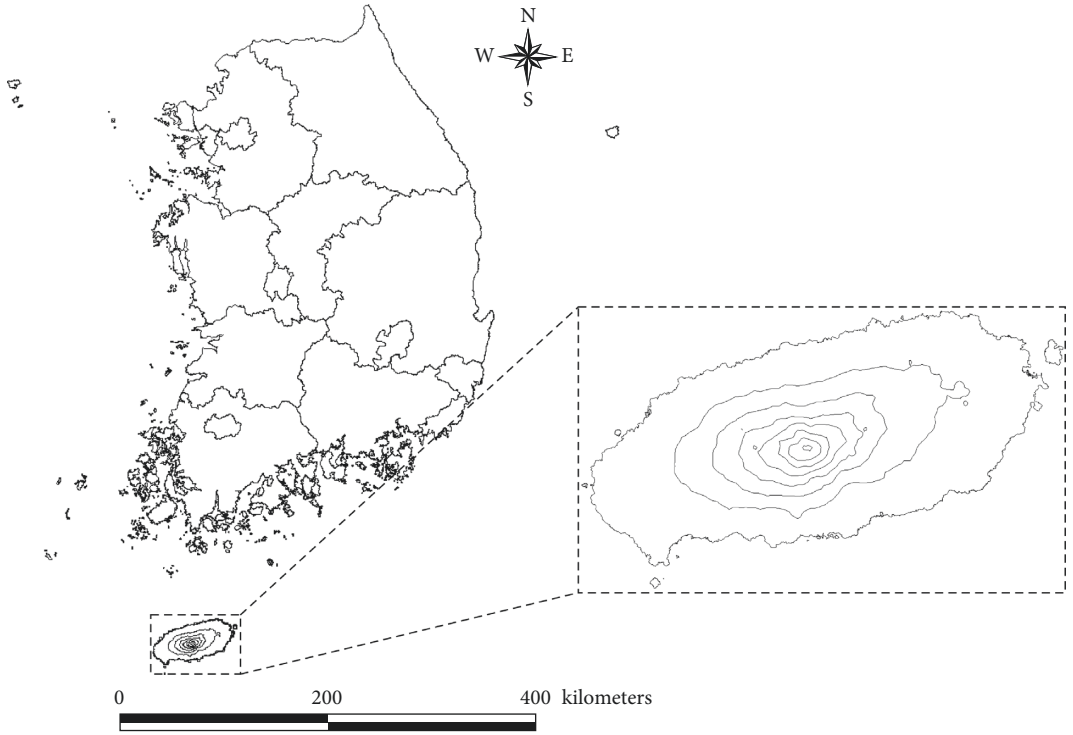


Figure 3: Location of Jeju Island, Korea (the contour lines over Jeju Island represent the 250 m altitude interval).

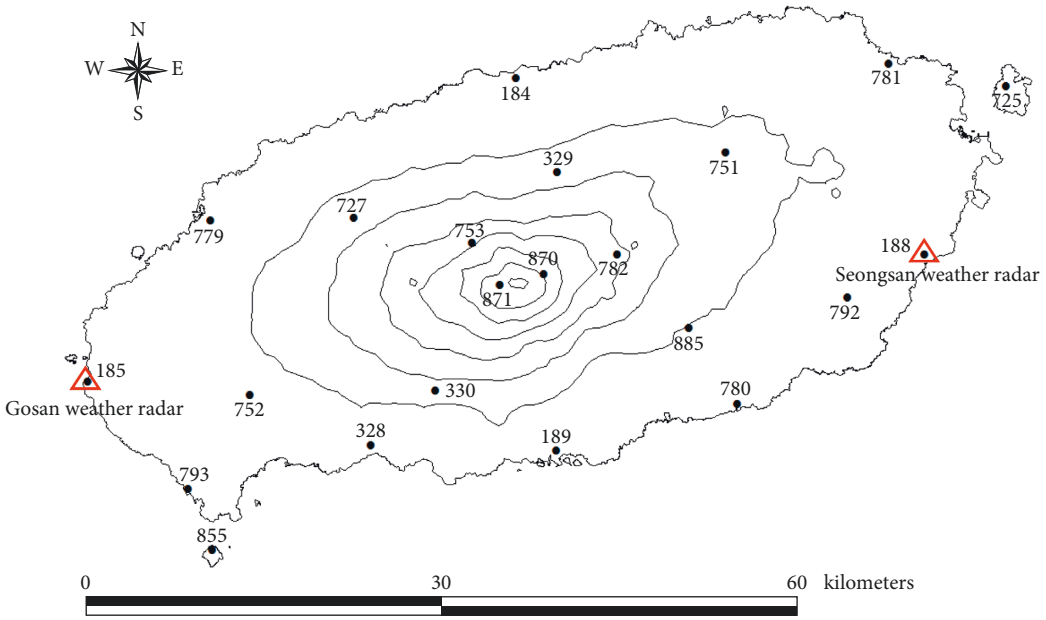


Figure 4: Locations of rain gauges over Jeju Island and two radars located at Gosan and Seongsan, Jeju Island.

they were assumed so at this point. These two datasets were then quantified by probability density functions (Figure 6). Here the Gaussian distribution was assumed since the dBZ unit was used for the radar reflectivity [25–27]. For the rainfall case, radar reflectivity data were distributed over a range of 20 to 50 dBZ but for the snowfall over the range of 30 to 55 dBZ. They obviously overlapped, indicating the possibility of uncertainty in the separation of snowfall from rainfall.

As can be seen in Figure 6, the mean of the radar reflectivity for the rainfall was 26.1 dBZ and that, for the snowfall case, was 41.8 dBZ. Their standard deviations were similar at 5.6 dBZ and 6.6 dBZ, respectively. The range of overlapping radar reflectivity for both the rainfall and snowfall was found to be between 24 and 42 dBZ. Theoretically, both the rainfall and snowfall can happen if the radar reflectivity is within this range. However, its possibility

Table 3: Major specification of the Gosan and Seongsan radars.

| | Radar type | | Gosan radar S band | Seongsan radar S band |
|---|---|---|---|---|
| Transmitter | Transmitting tube | | Klystron | Klystron |
| Receiver | Frequency | | 2,825 MHz | 2,755 MHz |
| | Peak power | | 750 kW | 750 kW |
| | Pulse width | Short | 1.0 $\mu$s | 1.0 $\mu$s |
| | | Long | 4.5 $\mu$s | 4.5 $\mu$s |
| | PRF | Short pulse | 250~1,200 Hz | 250~1,200 Hz |
| | | Long pulse | 250~350 Hz | 250~350 Hz |
| | Occupied bandwidth | | 8 MHz | 8 MHz |
| Antenna | Dynamic range | | 95 dB | 95 dB |
| | Intermediate frequency | | 10 MHz | 10 MHz |
| | Antenna diameter | | 8.5 m | 8.5 m |
| | Beam width | | 1.0° | 1.0° |
| | Antenna gain | | 45 dB | 45 dB |

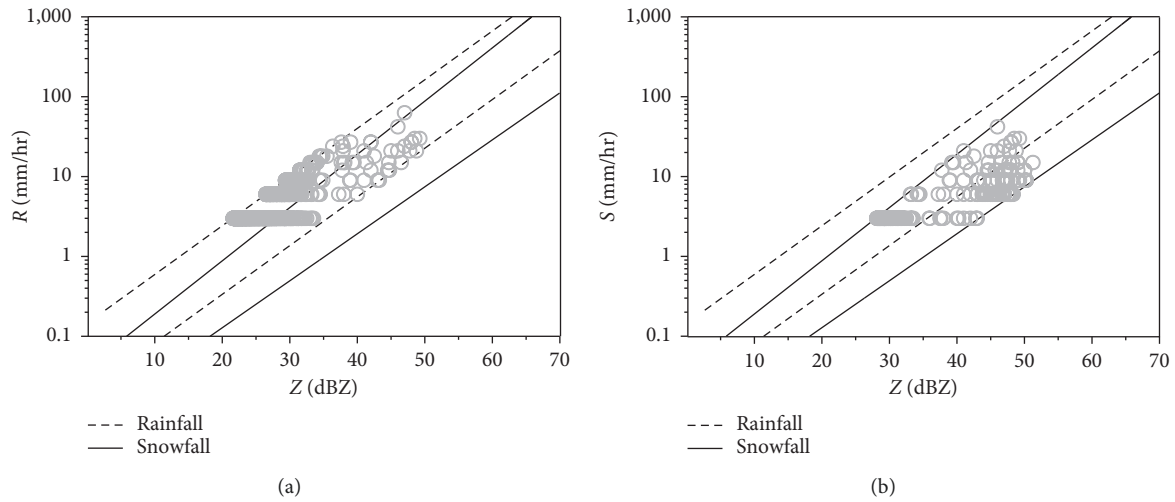


Figure 5: Comparison of observed (a) rainfall and (b) snowfall data along with their radar reflectivity collected over the elevation zone of 250~500 m (data collected during winter from 2007 to 2016).

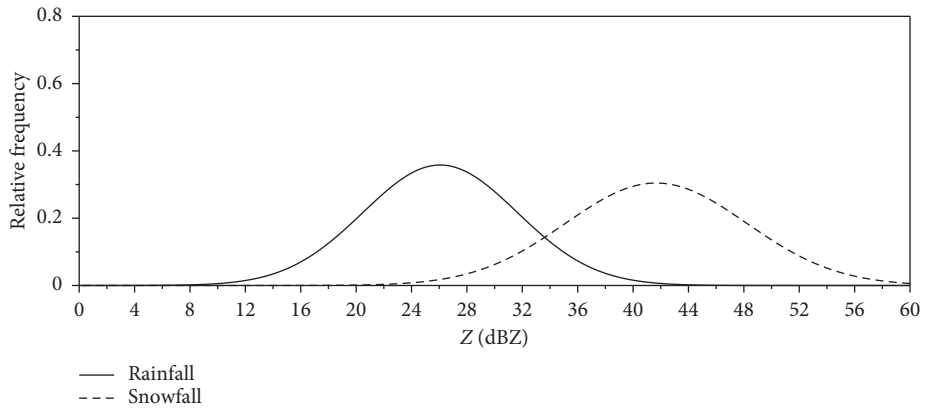


Figure 6: Comparison of probability density functions for rainfall and snowfall data over the elevation zone of 250~500 m.

(or the probability) is totally different. Near the low bound of this range, it is more like the rainfall, and near the upper bound of this range, it is more like the snowfall. In this study, the concept of a contingency table was used to determine the threshold value of the radar reflectivity to separate the rainfall and snowfall conditions. A contingency table is composed of four different probabilities indicating the true and false probabilities under the assumption of rainfall or snowfall.

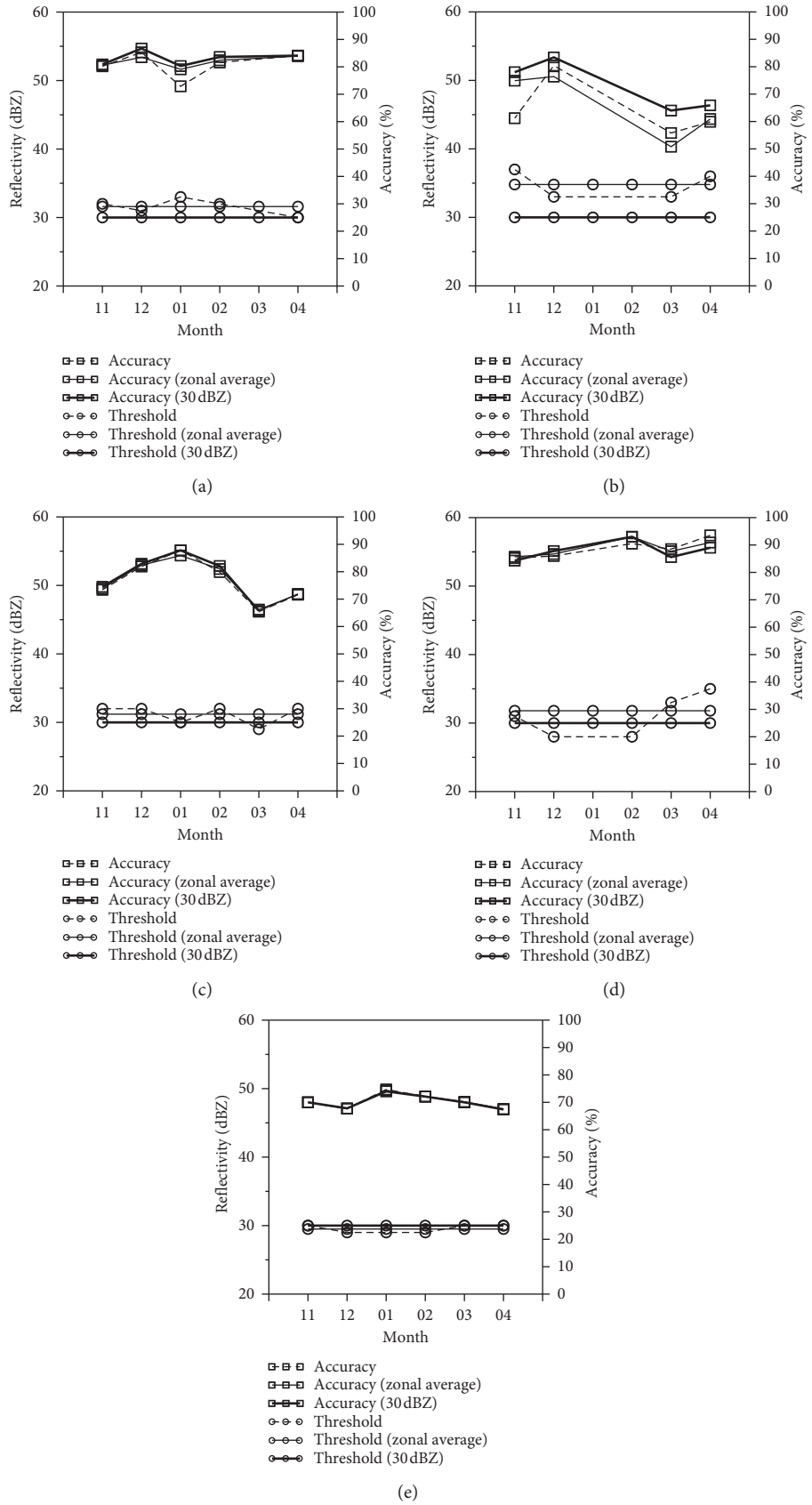


Figure 7: Monthly variation of the threshold radar reflectivity value (○) and its accuracy (□) for each elevation zone (the zonal-average threshold value and fixed threshold value (30 dBZ) are also given for the comparison): (a) 1,750 m; (b) 1,500 m; (c) 1,000 m; (d) 500 m; (e) 250 m.

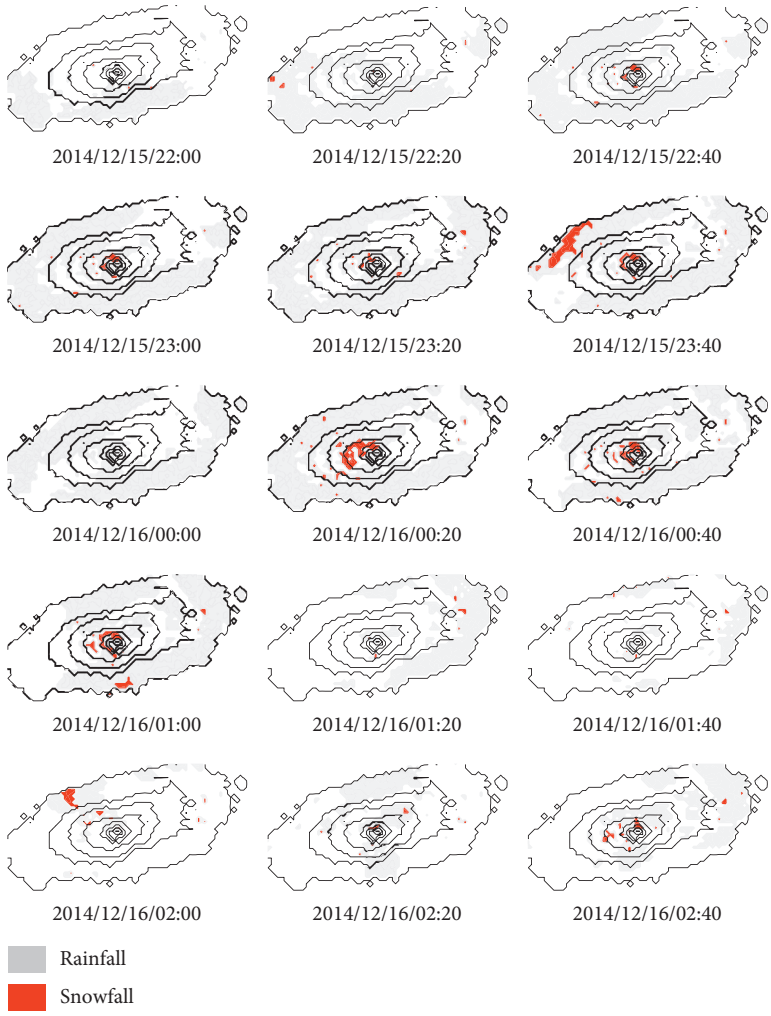


Figure 8: Mapping result of the snowy region by applying the fixed threshold method (from 22:00 December 15 to 02:40 December 16, 2015).

By changing the threshold value of the radar reflectivity, the average accuracy of rainfall and snowfall predictions as well as their difference was calculated. It is obvious that the accuracy of the rainfall prediction increases as the threshold value decreases. On the contrary, the accuracy of the snowfall prediction increases as the threshold value increases. Thus, the average accuracy should be determined somewhere in between the low and high threshold values, which was around 33~35 dBZ in this case. However, the difference in the accuracy between the rainfall and snowfall prediction was the smallest at a threshold value of 33 dBZ, which increased rather highly as the threshold value increased. Since both the average accuracy and the difference in the accuracy between the rainfall and snowfall prediction were important, this study determined the threshold value to be 33 dBZ.

Following the same procedure, this study determined the threshold value for each elevation zone from November to April, when the snowfall is observed in the mountain area of Jeju Island. The results are summarized in Figure 7. In this figure, the symbol "○" represents the threshold values, and the symbol "□" represents the average accuracy. This figure shows that the threshold values that were determined monthly were more or less the same at most elevation zones except for the elevation zone of 250~500 m. Even in the elevation zone of 250~500 m, the threshold value remained similarly from November to February, but it increased a bit from March. In the case of applying a fixed threshold value for each elevation zone, the average accuracy was found not to change significantly from that estimated by applying the value determined monthly (Figure 7). It is also noticeable that the threshold values were all determined at around 30 dBZ regardless of the elevation. Thus, this study decided to use the fixed threshold value of 30 dBZ to map the snowy region for every month and the elevation zones considered in this study. By applying this fixed threshold value, the accuracy deteriorates slightly, as shown in Figure 7.

Next, this study attempted to map the snowy region with a fixed threshold of the radar reflectivity value of 30 dBZ to the radar reflectivity data measured over Jeju Island from November 1, 2014, to April 30, 2015. As an example, Figure 8 shows the mapping results from 22:00 December 15 to 02:40 December 16, 2015. In this figure, the red colour represents the snowy region and the grey colour the rainy region.

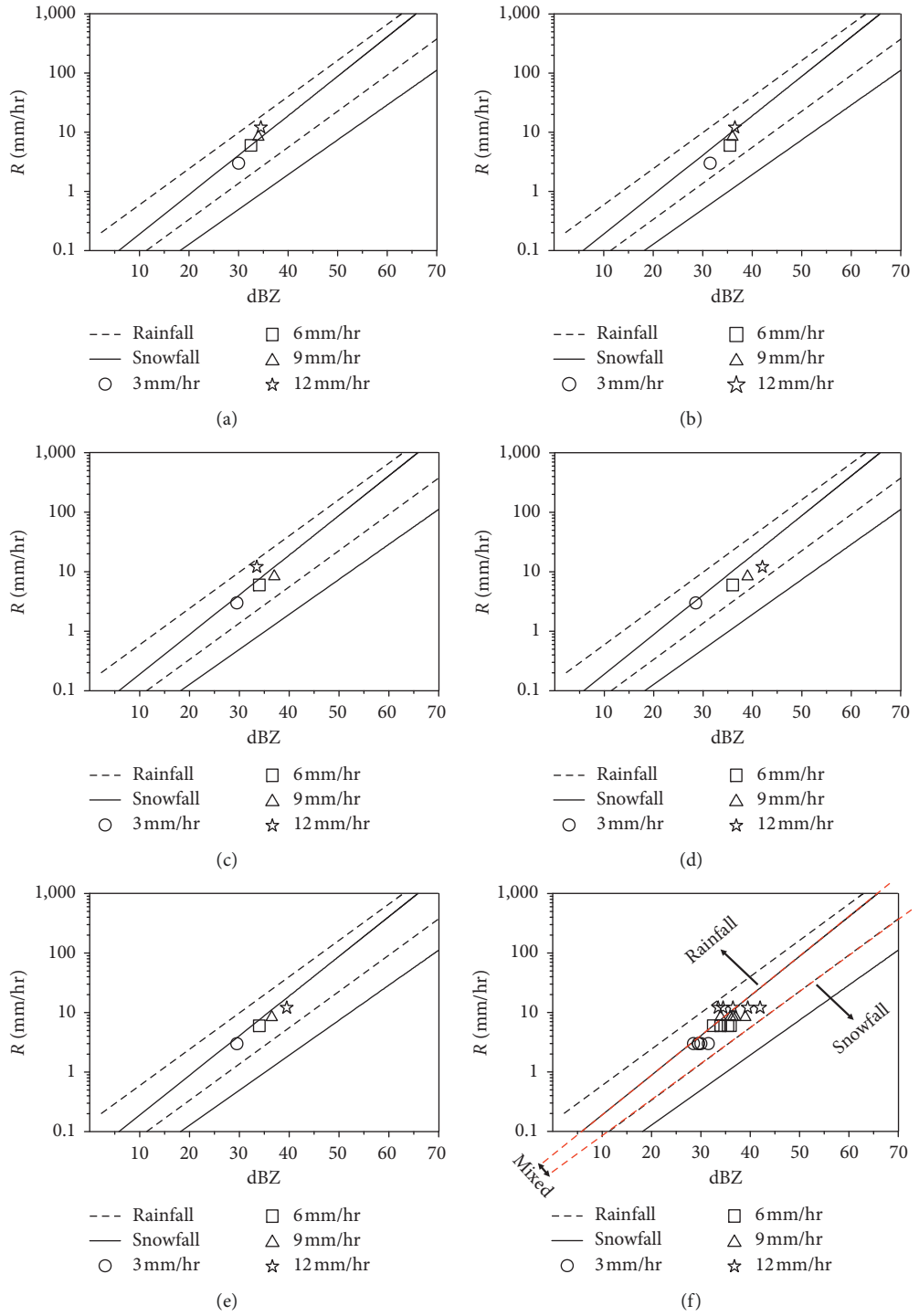


Figure 9: The threshold radar reflectivity values for snowfall determined by considering the rain gauge data in each elevation zone ((a)–(e)) and the overall result (f): (a) 1,750 m; (b) 1,500 m; (c) 1,000 m; (d) 500 m; (e) 250 m; (f) overall.

At this moment, it is not certain if the mapping result is correct or not. As the snowfall did not accumulate in the low elevation zone (the atmospheric temperature is generally above zero), the result could not be confirmed based on the snowfall measurements at four locations located in the low elevation zone of 0 to 250 m. However, Figure 8 shows that the snowy region occurred rather randomly over the Jeju Island, which is also inconsistent with the atmospheric temperature. Higher elevation zones were classified as the snowy zone, but some low elevation zones were also classified as the snowy zones even when the temperature was rather high. Overall, it is true that the mapping result contains lots of uncertainty. The behavior of snowfall in space is random, and also the mapping result lacks the physical consistency with the atmospheric temperature.

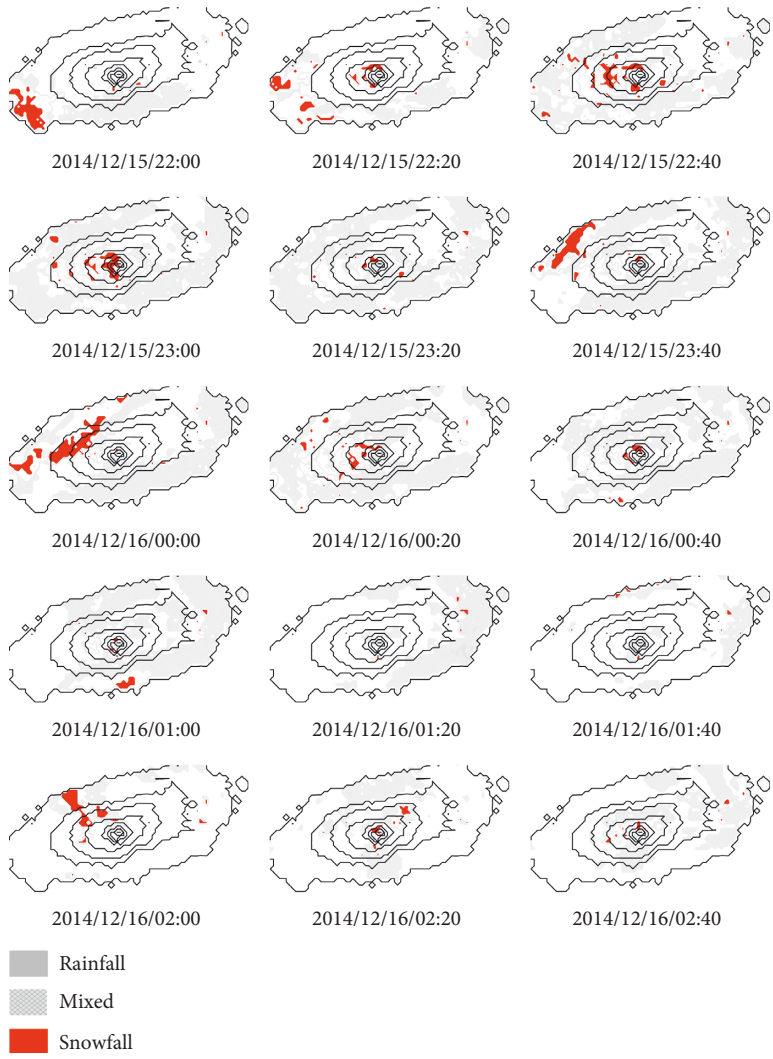


Figure 10: Mapping result of the snowy region by applying the variable threshold method (from 22:00 December 15 to 02:40 December 16, 2015).

*4.2. Using Both the Radar and Rain Gauge Information.* The radar reflectivity is proportional to the rain rate (=rainfall depth/duration) or snow rate (=snowfall depth/duration). Thus, in this study, to consider this behavior of the radar reflectivity, another method was proposed to additionally consider the rain rate data measured at each ground rain gauge station. All the rain gauges in Jeju Island are equipped with a melting device for snow and thus can measure the snowfall by units of rain rate. The monthly variation of the threshold value was not considered in this study, as it was found to be very small in the analysis in the previous section.

First, in this study, the threshold values were estimated again using the observed radar and rain gauge data by additionally considering the rain rate (or the snow rate). Since the rain rate during the winter was so low, only four ranges of the rain rate could be considered, which are 0~3.0 mm/hr, 3.0~6.0 mm/hr, 6.0~9.0 mm/hr, and 9.0~12.0 mm/hr. Figure 9 shows the results for each elevation zone given over the 95% significance interval derived in the previous section. As can be seen in this figure, in all elevation zones, the threshold radar reflectivity was determined to be proportional to the rain rate. The threshold values were also found to be all within the overlapping zone of confidence intervals of $Z$-$R$ and $Z$-$S$ relationships. In particular, the threshold values were found to be located nearer to the upper bound of the 95% confidence interval of the $Z$-$S$ relationship.

Based on above result, the study decided to use the upper bound of the 95% confidence interval of the $Z$-$S$ relationship as the threshold for snowfall. Similarly, as the threshold for rainfall, the lower bound of the 95% confidence interval of the $Z$-$R$ relationship was used. In between the two thresholds, a zone of the mixed rainfall and snowfall was assumed.

Next, this proposed method with a variable threshold was applied with the same data considered in the previous section. As was explained earlier, the variable threshold of the radar reflectivity was derived by considering the rain rate. Both thresholds for the rainfall and snowfall were defined, and additionally, the zone for the mixed rainfall and

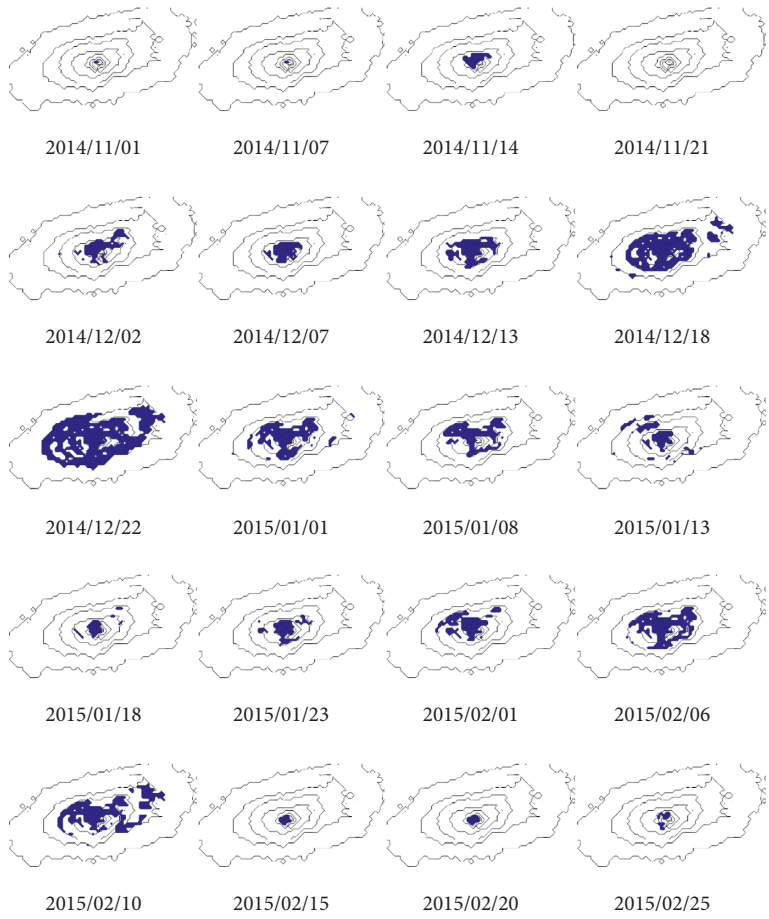


Figure 11: Change of the snow coverage over Jeju Island from November 1, 2014, to February 25, 2015, determined by applying the variable threshold method.

snowfall was also introduced to consider the uncertainty of classifying the rainfall and snowfall. An example applying the variable threshold method to the event observed on 22:00 December 15 to 02:40 December 16, 2015, is given in Figure 10. In this figure, the red colour indicates the snowfall and grey colour indicates rainfall. Additionally, the cross stripes represent the mixed rainfall and snowfall.

Different from previous results in Figure 8, Figure 10 shows somewhat distinct features. First, the snowy region in this case was larger than that in the previous case. If adding the area for the mixed rainfall and snowfall, the snowy region becomes much larger than that in the previous case. Second, especially on the top of Hallasan Mountain at subzero temperatures, radar reflectivity data were also classified into either snowfall or mixed. In the previous case, most of the radar reflectivity data in the high-elevation zone was classified into rainfall. Third, the behavior of a snow storm, i.e., directional property of the snowfall movement, could be clearly identified. In this example, the snowfall approached from the west or northwest to Jeju Island, which also scattered snowfall mostly on the rising limb of Hallasan Mountain. This behavior of the snowfall could not be detected when applying the fixed threshold method. Obviously, the variable threshold method showed a superior performance to classify the rainfall and snowfall. In addition, applying the variable threshold method was also found to be advantageous, especially when the rain rate was very low.

*4.3. Determination of the Snowline at Hallasan Mountain, Jeju Island.* Finally, in this study, the snowline of Hallasan Mountain was determined by applying the variable threshold method. The snowline in this case indicates the lowest elevation where snow is observed. In this study, snow was assumed to melt away if the temperature was higher than 5°Celsius [8], and that snow would disappear regardless of the snow depth. As an example, Figure 11 shows the change in the snow coverage over Jeju Island from 250 m to 2,000 m. At the early stages of winter, snow was detected around the top of Hallasan Mountain, but the snow-covered area increased significantly during winter and then decreased again at the end of the winter.

To determine the snowline, snowfall ratios of 10% and 90% were considered in this study (Figure 12). The snowfall ratio was calculated by dividing the number of snowy cells by the total number of cells at each elevation zone. In fact, the criterion 10% was a very weak one but was considered to show the snow-detectable elevation and its change during the winter. The second case was added to estimate the number of days when the snow-covered Hallasan Mountain

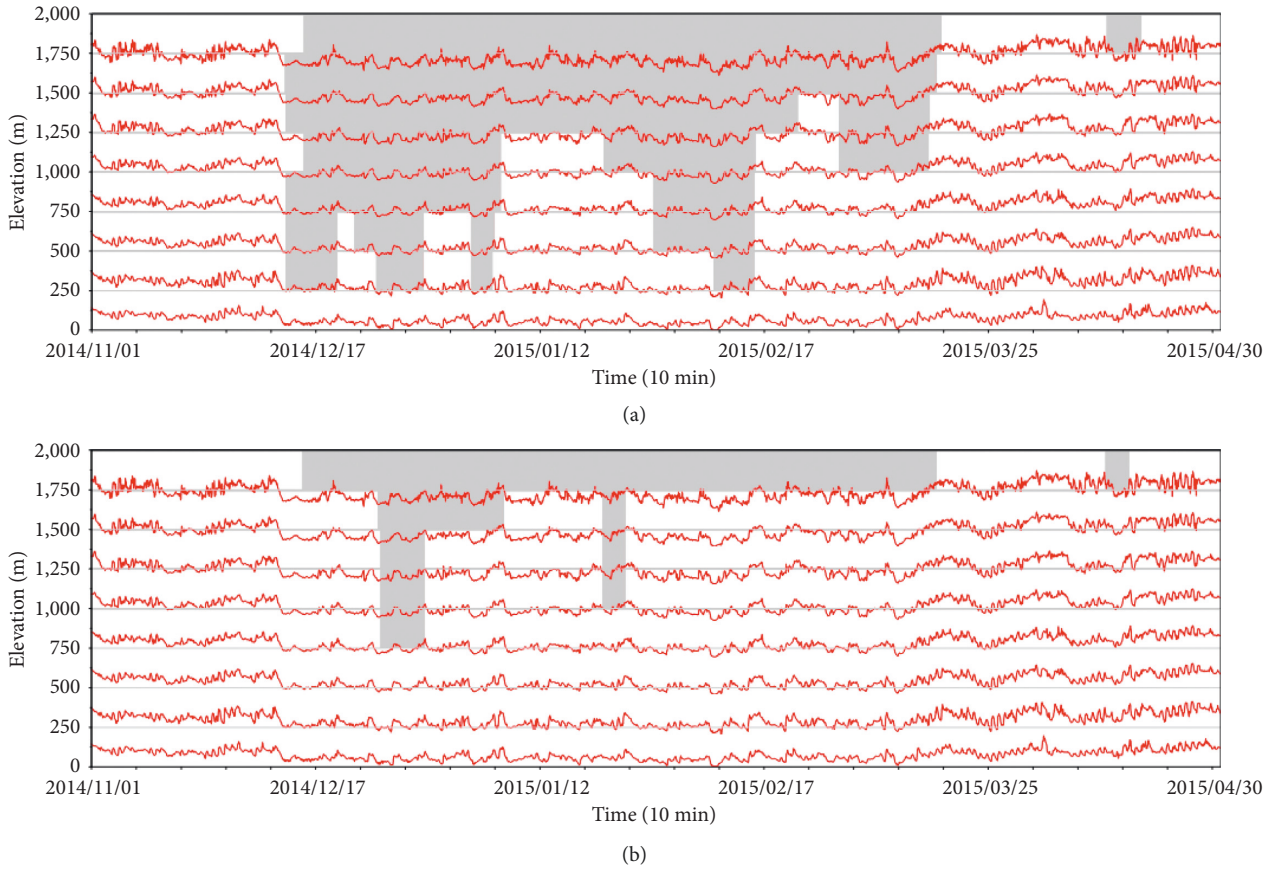


Figure 12: Change of the snowline (shaded area) over Jeju Island from November 1, 2014, to April 30, 2015, determined by applying the variable threshold method ((a) snow coverage 10% or higher; (b) snow coverage 90% or higher). Also, the thin wiggly line represents the air temperature measured at each elevation, which is moving around the reference temperature 0°C (i.e., the horizontal line at each elevation).

could be seen. The result shows that the snowy mountain top can be seen from December to the beginning of March in Jeju Island.

## 5. Summary and Conclusions

In this study, a method was proposed to map the snowy region using both the radar and rain gauge information. As a first step, this study analyzed the *Z*-*R* and *Z*-*S* relationships to derive a fixed threshold of radar reflectivity to separate snowfall from rainfall, and in the second step, this study additionally considered the observed rain rate information to address the problem of using the fixed threshold. This proposed method was applied to radar reflectivity data collected during November 1, 2014, to April 30, 2015, in Jeju Island, Korea. The results are summarized as follows.

For the case of using only the radar information, the threshold value of the radar reflectivity was determined to be 33 dBZ. However, the application of this threshold value did not show any satisfactory results. The results showed that the snowy region occurred rather randomly, which was also inconsistent with the atmospheric temperature.

For the case of using both the radar and rain gauge information, the threshold radar reflectivity was determined to be proportional to the rain rate. The threshold values were especially found nearer to the upper bound of the 95% confidence interval of the *Z*-*S* relationship. Similarly, as the threshold for the rainfall, the lower bound of the 95% confidence interval of the *Z*-*R* relationship was determined for use. Between the two thresholds was assumed to be the zone of the mixed rainfall and snowfall. Application of this proposed method resulted in somewhat distinct features like (1) obvious snowfall on the top of Hallasan Mountain in subzero temperature and (2) directional property of the snowfall movement. This method based on the variable threshold depending on the rain rate showed a superior performance in classifying the rainfall and snowfall, including a good performance particularly when the rain rate was very low.

Based on above results, the proposed method in this study based on the variable threshold value of radar reflectivity considering the observed rain rate could be confirmed to be effective when applied to map the snowy region. Especially, the AWS, which can measure the snowfall by the unit of water depth, was found to be beneficial to improve the quality of snowfall prediction. Even though this is a case study over Jeju Island, Korea, the same methodology may be applied anywhere with a similar environment. Especially, this methodology can be advantageous in the mountainous areas where snow measurements are not systematically taken.

## Data Availability

The radar data and ground data used in this study were collected from the Korean Meteorological Administration (https://data.kma.go.kr).

## Conflicts of Interest

The authors declare that they have no conflicts of interest regarding the publication of this paper.

## Acknowledgments

This work was supported by the "Basic Science Research Program," through the National Research Foundation of Korea, funded by the Ministry of Education (NRF-2016R1D1A1A09918155), and the Korea Environment Industry & Technology Institute (KEITI) of the Korea Ministry of Environment (MOE) through "Advanced Water Management Research Program" (79615).

## References

[1] Jeju Regional Meteorological Administration, *Detailed Climate Characteristics of Jeju Island*, Jeju Regional Meteorological Administration, Jeju, South Korea, 2010.

[2] J. S. Marshall and W. M. K. Palmer, "The distribution of raindrops with size," *Journal of Meteorology*, vol. 5, no. 4, pp. 165-166, 1948.

[3] D. C. Blanchard, "Raindrop size-distribution in Hawaiian rains," *Journal of Meteorology*, vol. 10, no. 6, pp. 457–473, 1953.

[4] D. M. A. Jones, *Research Report: Rainfall Drop-Size Distribution and Radar Reflectivity*, Illinois State Water Survey Meteorology Laboratory, Champaign, IL, USA, 1956.

[5] K. L. S. Gunn and J. S. Marshall, "The distribution with size of aggregate snowflakes," *Journal of Meteorology*, vol. 15, no. 5, pp. 452–461, 1958.

[6] I. Imai, "Raindrop size distributions and the *Z-R* relationship," in *Proceedings of the 8th Weather Radar Conference*, pp. 321–326, American Meteorological Society, Boston, MA, USA, 1960.

[7] Y. Fujiyoshi, T. Endoh, T. Yamada, K. Tsuboki, Y. Tachibana, and G. Wakahama, "Determination of a *Z-R* relationship for snowfall using a radar and high sensitivity snow gauges," *Journal of Applied Meteorology*, vol. 29, no. 2, pp. 147–152, 1990.

[8] The Korean Earth Science Society, *Concepts in Earth Science*, The Korean Earth Science Society, Seoul, South Korea, 2005.

[9] National Institute of Meteorological Research, *Development of Advanced Atmospheric Technology (III)*, National Institute of Meteorological Research, Seoul, South Korea, 2011.

[10] J. H. Lee and C. S. Ryu, *Radar Meteorology*, Sigma Press, Seoul, South Korea, 2009.

[11] J. O. Laws and D. A. Parsons, "The relation of raindrop-size to intensity," *Transactions, American Geophysical Union*, vol. 24, no. 2, pp. 452–460, 1943.

[12] R. Cataneo and G. E. Stout, "Raindrop-size distributions in humid continental climates, and associated rainfall rate-radar reflectivity relationships," *Journal of Applied Meteorology*, vol. 7, no. 5, pp. 901–907, 1968.

[13] G. E. Stout and E. A. Mueller, "Survey of relationships between rainfall rate and radar reflectivity in the measurement of precipitation," *Journal of Applied Meteorology*, vol. 7, no. 3, pp. 465–474, 1968.

[14] I. G. Doelling, J. Joss, and J. Riedl, "Systematic variations of *Z-R*-relationships from drop size distributions measured in northern Germany during seven years," *Atmospheric Research*, vol. 47-48, pp. 635–649, 1998.

[15] J. S. Marshall and K. L. S. Gunn, "Measurement of snow parameters by radar," *Journal of Meteorology*, vol. 9, no. 5, pp. 322–327, 1952.

[16] I. Imai, M. Fujiwara, I. Ichimura, and Y. Toyama, "Radar reflectivity of falling snow," *Papers in Meteorology and Geophysics*, vol. 6, no. 2, pp. 130–139, 1955.

[17] R. S. Sekon and R. C. Srivastava, "Snow size spectra and radar reflectivity," *Journal of the Atmospheric Sciences*, vol. 27, no. 2, pp. 299–307, 1970.

[18] T. Ohtake and T. Henmi, "Radar reflectivity of aggregated snowflakes," in *Proceedings of the 14th Conference on Radar Meteorology*, pp. 209-210, American Meteorological Society, Tucson, AZ, USA, 1970.

[19] P. E. Carlson and J. S. Marshall, "Measurement of snowfall by radar," *Journal of Applied Meteorology*, vol. 11, no. 3, pp. 494–500, 1972.

[20] T. Puhakka, "On the dependence of the *Z-R* relation on the temperature in snowfall," in *Proceedings of the 16th Conference on Radar Meteorology*, pp. 504–507, American Meteorological Society, Houston, TX, USA, 1975.

[21] R. Rasmussen, M. Dixon, S. Vasiloff et al., "Snow nowcasting using a real-time correlation of radar reflectivity with snow gauge accumulation," *Journal of Applied Meteorology*, vol. 42, no. 1, pp. 20–36, 2003.

[22] P. L. Smith, "Equivalent radar reflectivity factors for snow and ice particles," *Journal of Climate and Applied Meteorology*, vol. 23, no. 8, pp. 1258–1260, 1984.

[23] G. Choi, "Spatial patterns of seasonal extreme precipitation events in Mt. Halla," *Journal of Climate Research*, vol. 8, no. 4, pp. 267–280, 2013.

[24] National Geographic Information Institute, *The Geography of Korea—Jeju Special Self-Governing Province*, National Geographic Information Institute, Suwon, South Korea, 2013.

[25] J. A. Smith and W. F. Krajewski, "Estimation of the mean field bias of radar rainfall estimates," *Journal of Applied Meteorology*, vol. 30, no. 4, pp. 397–412, 1991.

[26] D.-J. Seo, J. P. Breidenbach, and E. R. Johnson, "Real-time estimation of mean field bias in radar rainfall data," *Journal of Hydrology*, vol. 223, no. 3-4, pp. 131–147, 1999.

[27] S. Chumchean, A. Seed, and A. Sharma, "Correcting of real-time radar rainfall bias using a Kalman filtering approach," *Journal of Hydrology*, vol. 317, no. 1-2, pp. 123–137, 2006.

Hindawi
Advances in Meteorology
Volume 2019, Article ID 4631609, 15 pages
https://doi.org/10.1155/2019/4631609

*Research Article*

# Seasonal and Regional Differences in Extreme Rainfall Events and Their Contribution to the World's Precipitation: GPM Observations

**Shailendra Kumar, Yamina Silva, Aldo S. Moya-Álvarez, and Daniel Martínez-Castro**

*Instituto Geofisico del Peru, Calle Badajoz 169, Urb. Mayorazgo IV Etapa, Ate, Lima, Peru*

Correspondence should be addressed to Shailendra Kumar; shailendrak89@gmail.com

Received 15 January 2019; Revised 19 March 2019; Accepted 2 May 2019; Published 30 May 2019

Guest Editor: Jongho Kim



In the present study, five-year of precipitation features (PFs) datasets, based on Global Precipitation Measurement (GPM), are used to investigate the global and regional characteristics of extreme rainfall events (EREs). The EREs are defined based on the PFs area, depth (maximum height of radar reflectivity), and the rain rate and called them largest, deepest, and intense EREs, respectively. The EREs are divided into top 10%, 1%, 0.1%, and 0.01% based on their frequency of occurrences. It is observed that occurrences of EREs belonging to less than top 0.01% EREs follow the tropical rainfall climatology over the tropics based on all the parameters. Subtropical oceanic areas consist of a higher frequency of largest EREs, whereas tropical land areas consist of the higher number of deepest EREs. The most intense EREs (top 0.01%) are uniformly distributed over tropical areas and subtropical oceans, and spatial distribution shows that a deepest ERE belongs to intense EREs in the tropical land areas. Large differences between the precipitation contribution from the largest and deepest EREs are seen; for example, the top 1% of largest EREs contribute to ~80.7% of Earth's precipitation, whereas the corresponding percentage for deepest EREs is only 53%. On the regional and seasonal scale, South Asia (SAsia) and South America (SA) nearly show common features, as oceanic and land areas consist of largest and deepest EREs, respectively, and contribute to higher precipitation. Subtropical latitudes over South America, including Sierra de Cordoba and La Plata basin, consist of deepest and intense EREs and match with those of the Indo-Gangetic plain over South Asia, which also shows the similar characteristics. EREs based on various parameters are strongly linked over SAsia compared to SA. For example, the largest top 10% EREs have a higher probability to be part of the top 10% deepest and intense EREs over SAsia. The seasonal and regional water budget reveals different characteristics, as in the southern hemisphere, the deeper EREs contribute to the higher fraction of rainfall, but over SAsia, the shallower EREs could also contribute to significant rainfall.

## 1. Introduction

Mesoscale convective systems (MCS) play a vital role in tropical large-scale circulation (e.g., [1, 2]) and Earth's water budget, as most of Earth's rainfall comes from them [3]. Therefore, it is very important to understand them globally, seasonally, and regionally. The extreme rainfall events (EREs) are related to atmospheric/weather conditions [4]. Some common EREs are associated with MCSs [5] and could produce a copious amount of rainfall over the tropical land and oceanic areas. Because of their large impact on the Earth's energy and water budget, the scientific community has studied their properties in many ways, including field campaigns (e.g., GATE, Monsoon Experiment (MONEX), TOGA COARE, DYNAMO, and COPE), satellite observations, and numerical modeling (e.g., [2, 6–9]). Passive microwave radiometers can detect the strength of ice scattering signals, whereas lightning data were used to identify the global distribution of storms [10–13]. The Tropical Rainfall Measuring Mission (TRMM) satellite was launched in 1997, consists of multiple sensors, and provides the three-dimensional structure of precipitation [14] from space.

The TRMM-based precipitation features (PFs) consist of valuable information of the precipitation, such as its depth, area, convective-stratiform fraction, rain rate (RR), and volumetric contribution to rainfall [15, 16]. Past studies detected the various properties of precipitation over the tropics and subtropics using the TRMM sensors [17–31], including their vertical characteristics, diurnal cycle, convective-stratiform separation, and other properties. Extreme and intense convection is defined using the radar reflectivity as a threshold in many studies over different tropical areas [24, 26, 27, 29, 30, 32]. For example, the maximum height of 40 dBZ is used as a convective proxy [23], and based on the criteria, it is observed that some of the most intense thunderstorms occur over the tropical land areas [33]. TRMM data are used to investigate the scale-based precipitation systems over the tropical globe [34], and the precipitation systems are classified into small ($<100\,km^2$) and large ($>10000\,km^2$) ones. The observations revealed that small precipitation systems do not show much diurnal variation, whereas large precipitation systems mostly occur in the afternoon. The geographical locations of 1000 extreme precipitation events with the highest volumetric rainfall amount showed that these events are unevenly distributed and mostly occur near South America and associated with the tropical cyclone [35]. Hamada et al. [35] defined the intense rainfall events using RR ($mm\,h^{-1}$). They considered the RR greater than 99.99 percentile in each $2.5^\circ \times 2.5^\circ$ grid box over the tropical areas [35] and showed that most of the volumetric higher rainfall events are associated with cyclones. A weak linkage is observed between the largest precipitating systems and their corresponding top height [4]. Table 1 lists the past studies where intense and extreme rainfall events are studied using the TRMM data.

Monsoon domains are defined based on the annual and seasonal rainfall criteria [37]. Monsoon domains consist of more than 70% of the total annual rainfall during local summer seasons. Based on the mentioned criteria, monsoon domains are defined over South East South Asia, Indonesia-Australia, Northern and Southern Africa, and North and South America. In the past, various studies were carried out to investigate the rainfall characteristics, such as monsoon circulation pattern, intraseasonal variation, and mesoscale convection (e.g., [37–41]). However, there are very few studies that have been carried out to understand the distribution and characteristics of EREs globally, regionally, and seasonally. The multiscale climatology of large, deep, and intense rain events will improve the estimation of rainfall by using microwave radiometers [42, 43]. The main objectives of the present study are to investigate the global view of the spatial distribution of EREs and their role/contribution to global precipitation. We also selected two monsoon seasons, namely, Indian summer monsoon (June to September, JJAS) and Austral summer monsoon (December to March, DJFM) over South Asia (SAsia, 55°E–110°E, 0–35°N) and South America (SA, 80°W–35°W, 10°N–55°S) to investigate the regional and seasonal distribution of EREs and their contribution in regional precipitation during two monsoon seasons. For this, we used the PFs from the Global Precipitation Measurement (GPM) observations. The core satellite of the GPM was launched in February 2014 and consists of a dual-polarized radar (DPR) and a microwave imager (GMI). In summary, the main objectives of the present study are to answer the following questions:

(a) What is the spatial distribution of the largest, deepest, and intense EREs on the Earth using 4-year GPM data (April 2014–December 2017) and their importance in world precipitation?

(b) What are the regional differences of occurrence of these EREs during two monsoon seasons over SAsia and SA, and how important is the contribution of these EREs relative to the seasonal and regional precipitation?

(c) How are these EREs interlinked based on their size, depth, and rainfall intensity during Indian and Austral summer monsoon seasons over SAsia and SA, respectively?

The paper is organized as follows. Section 2 provides a summary of the data used in the present study and introduces the method for defining EREs. Section 3 describes the global distribution of EREs and their characteristics on a global, regional, and seasonal scale. Summary and concluding remarks are given in section 4.

## 2. Global Precipitation Measurement (GPM), Precipitation Features (PFs), and Extreme Rainfall Events (EREs)

GPM, a successor of TRMM, is a joint multisatellite mission by NASA and the Japanese Space Agency, which provides the global information of precipitation [44]. The core observatory of GPM has a DPR and an advanced passive microwave radiometer, which measures the three-dimensional characteristics of precipitation. GPM covers the area between 65°S and 65°N compared to the TRMM, whose span was only 36°S–36°N. In the present study, we used the PFs based on GPM DPR and passive microwave radiometers sensors (http://atmos.tamucc.edu/trmm/data.html#datadownload) [33]. The PFs are defined as the connected pixels of PR beams with near-surface rain rate $>0.1\,mm\,h^{-1}$ [33]. These PFs are further used to extract the characteristics of EREs on a global, regional, and seasonal scale. Here, the extremely large, deep, and intense EREs are identified and their properties such as echo top height, area, and RR are explored. Last, the fractions of precipitation contributed by these EREs are estimated for comparing the global and regional precipitation budgets.

Basically, GPM based PFs are used to characterize the EREs based on various parameters [33]. Liu and Zipser [33] classified the EREs into the top 10%, 1%, 0.1%, and 0.01% based on their area and top height using one year of GPM data. We followed the methodology used in [33] and defined three types of EREs, namely, the largest, deepest and intense EREs based on the area, top height, and RR of PFs, respectively (Table 2). Basically, we plotted the cumulative frequency distribution (CDF) of all the parameters and then

Table 1: Past studies considered to investigate the extreme rainfall events using the TRMM satellite.

| Reference | Definition of extreme events |
|---|---|
| Zipser et al. [23] | Maximum height of 40 dBZ; minimum brightness temperature at 37 and 85 GHz; higher lightning flash rate |
| Houze et al. [24] | |
| Romatschke and Houze [32] | Deep intense convective echoes (40 dBZ echo reaching heights>10 km) |
| Romatschke et al. [32] | Wide intense convective echoes (40 dBZ echo > 1000 $km^2$ in horizontal dimension) |
| Rasmussen and Houze [36] | |
| Hirose et al. [34] | Small (<100 $km^2$) and large (>10000 $km^2$) precipitation systems |
| Hamada et al. [35] | Rain rate (mm $h^{-1}$) higher than the 99.99 percentile in each 2.5° × 2.5° grid box over the tropical areas |
| Bhat and Kumar [26] | Radar reflectivity > 20 dBZ at 12 km and top 5% radar reflectivity at 3 and 8 km |
| Kumar and Bhat [27] | |
| Kumar [28, 29] | Radar reflectivity > 40 dBZ at 3 km |
| Hamada et al. [4] | Rain rate (mm $h^{-1}$) higher than the 99.99 percentile in each 2.5° × 2.5° grid box over the tropical areas |
| Liu and Zipser [34] | Divided the PFs into top 10%, 1%, 0.1%, and 0.01% group based on the area and maximum height of PFs |

Table 2: Definition of extreme rainfall events.

| Types | Parameters |
|---|---|
| (1) Largest EREs | PFs area and volumetric area |
| (2) Deepest EREs | Maximum height of 20 and 40 dBZ (MH20 and MH40) |
| (3) Intense EREs | Rain rate (RR) |

divided them into the top 10%, 1%, 0.1%, and 0.01% based on their number of occurrences (Supplementary Figure 1). The largest EREs are defined based on the area of PFs ($km^2$) and area of volumetric rainfall contribution ($km^2$ mm $h^{-1}$), whereas the deepest EREs are defined based on the maximum height of 20 dBZ (MH20, in km) and the maximum height of 40 dBZ (MH40, in km). The intense EREs are defined based on the RR (in mm $h^{-1}$), and the parameters are mentioned in Table 2, which shows the definition of various kinds of EREs used in the present study.

## 3. Results and Discussions

*3.1. Global Distribution of Extreme Rainfall Events.* Figure 1 shows the spatial distribution of the largest EREs based on the area of PFs (top 10%, top 1%, top 0.1%, and top 0.01%). The first three panels (Figures 1(a)–1(c)) show the distribution of the largest EREs in each 1° × 1° box, whereas Figure 1(d) shows the actual geographical locations of the top 0.1% (green color) and the top 0.01% largest EREs (magenta color). The spatial distribution of less than 99.99% largest EREs follows the total rainfall climatology (Figures 1(a)–1(c)), and the higher number of EREs are observed over the tropical belt and at high latitudes over oceanic areas [45–47]. The largest EREs (top 0.01%) occur over the oceanic areas beyond the tropics. The most valuable benefit from GPM observations are apparent; because of their scanning at higher latitudes, it is clearly observed that mid latitude and high latitude over oceans (beyond 35°S and 35°N) consist of the largest EREs. Figures 2(a)–2(c) and 3(a)–3(c) show the spatial distribution of the deepest EREs in a 1° × 1° box based on MH20 and MH40, respectively, and they also follow the long-term rainfall climatology. Tropical oceanic areas and high latitudes (beyond 38°) consist of shallow EREs (up to 5 km, Figure 2(a)) and are consistent with the TRMM observation [31]. Tropical land-dominated areas such as the Indo-Gangetic plain (IGP), central India, Maritime Continent (MC), north Australia (NAUS), and central South America consist of the highest number of deepest EREs (e.g., top 0.01% EREs > 15.50 km). EREs with MH40 show similar characteristics but the corresponding altitude is > 15.875 km (Figure 3). The top 0.01% deepest EREs based on MH40 are mostly found over land-dominated areas, such as South Asia, central Africa, central South America, and the south of United States of America. The EREs with higher 40 dBZ echoes are also found over the mid latitude and subtropical areas, such as northern Europe, Siberian Russia, and central Canada. It clearly indicates that even if the oceanic areas and mid latitude have largest EREs, they are not deep enough. Figure 4 shows the global distribution of intense EREs. Again, up to top 0.1% intense rainy events (>130.06 mm $h^{-1}$) follow the rainfall climatology, but the top 0.01% (>299.62 mm $h^{-1}$) intense rainy events show the different characteristics compared to the largest and deepest EREs. For example, both land and oceanic areas consist of the top 0.01% intense rain events, and most of the intense EREs occur over central South America, central Africa, South East South Asia, Maritime Continent, coastal regimes, central Pacific, southern Atlantic, and South America.

Spatial distribution of EREs shows the land-ocean contrast as well as the regional characteristics. The largest and deepest EREs (top 0.01%) occurrences show the land and ocean contrast, as mostly subtropical oceans and tropical land areas, consist of the largest and deepest EREs, respectively. However, intense EREs occur both over the tropical land and oceanic areas (Figure 4(d)). It clearly indicates that largest EREs do not correspond to the deepest or intense EREs over land (quantified later), and over land, the intense EREs are deeper, compared to the ocean where shallower EREs may be an intense one as shown in

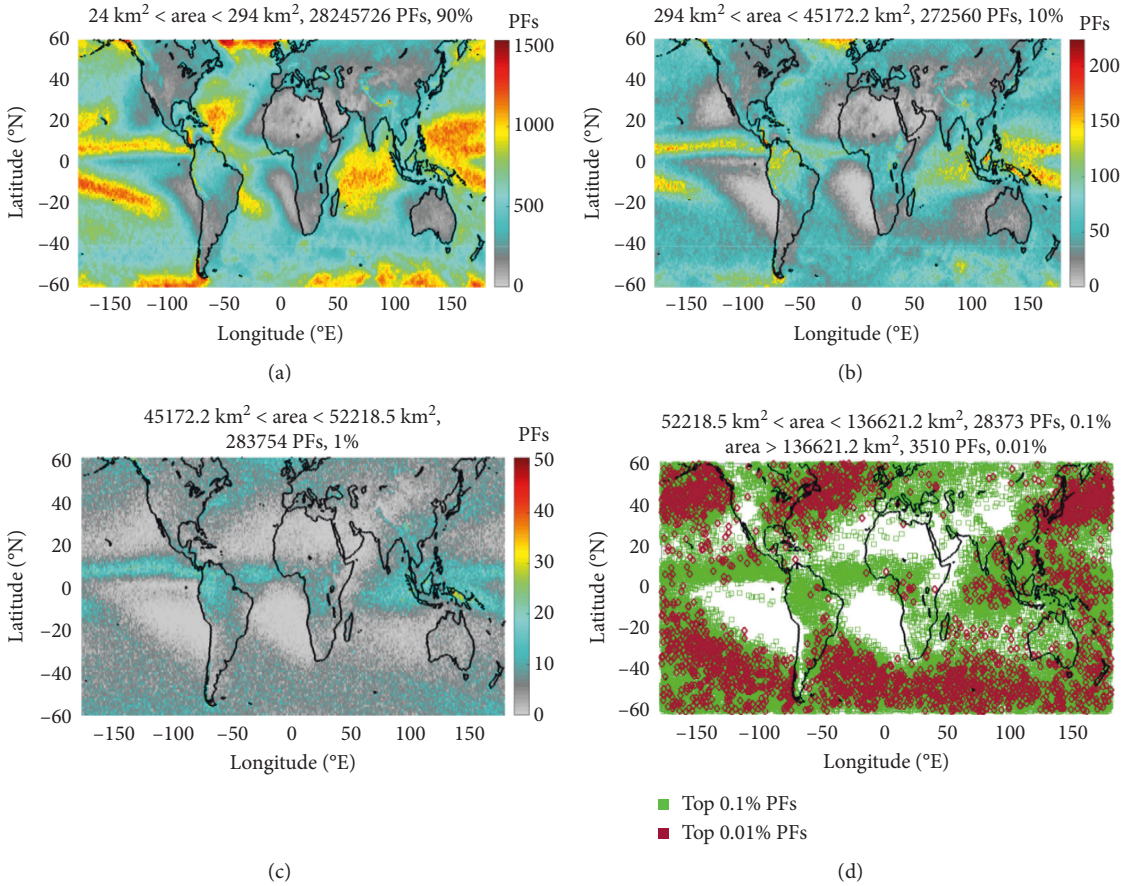


Figure 1: Spatial distribution of largest (in size) extreme rainfall events over the globe. (a–c) The distribution of largest extreme rainfall events in each $1^\circ \times 1^\circ$ box; (d) the actual geographical locations of largest extreme rainfall events. Color bar in (a)–(c) shows the number of extreme rainfall events. (d) The green color refers to the top 0.1% PFs, whereas magenta refers to the top 0.01% largest PFs.

[4, 34, 35]. In the next section, we will discuss the importance of these EREs in world precipitation.

*3.2. The Fraction of the Global Precipitation from Extreme Rainfall Events.* EREs are very important as they contribute to most of the global precipitation [33]. Figure 5 shows the fraction of global precipitation in each $1^\circ$ latitude belt for the EREs based on MH20. Here, two important features are observed. First, tropical areas have a higher number of deeper EREs, which contribute to a higher fraction of rainfall in world precipitation, whereas, beyond $25^\circ$, a higher fraction of precipitation comes from shallower EREs. The deeper EREs (top 1% > 15.50 km) are less but contribute to the highest fraction of precipitation over the tropics, whereas over the mid latitude, most of the precipitation comes from the EREs less than 7.5 km altitude and mostly belongs to the top 10% of the deepest EREs. These findings are consistent with the past studies [33, 48, 49]. The higher fraction from shallow precipitation over the southern hemisphere is due to the large regions of weak and shallow rainfall over the area (e.g., stratocumulus regions west coast of Chile and Africa). A clear difference is observed between the northern and southern hemisphere, and each latitude in the northern hemisphere has higher deeper EREs compared to the corresponding latitude in the southern hemisphere.

Table 3 provides a brief information of the fraction of the global precipitation contributed by different types of EREs. The top 1% largest EREs contribute more than 36% of the total global precipitation, whereas the corresponding contribution for top 1% deepest EREs based on MH20 (>10.625 km) and MH40 (>9.5 km) are only 14.3 and 4.5%. The land and ocean contrast are also visible as land-based deepest EREs contribute to higher global precipitation compared to oceanic based deepest EREs; however, the largest EREs show the opposite characteristics. The top 0.01% largest EREs contribute to more than ~8.0% rainfall over the oceans, compared to the land where the top 0.01% largest EREs only contribute to ~2.6% rainfall. Although the deepest EREs based on MH40 contribute to a higher fraction of rainfall (3.1%) over land-dominated areas compared to oceanic areas (1.8%).

*3.3. Regional Distribution of Extreme Rainfall Events over SA and SAsia during Different Seasons.* We selected two monsoon domains/zone, namely, SAsia and SA, during JJAS and DJFM months to compare the characteristics of EREs. Figure 6 shows the geographical locations of top 10% (blue),

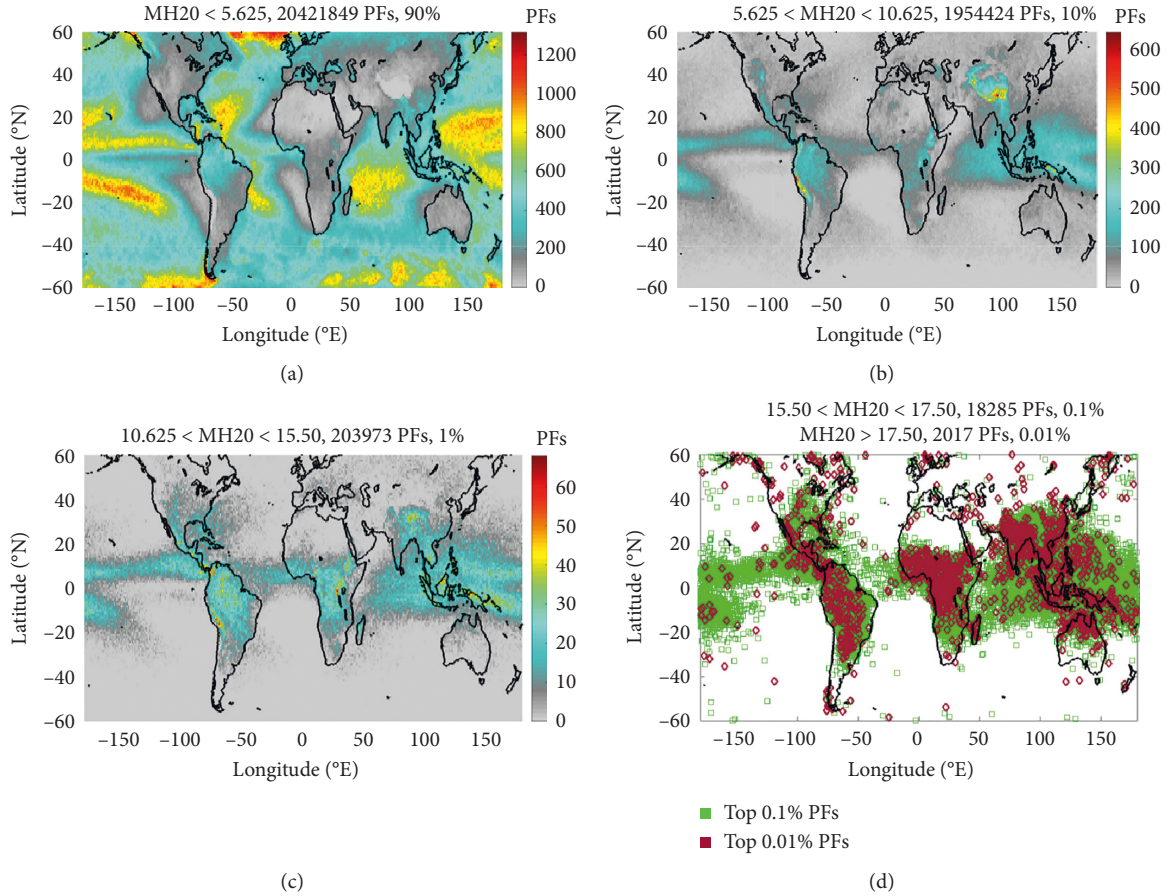


Figure 2: Spatial distribution of deepest (in depth, km) extreme rainfall events over the globe based in the maximum height of 20 dBZ. (a–c) The distribution of deepest extreme rainfall events in each $1^{\circ} \times 1^{\circ}$ box; (d) the actual geographical locations of deepest extreme rainfall events. Color bar in (a)–(c) shows the number of extreme rainfall events. (d) The green color refers to the top 0.1% deepest PFs, whereas magenta refers to the top 0.01% deepest PFs.

1% (green), 0.1% (violet) and 0.01% (black) EREs based on the various criteria (Table 2) over SA and SAsia. Table 4 shows the thresholds used in the present study for DJFM and JJAS seasons. During DJFM months, the largest EREs (top 0.1% largest PFs, 53320 $km^2$) occur over central SA, southern Chile, south of the Atlantic Ocean, and Amazon basin [32, 36]. The largest EREs over the Amazon is linked to low-level jets (LLJ), which carry the moist air from the Amazon and produces the heavy precipitation at the eastern flank of the Andes [50]. The deepest EREs show the different characteristics compared to the largest EREs, and the regional differences are much higher. For example, the deepest EREs (top 0.1% EREs>16.25 km) mostly occur over central SA including the north SA, La Plata basin, Sierra de Cordoba, central Andes, and southern Chile. The higher number of deepest EREs over/near the Andes reflects the orographic-induced convection [32, 36]. The Atlantic Ocean does not consist of a single ERE categorized by the top 0.01% deepest EREs and is consistent with the weak convection over the Atlantic [23, 28, 29, 32]. The deepest EREs based on MH40 show the most interesting characteristics, as both Atlantic Ocean and Pacific Ocean do not consist of a single ERE belong to the top 1% deepest EREs, and the deepest EREs mostly occur over the land area (top 0.01%; >14.0 km). The spatial distribution of the largest volumetric rainfall EREs shows that most of the largest EREs are located near the Brazilian highlands and the Atlantic Ocean and nearly coincides with the locations of the largest EREs. The intense EREs (top 1%) reveal the importance of the role of orography in intense rainfall events, as during DJFM seasons, the areas near and at the Andes have the higher number of intense rainfall events (top 1% EREs>44 mm $h^{-1}$), along with the La Plata basin and Brazilian Highlands. Overall, northern SA has higher intense EREs compared to southern SA.

Figure 6(b) shows the geographical locations of EREs over SAsia during JJAS months. The spatial distribution shows that the Bay of Bengal (BOB) and the head of the Bay have a higher number of the largest EREs (top 0.1% largest EREs; 53000 $km^2$). These findings are consistent with the past studies that the BOB has the most organized larger convective systems [23, 33, 35, 37]. The Western Ghats (WG), Arabian Sea, and tropical Indian Ocean also consist of fewer largest EREs (>53000 $km^2$). The deepest EREs based on MH20 show different characteristics, as the IGP and WG have the higher number of deeper EREs (top 0.1%; >11.5 km). Myanmar and Karakoram hills also consist of

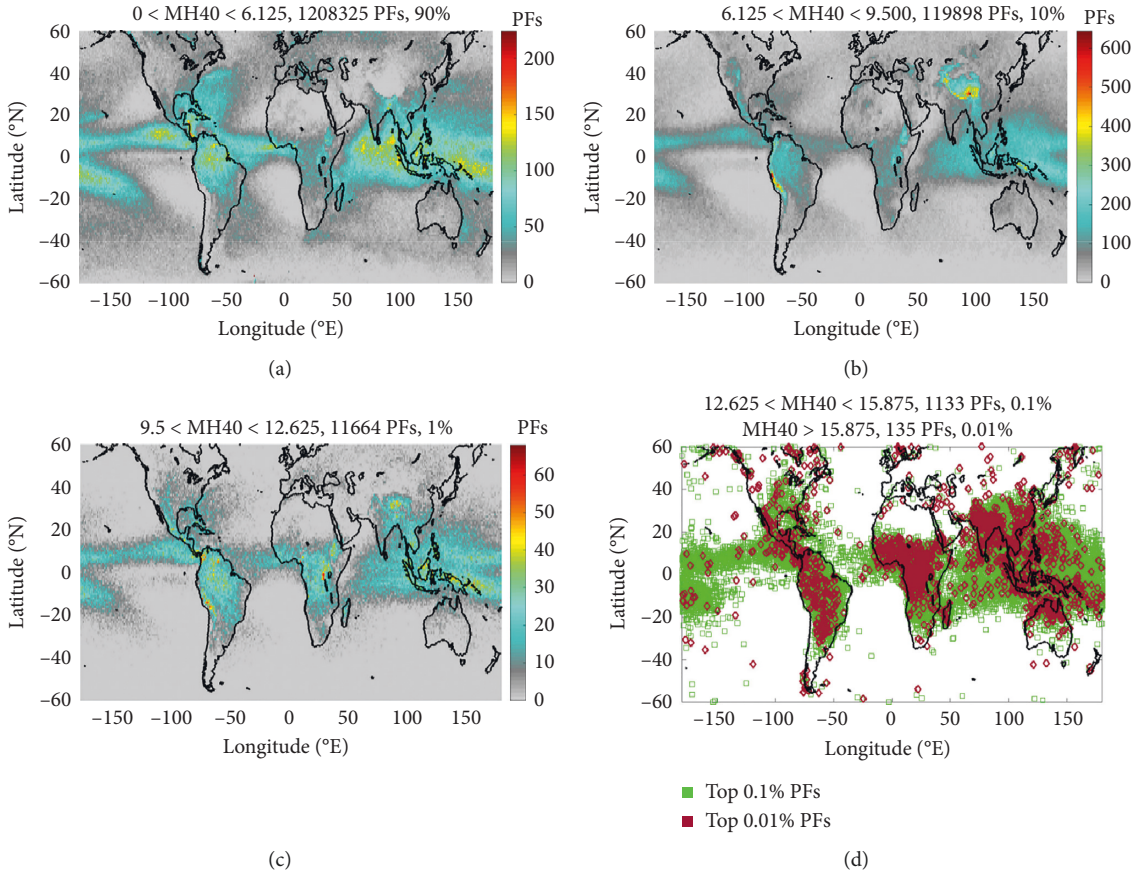


Figure 3: Spatial distribution of deepest (in depth, km) extreme rainfall events over the globe based in the maximum height of 40 dBZ. (a–c) The distribution of deepest extreme rainfall events in each $1^{\circ} \times 1^{\circ}$ box; (d) the actual geographical locations of deepest extreme rainfall events. Color bar in (a)–(c) shows the number of extreme rainfall events. (d) The green color refers to the top 0.1% deepest PFs, whereas magenta refers to the top 0.01% deepest extreme rainfall events.

fewer deeper EREs [26]. The deepest EREs based on MH40 show an interesting characteristic as they (top 0.1% EREs > 13.5 km) are located mostly over the land areas, such as over the Western Himalaya Foothills (WHF), IGP, and central India and reflect the land and ocean differences. The WG and Arabian Sea have the shallowest EREs (<5.0 km) during the monsoon season [28, 31]. The largest EREs based on the amount of volumetric rainfall follow the largest EREs distribution, and most of the largest EREs correspond to the higher volumetric rainfall, especially over the BOB and Arabian Sea. The land-dominated areas have fewer largest EREs, which contribute to higher volumetric rainfall compared to oceanic areas. The most intense EREs show the interesting characteristics, and both land and oceanic areas consist of intense EREs. Areas over the head of the Bay, BOB, Arabian Sea, Karakoram hills, and WG have the highest intense EREs (top 0.1% intense EREs>125 mm $h^{-1}$), but they do not coincide with the largest EREs, except over the BOB. During JJAS months, the topographic areas such as the IGP and WHF consist of fewer intense EREs (top 0.1% > 133 mm $h^{-1}$) and reflect the mountain's role [51]. The WG and the Arabian Sea also have few large and intense EREs [26].

The spatial distribution of the deepest, largest, and intense EREs indicates the effect of specific geographical features, climatological wind pattern, humidity, topography, and role of cloud condensation nuclei (CCN). It has been long known that the wind shear and upslope motion at the wind-ward and lee side of the mountain can alter the microphysical processes and lead to a change in rainfall characteristics [51]. The smaller number of the largest and deepest EREs at west of the Andes and south most (including Pacific Ocean) of the Andes are related to South-East Subtropical Anticyclone (SPSA) in the South Pacific basin. The SPSA generates the stable and arid condition at the western slope of the Andes [52], which does not allow the deep convection and does not allow the moisture to rise above 900 hPa. South American LLJ transports the moisture along the eastern edge of the Andes from the tropical regions to the subtropical part of the continent (850 level), and it triggers the deep and intense convection mostly at the eastern flank of the Andes [32]. The deepest convections over the WHF and Sierra de Cordoba along with La Plata basin are due to their specific geographical feature and wind pattern. Median et al. [53] and Romatscheke and Houze [32] explained that instability generated within the moist boundary layer in two areas is not easily released. The only way to produce the deep and intense convection over these areas is the orographic motion. Whenever an unstable and orographically induced flow moves along the steep slope and reaches up to the saturation level, it

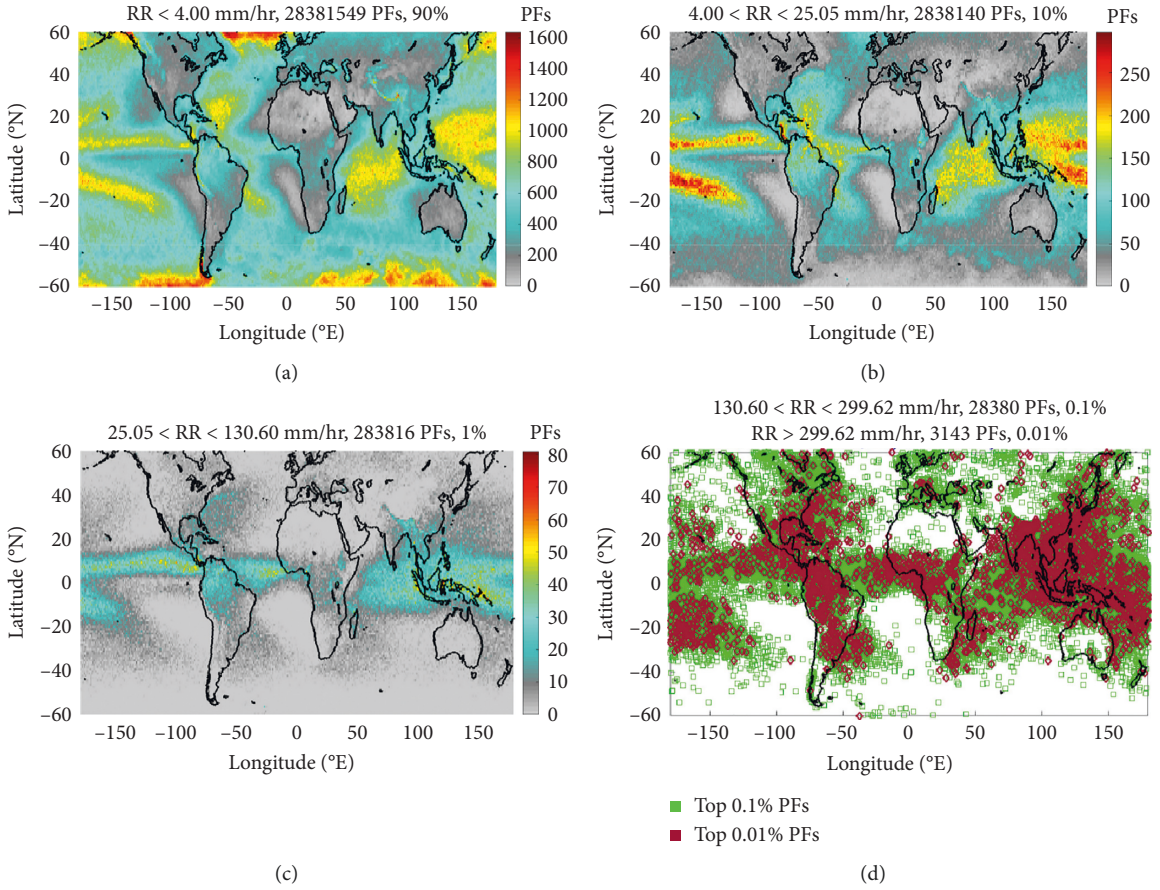


Figure 4: Spatial distribution of intense extreme rainfall events (in mm $h^{-1}$) over the globe based on the rainfall rate. (a–c) The distribution of intense extreme rainfall events in each $1^{\circ} \times 1^{\circ}$ box; (d) the actual geographical locations of intense extreme rainfall events. Color bar in (a)–(c) shows the number of extreme rainfall events. (d) The green color refers to the top 0.1% intense extreme rainfall events, whereas magenta refers to the top 0.01% intense extreme rainfall events.

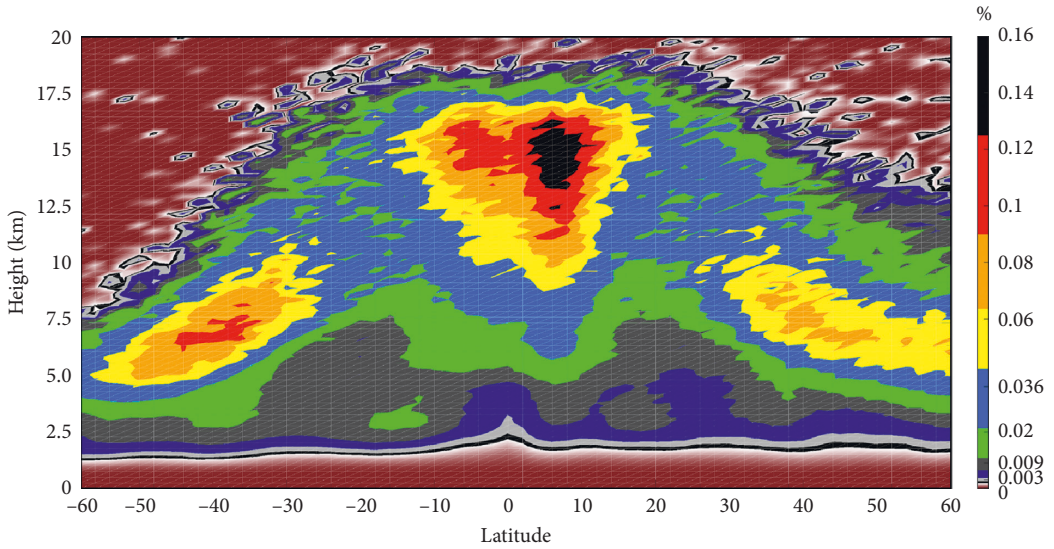


Figure 5: Contribution to global precipitation from extreme rainfall events of different maximum heights of the 20 dBZ echo. Here, the statistics are computed in $1^{\circ}$ latitude bins.

Table 3: Contribution to global precipitation by largest, deepest, and intense PFs.

| PFs | Intensity | Top 10% | Top 1% | Top 0.1% | Top 0.01% |
|---|---|---|---|---|---|
| Largest (area) | Total | 96.4 | 80.7 | 36.1 | 7.1 |
| | Ocean | 96.2 | 82.2 | 40.5 | 8.6 |
| | Land | 97.2 | 76.3 | 23.0 | 2.6 |
| Maximum height of 20 dBZ (MH20) | Total | 90.6 | 53.1 | 15.4 | 1.8 |
| | Ocean | 89.1 | 51.5 | 14.3 | 1.4 |
| | Land | 94.9 | 57.8 | 18.8 | 3.1 |
| Maximum height of 40 dBZ (MH40) | Total | 86.7 | 53.3 | 9.5 | 1.2 |
| | Ocean | 86.3 | 49.8 | 4.5 | 0.4 |
| | Land | 87.6 | 63.9 | 24.8 | 4.0 |

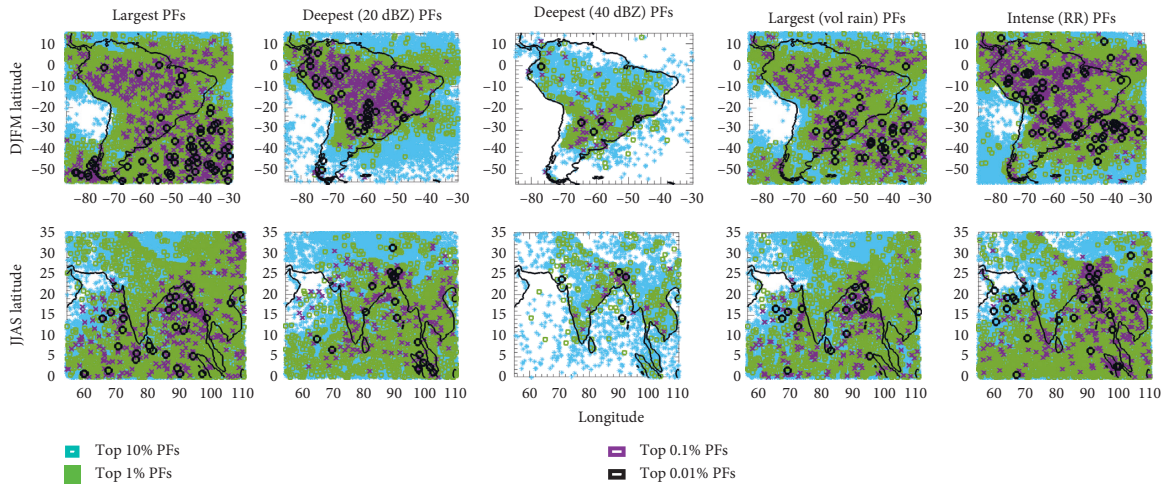


Figure 6: Spatial distribution of largest, deepest, and intense extreme rainfall events over South America (upper rows) and South Asia (bottom rows) during December to March (DJFM) and June to September (JJAS) months, respectively. The different seasons are mentioned in the *Y*-axis. The first, second, third, fourth, and fifth columns are for the largest extreme rainfall events based on area, deepest extreme rainfall events based on maximum height of 20 dBZ, deepest extreme rainfall events based on maximum height of 40 dBZ, largest extreme rainfall events based on the quantity of volumetric rainfall, and intense extreme rainfall events based on the rain rate.

Table 4: Fraction contribution in seasonal and regional precipitations by extreme events based on the area over the land and ocean.

| Season and number of PFs | | Volumetric rainfall contribution (in %) | | | | Thresholds | | | |
|---|---|---|---|---|---|---|---|---|---|
| | | Top 10% | Top 1% | Top 0.1% | Top 0.01% | Top 10% | Top 1% | Top 0.1% | Top 0.01% |
| *For the largest PFs ($km^2$ )* | | | | | | | | | |
| DJFM/land | 290919 | 94.97 | 67.95 | 22.07 | 3.68 | 540.1000 | 8.9362$e+03$ | 5.4077$e+04$ | 1.0730$e+05$ |
| DJFM/ocean | 388683 | 96.74 | 84.06 | 36.18 | 8.21 | 270.05 | 4.1735$e+03$ | 5.1749$e+04$ | 1.4738$e+05$ |
| JJAS/ocean | 253470 | 97.28 | 82.61 | 32.42 | 5.52 | 343.7000 | 6.0639$e+03$ | 5.9044$e+04$ | 1.2510$e+05$ |
| JJAS/land | 235396 | 94.32 | 64.93 | 21.91 | 4.10 | 540.1000 | 8.1997$e+03$ | 4.8941$e+04$ | 1.0320$e+05$ |
| *Maximum height of 20 dBZ (MH20)* | | | | | | | | | |
| DJFM/land | 237542 | 84.54 | 28.50 | 4.64 | 0.62 | 8.500 | 14.500 | 16.875 | 18.250 |
| DJFM/ocean | 286051 | 91.16 | 53.12 | 12.82 | 2.60 | 5.250 | 9.250 | 13.750 | 16.125 |
| JJAS/ocean | 191865 | 94.69 | 57.98 | 12.49 | 1.57 | 7.00 | 12.250 | 16.000 | 18.250 |
| JJAS/land | 185994 | 81.03 | 28.30 | 4.38 | 0.38 | 9.375 | 15.000 | 17.565 | 19.985 |
| *Maximum height of 40 dBZ (MH40)* | | | | | | | | | |
| DJFM/land | 36953 | 38.8 | 8.36 | 1.75 | 0.20 | 7.125 | 10.750 | 14.250 | 16.450 |
| DJFM/ocean | 17490 | 52.96 | 10.44 | 2.34 | 0.14 | 5.125 | 7.500 | 11.375 | 16.125 |
| JJAS/ocean | 26522 | 64.9 | 14.65 | 2.79 | 0.18 | 5.875 | 8.250 | 11.2475 | 16.500 |
| JJAS/land | 28598 | 54.62 | 39.42 | 4.93 | 1.01 | 8.000 | 11.250 | 14.475 | 16.625 |
| *Intense rainfall events (mm/hr)* | | | | | | | | | |
| DJFM/land | 290919 | 88.26 | 50.63 | 10.20 | 1.95 | 7.37 | 59.35 | 216.30 | 299.90 |
| DJFM/ocean | 388683 | 94.45 | 69.50 | 25.10 | 5.01 | 4.74 | 30.75 | 125.62 | 299.61 |
| JJAS/ocean | 253470 | 96.23 | 77.24 | 24.31 | 3.22 | 6.67 | 55.12 | 206.04 | 299.96 |
| JJAS/land | 235396 | 87.33 | 45.94 | 10.06 | 1.42 | 7.72 | 73.43 | 299.11 | 299.97 |

causes the instability to release and produces the deep and intense convection. The west side/coast of SAsia has lower CCN concentration [54], which increases the warm rain frequency that allows a few hydrometeors to go into the deep atmosphere [55], and at the same time, the higher CCN concentration over the land-dominated areas specially over the central and IGP delays the precipitation processes [55, 56] and is responsible for the deep and intense convection. The Arabian Sea has less deeper EREs during JJAS months because of Giant CCNs, which initiate the early warm rain processes and do not allow the deep convection [55]. The weak vertical velocity over the oceanic area is not able to lift the hydrometeors at a higher altitude and responsible for less cloud depth or cloud tops over the oceanic areas.

Figure 6 shows that the largest EREs are not the deepest ones, and the geographical location of EREs based on different parameters show the weak linkage between the largest, deepest, and intense EREs. These are quantified in detail in the next section. This reveals the atmospheric conditions which produce intense EREs are different from those produce the largest and deepest EREs. The regional and seasonal differences in EREs are related to different atmospheric conditions (e.g., [57]). This situation is well observed in [26, 27], where they showed the geographical features, and specific locations could produce very deep convection although their frequency could be less. For example, Zipser et al. [23] explained that the Amazon has a higher number of EREs in December–February (DJF), but the intense and deepest convection occurs mostly in the post-monsoon season [48]. The highest land and ocean contrasts are visible in the deepest EREs, as the Pacific, Atlantic, BOB, and Arabian Sea do not have a higher number of the deepest EREs. These EREs are not crossing 12 km altitude, whereas EREs of the nearby land areas are higher than 17 km. Both SA and SAsia show the mountain's (topographic) role in the generation of intense EREs, and most of the intense EREs occur near the topographic areas [51]. Land vs ocean contrast in the deepest EREs could be related to the weaker vertical velocity over the oceanic areas, which are not able to carry the hydrometeors at a higher altitude.

*3.4. Linage between Extreme Events Based on Various Parameters.* Hamada et al. [4] observed a weak linkage between the extreme convective and rainfall events, e.g., a very small fraction of extreme convective events produce the higher rainfall over the tropics and subtropics. The correlation was stronger over the tropical oceans (~50%) compared to land areas (~10%). A similar characteristic is observed in [33] where geographical locations of the largest and deepest EREs do not match. Here, we examined the linkage between the top 10% EREs based on various parameters. For example, for the largest EREs, parameters such as MH20, MH40, volumetric rainfall area, and RR are estimated. In Figure 7, the first row shows the CDF of MH20, MH40, volumetric rainfall area, and RR for the top 10% largest EREs (see the figure comment for more details). The second row shows the CDF of the area, MH20, volumetric rainfall area, and RR for the top 10% deepest EREs based on the MH40, whereas the third row shows the CDF of area, MH20, MH40, and volumetric rainfall area for top 10% intense EREs based on the RR.

For the largest top 10% EREs (Figure 7(a1)), the seasonal and regional differences are apparent. For example, SAsia has a higher frequency of the deepest EREs (MH20 is higher) compared to SA for the largest EREs. For 50% of the largest top 10% EREs during JJAS months, MH20 is higher than 7 km altitude, whereas the corresponding altitude for SA is ~5.5 km (Figure 7(a1)). EREs with MH20 higher than 8.5 km altitude correspond to only the top 10% deepest EREs, and so within the largest 10% EREs, ~20% of them correspond to the top 10% deepest EREs over SAsia (~7 km), whereas over SA ~30% largest EREs corresponds to the top 10% deepest EREs. Also, for ~50% of the largest top 10% EREs, MH40 are crossing the 12 km altitude, whereas the corresponding percentage and altitude over SA is 70% and ~8–9 km (Figure 7(a2)). It indicates that there is a higher probability that the largest EREs could be the deepest during JJAS months compared to DJFM months. Volumetric rainfall area shows the opposite characteristics, and the top 10% largest EREs over SAsia do not provide the much volumetric rainfall amount compared to SA. This indicates that small EREs are also able to contribute to significant rainfall over SAsia during JJAS months. The RR is also higher during JJAS seasons over SAsia compared to SA for the top 10% largest EREs. More than ~50% of the top 10% largest EREs have a RR higher than 75 mm $h^{-1}$ during JJAS months, whereas the corresponding RR is only 50 mm $h^{-1}$ during DJFM over SA (Figure 7(a4)). Over both the areas, only 35–45% of the largest EREs have a RR that is higher than the top 1% intense RR (Table 4) which indicates that very few of the largest EREs correspond to intense rainy events (~63 and ~50 mm $h^{-1}$ during JJAS and DJFM over SAsia and SA).

MH40 also shows the regional and seasonal differences for the top 10% deepest EREs, and JJAS months have higher deeper EREs over SAsia. For the ~50% of the top 10% deepest EREs, MH20 is higher than 8.5 km (top 10% deepest EREs) over SAsia, whereas over SA, for the ~40% deepest EREs, MH20 corresponds to the top 10% deepest EREs (7 km, Table 4). Area for the top 10% deepest EREs does not show much seasonal differences (Figure 7(b2)). Although in small differences, SA has a higher frequency of the deepest EREs, which can produce a higher amount of volumetric rainfall. The deepest EREs have a higher chance to be intense during DJFM months and more than ~40% of the deepest EREs have a RR higher than 50 mm $h^{-1}$, which corresponds to the top 1% intense EREs. Importantly, thresholds over SAsia (63 mm $h^{-1}$ for top 1%) is higher compared to SA (50 mm $h^{-1}$ for top 1%), but there is a higher probability (~45%) for them to be quantified as a part of the top 1% intense rainy events over SAsia for the deepest EREs. For the top 10% intense rainfall EREs, MH20 and MH40 show the least regional and seasonal differences (Figures 7(c1) and 7(c2)), and EREs over SAsia are deeper when compared to SA. The area and volumetric rainfall area do not show much regional differences for intense EREs.

Figure 7 shows that the linkage between the EREs is higher over SAsia compared to SA, and there is a higher

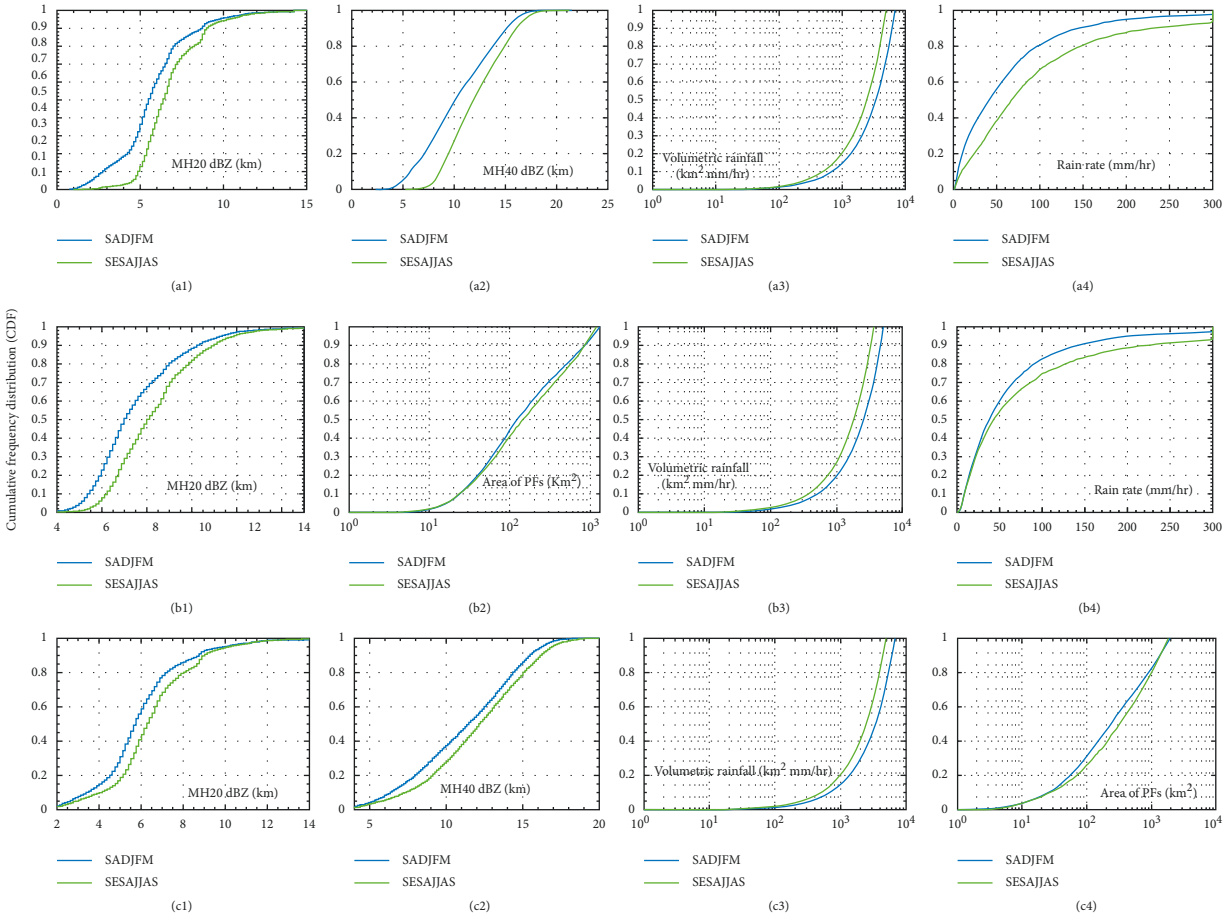


Figure 7: The cumulative frequency distribution (CDF) of area, maximum height of 20 dBZ, maximum height of 40 dBZ, volumetric rainfall, and rain rate for each type of extreme rainfall events. As an example, in the first row, the MH20, MH40, volumetric rainfall area, and rain rate are calculated for the top 10% largest PFs.

probability that the largest EREs belong to the deepest and intense EREs over SAsia, compared to SA. It is very important to see that thresholds for EREs area, MH20, MH40, and rain rate over SA are higher/lower compared to SAsia, depending on the land and ocean. The land areas have higher deepest EREs over SAsia (>14.75 for top 0.1% EREs) compared to SA (>12.75 for top 0.1% EREs). The opposite characteristics are observed over the oceans. The least regional and seasonal differences are observed in intense EREs, it could be the orthographically induced convection produced them [51].

*3.5. Fraction of the Global Precipitation from Extreme Rainfall Events during JJAS and DJFM Months.* Figure 8 shows the fraction of precipitation from the deepest EREs based on MH20 at different latitudes in 1° latitude belts over SA and SAsia (Figures 8(a) and 8(b)) during DJFM and JJAS month. During both the seasons, the deepest EREs based on MH20 are crossing 12.5–17 km over the tropics and contribute to the higher fraction of seasonal and regional precipitation, although they are relatively rare (belongs to only top 0.1 deepest EREs, Table 4). MH20 higher than 12 km could be related to Cumulonimbus clouds [26, 27, 58] and is responsible for the large precipitation contribution. At the mid and higher latitude, shallower EREs are contributing to the higher amounts of rainfall [31], as in Figure 5. In a small seasonal difference, SA (during DJFM month) has a higher fraction of rainfall from little deeper EREs (14 km < MH20 < 17.5 km) compared to SAsia, where the maximum fraction on rainfall comes from EREs with MH20 lies between 11 and 16.5 km altitude. The northern hemisphere has higher precipitation contribution by deeper EREs compared to the southern hemisphere and possibly the higher land areas in the northern hemisphere are responsible for them. There are a higher number of shallower EREs, but their precipitation contribution is not as significant, which is consistent with past studies (e.g., [26, 33, 52]). Satellite-based observations show that during the DJFM season, the Andes Mountain along with the surface wind flow affects the distribution of the precipitating cloud systems [59–62], and wind shear could also affect the microphysical processes and leads the different cloud tops with different rainfall intensities [63].

Figure 9 shows the fraction of precipitation from the deepest EREs based on MH40 at different latitudes in 1° latitude belts over SA and SAsia (Figures 9(a) and 9(b))

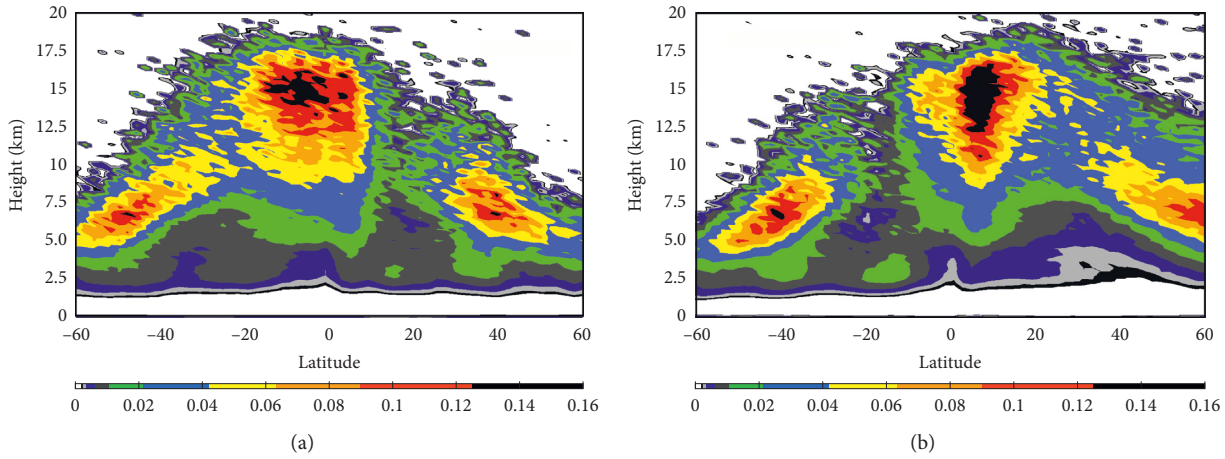


FIGURE 8: Contributions to global precipitation from extreme rainfall events of different maximum heights of the 20 dBZ echo. In all cases, the statistics are computed in 1° latitude bins. Total values add up to 100%. (a) DJFM; (b) JJAS.

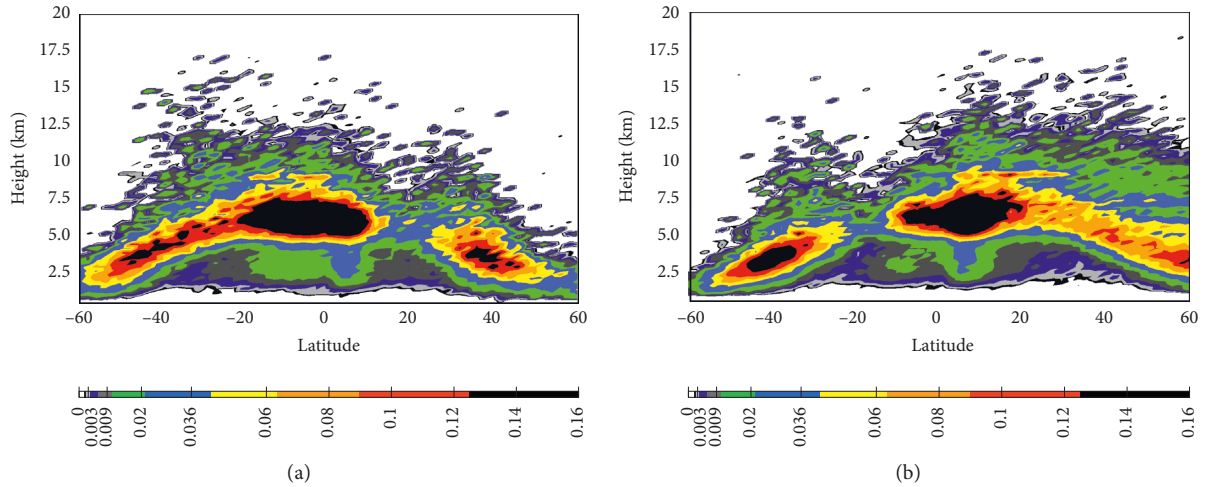


FIGURE 9: Contributions to global precipitation from PFs of different maximum heights of the 40 dBZ echo. In all cases, the statistics are computed in 1° latitude bins. Total values add up to 100%. (a) DJFM; (b) JJAS.

during DJFM and JJAS months, respectively. The regional and seasonal differences are higher here; and a higher fraction of precipitation comes from deeper EREs (5 km < MH40 < 10 km) during DJFM months. JJAS also shows the similar trends, but at the southern latitudes, it also shows a maxima from the sallower clouds. At mid and higher latitudes, shallower EREs contribute to a higher fraction of rainfall, as in Figure 6. Figure 10 shows the contributions to seasonal and regional precipitations from the deepest EREs based on MH40 at different latitudes in 1° latitude belts over SA and SAsia for land and ocean separately. Land and ocean contrasts are observed, and land areas have a higher fraction of rainfall from deeper EREs, compared to oceanic areas, during both the seasons. The land differences are higher in both the seasons compared to oceanic areas, as oceanic areas show similar characteristics, and the maximum amount of the rainfall comes from the EREs, with MH40 lying between 4 and 6 km, within tropical areas. Interestingly, JJAS shows the two bands over the land-dominated areas, namely, at 7 and 9 km altitude.

Table 4 shows brief information about the fraction of global precipitation by the EREs over land and oceanic areas during JJAS and DJFM months. For example, the top 0.1% largest EREs contribute more than 22% of the regional precipitation over land during DJFM months, whereas during JJAS month, the corresponding number is higher than 32%. During both the seasons largest EREs contribute to higher volumetric rainfall compared to that over the land. The deepest EREs also show the regional and seasonal differences, as the top 0.1% deepest EREs based on MH20 (MH40) contribute nearly ~12.4% ((~2.8%) over ocean) and ~4.3% ((4.9%) over land) of regional precipitation during JJAS months, whereas the corresponding contribution during DJFM months is only ~4.6% ((~12.8%) over ocean) and ~4.6% ((1.79%) over land). For all the parameters, the land and oceanic differences are evident and tabulated in Table 4.

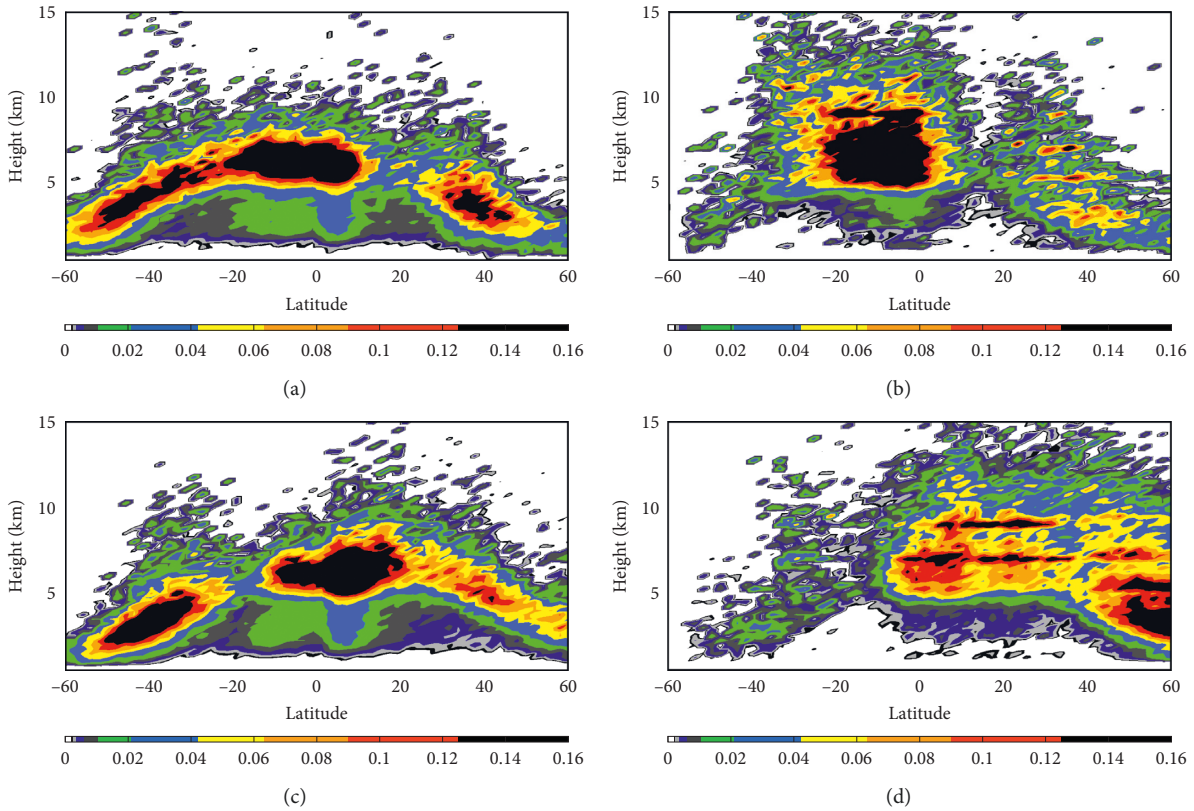


Figure 10: Contributions to global precipitation from extreme rainfall events of different maximum heights of the 40 dBZ echo over the land and ocean. In all cases, the statistics are computed in 1° latitude bins. (a) DJFM-ocean; (b) DJFM-land; (c) JJAS-ocean; (d) JJAS-land.

## 4. Conclusions

PFs data based on GPM satellite are used to explore the spatial distribution of extreme rainfall events/PFs on a global scale as well as the regional scale. We also selected the two main monsoon zones, namely, over South Asia and South America during different seasons to explore the spatial distribution of extreme rainfall events. The main conclusions from the present study are the following:

(1) The spatial distribution shows a large regional variation in EREs based on the area, depth, and rain rate. The spatial distribution of the largest and deepest EREs (top 0.01% EREs) shows the land and ocean differences. Subtropical oceans and tropical land-dominated areas consist of the largest and deepest EREs, respectively. It is clear that the largest EREs do not correspond to the deepest EREs. However, the intense EREs occur both over the tropical land and oceanic areas. Geographical locations of the deepest and intense EREs over the land-dominated area indicate that the intense EREs are deeper ones compared to the ocean, where the shallower EREs could also be an intense one.

(2) The top 1% largest EREs contribute to ~80.7% of Earth's precipitation, whereas the corresponding % for the deepest EREs is only 53%. Tropical areas have a higher number of deeper EREs contributing to a higher fraction of rainfall in world precipitation, whereas, beyond 25°, the higher fraction of precipitation comes from shallower EREs. The deeper extreme rainfall events (top 1% > 15.50 km) are less but contribute to the highest fraction of precipitation over the tropics, whereas over the mid latitude, most of the precipitation comes from the EREs less than 7.5 km altitude and mostly belongs to the top 10% of the deepest extreme rainfall events.

(3) Geographical locations of the largest, deepest, and intense EREs over South Asia are regions dependent. The Bay of Bengal along with the Arabian Sea and Equatorial Indian Ocean consists of the largest EREs, whereas the deepest EREs mostly occur over the land-dominated areas. The Western Himalaya foothills, Western Ghats, and Indo-Gangetic plain consist of the deepest EREs during Indian summer monsoon seasons. South America also shows similar characteristics and the Atlantic Ocean consists of the largest EREs followed by the Amazon and southern Chile. The deepest extreme rainfall events show different characteristics, as the Amazon also has the deepest EREs along with east side of the Andes. Subtropical South America including Sierra de Cordoba and La Plata basin consists of the largest, deepest, and extreme EREs during DJFM.

(4) Extreme rainfall events are highly linked over South Asia compared to South America based on different thresholds. For example, the top 10% largest extreme

rainfall events have a higher probability to be the part of the top 10% deepest and intense extreme rainfall events. Also, the deeper and intense rainy extreme events are highly linked over South Asia compared to South America.

(5) The seasonal and regional water budget reveals the regional characteristics, as the southern hemisphere has higher deeper extreme rainfall events, contributing to seasonal and regional precipitation budget. The tropical ocean has a higher number of shallower extreme rainfall events that contribute to higher water budget compared to land, where more precipitations occur due to deeper extreme rainfall events.

## Data Availability

The data used to support the findings of this study are available from the corresponding author upon request.

## Disclosure

The present study was performed under the project "MAGNET-IGP: strengthening the research line in physics and microphysics of the atmosphere" (agreement no. 010-2017-FONDECYT).

## Conflicts of Interest

The authors declare that there are no conflicts of interest regarding the publication of this paper.

## Acknowledgments

The authors would like to thank the CONCYTEC, Peru, for financial support and the Inter-American Institute for Cooperation on Agriculture (IICA) for administrative support.

## Supplementary Materials

Supplementary Figure 1: the selection of largest PFs based on the area. (*Supplementary Materials*)

## References

[1] C. Schumacher, R. A. Houze, and I. Kraucunas, "The tropical dynamical response to latent heating estimates derived from the TRMM Precipitation Radar," *Journal of the Atmospheric Sciences*, vol. 61, no. 12, pp. 1341–1358, 2004.

[2] R. A. Houze, "Mesoscale convective systems," *Reviews of Geophysics*, vol. 42, no. 4, article RG4003, 2004.

[3] R. Roca, J. Aublanc, P. Chambon, T. Fiolleau, and N. Viltard, "Robust observational quantification of the contribution of mesoscale convective systems to rainfall in the tropics," *Journal of Climate*, vol. 27, no. 13, pp. 4952–4958, 2014.

[4] A. Hamada, Y. N. Takayabu, C. Liu, and E. J. Zipser, "Weak linkage between the heaviest rainfall and tallest storms," *Nature Communication*, vol. 24, no. 6, p. 7213, 2015.

[5] R. A. Houze, K. L. Rasmussen, S. Medina, S. R. Brodzik, and U. Romatschke, "Anomalous atmospheric events leading to the summer 2010 floods in Pakistan," *Bulletin of the American Meteorological Society*, vol. 92, no. 3, pp. 291–298, 2011.

[6] R. A. Houze Jr and A. K. Betts, "Convection in GATE," *Reviews of Geophysics*, vol. 19, no. 4, pp. 541–576, 1981.

[7] R. A. Houze, "Cloud clusters and large-scale vertical motions in the tropics," *Journal of the Meteorological Society of Japan*, vol. 60, pp. 396–410, 1982.

[8] J. L. Redelsperger, *The mesoscale organization of deep convection The Physics and Parameterization of Moist Atmospheric Convection*, NATO ASI Series, R. K. Smith, Ed., vol. 505, Springer, Berlin, Germany, 1997.

[9] R. A. Houze, K. L. Rasmussen, M. D. Zuluaga, and S. R. Brodzik, "The variable nature of convection in the tropics and subtropics: a legacy of 16 years of the Tropical Rainfall Measuring Mission (TRMM) satellite," *Reviews of Geophysics*, vol. 53, no. 3, pp. 994–1021, 2015.

[10] R. W. Spencer and D. A. Santek, "Measuring the global distribution of intense convection over land with passive microwave radiometry," *Journal of Climate and Applied Meteorology*, vol. 24, no. 8, pp. 860–864, 1985.

[11] R. W. Spencer, H. M. Goodman, and R. E. Hood, "Precipitation retrieval over land and ocean with the SSM/I: identification and characteristics of the scattering signal," *Journal of Atmospheric and Oceanic Technology*, vol. 6, no. 2, pp. 254–273, 1989.

[12] K. I. Mohr and E. J. Zipser, "Defining mesoscale convective systems by their 85-GHz ice-scattering signatures," *Bulletin of the American Meteorological Society*, vol. 77, no. 6, pp. 1179–1189, 1996.

[13] R. E. Orville and R. W. Henderson, "Global distribution of midnight lightning: September 1977 to August 1978," *Monthly Weather Review*, vol. 114, no. 12, pp. 2640–2653, 1986.

[14] C. Kummerow, W. Barnes, T. Kozu, J. Shiue, and J. Simpson, "The tropical rainfall measuring mission (TRMM) sensor package," *Journal of Atmospheric and Oceanic Technology*, vol. 15, no. 3, pp. 809–817, 1998.

[15] S. W. Nesbitt, R. Cifelli, and S. A. Rutledge, "Storm morphology and rainfall characteristics of TRMM Precipitation Features," *Monthly Weather Review*, vol. 134, no. 10, pp. 2702–2721, 2006.

[16] C. Liu, E. J. Zipser, D. J. Cecil, S. W. Nesbitt, and S. Sherwood, "A cloud and precipitation feature database from nine years of TRMM observations," *Journal of Applied Meteorology and Climatology*, vol. 47, no. 10, pp. 2712–2728, 2008.

[17] S. W. Nesbitt, E. J. Zipser, and D. J. Cecil, "A census of precipitation features in the tropics using TRMM: radar, ice scattering, and lightning observations," *Journal of Climate*, vol. 13, no. 23, pp. 4087–4106, 2000.

[18] Y. N. Takayabu, "Spectral representation of rain profiles and diurnal variations observed with TRMM PR over the equatorial area," *Geophysical Research Letters*, vol. 29, pp. 1–4, 2002.

[19] S. Kumar, "Three dimensional characteristics of precipitating cloud systems observed during Indian summer monsoon," *Advances in Space Research*, vol. 58, no. 6, pp. 1017–1032, 2016.

[20] D. J. Cecil, S. J. Goodman, D. J. Boccippio, E. J. Zipser, and S. W. Nesbitt, "Three years of TRMM precipitation features. Part I: radar, radiometric, and lightning characteristics," *Monthly Weather Review*, vol. 133, no. 3, pp. 543–566, 2005.

[21] H. Masunaga, T. S. L'Ecuyer, and C. D. Kummerow, "Variability in the characteristics of precipitation systems in the

tropical pacific. Part I: spatial structure," *Journal of Climate*, vol. 18, no. 6, pp. 823–840, 2005.

[22] C. Liu and E. Zipser, "Global distribution of convection penetrating the tropical tropopause," *Journal of Geophysical Research*, vol. 110, article D23210, 2005.

[23] E. J. Zipser, D. J. Cecil, C. Liu, S. W. Nesbitt, and D. P. Yorty, "Where are the most intense thunderstorms on Earth?," *Bulletin of the American Meteorological Society*, vol. 87, no. 8, pp. 1057–1072, 2006.

[24] R. A. Houze, D. C. Wilton, and B. F. Smull, "Monsoon convection in the Himalayan region as seen by the TRMM precipitation radar," *Quarterly Journal of the Royal Meteorological Society*, vol. 133, pp. 1389–1411, 2007.

[25] C. Liu and E. J. Zipser, ""Warm rain" in the tropics: seasonal and regional distributions based on 9 yr of TRMM data," *Journal of Climate*, vol. 22, no. 3, pp. 767–779, 2009.

[26] G. S. Bhat and S. Kumar, "Vertical structure of cumulonimbus towers and intense convective clouds over the South Asian region during the summer monsoon season," *Journal of Geophysical Research: Atmospheres*, vol. 120, no. 5, pp. 1710–1722, 2015.

[27] S. Kumar and G. S. Bhat, "Vertical profiles of radar reflectivity factor in intense convective clouds in the tropics," *Journal of Applied Meteorology and Climatology*, vol. 55, no. 5, pp. 1277–1286, 2016.

[28] S. Kumar and G. S. Bhat, "Vertical structure of orographic precipitating clouds observed over south Asia during summer monsoon season," *Journal of Earth System Science*, vol. 126, no. 8, p. 114, 2017.

[29] S. Kumar, "A 10-year climatology of vertical properties of most active convective clouds over the Indian regions using TRMM PR," *Theoretical and Applied Climatology*, vol. 127, no. 1-2, pp. 429–440, 2017.

[30] S. Kumar, "Vertical characteristics of reflectivity in intense convective clouds using TRMM PR data," *Environment and Natural Resources Research*, vol. 7, no. 2, p. 58, 2017.

[31] S. Kumar, "Vertical structure of precipitating shallow echoes observed from TRMM during Indian summer monsoon," *Theoretical and Applied Climatology*, vol. 133, no. 3-4, pp. 1051–1059, 2018.

[32] U. Romatschke and R. A. Houze Jr, "Extreme summer convection in South America," *Journal of Climate*, vol. 23, no. 14, pp. 3761–3791, 2010.

[33] C. Liu and E. J. Zipser, "The global distribution of largest, deepest, and most intense precipitation systems," *Geophysical Research Letters*, vol. 42, no. 9, pp. 3591–3595, 2015.

[34] M. Hirose, R. Oki, D. A. Short, and K. Nakamura, "Regional characteristics of scale-based precipitation systems from ten years of TRMM PR data," *Journal of the Meteorological Society of Japan*, vol. 87A, pp. 353–368, 2009.

[35] A. Hamada, Y. Murayama, and Y. N. Takayabu, "Regional characteristics of extreme rainfall extracted from TRMM PR measurements," *Journal of Climate*, vol. 27, no. 21, pp. 8151–8169, 2014.

[36] K. L. Rasmussen and R. A. Houze Jr, "Orogenic convection in subtropical south America as seen by the TRMM satellite," *Monthly Weather Review*, vol. 139, no. 8, pp. 2399–2420, 2011.

[37] B. Wang, Q. Ding, and J. Liu, "Concept of global monsoon," in *The Global Monsoon 650 System: Research and Forecast 3–14*, C.-P. Chang, Ed., World Scientific Publishing, Singapore, 2011.

[38] P. J. Webster, V. O. Magaña, T. N. Palmer et al., "Monsoons: processes, predictability, and the prospects for prediction," *Journal of Geophysical Research: Oceans*, vol. 103, no. C7, pp. 14451–14510, 1998.

[39] D. I. Lee, S. M. Jang, C. H You et al., "The characteristics of summer monsoon rainfall at the southwestern ocean area of Korea: a study of the 2007 season," in *The Global Monsoon System: Research and Forecast 319–338*, C.-P. Chang, Ed., World Scientific Publishing, Singapore, 2011.

[40] B. N. Goswami, M. C. Wheeler, J. C. Gottschalck, and D. E. Waliser, "Intraseasonal variability and forecasting: a review of recent research," in *The Global Monsoon System: Research and Forecast*, C.-P. Chang, Ed., pp. 389–407, World Scientific Publishing Co. Pte. Ltd, Singapore, 2nd edition, 2011.

[41] D. R. Sikka, "Synoptic and meso-scale weather disturbances over South Asia during the Southwest Summer monsoon season," in *The Global Monsoon System: Research and Forecast*, C.-P. Chang, Ed., pp. 183–204, World Scientific Publishing, Singapore, 2011.

[42] C. Kidd, "Satellite rainfall climatology: a review," *International Journal of Climatology*, vol. 21, no. 9, pp. 1041–1066, 2001.

[43] P. Xie, J. E. Janowiak, P. A. Arkin et al., "GPCP Pentad precipitation analyses: an experimental dataset based on gauge observations and satellite estimates," *Journal of Climate*, vol. 16, no. 13, pp. 2197–2214, 2003.

[44] A. Y. Hou, R. K. Kakar, S. Neeck et al., "The global precipitation measurement mission," *Bulletin of the American Meteorological Society*, vol. 95, no. 5, pp. 701–722, 2014.

[45] S. Liu, X. Mo, H. Li, G. Peng, and A. Robock, "Spatial variation of soil moisture in China: geostatistical characterization," *Journal of the Meteorological Society of Japan*, vol. 79, no. 1B, pp. 555–574, 2001.

[46] A. K. Varma and G. Liu, "Small-scale horizontal rain-rate variability observed by satellite," *Monthly Weather Review*, vol. 134, no. 10, pp. 2722–2733, 2006.

[47] A. K. Varma and G. Liu, "On classifying rain types using satellite microwave observations," *Journal of Geophysical Research: Atmospheres*, vol. 16, no. D7, p. 115, 2010.

[48] C. Liu, "Rainfall contributions from precipitation systems with different sizes, convective intensities, and durations over the tropics and subtropics," *Journal of Hydrometeorology*, vol. 12, no. 3, pp. 394–412, 2011.

[49] T. M. Rickenbach and S. A. Rutledge, "Convection in TOGA COARE: horizontal scale, morphology, and rainfall production," *Journal of the Atmospheric Sciences*, vol. 55, no. 17, pp. 2715–2729, 1998.

[50] S. P. Chavez and K. Takahashi, "Orographic rainfall hot spots in the Andes-Amazon transition according to the TRMM precipitation radar and in situ data," *Journal of Geophysical Research: Atmospheres*, vol. 122, no. 11, pp. 5870–5882, 2017.

[51] R. A. Houze, "Orographic effects on precipitating clouds," *Reviews of Geophysics*, vol. 50, no. 1, 2012.

[52] J. Houston and A. J. Hartley, "The central Andean west-slope rainshadow and its potential contribution to the origin of hyper-aridity in the Atacama Desert," *International Journal of Climatology*, vol. 23, no. 12, pp. 1453–1464, 2003.

[53] S. Medina, R. A. Houze Jr, A. Kumar, and D. Niyogi, "Summer monsoon convection in the Himalayan region: terrain and land cover effects," *Quarterly Journal of the Royal Meteorological Society: A Journal of the Atmospheric Sciences, Applied Meteorology and Physical Oceanography*, vol. 136, no. 648, pp. 593–616, 2010.

[54] H. R. Pruppacher and J. D. Klett, *Microphysics of Clouds and Precipitation*, p. 961, Kluwer Academic, Dordrecht, Netherlands, 1997.

[55] M. Konwar, R. S. Maheskumar, J. R. Kulkarni, E. Freud, B. N. Goswami, and D. Rosenfeld, "Aerosol control on depth of warm rain in convective clouds," *Journal of Geophysical Research: Atmospheres*, vol. 117, no. D13, 2012.

[56] C. Lucas, E. J. Zipser, and M. A. LeMone, "Vertical velocity in oceanic convection off tropical Australia," *Journal of the Atmospheric Sciences*, vol. 51, no. 21, pp. 3183–3193, 1994.

[57] R. Fu, B. Zhu, and R. E. Dickinson, "How do atmosphere and land surface influence seasonal changes of convection in the tropical Amazon?," *Journal of Climate*, vol. 12, no. 5, pp. 1306–1321, 1999.

[58] G. M. Heymsfield, L. Tian, A. J. Heymsfield, L. Li, and S. Guimond, "Characteristics of deep tropical and subtropical convection from nadir-viewing high-altitude airborne doppler radar," *Journal of the Atmospheric Sciences*, vol. 67, no. 2, pp. 285–308, 2010.

[59] S. Kumar, Y.-S. Vidal, A. S. Moya-Álvarez, and D. Martínez-Castro, "Effect of the surface wind flow and topography on precipitating cloud systems over the Andes and associated Amazon basin: GPM observations," *Atmospheric Research*, vol. 225, pp. 193–208, 2019.

[60] E. E. Villalobos, D. Martinez-Castro, S. Kumar, Y. Silva, and O. Fashe, "Estudio de tormentas convectivas sobre los Andes Centrales del Perú usando los radares PR-TRMM y KuPR-GPM," *Revista Cubana de Meteorología*, vol. 25, no. 1, pp. 59–75, 2019.

[61] A. S. Moya-Álvarez, D. Martínez-Castro, S. Kumar, R. Estevan, and Y. Silva, "Response of the WRF model to different resolutions in the rainfall forecast over the complex Peruvian orography," *Theoretical and Applied Climatology*, pp. 1–15, 2019.

[62] A. Moya-Álvarez, J. Gálvez, A. Holguín et al., "Extreme rainfall forecast with the WRF-ARW model in the Central Andes of Peru," *Atmosphere*, vol. 9, no. 9, p. 362, 2018.

[63] S. Lasher-Trapp, S. Kumar, D. H. Moser et al., "On different microphysical pathways to convective rainfall," *Journal of Applied Meteorology and Climatology*, vol. 57, no. 10, pp. 2399–2417, 2018.

Hindawi
Advances in Meteorology
Volume 2019, Article ID 8512727, 11 pages
https://doi.org/10.1155/2019/8512727

*Research Article*

# Hydrological Drought Assessment of Energy-Based Water Deficit Index (EWDI) at Different Geographical Regions

**Chanyang Sur,[1] Dongkyun Kim,[2] Joo-Heon Lee,[3] Muhammad Mazhar Iqbal,[4] and Minha Choi[4]**

[1]*Drought Research Center, Joongbu University, Goyang, Gyeonggi, Republic of Korea*
[2]*Department of Civil Engineering, Hongik University, Seoul, Republic of Korea*
[3]*Department of Civil Engineering, Joongbu University, Goyang, Gyeonggi, Republic of Korea*
[4]*Department of Water Resources, Graduate School of Water Resources, Sungkyunkwan University, Suwon, Republic of Korea*

Correspondence should be addressed to Minha Choi; mhchoi@skku.edu

Received 29 November 2018; Revised 25 February 2019; Accepted 23 April 2019; Published 29 May 2019

Academic Editor: Giacomo Gerosa



This study applied the remote sensing-based drought index, namely, the Energy-Based Water Deficit Index (EWDI), across Mongolia, Australia, and Korean Peninsula for the period between 2000 and 2010. The EWDI is estimated based on the hydrometeorological variables such as evapotranspiration, soil moisture, solar radiation, and vegetation activity which are derived from the Moderate Resolution Imaging Spectroradiometer (MODIS) imageries. The estimated EWDI was compared with the Evaporative Stress Index (ESI), the Vegetation Condition Index (VCI), and the Standardized Precipitation Index (SPI). The correlation coefficients between the drought indices are as follows: 0.73–0.76 (EWDI vs ESI), 0.64–0.71 (EWDI vs VCI), 0.54–0.64 (EWDI vs SPI-3), 0.69–0.71 (ESI vs VCI), 0.55–0.62 (ESI vs SPI-3), and 0.53–0.57 (VCI vs SPI-3). The drought prediction accuracy of each index according to error matrix analysis is as follows: 83.33–94.17% (EWDI), 70.00–91.67% (ESI), 47.50–85.00% (VCI), and 61.67–88.33% (SPI-3). Based on the results, the EWDI and ESI were found to be more accurate in capturing moderate drought conditions than the SPI at different geographical regions.

## 1. Introduction

In general, drought is considered from numerous perceptions. Firstly, meteorological drought which is usually interpreted by degree of aridness and duration of aridness and its extent, which shows anomalies, correspond to cumulative precipitation. Secondly, hydrological drought is related to the precipitation deficits on water supply, which is quantified by short runoff, deepened ground water level, and water resource deficiencies. Thirdly, agriculture drought accounts for the variable susceptibility of vegetation during different statuses of vegetation development which is estimated by measuring diminution in crop yield and soil moistness as well as differences among actual and potential evapotranspiration.

Due to these assorted definitions of drought as well as troublesome in estimating the precise commencement, range, level, and end of drought, substantial efforts have been utilized to delineate techniques for investigation and monitoring of drought. However, the conventional drought has been considered based on the hydrometeorological variables measured by the network of in situ data tools, whereas remote sensing technology is robust substituted by providing decisive hydrometeorological variables for drought analysis at the enormously higher spatial scale than the capability of in situ network devices. Several studies have presented remote sensing-based drought indices. Likewise, Kogan [1] introduced the Vegetation Condition Index (VCI) by using remote sensing-based Normalized Difference Vegetation Index (NDVI) data, and Kogan [2] developed the Vegetation Health Index (VHI) by using remotely sensed data of TIR imageries to monitor variation in canopy temperatures. Anderson et al. [3–5] developed a new drought index known as "Evaporative Stress Index" (hereafter ESI). They assessed

the ESI crosswise the globe based on water vapor and temperature that is attained from the remote sensing model named "Atmosphere-Land Exchange Inverse (ALEXI) remote sensing model" [3–5]. They described that the ESI correlated soundly with the Palmer Drought Severity Index (PDSI) and Standardized Precipitation Index (SPI). Mu et al. [6] proposed the Drought Severity Index (DSI) which was based on MODIS data. Their proposed DSI matched well not only with the Palmer Drought Severity Index (PDSI) and Standardized Precipitation Index (SPI) but also with the vegetation net primary production (NPP) data which designated that the index was useful for assessing drought stimuli on crop production and forest growth. Keshavarz et al. [7] proposed and evaluated a new drought index, Soil Water Deficit Index (SWDI), to study the agricultural drought. Here, it is remarkable that almost all of these drought indices focus on specific aspects of various and complex drought conditions in reality. For example, SPI, ESI, EDI, and PDSI were estimated primarily based on meteorological variables, so these indices did not reflect the level of soil moisture that could mainly influence crop growth and ecology. Moreover, VHI and SWDI are mainly estimated based on other variables related to vegetative greening conditions, so they cannot accurately reveal the instant of meteorological phenomena that can improve drought severity. For tenacity of this issue, Sur et al. [8] assessed a progressive drought index named "Energy-Based Water Deficit Index" (EWDI), which concurrently considered the circulation of energy, water, and carbon across the soil surface and atmosphere to reflect the complex conditions of droughts related to atmosphere and vegetation. They estimated this index across Korean Peninsula using MODIS-based datasets and exposed that the EWDI performed well and showed favorable association with the ESI (correlation coefficient within 0.73 and 0.76 based on their specific study area) as well as the conventional drought indices such as PDSI (correlation coefficient within 0.57 and 0.67) and SPI (correlation coefficient within 0.61 and 0.64). As outcomes of their research were achieved based on the data of Korean Peninsula which is located on the northeastern brink of the Asian continent, they could not interpret an overall conclusion for the applicability and legitimacy of the EWDI on a wide range of spatial scales across the globe.

In this view, the main purpose of this research is to enhance the application of EWDI by validating the EWDI at other geographical locations with greater spatial scales that are prone to drought. To attain this goal, the EWDI, ESI, VCI, and SPI were estimated across Mongolia (north-central Asia), the Australian continent, and the remaining part of Korean Peninsula for the duration of 2000–2010. Linear regression and error matrices were used to compare estimated indices with each other.

## 2. Study Area and Datasets

### 2.1. Study Area

*2.1.1. Mongolia.* The first study area was the north-central Asian country Mongolia located between 42–51°N (latitude) and 85–120°E (longitude) (Figure 1). The total area of Mongolia is nearly 1.6 million square kilometers, and the elevation ranges from 1,000 m to 2,500 m above the mean sea level. The country is divided into six types of natural zones having different soil types and plant life in each zone. In this study, meteorological data are obtained from six selected stations which cover the entire country. The climate of Mongolia is described by a dry and hot summer, a long-lasting cold winter, high temperature variations, low precipitation, and a relatively high total of sunny days (on average 260 days per year) [9]. Mongolia, which is relatively a dry region, has a less mean annual precipitation, accumulating to approximately 100–200 mm in the dry southern mountainous regions and 200–350 mm in the northern mountainous regions [10]. The entire area has a total annual precipitation about 90 mm. The northern part of Mongolia is mountainous ranges characterized by dense forests in a dry subhumid climate, whereas the southern region is the Gobi Desert characterized by a drier climate at lower elevations [9]. The above-mentioned climatic array as a function of latitude also described the vegetation pattern athwart Mongolia.

*2.1.2. Australia.* The second study area was Australia located between 10–40°S (latitude) and 113–153°E (longitude) (Figure 1). The total area of Australia is 7,617,930 $km^2$ setting on the Indo-Australian Plate. Australia is separated into eight climate zones which are defined by the Building Code of Australia (BCA). Based on the local geographical varieties including wind patterns and elevation above the mean sea level, each climate zone is further subdivided into many subzones.

*2.1.3. Korean Peninsula.* Korean Peninsula is located on the northeast brink of Asia at 33–43°N (latitude) and 124–132°E (longitude) (Figure 1). Even though Korean Peninsula has been previously investigated by Sur et al. [8], this study presents the result of the additional analysis performed in the north Korean region. Korean Peninsula covers an area of 219,020 $km^2$, located in the Asian monsoon region, having a mean annual precipitation approximately 1,100 mm (North Korea, 919.7 mm; South Korea, 1,307.7 mm). The topography of the study area represents an elevation range about 0–1,915 m [11]. The land use is mainly composed of croplands (29.7%), mixed forests (39.6%), deciduous broadleaf forests (14.4%), woody savannas (6.3%), and residential and commercial areas (5.2%). Table 1 describes the geographical features of meteorological observations.

Validations of various drought indices were performed for the selected three meteorological measurement sites (Hamheung, Anju, and Kimchaek). The meteorological observation stations and flux tower are presented in Figure 1, and the features of each meteorological station are described in Table 1.

*2.2. Datasets.* In this study, to calculate drought indices, input datasets were obtained from the MODIS satellite and ground observation for the duration of 2000–2010. The

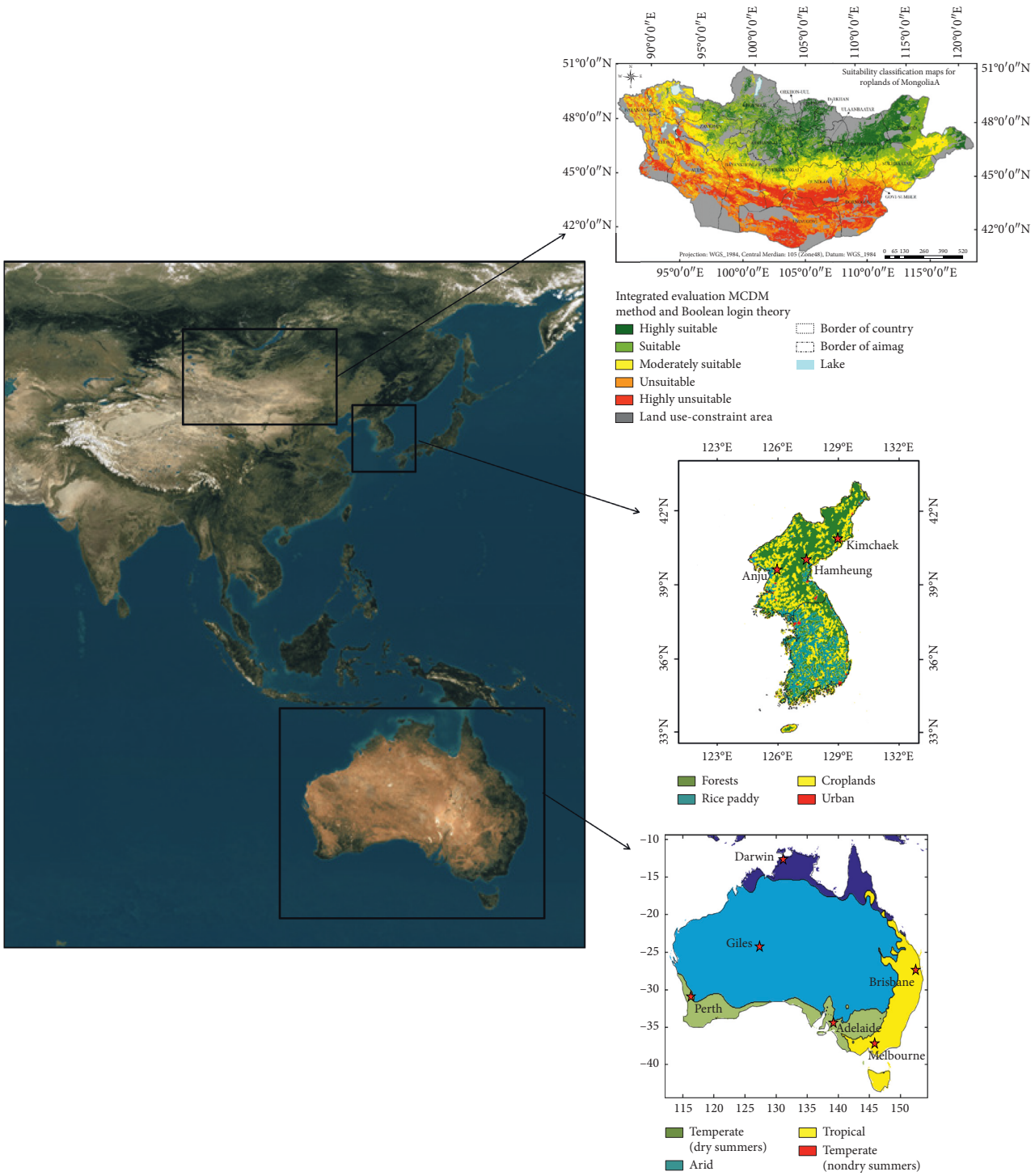


Figure 1: Geographical locations of study areas.

MODIS multispectral sensor that is the scientific instrument sent off into the earth circle by NASA's Earth Observing System (EOS) was developed to observe the atmosphere, land, and ocean. The temporal resolution is 1 day, and the spatial resolutions of the sensor estimations are 1 km, 500 m, and 250 m. The sensors are found on board the Terra and Aqua satellites, which were launched in December 1999 and May 2002, respectively. The Terra satellite has an overpass time around 10 : 30 PM when ascending and 10 : 30 AM when descending. The Aqua satellite's overpass time is roughly 1 : 30 PM when ascending and 1 : 30 AM while descending.

MODIS has been widely used in the field of energy balance studies since it gives a firm footing for spatiotemporally continuous information over the entire surface of the globe [12]. MODIS information from the Terra spacecraft (10 : 30 overpass) is used to estimate ET using various equations. MOD07 having a spatial resolution of 5 km is

Table 1: General characteristics of the study sites.

| ID | Latitude | Longitude | Altitude (m) | Temperature (°C) | Precipitation (mm) |
|---|---|---|---|---|---|
| Hamheung | 39.93°N | 127.55°E | 13 | 9.8 | 890.3 |
| Anju | 39.62°N | 125.65°E | 125 | 9.2 | 1072.0 |
| Kimchaek | 40.67°N | 129.20°E | 540 | 8.4 | 700.0 |
| Tsetserleg | 47.45°N | 101.47°E | 1695 | 0.5 | 336.0 |
| Darkhan | 49.47°N | 105.98°E | 709 | −0.6 | 309.0 |
| Sainshand | 44.90°N | 110.12°E | 915 | 4.0 | 119.0 |
| Dalanzadgad | 43.58°N | 104.42°E | 1469 | 4.6 | 127.0 |
| Khovd | 48.02°N | 91.65°E | 1405 | 0.3 | 119.0 |
| Murun | 49.63°N | 100.17°E | 1288 | −1.3 | 207.0 |
| Darwin | 12.46°S | 131.05°E | 34 | 27.4 | 1694 |
| Giles | 25.03°S | 128.30°E | 598 | 22.7 | 291.7 |
| Perth | 31.88°S | 116.13°E | 25 | 18.7 | 807.0 |
| Brisbane | 27.48°S | 153.04°E | 8 | 20.3 | 1168.0 |
| Adelaide | 34.87°S | 138.87°E | 48 | 16.4 | 536.0 |
| Melbourne | 37.88°S | 145.04°E | 49 | 14.8 | 666.0 |

chosen among all current MODIS items given by NASA as it incorporates air and dew point temperatures. The MOD07 provides instantaneous geophysical variables such as latitude, longitude, dew point and air temperatures, surface pressure, solar zenith angle, and brightness temperature and total perceptible water vapor with moderate resolution [13, 14]. Together with these geophysical variables, air and dew point temperatures were considered a part of this study. The MODIS cloud product (MOD06) was used for calculation of radiation under cloudy sky conditions. The cloud parameters including cloud fraction, cloud top temperature, and cloud optical thickness with 1 km spatial determination and cloud emissivity with 5 km spatial resolution [15] were used in this study. The sinusoidal projection was implemented to the land products to peruse various needs for major discipline groups: Korean Peninsula placed on horizontal tile numbers 27 to 28 and vertical tile numbers 4 to 5 (H27V04, H27V05, H28V04, and H28V05) in the sinusoidal projection. In the case of Mongolia, the HDF tiles are H23V03, H23V04, H24V03, H24V04, H25V03, H25V04, H26V03, and H26V04. For Australia, the HDF tiles are H27V12, H28V11, H28V12, H29V10, H29V11, H29V12, H30V10, H30V11, H30V12, H31V10, H31V11, and H31V12. The MOD13A2 provides NDVI and the Enhanced Vegetation Index (EVI) at a temporal resolution of 16 days and spatial resolution of 1 km [16], and the MOD15A2 provides Leaf Area Index (LAI) and the Fraction of Photosynthetically Active Radiation (fPAR) for every 8 days. The MOD17A2 provides vegetation information at 1 km spatial resolution in every 8-day intervals through gross primary productivity (GPP) and net primary productivity (NPP) products. Hemispherical reflectance (white sky albedo) and bihemispherical reflectance (black sky albedo) were offered by the MOD43 albedo product. Reflected solar radiation was estimated by using the shortwave infrared band (10th band) of the white sky albedo from the MCD43B3 albedo product [17].

For estimation of SPI, the climatological ground measurement data were obtained from the weather stations. Because SPI is calculated from more than 30 years of data, we have chosen a location that provides over 30 years of precipitation data in Korean Peninsula, Australia, and Mongolia (12 sites from Mongolia: http://worldweather.wmo.int/en/country.html?countryCode=MNG; 32 sites from Australia: http://www.bom.gov.au/climate/data/stations/; 60 sites from Korean Peninsula: http://www.kma.go.kr/weather/climate/past_cal.jsp). The streamflow data were obtained from Global Land Data Assimilation System (GLDAS) for drought status validation [18]. The GLDAS Noah dataset having 25 km spatial resolution and 1-month estimated data were used as the ground basis observation for validation purposes.

## 3. Methodology

In this study, the following four drought indices were estimated and compared: EWDI, ESI, SPI-3, and VCI. Since selected drought indices have different data ranges, they were normalized for more intuitive comparison with EWDI. Following sections briefly describe the four drought indices.

*3.1. Evaporative Stress Index (ESI).* ESI is calculated by using AET-PET ratios denoted by $f_{\mathrm{PET}}$:

$$f_{\mathrm{PET}} = \frac{\mathrm{AET}}{\mathrm{PET}}. \tag{1}$$

A well-known Priestley–Taylor algorithm (Priestley and Taylor, 1972) was used for calculations of potential evapotranspiration (PET). For PET calculation, all hydrometeorological data were derived from satellite observations. We modified the algorithm of Cleugh et al. [19] and Mu et al. [17] which estimates AET based on the following Penman–Monteith equation [20]:

$$\lambda E = \frac{\Delta\left(R_{\mathrm{N}} - G\right) + \left(\rho C_{\mathrm{p}}\left(e_{\mathrm{sat}} - e\right)\right)/r_{\mathrm{a}}}{\Delta + \gamma\left(\left(1 + r_{\mathrm{s}}\right)/r_{\mathrm{a}}\right)}, \tag{2}$$

where $\lambda E$ is the latent heat flux ($\mathrm{W{\cdot}m^{-2}}$), $\lambda$ is the latent heat of vaporization ($\mathrm{J{\cdot}kg^{-1}}$), $\Delta$ is the slope of the curve relating the saturated water vapor pressure to temperature ($\mathrm{kPa{\cdot}K^{-1}}$), $R_{\mathrm{N}}$ is the net radiation flux ($\mathrm{W{\cdot}m^{-2}}$), $G$ is the soil heat flux ($\mathrm{W{\cdot}m^{-2}}$), $\rho$ is the air density ($\mathrm{kg{\cdot}m^{-3}}$), $C_{\mathrm{P}}$ is the

specific heat capacity of air ($J \cdot kg^{-1} \cdot K^{-1}$), $e_{sat}$ is the saturated water vapor pressure (Pa), $e$ is the actual water vapor pressure (Pa), $r_a$ is the aerodynamic resistance ($s \cdot m^{-1}$), $\gamma$ is the psychrometric constant and is set as a constant with a value of 0.66 Pa $K^{-1}$, and $r_s$ is the surface resistance ($s \cdot m^{-1}$).

All required parameters of equation (2) were obtained from satellite observations using the algorithms of Cleugh et al. [19] and Mu et al. [17]. In this study, the only difference was EVI instead of NDVI because the EVI might enhance the accuracy of the estimated AET value [17]. This study enhanced the accuracy of the AET estimation by introducing the gross primary productivity (GPP) values for the estimation of the surface resistance ($r_s$). The GPP can be derived from the MOD17 product, and it is known to precisely reflect the impact of photosynthesis which EVI and NDVI cannot reflect [21]. To enhance the accuracy of the algorithm, this study revised the equation for calculating the vegetation cover fraction by the following equation:

$$F_{cc_i} = \frac{1}{2}\left[\frac{EVI_i - EVI_{min}}{EVI_{max} - EVI_{min}} + \frac{GPP_i - GPP_{min}}{GPP_{max} - GPP_{min}}\right], \quad (3)$$

where $F_{cc_i}$ stands for the $i$th day's vegetation cover fraction and the subscripts max and min symbolize the maximum and minimum value of all GPP and EVI values attained for all observation periods.

This calculated value of vegetation cover fraction is subsequently used as the input of the set of equations [8] to estimate the surface resistance value ($r_s$) to be used in equation (2). Figure 2 shows the comparison among the AET values estimated based on the method of this study ($y$) to the reference flux tower ET value ($x$) at Cheongmicheon (CFC) and Seolmacheon (SMC) gages located in Korean Peninsula. The AET value based on the method of Mu et al. [17] is shown for comparison. It can be noted that the method of this study has greater accuracy compared to the method of Mu et al. [17] in terms of correlation coefficient (Figure 2).

Lastly, the Evaporative Stress Index (ESI) is obtained by normalizing the estimated $f_{PET}$ value:

$$ESI = \frac{f_{PET} - \mu_{f_{PET}}}{\sigma_{f_{PET}}}, \quad (4)$$

where $\mu_{f_{PET}}$ and $\sigma_{f_{PET}}$ represent the mean and the standard deviation of all $f_{PET}$ values estimated for the entire study period at a given grid cell location.

*3.2. Energy-Based Water Deficit Index (EWDI).* The water status of the land surface under different conditions can be estimated by considering the EWDI which represents the water deficit condition. Based on apparent thermal inertia (ATI), the EWDI was corporated using the ESI and Soil Moisture Saturation Index (SMSI). The ATI evaluates the spatiotemporal variability of soil moisture and is derived directly from multispectral satellite imageries [22].

Using the differences in land surface temperature ($\Delta LST$) and land surface albedo, the ATI is calculated as follows:

$$ATI = \frac{1 - \alpha}{\Delta LST},$$
$$Z(ATI)_{i,j} = SMSI = \frac{ATI_{i,j} - ATI_{min}}{ATI_{max} - ATI_{min}}, \quad (5)$$

where $\alpha$ represents the land surface albedo and $\Delta LST$ is the diurnal land surface temperature, which is the difference of temperature between the daytime and nighttime. Since the ATI represents the sum of canopy and soil moisture variability, the higher the value, the higher the soil water content of the land surface [22, 23]. ATI values are normalized by using SMSI for the purpose of calculating EWDI. $ATI_{i,j}$ represents the ATI value at the $i$th latitude and $j$th longitude.

After calculation of the EWDI, the ESI and SMSI terms are differences in the standardized anomaly:

$$EWDI_{i,j} = Z\left(ESI_{i,j} + SMSI_{i,j}\right)_{i,j}, \quad (6)$$

where the EWDI is a dimensionless index ranging from infinite negative values (drier than normal) to infinite positive values (wetter than normal). Surface albedo products (MCD43B3) in 8 days were used in this study. Leaf Area Index (MOD15A2), NDVI and EVI (from the MOD13A2 product), and atmospheric products (MOD07_L2 atmosphere product) were used for calculating EWDI.

*3.3. Standardized Precipitation Index (SPI).* The SPI was established by McKee et al. [24]. The SPI is assessed by using the monthly average precipitation dataset, for a continuous period of at least 30 years. Because SPI is calculated from more than 30 years of data, we have chosen a location that provides over 30 years of monthly precipitation data. The SPI uses monthly precipitation aggregated at various time scales (1 month, 3 months, 6 months, 12 months, etc.). In general, gamma fitting function is applied for each dataset to describe probability interactions. The distinction of the SPI is that it does not depend upon the model. A straightforward valuation of precipitation is the input, disparate with the PDSI, which makes assumptions about water storage and deficit.

*3.4. Vegetation Condition Index (VCI).* The Vegetation Condition Index (VCI hereafter) [1] is the most widely used satellite-based drought index to monitor vegetation conditions. VCI is determined based on the Normalized Difference Vegetation Index (NDVI) which assesses live green vegetation for the observed target. VCI is determined using the following equation:

$$VCI = Z\left[\frac{NDVI - NDVI_{min}}{NDVI_{max} - NDVI_{min}}\right], \quad (7)$$

where NDVI, $NDVI_{min}$, and $NDVI_{max}$ are the smoothed monthly normalized difference vegetation index at a given grid cell location, its multiyear maximum, and its multiyear minimum, respectively, and $Z$ is the meaning of standardized normalization. Since the VCI is an index value which normalizes the value varying between 0 and 1,

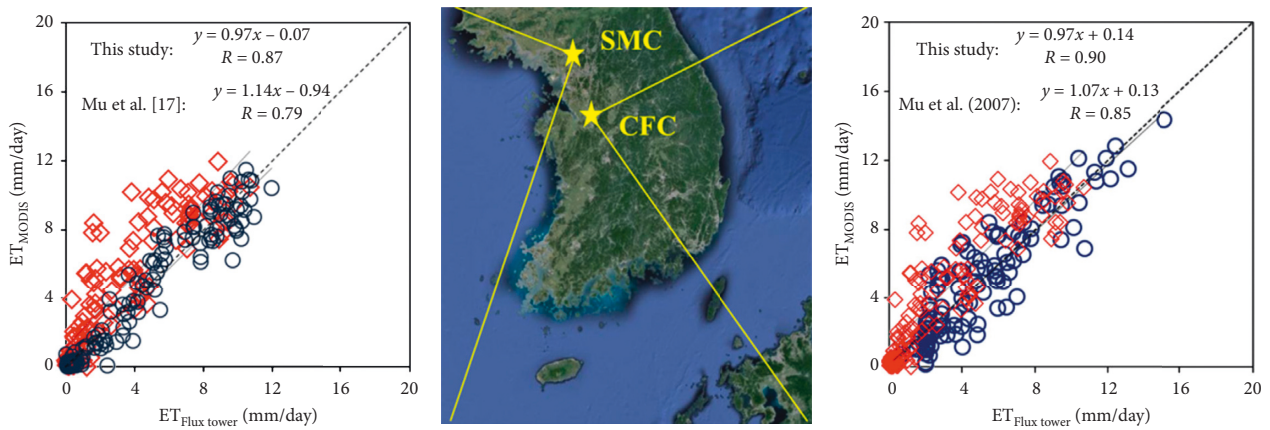


Figure 2: Comparison of the actual evapotranspiration estimated by the method of this study.

Table 2: Error matrix result for Korean Peninsula (Hamheung site) during 2001–2010.

| Hamheung | Streamflow | | Sum | Drought accuracy (%) | Overall accuracy (%) |
|---|---|---|---|---|---|
| | Drought | No drought | | | |
| Moderate drought ($Streamflow_{lower\ quartile}$ = 0.03137 cfs) | | | | | |
| ESI | | | | | |
| Drought | 54 | 4 | 58 | 54/58 = 93.10 | 110/120 = 91.67 |
| No drought | 6 | 56 | 62 | | |
| Sum | 60 | 60 | 120 | | |
| EWDI | | | | | |
| Drought | 54 | 3 | 57 | 54/57 = 94.74 | 113/120 = 94.17 |
| No drought | 4 | 59 | 63 | | |
| Sum | 58 | 62 | 120 | | |
| SPI-3 | | | | | |
| Drought | 45 | 7 | 52 | 45/52 = 86.54 | 100/120 = 83.33 |
| No drought | 13 | 55 | 68 | | |
| Sum | 58 | 62 | 120 | | |
| VCI | | | | | |
| Drought | 35 | 18 | 53 | 35/53 = 66.04 | 85/120 = 70.83 |
| No drought | 17 | 50 | 67 | | |
| Sum | 52 | 68 | 120 | | |

Table 3: Error matrix result for Australia (Brisbane site) during 2001–2010.

| Brisbane | Streamflow | | Sum | Drought accuracy (%) | Overall accuracy (%) |
|---|---|---|---|---|---|
| | Drought | No drought | | | |
| Moderate drought ($Streamflow_{lower\ quartile}$ = 0.04784 cfs) | | | | | |
| ESI | | | | | |
| Drought | 45 | 7 | 52 | 45/52 = 86.54 | 100/120 = 83.33 |
| No drought | 13 | 55 | 68 | | |
| Sum | 58 | 62 | 120 | | |
| EWDI | | | | | |
| Drought | 54 | 3 | 57 | 54/57 = 94.74 | 113/120 = 94.17 |
| No drought | 4 | 59 | 63 | | |
| Sum | 58 | 62 | 120 | | |
| SPI-3 | | | | | |
| Drought | 39 | 17 | 56 | 39/56 = 69.64 | 84/120 = 70.00 |
| No drought | 19 | 45 | 64 | | |
| Sum | 58 | 62 | 120 | | |
| VCI | | | | | |
| Drought | 29 | 28 | 57 | 29/57 = 50.88 | 91/120 = 75.83 |
| No drought | 1 | 62 | 63 | | |
| Sum | 30 | 90 | 120 | | |

Table 4: Error matrix result for Mongolia (Tsetserleg site) during 2001–2010.

| Tsetserleg | Streamflow | | Sum | Drought accuracy (%) | Overall accuracy (%) |
|---|---|---|---|---|---|
| | Drought | No drought | | | |
| Moderate drought ($Streamflow_{lower\ quartile}$ = 0.04314 cfs) | | | | | |
| ESI | | | | | |
| Drought | 45 | 7 | 52 | 45/52 = 86.54 | 100/120 = 83.33 |
| No drought | 13 | 55 | 68 | | |
| Sum | 58 | 62 | 120 | | |
| EWDI | | | | | |
| Drought | 54 | 3 | 57 | 54/57 = 94.74 | 113/120 = 94.17 |
| No drought | 4 | 59 | 63 | | |
| Sum | 58 | 62 | 120 | | |
| SPI-3 | | | | | |
| Drought | 39 | 17 | 56 | 39/56 = 69.64 | 84/120 = 70.00 |
| No drought | 19 | 45 | 64 | | |
| Sum | 58 | 62 | 120 | | |
| VCI | | | | | |
| Drought | 17 | 33 | 50 | 17/50 = 34.00 | 74/120 = 61.67 |
| No drought | 13 | 57 | 70 | | |
| Sum | 30 | 90 | 120 | | |

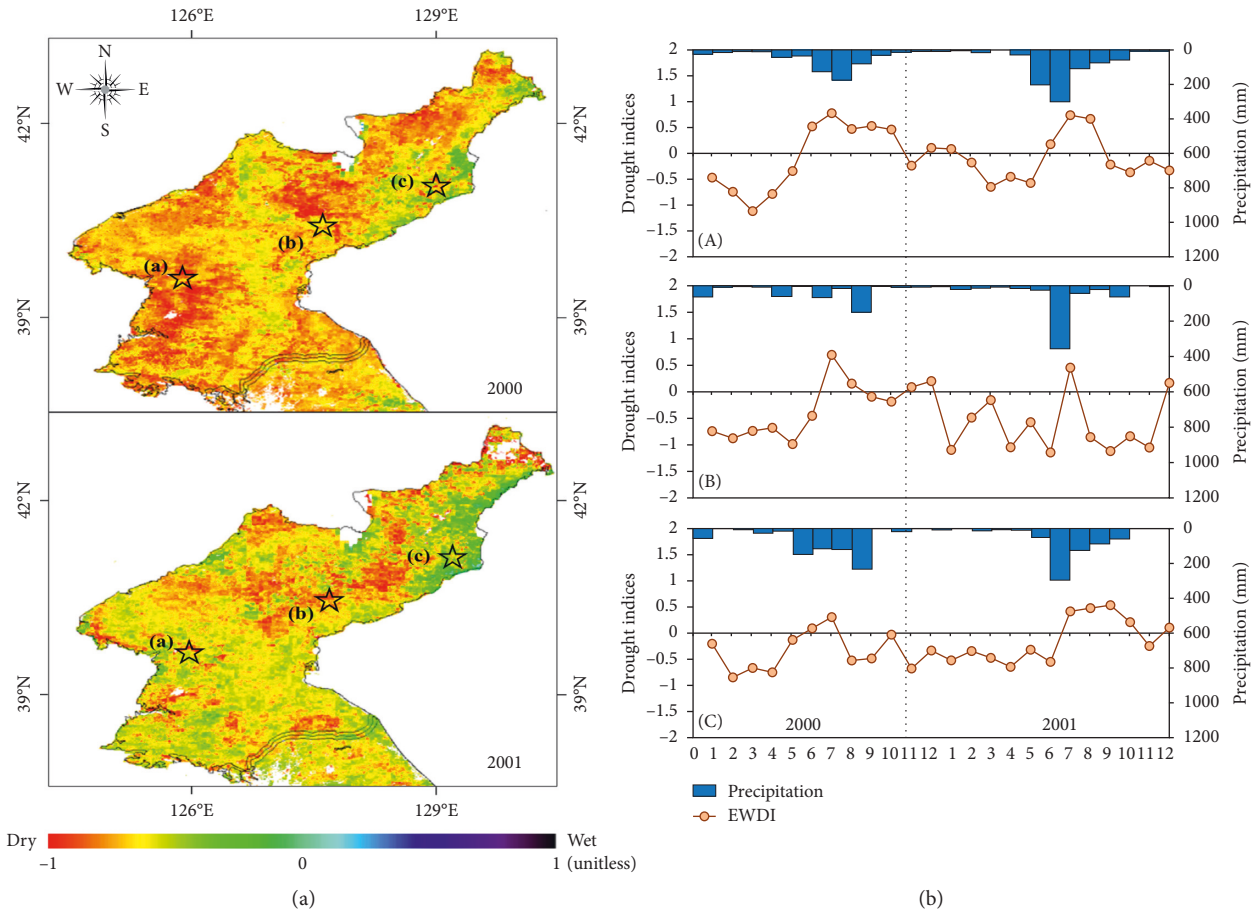


(a) (b)

Figure 3: (a) Spatial distributions of EWDI for 2000 and 2001 in North Korea; (b) temporal distributions of EWDI and precipitation in the (A) Anju, (B) Hamheung, and (C) Kimchaek sites.

approximately 95 percent of the VCI at a given grid cell location varies from −2 (harsh drought) to 2 (healthy vegetation condition).

*3.5. Error Matrix Method.* To correctly detect the drought event and severity, numerous drought indices were evaluated using an error matrix method [25, 26]. An error

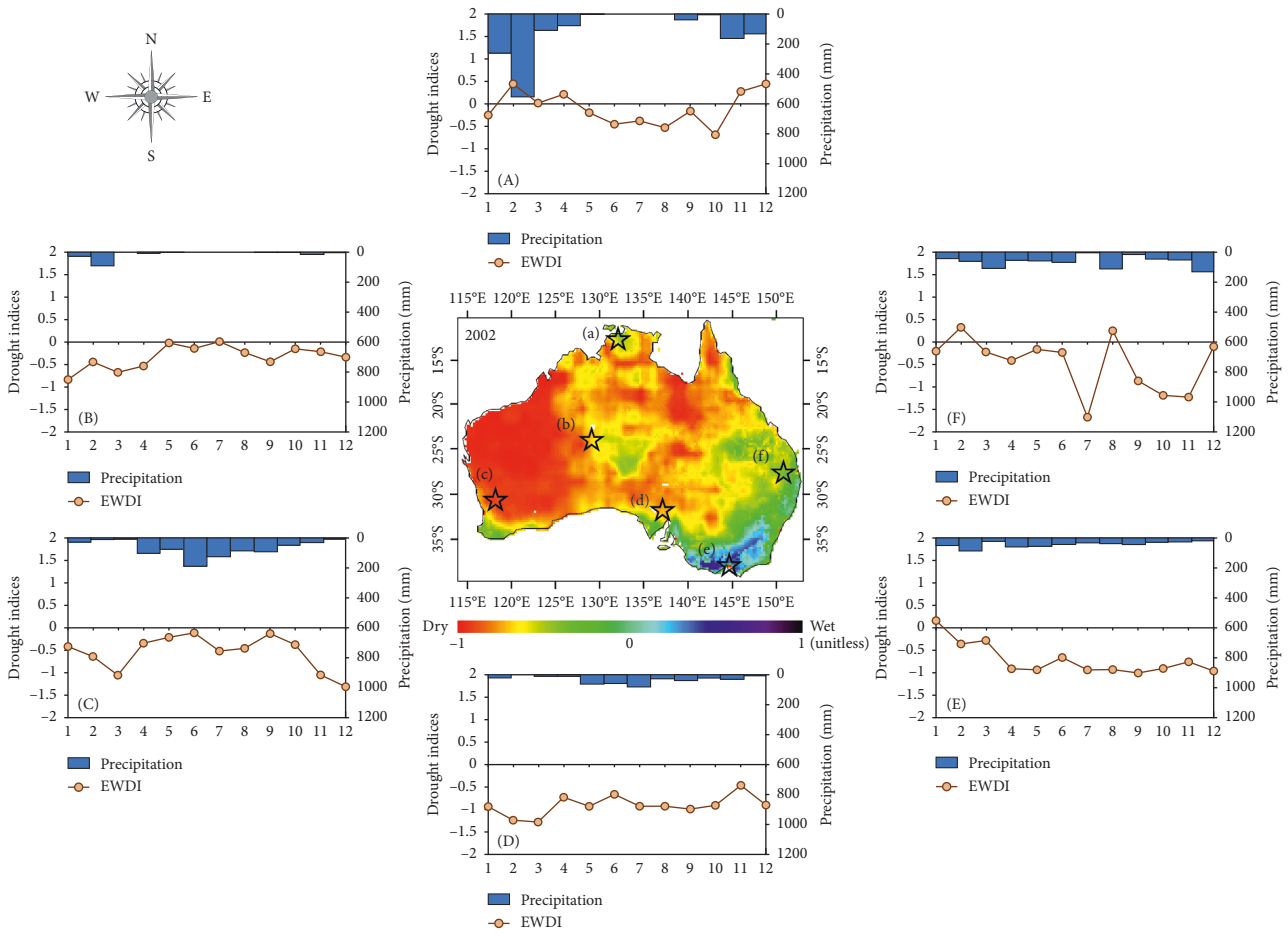


Figure 4: Spatial distributions of EWDI for 2002 in Australia (central part); temporal distributions of EWDI and precipitation in the (A) Darwin, (B) Giles, (C) Perth, (D) Adelaide, (E) Melbourne, and (F) Brisbane sites (external parts).

matrix method is a formed array that consists of drought or wet condition as compared to the category of drought suggested by the observation data such as streamflow and soil moisture. When the value of the standardized streamflow is less than 0, it is defined as a drought status. The fallouts of matrix are represented to obtain the accuracy of drought, and the accuracy of drought is the ratio of all observation datasets that are certificated as drought by both the index and the observation datasets to the total number of drought statuses.

## 4. Results and Discussions

*4.1. Analysis of Drought Accuracy Using Error Matrix Method.* Error matrix derived from GLDAS streamflow dataset in Tables 24 showed overall accuracy from 75 to 92%, with approximately 90% accuracy during dry season. This result indicates that all four drought indices (EWDI, ESI, VCI, and SPI-3) have a good degree of reliability for analyzing the drought status at each site. The applicability of the EWDI was best compared to that of another drought index under drought conditions. For streamflow, the EWDI and ESI had markedly better results than did the VCI and SPI-3, with drought and overall accuracies ranging between 75% and 90% at every study site. The patterns of SPI-3 were relatively slow because it related to the precipitation variation.

These intercomparison fallouts prove the applicability of the satellite-based drought indices and the impact of drought on streamflow [25]. However, some limitations may exist. As noted by Karnieli et al. [27] and Choi et al. [25], the vegetation-based drought indices such as the VCI and Evapotranspiration-Based Drought Index (ESI) might be less appropriate for the time and the places where drought conditions cannot be fully represented by vegetation conditions such as dormant season and the area with high latitudes and elevations. For the aforementioned results, the EWDI precisely predicts the drought status, compared to the SPI-3. The EWDI, ESI, VCI, and SPI-3 were good indices of extreme drought status.

*4.2. Spatiotemporal Patterns of Various Drought Indices.* In Section 4.2, the spatiotemporal patterns of EWDI and actual drought situations were compared. In the case of North Korea, several previous studies have reported that there has been a serious drought situation from February to May in 2000 and from March to June in 2001, respectively [28–30]. Jang et al. [28] examined the cases of drought

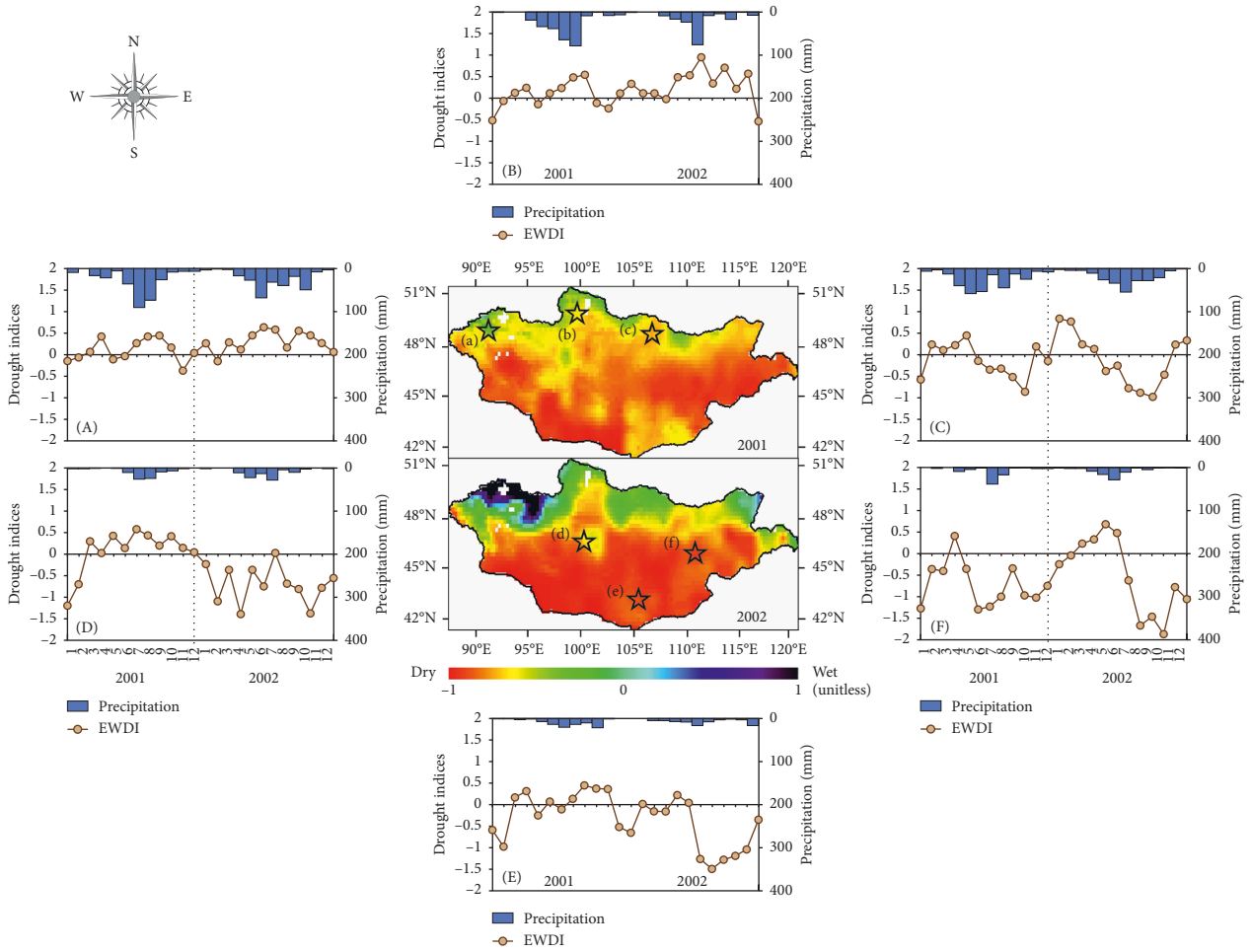


FIGURE 5: Spatial distributions of EWDI for 2001 and 2002 in Mongolia (central part); temporal distributions of EWDI and precipitation in the (A) Khovd, (B) Murun, (C) Darkhan, (D) Tsetserleg, (E) Dalanzadgad, and (F) Sainshand sites (external parts).

damage in North Korea from 2000 to 2001 and showed the spatial distribution of drought damage regions. Nam et al. [30] reported that severe drought conditions occurred in the western part of North Korea in 2000 and in the eastern part of North Korea in 2001.

Figure 3 represents the annual mean spatial distributions of EWDI for 2000 and 2001 in North Korea. It also shows the temporal distribution of EWDI and precipitation in the Anju, Hamheung, and Kimchaek sites.

Comparing the results of this study with those of previous studies, it can be seen that a more severe drought condition occurred during 2000 than 2001 at Anju, which is located in the western part of North Korea. On the contrary, in Kimchaek and Hamheung areas located in the eastern part of the country, a more severe drought occurred in 2001 than in 2000. The main reason of this phenomenon can be explained by the lack of precipitation. In 2000, the amount of precipitation in the western region was 20% of that in the normal year, while in 2001, precipitation in the eastern region was only 17% lower than that in the normal year. For this reason, the spatial distribution of drought was shown differently by year [30].

In the case of Australia, Horridge et al. [31] reported that there has been a serious drought situation from April to December 2002. Horridge et al. [31] showed the cases of drought damage in Australia in 2002 and reported the spatial distribution of drought damage regions.

Figure 4 represents the annual mean spatial distributions of EWDI for 2002 in Australia. It also shows the temporal distribution of EWDI and precipitation in the Darwin, Giles, Perth, Adelaide, Melbourne, and Brisbane sites. Among the six validation sites, Perth had the lowest annual average precipitation of 688 mm in 2002, which was 32% lower than that in the normal year [31]. The value of the drought index for that period indicated the drought status. In the case of the Darwin site, there was an extreme drought situation from April to August, but there was a lot of precipitation during the rest of the year. For this reason, the annual average drought condition was expressed moderately (Figure 4).

Finally, in the case of Mongolia, several previous researches have reported that there has been a serious drought situation from February to October 2001 and from March to December 2002, respectively [32, 33]. Bayarjargal et al. [32] examined the cases of drought damage in Mongolia in 2001 and 2002. They reported that the overall drought condition was serious in 2001, but in 2002, there was extreme drought condition in the southern region.

Davi et al. [33] showed the spatial distribution of drought condition regions.

Figure 5 represents the annual mean spatial distributions of EWDI for 2001 and 2002 in Mongolia. It also shows the temporal distributions of EWDI and precipitation in the Khovd, Murun, Darkhan, Tsetserleg, Dalanzadgad, and Sainshand sites. Among the six validation sites, the Dalanzadgad site had the lowest annual average precipitation of 95 mm in 2001 and 76 mm in 2002, which were 58% lower than that in the normal year [32]. The value of the drought index for that period also indicated the drought status. In the case of the Khovd and Murun sites, there were extreme drought situations from February to April, but there was a lot of precipitation during the rest of the year. For this reason, the annual average drought condition was expressed moderately (Figure 5).

## 5. Conclusions

In this study, conventional and satellite-based drought indices were compared over drought-vulnerable sites (Korean Peninsula, Mongolia, and Australia) from 2000 to 2010. The EWDI showed the highest drought accuracy through the error matrix method (drought accuracy ranged from 85.71 to 94.74%; Hamheung in North Korea, Brisbane in Australia, and Tsetserleg in Mongolia: 94.74%).

The applicability of the EWDI was determined by comparing the estimated EWDI with actual drought conditions. The results of the EWDI and the spatiotemporal distribution of the actual drought situation showed a similar tendency. In the case of North Korea, there has been a serious drought situation from February to May in 2000 and from March to June in 2001, respectively. More severe drought condition occurred during 2000 than 2001 at the Anju region, which is located in the western part of North Korea. On the one hand, in Kimchaek and Hamheung areas located in the eastern part of the country, a more severe drought occurred in 2001 than in 2000. In the case of Australia, there has been a serious drought situation from April to December 2002. The most severe droughts in Perth were examined because the precipitation was only about 32% lower than that in the normal year. On the other hand, Darwin was relatively less drought prone due to heavy rainfall during the summer season (from September to March). Finally, in the case of Mongolia, there has been a serious drought situation from February to October 2001 and from March to December 2002, respectively. During the drought period, the most serious droughts occurred in the Dalanzadgad region and the less severe drought conditions in the Khovd and Murun regions.

Through the above-mentioned results, the applicability of EWDI was good compared to that of the other drought indices. Based on the results, RS-based indices were identified as good indicators for detecting the drought status especially when climate data were not available or were sparsely distributed.

## Data Availability

The data used to support the findings of this study are available from the corresponding author upon request.

## Conflicts of Interest

The authors declare that they have no conflicts of interest.

## Acknowledgments

This research was supported by Basic Science Research Program through the National Research Foundation of Korea (NRF) funded by the Ministry of Science, ICT and Future Planning (2018R1C1B6008805) and the Ministry of Education, Science and Technology (Project No. NRF-2017R1C1B2003927).

## References

[1] F. N. Kogan, "Droughts of the late 1980s in the United States as derived from NOAA polar-orbiting satellite data," *Bulletin of the American Meteorological Society*, vol. 76, no. 5, pp. 655–668, 1995.

[2] F. N. Kogan, "Global drought watch from space," *Bulletin of the American Meteorological Society*, vol. 78, no. 4, pp. 621–636, 1997.

[3] M. C. Anderson, J. Norman, J. Mecikalski, J. Otkin, and W. P. Kustas, "A climatological study of evapotranspiration and moisture stress across the continental United States based on thermal remote sensing: 1. Model formulation," *Journal of Geophysical Research: Atmospheres*, vol. 112, no. 10, 2007.

[4] M. C. Anderson, J. Norman, J. Mecikalski, J. Otkin, and W. P. Kustas, "A climatological study of evapotranspiration and moisture stress across the continental United States based on thermal remote sensing. 2. Surface moisture climatology," *Journal of Geophysical Research*, vol. 112, no. 11, 2007.

[5] M. C. Anderson, C. Hain, B. Wardlow, A. Pimstein, J. R. Mecikalski, and W. P. Kustas, "Evaluation of drought indices based on thermal remote sensing of evapotranspiration over the continental United States," *Journal of Climate*, vol. 24, no. 8, pp. 2025–2044, 2011.

[6] Q. Mu, M. Zhao, J. S. Kimball, N. G. McDowell, and S. W. Running, "A remotely sensed global terrestrial drought severity index," *Bulletin of the American Meteorological Society*, vol. 94, no. 1, pp. 83–98, 2013.

[7] M. R. Keshavarz, M. Vazifedoust, and A. Alizadeh, "Drought monitoring using a soil wetness deficit index (SWDI) derived from MODIS satellite data," *Agricultural Water Management*, vol. 132, pp. 37–45, 2014.

[8] C. Sur, J. Hur, K. Kim, W. Choi, and M. Choi, "An evaluation of satellite-based drought indices on a regional scale," *International Journal of Remote Sensing*, vol. 36, no. 22, pp. 5593–5612, 2015.

[9] P. Batima, *Climate Change Vulnerability and Adaptation in the Livestock Sector of Mongolia: A Final Report Submitted Assessments of Impacts and Adaptations to Climate Change (AIACC)*, The International Start Secretariat, Washington, DC, USA, 2006.

[10] T. Sato, F. Kimura, and A. Kitoh, "Projection of global warming onto regional precipitation over Mongolia using a regional climate model," *Journal of Hydrology*, vol. 333, no. 1, pp. 144–154, 2007.

[11] K. Hwang, M. Choi, S. O. Lee, and J.-W. Seo, "Estimation of instantaneous and daily net radiation from MODIS data under clear sky conditions: a case study in East Asia," *Irrigation Science*, vol. 31, pp. 1173–1184, 2013.

[12] B. Tang and Z. Li, "Estimation of instantaneous net surface longwave radiation from MODIS cloud-free data," *Remote Sensing of Environment*, vol. 112, no. 9, pp. 3482–3492, 2008.
[13] W. P. Menzel, S. W. Seemann, J. Li, and L. E. Gumley, *MODIS Atmospheric Profile Retrieval Algorithm Theoretical Basis Document (MOD07)*, University of Winconsin-Madison Press, Madison, WI, USA, 2002.
[14] S. W. Seemann, J. Li, W. P. Menzel, and L. E. Gumley, "Operational retrieval of atmospheric temperature, moisture, and ozone from MODIS infrared radiances," in *Journal of Applied Meteorology*, vol. 42, pp. 1072–1091, 2003.
[15] G. Bisht and R. L. Bras, "Estimation of net radiation from the MODIS data under all sky conditions: southern great plains case study," *Remote Sensing of Environment*, vol. 114, pp. 1522–1534, 2010.
[16] A. R. Huete, K. Didan, T. Miura, E. P. Rodriguez, X. Gao, and L. G. Ferreira, "Overview of the radiometric and biophysical performance of the MODIS vegetation indices," *Remote Sensing of Environment*, vol. 83, no. 1-2, pp. 195–213, 2002.
[17] Q. Mu, F. A. Heinsch, M. Zhao, and S. W. Running, "Development of a global evapotranspiration algorithm based on MODIS and global meteorology data," *Remote Sensing of Environment*, vol. 111, no. 4, pp. 519–536, 2007.
[18] M. Rodell, P. R. Houser, U. Jambor et al., "The global land data assimilation system," *Bulletin of the American Meteorological Society*, vol. 85, no. 3, pp. 381–394, 2004.
[19] H. A. Cleugh, R. Leuning, Q. Mu, and S. W. Running, "Regional evaporation estimates from flux tower and MODIS satellite data," *Remote Sensing of Environment*, vol. 106, no. 3, pp. 285–304, 2007.
[20] J. L. Monteith, "Evaporation and environment," *Symposia of the Society for Experimental Biology*, vol. 19, pp. 205–234, 1965.
[21] W. Yuan, S. Liu, G. Yu et al., "Global estimates of evapotranspiration and gross primary production based on MODIS and global meteorology data," *Remote Sensing of Environment*, vol. 114, no. 7, pp. 1416–1431, 2010.
[22] W. W. Verstraeten, F. Veroustraete, C. J. van der Sande, I. Grootaers, and J. Feyen, "Soil moisture retrieval using thermal inertia, determined with visible and thermal spaceborne data, validated for European forests," *Remote Sensing of Environment*, vol. 101, no. 3, pp. 299–314, 2006.
[23] T. Y. Chang, Y. C. Wang, C. C. Feng, A. D. Ziegler, T. W. Giambelluca, and Y. A. Liou, "Estimation of root zone soil moisture using apparent thermal inertia with MODIS imagery over a tropical catchment in Northern Thailand," *IEEE Journal of Selected Topics in Applied Earth Observations and Remote Sensing*, vol. 5, no. 3, pp. 752–761, 2012.
[24] T. B. McKee, N. J. Doesken, and J. Kleist, "The relationship of drought frequency and duration to time scales," in *Proceedings of the Preprints of the 8th Conference on Applied Climatology*, vol. 17–22, pp. 179–184, Anaheim, CA, USA, January 1993.
[25] M. Choi, J. M. Jacobs, M. C. Anderson, and D. D. Bosch, "Evaluation of drought indices via remotely sensed data with hydrological variables," *Journal of Hydrology*, vol. 476, pp. 265–273, 2013.
[26] R. G. Congalton, "A review of assessing the accuracy of classifications of remotely sensed data," *Remote Sensing of Environment*, vol. 37, no. 1, pp. 35–46, 1991.
[27] A. Karnieli, N. Agam, and R. T. Pinker, "Use of NDVI and land surface temperature for drought assessment: merits and limitations," *Journal of Climate*, vol. 23, no. 3, pp. 618–633, 2010.
[28] M. W. Jang, S. H. Yoo, and J. Y. Choi, "Analysis of spring drought using NOAA/AVHRR NDVI for North Korea," *Journal of the Korean Society of Agricultural Engineers*, vol. 49, no. 6, pp. 21–33, 2007.
[29] S. U. Kang and J. W. Moon, "Drought analysis using SC-PDSI and derivation of drought severity-duration-frequency curves in North Korea," *Journal of Korea Water Resources Association*, vol. 47, no. 9, pp. 813–824, 2014.
[30] W. H. Nam, S. H. Yoo, M. W. Jang, and J. Y. Choi, "Application of meteorological drought indices for North Korea," *Journal of the Korean Society of Agricultural Engineers*, vol. 50, no. 3, pp. 3–15, 2008.
[31] M. Horridge, J. Madden, and G. Wittwer, "Using a highly disaggregated multi-regional single-country model to analyse the impacts of the 2002-03 drought on Australia," *Journal of Policy Modelling*, vol. 27, pp. 285–308, 2005.
[32] A. Bayarjargal, A. Karnieli, M. Bayasgalan, S. Khudulmur, C. Gandusha, and T. J. Tucker, "A comparative study of NOAA–AVHRR derived drought indices using change vector analysis," *Remote Sensing of Environment*, vol. 105, no. 1, pp. 9–22, 2006.
[33] N. K. Davi, G. C. Jacoby, R. D. D'Arrigo, N. Baatarbileg, L. Jinbao, and A. E. Curtis, "A tree-ring-based drought index reconstruction for far-Western Mongolia: 1565–2004," *International Journal of Climatology*, vol. 29, no. 10, pp. 1508–1514, 2009.

Hindawi
Advances in Meteorology
Volume 2019, Article ID 8413964, 18 pages
https://doi.org/10.1155/2019/8413964

*Research Article*

# Using CHIRPS Dataset to Assess Wet and Dry Conditions along the Semiarid Central-Western Argentina

**Juan A. Rivera**,[1,2] **Sofía Hinrichs**,[2] **and Georgina Marianetti**[2]

[1]*Instituto Argentino de Nivología, Glaciología y Ciencias Ambientales (CCT-Mendoza/CONICET), Mendoza 5500, Argentina*
[2]*Facultad de Ciencias Veterinarias y Ambientales, Universidad Juan Agustín Maza, Mendoza 5519, Argentina*

Correspondence should be addressed to Juan A. Rivera; jrivera@mendoza-conicet.gob.ar

Received 16 December 2018; Revised 5 March 2019; Accepted 13 March 2019; Published 4 April 2019

Guest Editor: Minha Choi



The Climate Hazards group Infrared Precipitation with Stations (CHIRPS) dataset was conceived as a tool for monitoring drought and environmental change over land. Recent validation efforts along South America have assessed its suitability for reproducing the main spatial and temporal features of precipitation. Nevertheless, little has been done regarding the ability of CHIRPS for the assessment of wet and dry conditions, particularly in areas where in situ precipitation records are scarce. In this paper, we investigated the performance of CHIRPS for monitoring wet and dry events along the semiarid Central-Western Argentina. Using the Standardized Precipitation Index (SPI), we compared the CHIRPS database with records from 49 meteorological stations along the study area for the period 1987–2016. Results indicate that the CHIRPS dataset adequately reproduced the temporal variability of SPI on multiple timescales (1 month, 3 months, and 6 months), particularly in the region dominated by warm season precipitation. The large overestimation of the seasonal precipitation in the region dominated by cold season precipitation can introduce errors that are reflected in the performance of CHIRPS over the western portion of the domain. The frequency of wet and dry classes was accurately reproduced by CHIRPS on timescales larger than 1 month (SPI1), given the existence of a wet bias that produces an underestimation of the frequency of zero values. This bias is further translated to the evaluation of the SPI1 during the spatial and temporal assessment of historical dry (1998) and wet (2016) events, especially for the classification of extreme dry/wet months. The results from the evaluation indicate that CHIRPS is a suitable tool for assessing dry and wet conditions for timescales longer than 1 month and can support decision-making process within the hydrometeorological agencies over the region.

## 1. Introduction

A wide range of satellite-derived precipitation products have emerged in the last decades, providing a spatial coverage that is superior to gauge products, considering that rain gauges had the obvious queries such as the density of site networks, the continuous time series, and the financial limitation [1]. Some of these products are the Precipitation Estimation from Remotely Sensed Information using Artificial Neural Networks (PERSIANN) [2], the Climate Prediction Center Morphing (CMORPH) technique [3], the Global Satellite Mapping of Precipitation (GSMaP) [4], the TRMM Multi-satellite Precipitation Analysis (TMPA) 3B42RT [5], and the Multisource Weighted-Ensemble Precipitation (MSWEP) [6]. A comprehensive overview of these products can be found in Beck et al.'s studies [7].

To satisfy the demand of studies and applications of climate and drought, some of these satellite-based estimations provide long-term precipitation records. Some of the products with the most extense records are the MSWEP [6], the PERSIANN-CDR [8], and the Climate Hazards Group Infrared Precipitation with Stations (CHIRPS) data archive [9]. The CHIRPS database comprises a quasi-global (50°S-50°N, 180°E-180°W), 0.05° resolution, and 1981 to near-present gridded precipitation time series. This dataset merges three types of information: global climatology, satellite estimates, and in situ observations [10], generating several precipitation products with time steps from 6-hourly to 3-monthly aggregates.

This database was mainly used for the assessment of monthly, seasonal, and annual precipitation variability in several regions of the world. Monthly CHIRPS estimations

were applied for drought monitoring in Nepal [11], Chile [12], and China [1]. The research of López-Carr et al. [13] used 3-month accumulations to identify changes in the growing season precipitation patterns over Africa. Trends in CHIRPS annual rainfall estimations were compared with gridded gauge-only precipitation datasets and climate models simulations from the CMIP5 dataset [14]. The daily version of CHIRPS also gained attention recently. Examples of its use can be found in the detection of trends of extreme precipitation indices [15], the assessment of the relation between weather regimes and wet/dry conditions along East Africa [16], and the evaluation of the evolution of dry-day frequency and its impacts on Amazonian seasonal rainfall [17].

The performance of these satellite-based products needs to be evaluated over different regions of the world in order to identify retrieval errors and biases [18]. The Central-Western Argentina (CWA) is a region where the interplay between the complex topography and the atmospheric circulation determines a wide range of precipitation features, from intense winter orographic precipitation [19], extreme summer precipitation events leading to the occurrence of landslides along the Andes range [20], and hailstorms over the lowlands [21] to multiannual severe drought events [22, 23]. Considering these multiple characteristics over the CWA, the lack of ground observations makes mandatory the use of high-resolution satellite-based precipitation products in order to provide a better understanding of precipitation variability and change. A recent study performed the validation of CHIRPS for a 30-year period along the CWA, analysing the representation of the main climatological features of precipitation [24]. The CHIRPS dataset captured the rainy season characteristics over the region, considering the Mediterranean climate features over the Andes ranges and the monsoonal regime in the lowlands. Moreover, CHIRPS achieved better results in the region with summer precipitation maximum, given that precipitation was largely overestimated during the cold semester maximum. In view of this performance, the CHIRPS database was used for the assessment of a glacier collapse over the Central Andes of Argentina in a region with scarce meteorological information [25]. The CHIRPS estimations also gained attention as input for climate monitoring tools. Six countries in southern South America have established the World Meteorological Organization Regional Climate Center (RCC-SSA) that involves a strong collaboration between weather services and academic institutions [26]. The RCC-SSA periodically generates CHIRPS precipitation estimates maps on pentadal and monthly time steps, providing relevant information for decision-making needed for agricultural activities and water management purposes.

Besides the efforts for the use of the CHIRPS database as a tool for regional precipitation monitoring, few validation studies evaluated its suitability for the assessment of dry and wet conditions. Guo et al. [27] found that CHIRPS can properly capture the drought characteristics at various timescales with the best performance at the three-month timescale. Zambrano et al. [12] concluded that, in order to use the CHIRPS dataset to monitor drought intensity conditions, the product should be calibrated to adjust for the overestimation/underestimation of rainfall geographically. Recently, Gao et al. [1] and Zhong et al. [28] indicated that CHIRPS successfully captured the spatial patterns of drought over China. These studies also show that wet conditions are not focus of assessment, which could be attributed to the design of CHIRPS for agricultural drought monitoring [9]. Nevertheless, over the study area, the occurrence of wet conditions affects the farming and particularly the quality of the grapes, which require plenty of solar radiation to achieve sufficient quality for wine production [29]. Moreover, during wet conditions, the probabilities for the occurrence of deep convection episodes during the warm season increases, which strongly affects the cultivated areas over the CWA, causing big damages and economic losses, particularly during hailstorms over the vineyards [30]. These factors make the assessment of both dry and wet conditions mandatory over the study area.

The objective of this study is to assess the suitability of CHIRPS precipitation estimations for the representation of wet and dry periods in the CWA. For this assessment, the Standardized Precipitation Index (SPI) [31] was selected as an indicator for the definition of wet and dry conditions. The SPI will be calculated based on rain gauges observations and CHIRPS estimations considering several timescales. The performance of CHIRPS will be evaluated through a comparison of the spatiotemporal characteristics of wet and dry events over the study area over the last 30 years. This assessment is being conducted in a region where observed precipitation is at low spatial density, the information from rain gauges is not always available, and time series are often interrupted, facts that highlight the crucial nature of validating satellite precipitation estimations for extreme precipitation monitoring. It is expected that the outcomes of this study will constitute a significant contribution for the improvement of regional monitoring of wet and dry conditions.

## 2. Materials and Methods

*2.1. Study Area.* The CWA is a semiarid region located leeward of the Andes ranges, between 30°S and 40°S (Figure 1). This area is characterized by a strong influence of topography on the regional and local climate. The climate at high elevations has a Mediterranean regime with higher precipitations during the cold season (April to September) and dry warm seasons (October to March), in response to the seasonal displacement of the Southeastern Pacific High [32]. North of 35°S, the Andes is a considerable topographic barrier with peaks exceeding 6000 m.a.s.l., preventing the wet Pacific air masses arriving at the eastern slopes [33]. Due to the strong rain shadow effect, climate in the east of the Andes is arid to semiarid, where convective warm season rainfalls favored by moist air masses from the Amazon and Atlantic basins play a relevant role [34]. South of 35°S, precipitation is mainly generated by the passage of cold fronts moving eastward from the Pacific [35], with a strong west-east precipitation gradient.

The agroindustrial activities in CWA depend largely on grape production, an activity only possible through

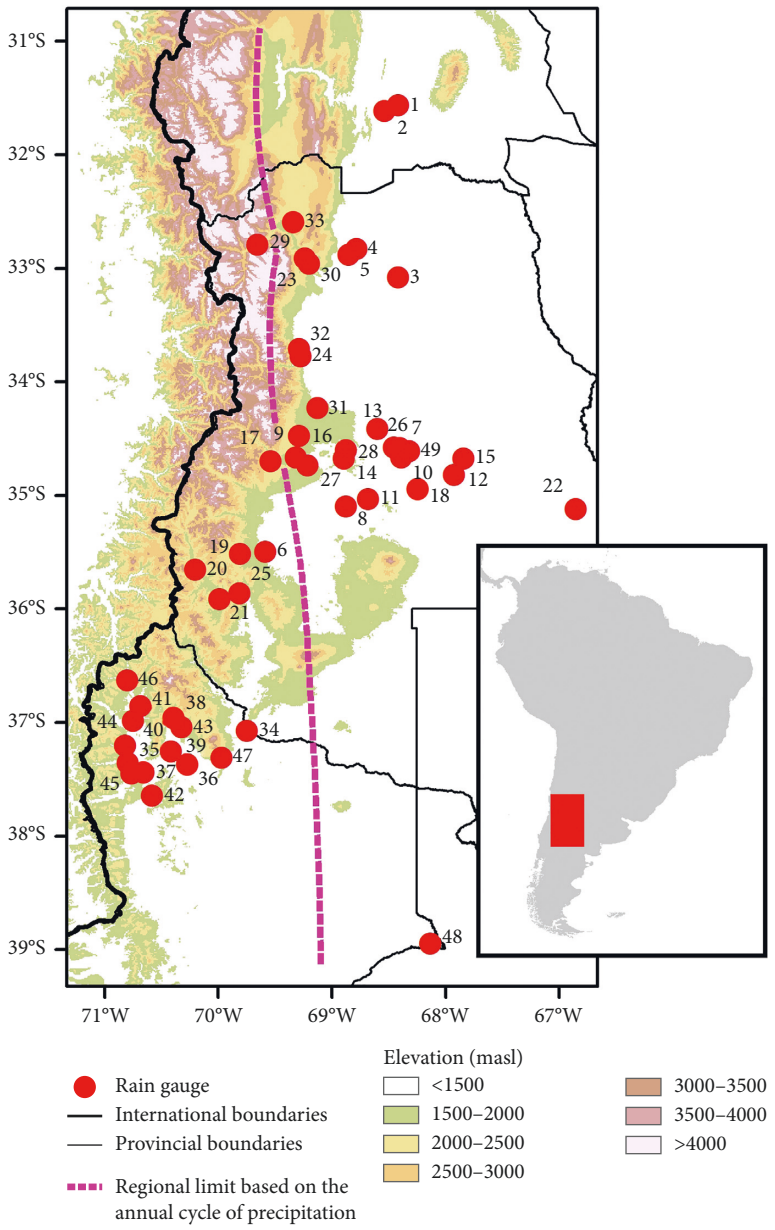


Figure 1: Map of the Central-Western Argentina, with the location and ID (see Table 1 for details) of the rain gauges used for the validation of CHIRPS. The dashed line represents the division between the rainy season characteristics: the stations located west of the line are dominated by winter precipitation, while the stations located east of the line are dominated by summer precipitation.

irrigation, considering the arid to semiarid climate of the region. The interannual rainfall variability over this region has been partially related to El Niño-Southern Oscillation (ENSO), with El Niño events providing large precipitation (both snow and rainfall) amounts and La Niña events accounting for drought situations [22, 36].

*2.2. Data.* Monthly precipitation data from 49 hydrometeorological stations located along the CWA were obtained through the Water Resources Agency of Argentina and the National Weather Service. The location of these rain gauges is shown in Figure 1, and the detailed information of each station can be found in Table 1. This database was built for the assessment performed by Rivera et al. [24], including quality control procedures and the detection of inhomogeneities. A common period of 30 years, between 1987 and 2016, was selected based on the availability and quality of precipitation records and the spatial representativeness of the stations. Missing precipitation values, ranging from 1 to 27 nonconsecutive months, were replaced by applying linear regressions with neighbouring stations, only for reference stations that explain >80% ($R^2 > 0.8$) of the temporal variability of precipitation. The behaviour of precipitation over the study area was shown to be homogeneous both over the region dominated by summer precipitation [22, 29] and the region dominated by winter precipitation [33]. This was further verified with the use of rotated principal components

Table 1: Geographic and climatic features of the selected meteorological stations over the period 1987–2016.

| ID | Name | Lat. (°S) | Lon. (°W) | Mean annual precipitation (mm) | Wet season |
|---|---|---|---|---|---|
| 1 | San Juan | 31.57 | 68.42 | 98.2 | Summer |
| 2 | San Juan INTA | 31.62 | 68.53 | 99.7 | Summer |
| 3 | San Martín | 33.08 | 68.42 | 253.7 | Summer |
| 4 | Mendoza Aero | 32.83 | 68.78 | 236.3 | Summer |
| 5 | Mendoza Observatorio | 32.88 | 68.85 | 261.6 | Summer |
| 6 | Malargüe | 35.50 | 69.58 | 327.8 | Winter |
| 7 | San Rafael | 34.58 | 68.40 | 360.6 | Summer |
| 8 | La Angostura | 35.09 | 68.87 | 256.5 | Summer |
| 9 | La Jaula | 34.67 | 69.32 | 252.3 | Summer |
| 10 | Rama Caída | 34.67 | 68.38 | 347.5 | Summer |
| 11 | El Nihuil | 35.03 | 68.67 | 268.4 | Summer |
| 12 | Villa Atuel | 34.82 | 67.92 | 335.5 | Summer |
| 13 | Capitán Montoya | 34.58 | 68.45 | 361.5 | Summer |
| 14 | Puesto Canales | 34.67 | 68.89 | 293.0 | Summer |
| 15 | Puesto Carmona | 34.68 | 67.84 | 541.5 | Summer |
| 16 | Arroyo Hondo | 34.48 | 69.28 | 287.1 | Summer |
| 17 | Las Aucas | 34.70 | 69.54 | 253.3 | Winter |
| 18 | Las Malvinas | 34.94 | 68.24 | 278.4 | Summer |
| 19 | Los Mayines | 35.66 | 70.20 | 458.8 | Winter |
| 20 | Bardas Blancas | 35.87 | 69.81 | 379.4 | Winter |
| 21 | Arroyo La Vaina | 35.92 | 69.99 | 356.9 | Winter |
| 22 | Puesto Las Moras | 35.12 | 66.85 | 516.3 | Summer |
| 23 | Guido | 32.92 | 69.24 | 223.3 | Summer |
| 24 | Valle de Uco | 33.78 | 69.27 | 472.0 | Summer |
| 25 | Pincheira | 35.52 | 69.81 | 360.9 | Winter |
| 26 | Las Vertientes | 34.42 | 68.59 | 400.4 | Summer |
| 27 | Juncalito | 34.74 | 69.21 | 338.4 | Summer |
| 28 | Puesto Morales | 34.60 | 68.87 | 313.4 | Summer |
| 29 | Polvaredas | 32.79 | 69.65 | 178.6 | Winter |
| 30 | Potrerillos | 32.96 | 69.20 | 240.1 | Summer |
| 31 | Puesto Papagayos | 34.23 | 69.12 | 321.4 | Summer |
| 32 | La Remonta | 33.71 | 69.29 | 531.6 | Summer |
| 33 | Uspallata | 32.59 | 69.34 | 147.6 | Summer |
| 34 | Buta Ranquil | 37.07 | 69.75 | 184.3 | Winter |
| 35 | El Cholar | 37.44 | 70.65 | 525.0 | Winter |
| 36 | Chos Malal | 37.37 | 70.27 | 217.6 | Winter |
| 37 | Vilu Mallín | 37.46 | 70.76 | 481.5 | Winter |
| 38 | Cajón Curileuvú | 36.96 | 70.39 | 476.7 | Winter |
| 39 | El Alamito | 37.26 | 70.42 | 247.6 | Winter |
| 40 | Las Ovejas | 36.98 | 70.75 | 718.0 | Winter |
| 41 | Varvarco | 36.86 | 70.68 | 627.0 | Winter |
| 42 | El Huecu | 37.65 | 70.58 | 432.9 | Winter |
| 43 | Tricao Malal | 37.04 | 70.32 | 366.5 | Winter |
| 44 | Los Miches | 37.21 | 70.82 | 607.8 | Winter |
| 45 | Chochoy Mallín | 37.36 | 70.79 | 516.0 | Winter |
| 46 | Pichi Neuquén | 36.63 | 70.80 | 778.5 | Winter |
| 47 | Auquinco | 37.32 | 69.97 | 336.3 | Winter |
| 48 | Neuquén | 38.95 | 68.13 | 204.9 | Summer |
| 49 | San Rafael | 34.61 | 68.32 | 439.1 | Summer |

analysis (RPCA) [37] applied in the S-mode with varimax rotation (not shown), a methodology that allowed to obtain the regional separation observed in Figure 1 after assigning each station to the component upon which it loads most highly [38]. Moreover, time series of regional precipitation are significantly uncorrelated [39], highlighting the presence of different water vapor sources over the region that are dependent of the season of the year. Even when every gap filling routine introduces errors to the precipitation estimation, we assume that the strong homogeneity within the regions guarantees an adequate estimation of the real precipitation totals.

The spatial pattern of mean annual precipitation shows the semiarid condition of the study area, with values ranging from less than 150 mm/year north of 32°S to over 700 mm/year between 37° and 39°S, at the high elevations of the continental divide (Figure 2, Table 1). A narrow region along the central-east portion of the Mendoza province (approximately from 34° to 35°S) exhibits a relative maximum of precipitation, with values higher than 400 mm/year. South of

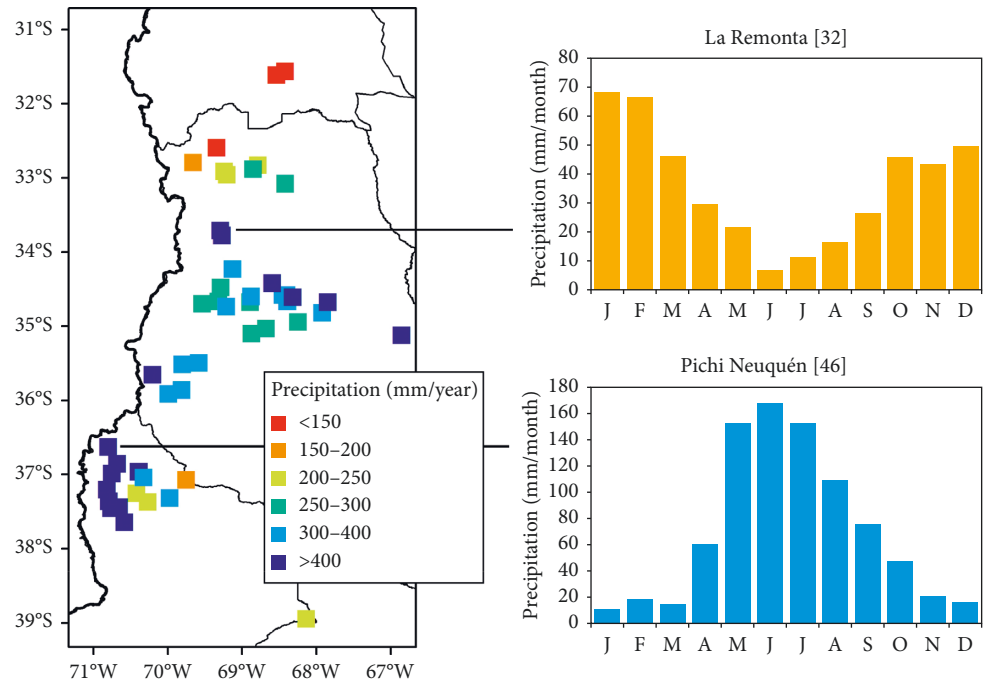


Figure 2: Spatial distribution of the mean annual precipitation over the study area, together with the annual precipitation cycle at two reference stations.

36°S, there is a strong precipitation gradient from west to east due to the rain shadow effect of the Andes (Figure 2). The clear distinct seasonality in precipitation over the CWA is illustrated for two selected locations (Figure 2). The annual cycle of precipitation in La Remonta shows a monsoonal regime, dominated by convective warm season rainfalls associated with the southward movement of the South American low-level jet (SALLJ) from northern Argentina [40] and the moisture transport from the southeast of Brazil and Uruguay or even directly from the Atlantic Ocean [41]. Conversely, the annual cycle in Pichi Neuquén shows a Mediterranean regime, with higher precipitation during the cold season associated with a strong water vapor transport from the Pacific Ocean in the pre-cold-front environment of extratropical cyclones [19, 42].

Gridded monthly precipitation estimates from the CHIRPS, developed at the University of California at Santa Barbara (UCSB) Climate Hazards Group (CHG) in collaboration to the U.S. Geological Survey (USGS) Earth Resources Observation and Science (EROS) center, were used to identify its accuracy reproducing extreme precipitation events along the CWA. Data from 1987 to 2016 were obtained through the CHG web page (http://chg.geog.ucsb.edu/data/chirps/index.html). As described by Funk et al. [9], the CHIRPS algorithm (i) is built around a 0.05° climatology that incorporates satellite information to represent sparsely gauged locations, (ii) incorporates monthly 1981-present 0.05° infrared cold cloud duration-based precipitation estimates, (iii) blends station data to produce a preliminary information product with a latency of about 2 days after the end of a pentad and a final product with an average latency of about 3 weeks, and (iv) uses a novel blending procedure incorporating the spatial correlation structure of infrared cold cloud duration estimates to assign interpolation weights. This dataset was found to reproduce adequately several characteristics of precipitation over South America [12, 17, 43] and particularly over the CWA, showing a good agreement for the representation of the seasonal and interannual variability of precipitation and its spatial patterns [24].

## 3. Methods

In order to identify the occurrence of dry and wet events, we used the SPI, a widely accepted index as a universal tool for drought monitoring and assessment. Based on a comparison among six precipitation-based drought indices, the SPI was selected as the most adequate for analysing meteorological droughts along southern South America [44]. For the calculation of the SPI, time series of 1-month, 3-month, and 6-month accumulations were generated and fitted to a two-parameter gamma distribution function, following previous recommendations for the study area [22] and in other regions [12, 13, 27]. Finally, an equiprobability transformation from the cumulative density functions to the standard normal distribution with the mean of 0 and the variance of 1 were performed to obtain the SPI. Therefore, the values of the SPI are expressed in standard deviations, with positive SPI values indicating greater than median precipitation and negative values indicating less than median precipitation. Three dry and wet categories and a normal category can be defined based on the SPI values, as shown in Table 2, following the classification of Lloyd-Hughes and Saunders [45]. As mentioned in the introduction, at the present time, monitoring of wet and dry events has been performed by the RCC-SSA using CHIRPS for the calculation of SPI for

Table 2: Standardized Precipitation Index (SPI) categories.

| Index value | Category |
|---|---|
| ≥2.00 | Extremely wet |
| 1.50 to 1.99 | Severely wet |
| 1.00 to 1.49 | Moderately wet |
| −0.99 to 0.99 | Normal |
| −1.49 to −1.00 | Moderately dry |
| −1.99 to −1.50 | Severely dry |
| ≤−2.00 | Extremely dry |

timescales of 3 and 6 months (http://www.crc-sas.org/en/monitoreo_precipitacion_chirps.php).

The 30-year period selected for this study provides rain gauges and CHIRPS records that are long enough for an accurate estimation of the SPI values, as recommended by the World Meteorological Organization [46]. For the comparison between the SPI based on rain gauge observations and CHIRPS estimations, we used the Pearson correlation coefficient and the mean absolute error. The correlation coefficient measures the linear relationship strength between the satellite estimations and the rain gauges observations, bounded by −1 and 1 with an optimal value of 1. The mean absolute error provides information on the average magnitude of error estimations, considering both systematic and random errors [24].

## 4. Results

*4.1. Regional Behaviour of SPI Based on CHIRPS and Rain Gauges.* For the comparison of the SPI based on the CHIRPS database and rain gauges data, the study area was divided according to the main regional features of the annual precipitation cycle: a region dominated by warm season (WS) precipitation, with a monsoonal regime associated with convective rainfalls over the lowlands and a relatively dry cold season; and a region dominated by cold season (CS) precipitation, with a Mediterranean regime close to the higher elevations of the Andes (see Figure 1). The time series of SPI at timescales of 1 month, 3 months, and 6 months for the WS and CS regions are shown in Figures 3 and 4, respectively.

The temporal evolution of the SPI based on CHIRPS estimations shows a good agreement with rain gauge observations, capturing the occurrence of the main dry and wet periods and its severity in both regions. For the WS region (Figure 3), the correlation coefficient between the SPI is higher than 0.8 ($p < 0.01$) for the three timescales considered, while this value ranges between 0.74 and 0.77 ($p < 0.01$) for the CS region. In line with the results obtained considering the correlation coefficients, the mean absolute error is slightly larger for the CS region (between 0.53 and 0.57) compared to the WS region (between 0.47 and 0.48).

The extremely wet period recorded between 2015 and 2016 along the WS region was well captured in timing by CHIRPS, although with an overestimation of its intensity in all the timescales (Figure 3). On the other hand, CHIRPS estimations detected the maximum severity period of the extreme drought between 2003 and 2004 along the WS region, although the intensity was underestimated compared to the observations. This behaviour is similar to the observed during the dry period of 2005-2006 (Figure 3).

For the CS region, the occurrence of wet periods recorded between 2000 and 2003 is represented by CHIRPS estimations, particularly for SPI3 and SPI6, with an overestimation of its severity (Figure 4). CHIRPS-SPI captured the dry periods of 1989, 1995–1997, and the extreme drought of 1998-1999, with a good agreement with the observed SPI. The extreme drought of 1999 affected the hydropower generation over Patagonia due to hydrological drought conditions that were also recorded over CWA [47]. The onset of this drought event was well identified by CHIRPS estimations and also the timing and severity of the maximum drought intensity (Figure 4). Nevertheless, the drought demise estimated by CHIRPS was anticipated by several months when compared with rain gauges-SPI (February 1999 versus September 1999). This condition could be attributed to a large overestimation of precipitation over the CS region compared with rain gauge data [24].

The observed difference in the agreement between CHIRPS-SPI and rain gauges-SPI over WS and CS regions can be associated with the large overestimation of monthly precipitation estimated from CHIRPS over the CS region (Figure 5). This result can be further attributed to the overestimations for the months of April to September, especially in zones above 1000 m.a.s.l. [24]. Monthly precipitation from CHIRPS over the WS region shows a slight underestimation and, thus, a better agreement between rain gauges-SPI and CHIRPS-SPI over the WS region.

*4.2. SPI Classification for Wet and Dry Categories.* Given that the SPI values fit a standard normal distribution, these values lie within one standard deviation at approximately 68% of the time, within two standard deviations 95% of the time and within three standard deviations 98% of the time [48]. In this sense, it is expected that approximately 16% of the months (~58 months) would be classified as dry (wet) months, given that this value corresponds to the probability of SPI ≤ −1.0 (SPI ≥ 1.0). In order to evaluate this requirement, we calculated the number of months with dry and wet conditions for each rain gauge and its corresponding CHIRPS pixel. Figure 6 shows the box plots for the number of months with dry and wet conditions for the SPI1, SPI3, and SPI6. The most relevant difference between rain gauge-SPI and CHIRPS-SPI classes is found for the timescale of 1 month considering dry conditions. In most of the rain gauges, the SPI values tend to underestimate the expected number of dry months. This can be related to the presence of zero values, given the arid and semiarid characteristics of the study area and its marked seasonal precipitation cycle. When a high frequency of zero values occurs, SPI tends to be nonnormally distributed, with a lower bound in the SPI time series at short timescales [49], thus failing to indicate drought occurrences. This is not observed considering CHIRPS estimations, given that this product tends to underestimate the occurrence of zero values. To illustrate this, Figure 7 shows the number of months with zero values for each rain gauge and CHIRPS

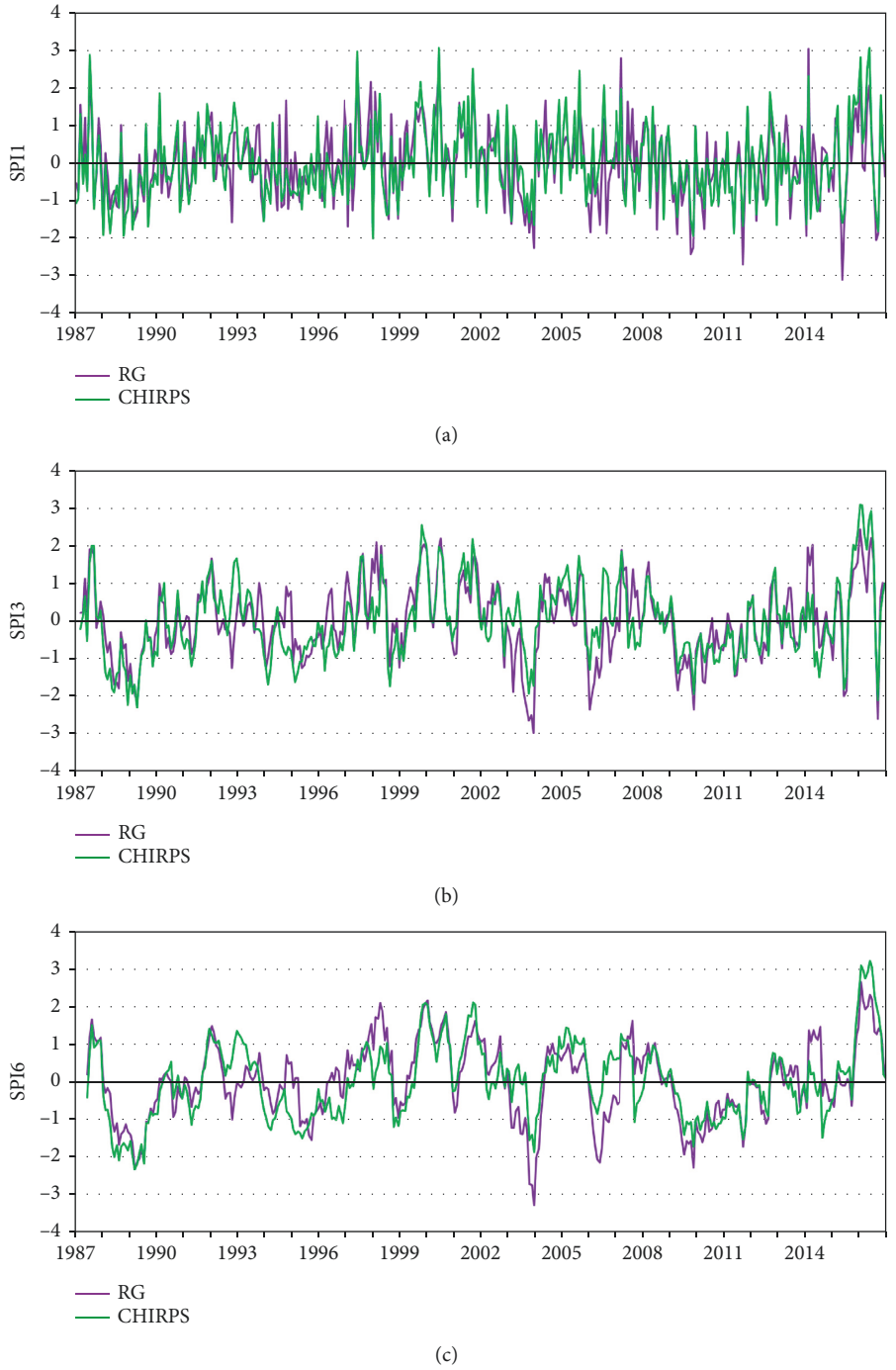


Figure 3: SPI time series for the WS region based on CHIRPS and rain gauges (RG) during 1987–2016: (a) SPI1, (b) SPI3, and (c) SPI6.

pixel. The differences observed in the SPI1D between rain gauges and CHIRPS can be attributed mainly to the underestimations over the CS region, although all the CWA exhibit the same underestimation pattern by CHIRPS. The lack of zero values can arise from the screening procedure developed to remove "false zeros" in the CHIRPS estimations [50], a bias previously reported by Zambrano et al. and Katsanos et al. [12, 51].

Regarding the remaining timescales and wet and dry categories, CHIRPS estimates and precipitation from rain gauges show a similar behaviour, although with larger regional dispersion considering the SPI6 (Figure 6). It must be noted that, for most of the timescales and SPI categories, the median number of months is slightly larger than the expected probabilistic value, a condition previously documented considering the SPI based on the two-parameter gamma distribution [52].

Temporal evolution of the number of pixels/rain gauges affected by dry conditions based on CHIRPS estimations.

From a vulnerability point of view, the situations when a great portion of the study area is under dry or wet conditions must be considered. In this sense, for each month from

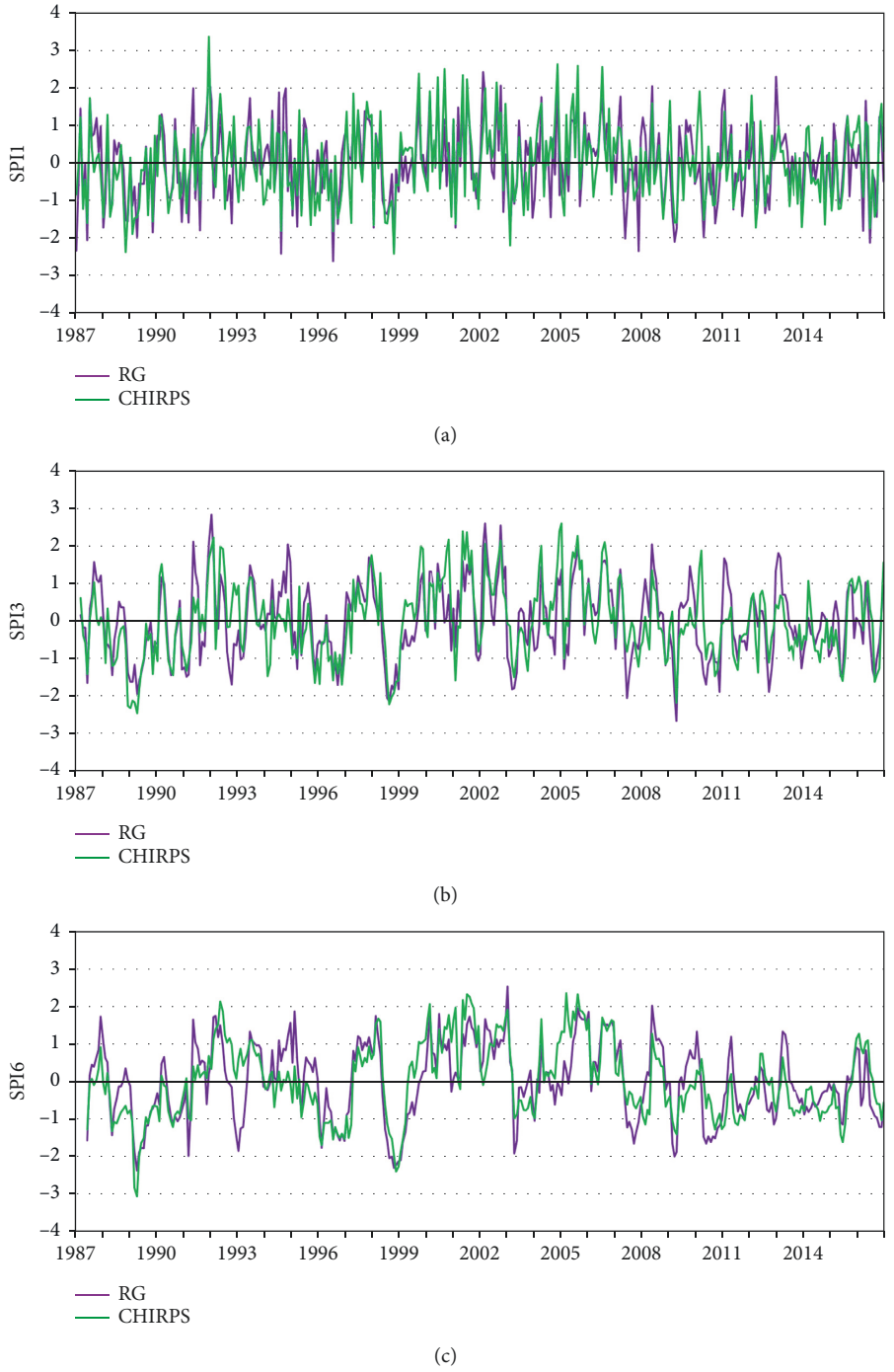


Figure 4: SPI time series for the CS region based on CHIRPS and rain gauges (RG) during 1987–2016: (a) SPI1, (b) SPI3, and (c) SPI6.

January 1987 to December 2016, we obtained the number of pixels with dry conditions. Figure 8 shows the temporal evolution of this regional index for the SPI1, SPI3, and SPI6 and the moderately (yellow), severely (orange), and extremely (vermillion) dry categories (see Table 2). According to CHIRPS estimations, the CWA experienced large-scale dry conditions particularly during the periods 1988-1989 and 1998-1999 (Figure 8). As the timescale for the calculation of the SPI increases, the high-frequency temporal variability in the time series decreases, allowing a better identification of the main dry periods considering the SPI6.

We repeated the procedure considering the time series of SPI based on rain gauges observations. This allowed calculating the difference between the CHIRPS and rain gauges areal estimations of dry conditions. The temporal evolution of this difference, for each timescale and dry category, is shown in Figure 8. Positive values indicate that CHIRPS is overestimating the number of pixels/rain gauges

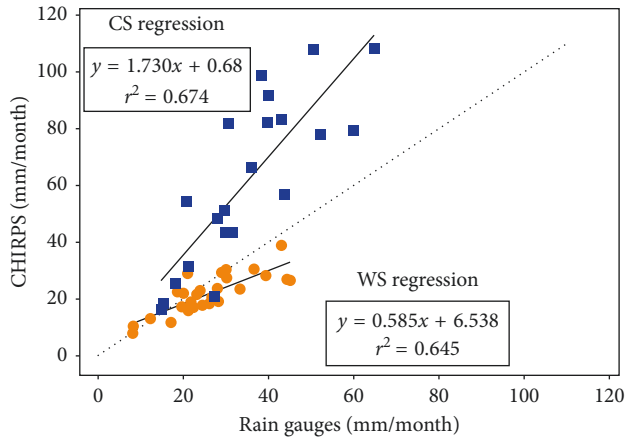


Figure 5: Scatter plot comparing the 49 rain gauge data with the corresponding grids of CHIRPS estimations in mm/month over the 1987–2016 period. Circles indicate the values of the stations located over the WS region, and squares indicate the values of the stations located over the CS region. The black lines indicate the linear regression fits. The dashed line represents a 1 : 1 relation.

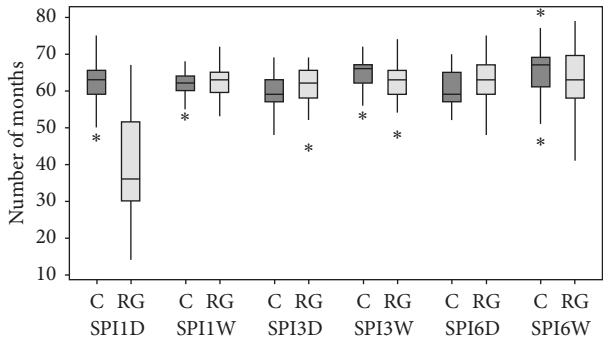


Figure 6: Boxplot of the number of months with dry and wet conditions (SPInD and SPInW, respectively, with $n = 1$-month, 3-month, and 6-month timescale) for the SPI based on CHIRPS estimations (C) and rain gauges (RG) observations. Dry months were defined when SPI $\leq -1.0$, and wet months were defined when SPI $\geq 1.0$. Each boxplot shows the median and first and third quartiles, while the whiskers extend to the data values that are 1.5 times the interquartile range above or below the quartiles. Outliers are represented by*.

with dry conditions, while negative values show an underestimation. Considering the SPI1, during most of the 1987–2016 period, the time series based on CHIRPS precipitation show an overestimation of the dry affected area. This is particularly evident during the large-scale dry periods identified in Figure 8. The result is in line with the observed bias in the number of months with dry conditions (Figure 6), suggesting that the SPI1 based on CHIRPS estimations is not adequate for meteorological drought monitoring over arid and semiarid regions. Similar temporal evolution is observed considering the differences between CHIRPS and rain gauges for SPI3 and SPI6, with large areal overestimation during 1988-1989 and a clear underestimation during 2003, particularly for the extremely dry category (Figure 9).

The monthly sum of simultaneously affected stations enables the identification of the large events and their durations, but does not show the regional patterns of meteorological drought and its severity [47]. Figure 10 shows a comparison of the spatial extension of the dry conditions recorded during October 1998 based on rain gauges and CHIRPS-SPI for the three timescales selected. As expected based on previous results, CHIRPS shows a large overestimation of the dry conditions considering SPI1, with a large number of pixels under severely dry and extremely dry category in comparison with the rain gauges-SPI1. Considering the spatial patterns based on SPI3 and SPI6, CHIRPS estimations accurately reproduce the observed dry conditions, both in location and intensity (Figure 10).

Temporal evolution of the number of pixels/rain gauges affected by wet conditions is based on CHIRPS estimations.

Following the assessment performed on the previous section, we repeated the methodology to analyse the areal patterns corresponding to wet conditions. Figure 11 shows the temporal evolution of the number of pixels/rain gauges affected by wet conditions considering the SPI1, SPI3, and SPI6 and the moderately (light blue), severely (blue), and extremely (dark blue) wet categories (see Table 2). A large fraction of the CWA was affected by wet periods based on CHIRPS estimations during 1999–2003, 2005–2008, and 2016. This is particularly evident considering the CHIRPS-based SPI6 (Figure 11). It is remarkable the large number of pixels affected by extremely wet conditions during 2016, a result that can be attributed to the major El Niño event of 2015/16 considering the precipitation response to this mode of climate variability events over CWA [22].

The temporal evolution of the difference between the number of pixels/rain gauges under wet conditions based on CHIRPS-SPI and rain gauges-SPI is shown in Figure 12. Similarly to what was found for the assessment of dry conditions, the cases where widespread wet conditions are observed by CHIRPS show a large overestimation in the number of affected pixels/rain gauges. This is particularly evident for the severely wet and extremely wet categories considering the SPI3 and SPI6 between 1999 and 2007 and during 2015-2016 (Figure 12). The comparison of the spatial pattern based on rain gauges-SPI and CHIRPS-SPI during the month of April 2016 shows a similar location of the wet categories, although CHIRPS tends to overestimate the wet categories classifying a large number of pixels under extremely wet conditions in comparison with the categories based on rain gauges (Figure 13).

The spatial distribution of both dry and wet conditions is critical for impact studies. The results from this comparison allowed identifying the strengths and weakness of CHIRPS estimations for wet and dry monitoring. Even when there is a tendency towards an overestimation of both dry and wet regional events, the spatial distribution of wet and dry cases was accurately captured by CHIRPS-SPI. Nevertheless, the bias in the SPI categorization can limit the usefulness of CHIRPS for dry or wet declaration. Nowadays, the WMO RCC-SSA offers climate services in support of the National Meteorological and Hydrometeorological Services (NMHS) and other users from the countries located in the southern

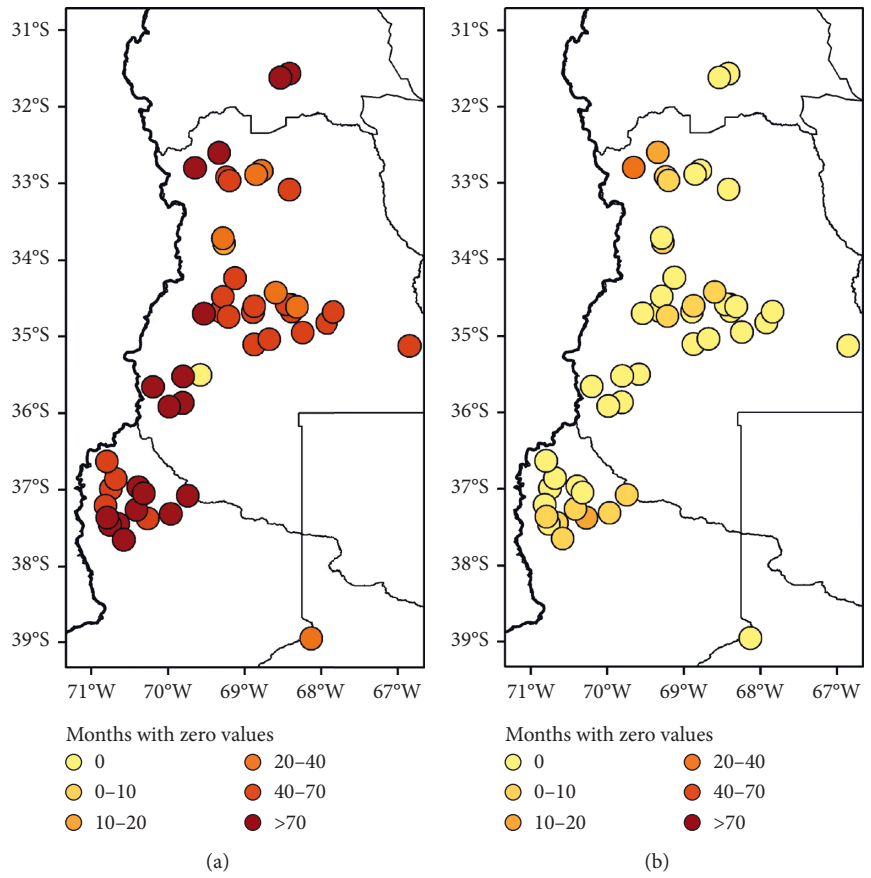


Figure 7: Frequency of zero precipitation months for each (a) rain gauge (RG) and (b) CHIRPS pixel.

South American region. Some of its monitoring tools are based on CHIRPS precipitation estimations, making the assessment performed in this paper a baseline to improve climate services over the region.

## 5. Discussion

Satellite remote sensing is increasingly being used as a complementary source of information to in situ monitoring networks and, in many cases, is the only feasible source [53]. Considering the importance of the water management for the sustainable regional development in arid and semiarid areas, much effort has gone into the development and use of satellite-based precipitation estimations for this purpose. In this sense, the performance of the CHIRPS dataset for the identification of wet and dry events was evaluated in the CWA, a semiarid region, with two distinct precipitation regimes based on available precipitation records from rain gauges, using a point-to-pixel comparison for the period 1987–2016.

Several indicators have been developed during recent decades for the monitoring of dry and wet events, based both on in situ information and remote sensing estimations, targeting aspects for meteorological, agricultural, hydrological, and socioeconomic dry and wet declaration. Each indicator has its own inherent strengths and weaknesses, and its utility is often tailored for a specific application or decision-making activity [54]. For this study, the SPI was used as a tool for the identification of wet and dry events, based on its performance for drought and wet monitoring over southern South America [22, 44, 55, 56]. This choice is also relevant given the simplicity of the SPI, considering that is calculated only based on precipitation data, being one its main advantages [57]. Considering that CHIRPS estimations only provide precipitation estimations and the meteorological stations over the study area only measure temperature in few reference stations, belonging to the National Weather Service, we consider unfair to use an index that rely on more variables for its calculation, for example, the Standardized Precipitation and Evapotranspiration Index (SPEI) [58]. In this sense, Quesada-Montano et al. [59] highlighted that the selection of the precipitation database was more important than the selection of the drought index. The use of CHIRPS precipitation estimates for drought monitoring based on the SPI has gained attraction nowadays, as shown by studies performed in Indonesia [60], China [1, 28], Nepal [11], Morocco [54], Southeast Asia [27], Central America [59], and Chile [12].

Uncertainties in the comparison of the SPI time series based on rain gauges and CHIRPS estimations arise from the input precipitation data. In the case of the observations, precipitation data have large latency (~3 months), which makes it unpractical for real-time decision-making. The sparse and uneven distribution of rain gauges also provides a

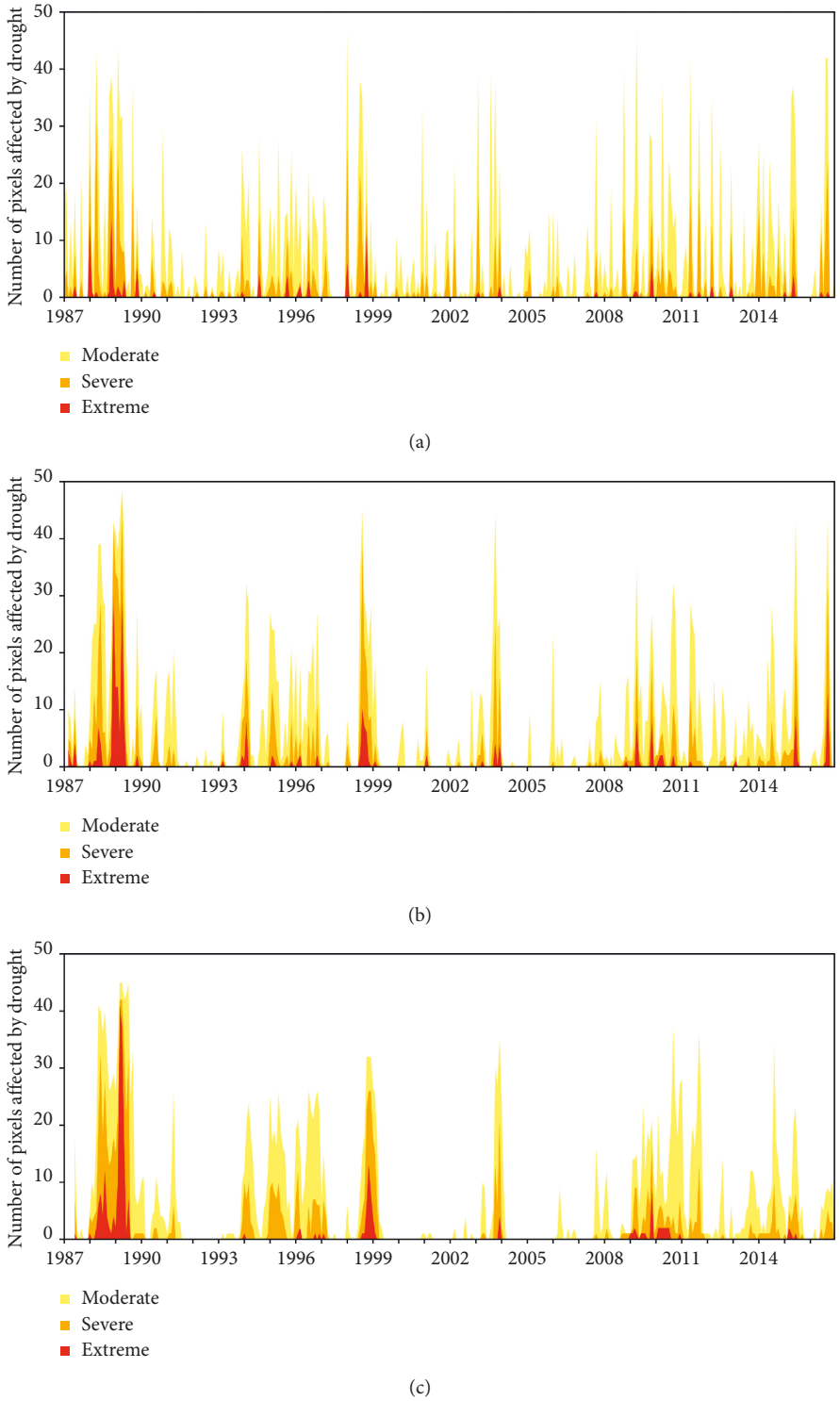


Figure 8: Temporal evolution of the number of pixels affected by dry conditions for the different dry categories and SPI timescales: (a) SPI1, (b) SPI3, and (c) SPI6.

source of uncertainty, even when the selected stations represent in an adequate way the main characteristics of precipitation over the CWA. A larger number of rain gauges can be used to overcome this limitation, however, with shorter records and without reaching the 30-year record recommendation for the estimation of the SPI parameters [46]. Moreover, gap filling methods like the linear regression used here are subject to uncertainty in the estimation of missing data. Nevertheless, given the limited number of missing months and the homogeneous behaviour of regional

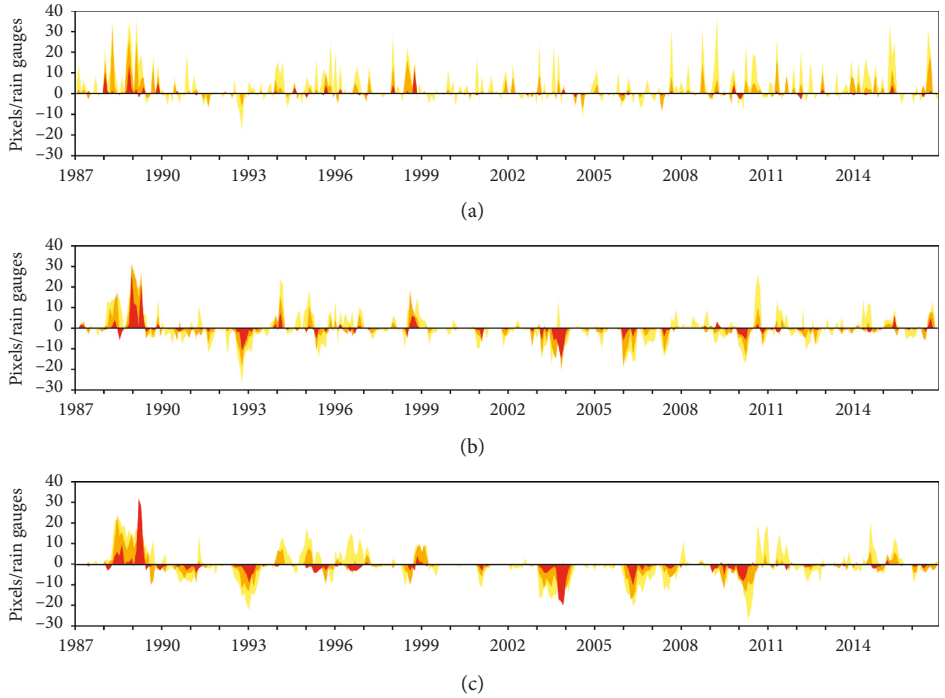


Figure 9: Temporal evolution of the difference between the number of CHIRPS pixels and the number of rain gauges with dry conditions for the different dry categories and timescales: (a) SPI1, (b) SPI3, and (c) SPI6.

precipitation, we consider that this contribution to uncertainty is negligible.

Regarding the CHIRPS estimations, one of the main sources of uncertainty arises from the anchor stations used for the blending procedure, as pointed out by Rivera et al. [24]. Firstly, in order to verify the independence of this validation, we analysed the temporal evolution of the anchor stations used in the blending procedure of CHIRPS. All the Argentinean stations were provided by the National Weather Service and obtained through either the Global Historical Climate Network (GHCN), the Global Summary of the Day (GSOD), and the World Meteorological Organization's Global Telecommunication System (GTS), as can be observed in ftp://ftp.chg.ucsb.edu/pub/org/chg/products/CHIRPS-2.0/diagnostics/monthly_station_data/. The maximum number of anchor stations during the period 1987–2016 is 12 (Figure S1, supplementary material), far from the 49 stations used in this study. A closer look to these data indicates that several of these anchor stations were discarded from our validation, like San Carlos, Uspallata, Chacras de Coria, or Cipolletti, most of them due to data issues (not shown). In this sense, we can conclude that at least 41 of the analysed stations were not included for the CHIRPS generation, which indicates that our validation can be considered as independent. Given that CHIRPS estimations are based on the use of stations from three different sources, another issue to report is the multiplication of anchor stations. In order to illustrate this, we analysed the anchor stations located over the domain 31° to 39°S and 68° to 70°W during the month of July 2015 (data accessed through ftp://ftp.chg.ucsb.edu/pub/org/chg/products/CHIRPS-2.0/diagnostics/monthly_station_data/2015.07.csv). We found that the list indicates a total of 14 anchor stations; nevertheless, Neuquén has 3 different precipitation values for that month (Neuquén Aero from GHCN 7 mm, Neuquén Aero from GSOD 7.8740001 mm, and Neuquén Airport 7.4 mm), with 3 different locations as can be seen in the latitude and longitude. The same problem can be observed for Mendoza Aero, San Juan, San Rafael, San Martín, and Malargüe. Therefore, even when the list shows the records from 14 stations, there are only 6 valid precipitation values. To evaluate how this duplication or triplication of information affects the final CHIRPS estimations is beyond the scope of this study, however, this must be considered as a potential main source of uncertainty.

## 6. Conclusions

This paper addressed some relevant features that need to be taken into account before using satellite precipitation products for regional dry and wet monitoring. Based on the SPI calculated on timescales of 1 month, 3 months, and 6 months, we used the quasi-global high-resolution CHIRPS monthly precipitation estimations to evaluate its utility over Central-Western Argentina from 1987 to 2016. This comparison was performed considering high-quality observations from 49 rain gauges over the study area. The main conclusions of this assessment can be summarized in the following:

(i) From a regional perspective, SPI time series based on CHIRPS accurately reproduce the occurrence of

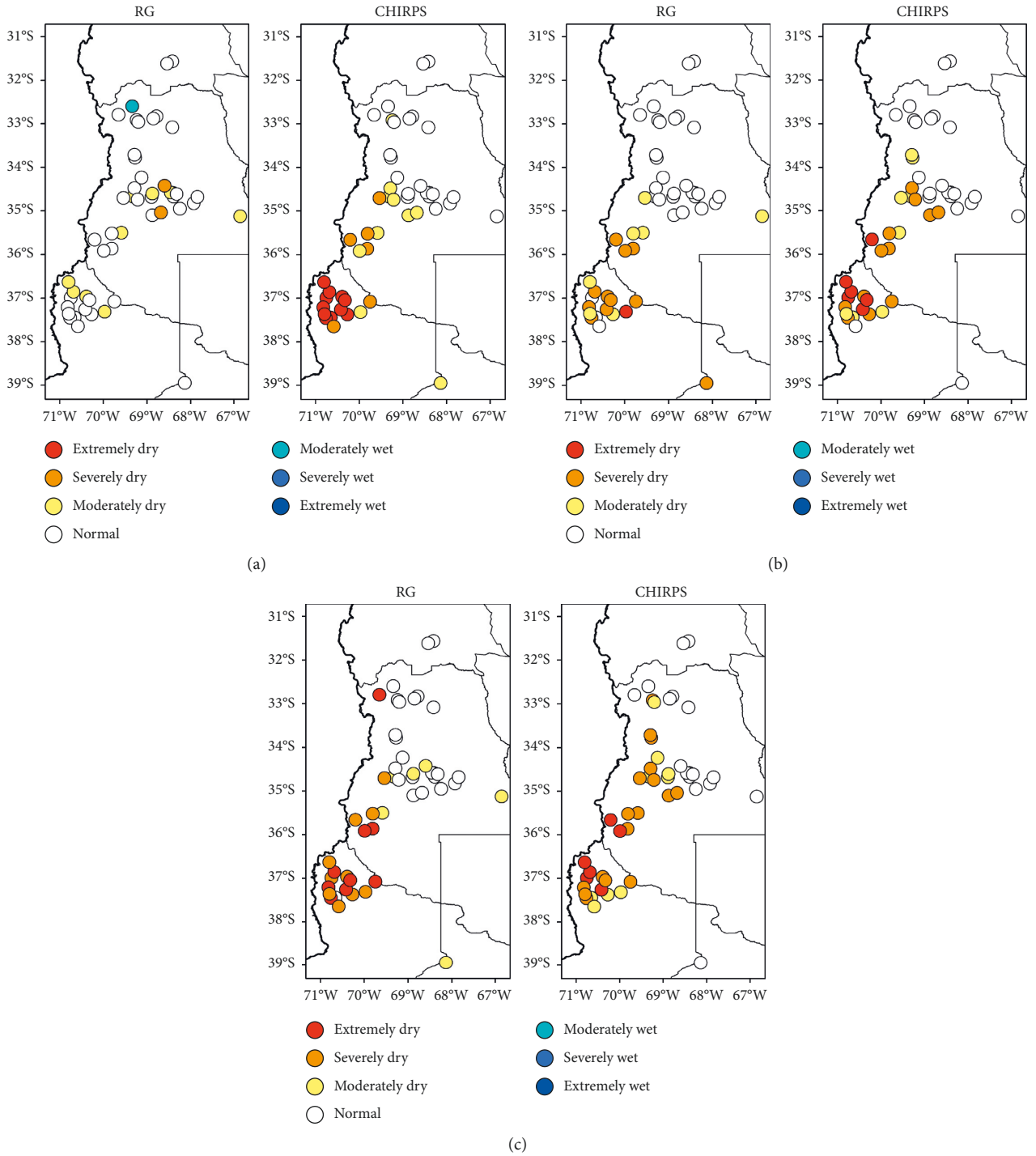


Figure 10: Spatial distribution of the SPI categories for timescales of (a) 1 month, (b) 3 months, and (c) 6 months during October 1998 considering rain gauges (RG) and CHIRPS estimations.

wet and dry conditions over the CWA. Considering the stations located in the region dominated by summer precipitation, the correlation between observations and CHIRPS estimations is significant ($r > 0.8$, $p < 0.01$). Even when the product exhibits a marked wet bias over the region dominated by winter precipitation, the temporal variability of the SPI resembles the observations ($r > 0.78$, $p < 0.01$), showing the suitability of the product for the SPI calculation.

(ii) For the monitoring and assessment of dry conditions over arid to semiarid regions like the CWA, it is recommended that the timescale for the calculation of the SPI based on CHIRPS estimations needs to be larger than 1 month. This is related to the bias in the frequency of zero values in

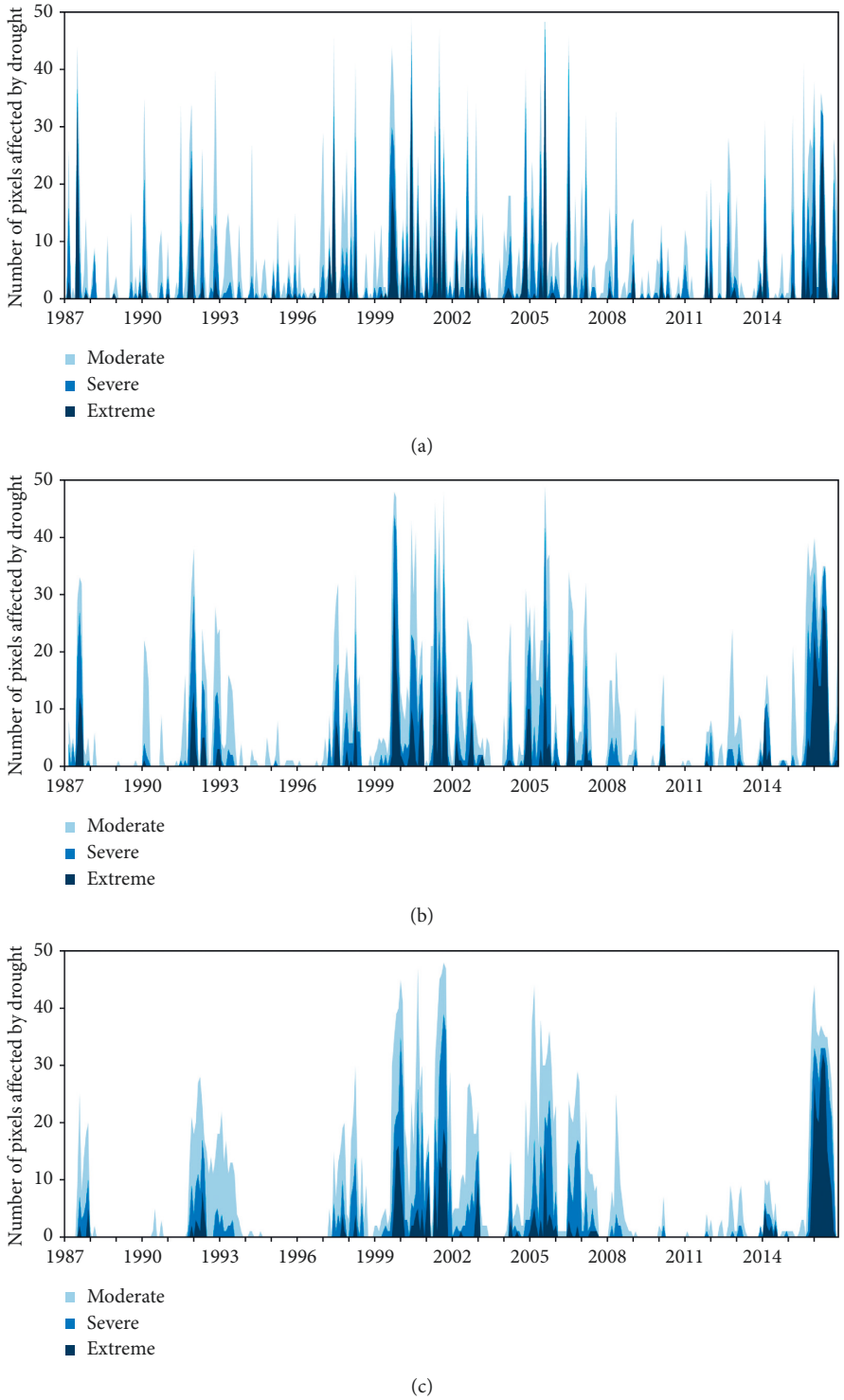


Figure 11: Temporal evolution of the number of pixels affected by wet conditions for the different wet categories and SPI timescales: (a) SPI1, (b) SPI3, and (c) SPI6.

comparison with the rain gauge observations, which fictitiously avoid the lower bounded SPI time series and lead to a normally distributed SPI.

(iii) The spatial pattern of selected wet and dry cases was accurately reproduced by CHIRPS, although there was a bias in the SPI categories towards extreme conditions. This drawback can affect its suitability for drought and excess declaration by the regional agencies. In this sense, the values for severe and extreme dry and wet classes based on CHIRPS-SPI should be complemented with in situ information for a more precise quantification of drought intensity.

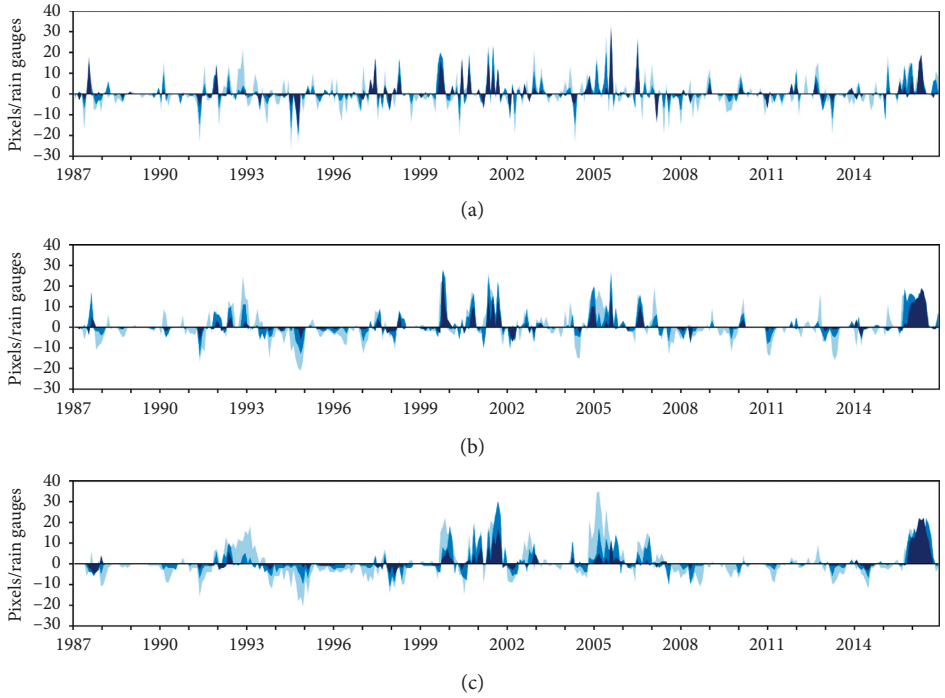


Figure 12: Temporal evolution of the difference between the number of CHIRPS pixels and the number of rain gauges with wet conditions for the different wet categories and timescales: (a) SPI1, (b) SPI3, and (c) SPI6.

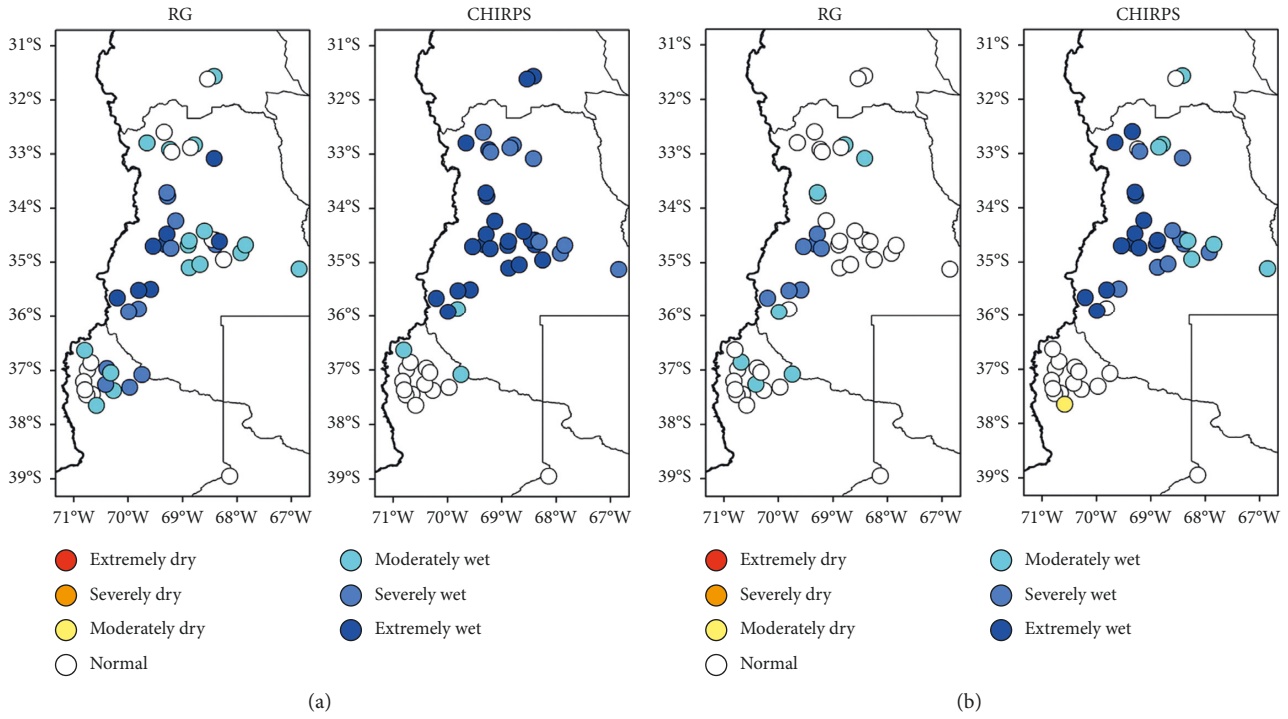


Figure 13: Continued.

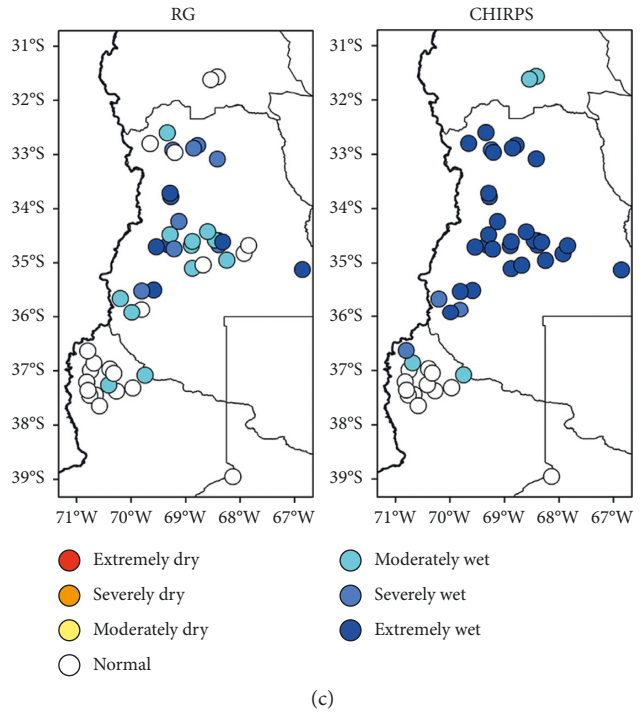


Figure 13: Spatial distribution of the SPI categories for timescales of (a) 1 month, (b) 3 months, and (c) 6 months during April 2016 considering rain gauges (RG) and CHIRPS estimations.

Considering the relatively short latency (~3 weeks) of the final CHIRPS product, available after blending with several station sources, its adequate performance for the identification of wet and dry events over the study area, and the sparse and uneven distribution of rain gauges along the CWA, this study provides a promising prospect of hydrometeorological utility of CHIRPS estimations. Given the ongoing efforts for precipitation monitoring and declaration of drought and flood conditions, this assessment can provide some insights into regarding the use of CHIRPS for the SPI calculation and application over an arid to semiarid region, making extensible the results to other similar areas with complex topography.

Future research should focus on the methodological aspects of the SPI calculation, considering several choices of probability distribution functions for the representation of precipitation. Moreover, operational thresholds for the definition of dry and wet conditions can also provide valuable information for decision-making, given that drought and flood monitoring is of paramount importance considering the socioeconomic activities over the region. Future validation studies should also include the Climate Hazards Group Infrared Precipitation (CHIRP) satellite-only product, given its short latency (available 2 days after the end of a pentad) and its performance after 1992 [11].

## Data Availability

Monthly precipitation records from 41 of the analysed sites can be accessed online through the Integrated Hydrological Database from the Water Resources Agency of Argentina (http://bdhi.hidricos.gob.ar). The records from the remaining 8 sites can be freely requested to the National Weather Service of Argentina through its Meteorological Information Center (cim@smn.gob.ar). The code for the calculation of the Standardized Precipitation Index can be obtained at http://drought.unl.edu/droughtmonitoring/SPI/SPIProgram.aspx. The CHIRPS products can be accessed through ftp://ftp.chg.ucsb.edu/pub/org/chg/products/CHIRPS-2.0.

## Conflicts of Interest

The authors declare that there are no conflicts of interest regarding the publication of this paper.

## Acknowledgments

The authors would like to thank Editor Minha Choi and the two anonymous reviewers for their valuable comments and critical reading of the manuscript. The authors thank Subsecretaría de Recursos Hídricos de Argentina and Servicio Meteorológico Nacional for providing the precipitation records used in the study. This work was supported by the National Agency for Scientific and Technological Promotion (ANPCyT) (Grant number PICT-2016-0431).

## Supplementary Materials

Figure S1: number of anchor stations used for the estimation of CHIRPS dataset in the domain 31°–39°S; 67°–71°W. Period 1987–2016. (*Supplementary Materials*)

## References


[1] F. Gao, Y. Zhang, X. Ren, Y. Yao, Z. Hao, and W. Cai, "Evaluation of CHIRPS and its application for drought monitoring over the Haihe River basin, China," *Natural Hazards*, vol. 92, no. 1, pp. 155–172, 2018.

[2] P. Nguyen, M. Ombadi, S. Sorooshian et al., "The PERSIANN family of global satellite precipitation data: a review and evaluation of products," *Hydrology and Earth System Sciences*, vol. 22, no. 11, pp. 5801–5816, 2018.

[3] R. J. Joyce, J. E. Janowiak, P. A. Arkin, and P. Xie, "CMORPH: a method that produces global precipitation estimates from passive microwave and infrared data at high spatial and temporal resolution," *Journal of Hydrometeorology*, vol. 5, no. 3, pp. 487–503, 2004.

[4] T. Ushio, K. Sasashige, T. Kubota et al., "A Kalman filter approach to the Global Satellite Mapping of Precipitation (GSMaP) from combined passive microwave and infrared radiometric data," *Journal of the Meteorological Society of Japan*, vol. 87A, pp. 137–151, 2009.

[5] G. J. Huffman, D. T. Bolvin, E. J. Nelkin et al., "The TRMM multisatellite precipitation analysis (TMPA): quasi-global, multiyear, combined-sensor precipitation estimates at fine scales," *Journal of Hydrometeorology*, vol. 8, no. 1, pp. 38–55, 2007.

[6] H. E. Beck, A. I. J. M. van Dijk, V. Levizzani et al., "MSWEP: 3-hourly 0.25 global gridded precipitation (1979–2015) by merging gauge, satellite, and reanalysis data," *Hydrology and Earth System Sciences*, vol. 21, no. 1, pp. 589–615, 2017.

[7] H. E. Beck, N. Vergopolan, M. Pan et al., "Global-scale evaluation of 22 precipitation datasets using gauge observations and hydrological modeling," *Hydrology and Earth System Sciences*, vol. 21, no. 12, pp. 6201–6217, 2017.

[8] H. Ashouri, K.-L. Hsu, S. Sorooshian et al., "PERSIANN-CDR: daily precipitation climate data record from multisatellite observations for hydrological and climate studies," *Bulletin of the American Meteorological Society*, vol. 96, no. 1, pp. 69–83, 2015.

[9] C. Funk, P. Peterson, M. Landsfeld et al., "The climate hazards infrared precipitation with stations—a new environmental record for monitoring extremes," *Scientific Data*, vol. 2, article 150066, 2015.

[10] L. Bai, C. Shi, L. Li, Y. Yang, and J. Wu, "Accuracy of CHIRPS satellite-rainfall products over mainland China," *Remote Sensing*, vol. 10, no. 3, article 362, 2018.

[11] N. K. Shresta, F. M. Qamer, D. Pedreros et al., "Evaluating the accuracy of Climate Hazard Group (CHG) satellite rainfall estimates for precipitation based drought monitoring in Koshi basin, Nepal," *Journal of Hydrology: Regional Studies*, vol. 13, pp. 138–151, 2017.

[12] F. Zambrano, B. Wardlow, T. Tadesse, M. Lillo-Saavedra, and O. Lagos, "Evaluating satellite-derived long-term historical precipitation datasets for drought monitoring in Chile," *Atmospheric Research*, vol. 186, pp. 26–42, 2017.

[13] D. López-Carr, N. G. Pricope, J. E. Aukema et al., "A spatial analysis of population dynamics and climate change in Africa: potential vulnerability hot spots emerge where precipitation declines and demographic pressures coincide," *Population and Environment*, vol. 35, no. 3, pp. 323–339, 2014.

[14] R. I. Maidment, R. P. Allan, and E. Black, "Recent observed and simulated changes in precipitation over Africa," *Geophysical Research Letters*, vol. 42, no. 19, pp. 8155–8164, 2015.

[15] G. Zittis, "Observed rainfall trends and precipitation uncertainty in the vicinity of the Mediterranean, Middle East and North Africa," *Theoretical and Applied Climatology*, vol. 134, no. 3-4, pp. 1207–1230, 2018.

[16] N. Vigaud, B. Lyon, and A. Giannini, "Sub-seasonal teleconnections between convection over the Indian Ocean, the East African long rains and tropical Pacific surface temperatures," *International Journal of Climatology*, vol. 37, no. 3, pp. 1167–1180, 2017.

[17] J. C. Espinoza, J. Ronchail, J. A. Marengo, and H. Segura, "Contrasting North–South changes in Amazon wet-day and dry-day frequency and related atmospheric features (1981–2017)," *Climate Dynamics*, vol. 52, 2018.

[18] F. J. Tapiador, A. Navarro, V. Levizzani et al., "Global precipitation measurements for validating climate models," *Atmospheric Research*, vol. 197, pp. 1–20, 2017.

[19] M. Viale and F. A. Norte, "Strong cross-barrier flow under stable conditions producing intense winter orographic precipitation: a case study over the subtropical Central Andes," *Weather and Forecasting*, vol. 24, no. 4, pp. 1009–1031, 2009.

[20] J. R. Santos, F. Norte, S. Moreiras, D. Araneo, and S. Simonelli, "Predicción de episodios de precipitación que ocasionan aludes en el área montañosa del noroeste de la provincia de Mendoza, Argentina," *Geoacta*, vol. 40, pp. 65–75, 2015.

[21] A. Calori, J. R. Santos, M. Blanco et al., "Ground-based GNSS network and integrated water vapor mapping during the development of severe storms at the Cuyo region (Argentina)," *Atmospheric Research*, vol. 176-177, pp. 267–275, 2016.

[22] O. C. Penalba and J. A. Rivera, "Precipitation response to El Niño/La Niña events in Southern South America—emphasis in regional drought occurrences," *Advances in Geosciences*, vol. 42, pp. 1–14, 2016.

[23] J. Rivera, O. Penalba, R. Villalba, and D. Araneo, "Spatio-temporal patterns of the 2010–2015 extreme hydrological drought across the Central Andes, Argentina," *Water*, vol. 9, no. 9, p. 652, 2017.

[24] J. A. Rivera, G. Marianetti, and S. Hinrichs, "Validation of CHIRPS precipitation dataset along the Central Andes of Argentina," *Atmospheric Research*, vol. 213, pp. 437–449, 2018.

[25] D. Falaschi, A. Kääb, F. Paul et al., "Brief communication: collapse of 4 $mm^3$ of ice from a cirque glacier in the Central Andes of Argentina," *The Cryosphere*, vol. 13, pp. 997–1004, 2019.

[26] O. V. Müller, M. A. Lovino, and E. H. Berbery, "Evaluation of WRF model forecasts and their use for hydroclimate monitoring over southern South America," *Weather and Forecasting*, vol. 31, no. 3, pp. 1001–1017, 2016.

[27] H. Guo, A. Bao, T. Liu et al., "Meteorological drought analysis in the lower Mekong Basin using satellite-based long-term CHIRPS product," *Sustainability*, vol. 9, no. 6, p. 901, 2017.

[28] R. Zhong, X. Chen, C. Lai et al., "Drought monitoring utility of satellite-based precipitation products across mainland China," *Journal of Hydrology*, vol. 568, pp. 343–359, 2019.

[29] R. H. Compagnucci, E. A. Agosta, and W. M. Vargas, "Climatic change and quasi-oscillations in central-west Argentina summer precipitation: main features and coherent behaviour with southern African region," *Climate Dynamics*, vol. 18, no. 5, pp. 421–435, 2002.

[30] V. Castex, E. M. Tejeda, and M. Beniston, "Water availability, use and governance in the wine producing region of Mendoza, Argentina," *Environmental Science & Policy*, vol. 48, pp. 1–8, 2015.

[31] T. B. McKee, N. J. Doesken, and J. Kleist, "The relationship of drought frequency and duration to time scales," in *Proceedings of the Eight Conference on Applied Climatology*,

pp. 179–184, American Meteorological Society, Anaheim, CA, USA, January 1993.

[32] M. Falvey and R. Garreaud, "Wintertime precipitation episodes in Central Chile: associated meteorological conditions and orographic influences," *Journal of Hydrometeorology*, vol. 8, no. 2, pp. 171–193, 2007.

[33] R. H. Compagnucci and W. M. Vargas, "Inter-annual variability of the Cuyo rivers' streamflow in the Argentinean Andes mountains and ENSO events," *International Journal of Climatology*, vol. 18, no. 14, pp. 1593–1609, 1998.

[34] W. Schwerdtfeger, "The atmospheric circulation over Central and South America," in *Climates of Central and South America*, W. Schwerdtfeger, Ed., vol. 2, pp. 2–12, Elsevier, New York, NY, USA, 1976.

[35] R. D. Garreaud, "The Andes climate and weather," *Advances in Geosciences*, vol. 22, pp. 3–11, 2009.

[36] M. H. Masiokas, R. Villalba, B. H. Luckman, C. Le Quesne, and J. C. Aravena, "Snowpack variations in the Central Andes of Argentina and Chile, 1951–2005: large-scale atmospheric influences and implications for water resources in the region," *Journal of Climate*, vol. 19, no. 24, pp. 6334–6352, 2006.

[37] M. B. Richman, "Rotation of principal components," *Journal of Climatology*, vol. 6, no. 3, pp. 293–335, 1986.

[38] J. A. Rivera, D. C. Araneo, O. C. Penalba, and R. Villalba, "Regional aspects of streamflow droughts in the Andean rivers of Patagonia, Argentina. Links with large-scale climatic oscillations," *Hydrology Research*, vol. 49, no. 1, pp. 134–149, 2018.

[39] L. O. Bianchi, J. A. Rivera, F. Rojas, M. Britos Navarro, and R. Villalba, "A regional water balance indicator inferred from satellite images of an Andean endorheic basin in central-western Argentina," *Hydrological Sciences Journal*, vol. 62, no. 4, pp. 533–545, 2017.

[40] C. Vera, J. Baez, M. Douglas et al., "The South American low-level jet experiment," *Bulletin of the American Meteorological Society*, vol. 87, no. 1, pp. 63–78, 2006.

[41] H. Teitelbaum, H. L. Treut, M. Moustaoui, G. C. Cabrera, and G. Ibañez, "Deep convec- tion east of the Andes Cordillera: a test case analysis of airmass origin," *Monthly Weather Review*, vol. 136, no. 6, pp. 2201–2209, 2008.

[42] M. Viale and M. N. Nuñez, "Climatology of winter orographic precipitation over the subtropical Central Andes and associated synoptic and regional characteristics," *Journal of Hydrometeorology*, vol. 12, no. 4, pp. 481–507, 2011.

[43] F. J. Paredes-Trejo, H. A. Barbosa, and T. V. Lakshmi Kumar, "Validating CHIRPS-based satellite precipitation estimates in Northeast Brazil," *Journal of Arid Environments*, vol. 139, pp. 26–40, 2017.

[44] O. C. Penalba and J. A. Rivera, "Comparación de seis índices para el monitoreo de sequías meteorológicas en el sur de Sudamérica," *Meteorológica*, vol. 40, no. 2, pp. 33–57, 2015.

[45] B. Lloyd-Hughes and M. A. Saunders, "A drought climatology for Europe," *International Journal of Climatology*, vol. 22, no. 13, pp. 1571–1592, 2002.

[46] World Meteorological Organization (WMO), *Standardized Precipitation Index User Guide*, WMO No. 1090, Geneva, Switzerland, 2012.

[47] J. A. Rivera and O. C. Penalba, "Spatio-temporal assessment of streamflow droughts over Southern South America: 1961–2006," *Theoretical and Applied Climatology*, vol. 133, no. 3-4, pp. 1021–1033, 2017.

[48] M. Naresh Kumar, C. S. Murthy, M. V. R. Sesha Sai, and P. S. Roy, "On the use of Standardized Precipitation Index (SPI) for drought intensity assessment," *Meteorological Applications*, vol. 16, no. 3, pp. 381–389, 2009.

[49] H. Wu, M. D. Svoboda, M. J. Hayes, D. A. Wilhite, and F. Wen, "Appropriate application of the Standardized Precipitation Index in arid locations and dry seasons," *International Journal of Climatology*, vol. 27, no. 1, pp. 65–79, 2007.

[50] C. C. Funk, P. J. Peterson, M. F. Landsfeld et al., "A quasi-global precipitation time series for drought monitoring," *U.S. Geological Survey Publication Series*, vol. 832, 2014.

[51] D. Katsanos, A. Retalis, and S. Michaelides, "Validation of a high-resolution precipitation database (CHIRPS) over Cyprus for a 30-year period," *Atmospheric Research*, vol. 169, pp. 459–464, 2016.

[52] J. A. Rivera and O. C. Penalba, "Distribución de probabilidades de los caudales mensuales en las regiones de Cuyo y Patagonia (Argentina). Aplicación al monitoreo de sequías hidrológicas," *Meteorológica*, vol. 43, no. 2, pp. 25–46, 2018.

[53] J. Sheffield, E. F. Wood, M. Pan et al., "Satellite remote sensing for water resources management: potential for supporting sustainable development in data-poor regions," *Water Resources Research*, vol. 54, no. 12, 2018.

[54] N. Bijaber, D. El Hadani, M. Saidi et al., "Developing a remotely sensed drought monitoring indicator for Morocco," *Geosciences*, vol. 8, no. 2, p. 55, 2018.

[55] R. A. Seiler, M. Hayes, and L. Bressan, "Using the standardized precipitation index for flood risk monitoring," *International Journal of Climatology*, vol. 22, no. 11, pp. 1365–1376, 2002.

[56] C. M. Krepper and V. Zucarelli, "Climatology of water excess and shortages in the La plata basin," *Theoretical and Applied Climatology*, vol. 102, pp. 13–27, 2012.

[57] A. K. Mishra and V. P. Singh, "A review of drought concepts," *Journal of Hydrology*, vol. 391, no. 1-2, pp. 202–216, 2010.

[58] S. M. Vicente-Serrano, S. Beguería, and J. I. López-Moreno, "A multiscalar drought index sensitive to global warming: the standardized precipitation evapotranspiration index," *Journal of Climate*, vol. 23, no. 7, pp. 1696–1718, 2010.

[59] B. Quesada-Montano, F. Wetterhall, I. K. Westerberg, H. G. Hidalgo, and S. Halldin, "Characterising droughts in Central America with uncertain hydro-meteorological data," *Theoretical and Applied Climatology*, 2018.

[60] A. M. Setiawan, Y. Koesmaryono, A. Faqih, and D. Gunawan, "Observed and blended gauge-satellite precipitation estimates perspective on meteorological drought intensity over South Sulawesi, Indonesia," *IOP Conference Series: Earth and Environmental Science*, vol. 54, article 012040, 2017.